



# Nanocomposite hydrogels from the self-assembly of an amphiphilic polymer and fullerene

Théo Merland

## ► To cite this version:

Théo Merland. Nanocomposite hydrogels from the self-assembly of an amphiphilic polymer and fullerene. Polymers. Le Mans Université, 2021. English. NNT : 2021LEMA1038 . tel-03604230

**HAL Id: tel-03604230**

**<https://theses.hal.science/tel-03604230>**

Submitted on 10 Mar 2022

**HAL** is a multi-disciplinary open access archive for the deposit and dissemination of scientific research documents, whether they are published or not. The documents may come from teaching and research institutions in France or abroad, or from public or private research centers.

L'archive ouverte pluridisciplinaire **HAL**, est destinée au dépôt et à la diffusion de documents scientifiques de niveau recherche, publiés ou non, émanant des établissements d'enseignement et de recherche français ou étrangers, des laboratoires publics ou privés.

# THESE DE DOCTORAT DE

LE MANS UNIVERSITE  
COMUE UNIVERSITE BRETAGNE LOIRE

ECOLE DOCTORALE N° 596  
*Matière, Molécules, Matériaux*  
Spécialité : « *Chimie et Physico-Chimie des Polymères* »

Par

**Théo MERLAND**

## **Nanocomposite hydrogels from the self-assembly of an amphiphilic polymer and fullerene**

Thèse présentée et soutenue à Le Mans, le 15 décembre 2021  
Unité de recherche : Institut des Molécules et Matériaux du Mans – UMR CNRS 6283  
MOLTECH Anjou – UMR CNRS 6200  
Thèse N° : 2021LEMA1038

### **Rapporteurs avant soutenance :**

François Ganachaud    Directeur de recherches CNRS, INSA Lyon  
Fabrice Cousin        Ingénieur de recherches, CEA Saclay

### **Composition du Jury :**

Examineurs :	Fabienne Gauffre	Directrice de recherches CNRS, Université de Rennes 1
	François Ganachaud	Directeur de recherches CNRS, INSA Lyon
	Fabrice Cousin	Ingénieur de recherches, CEA Saclay
	Thierry Aubry	Professeur, Université de Bretagne Occidentale
Dir. de thèse :	Christophe Chassenieux	Professeur, Le Mans Université
Co-dir. de thèse :	Stéphanie Legoupy	Directrice de recherches CNRS, Université d'Angers
Co-encadrant :	Lazhar Benyahia	Professeur, Le Mans Université

### **Invité**

Marc Schmutz            Ingénieur de recherches CNRS, ICS Strasbourg



## Remerciements

Je tiens tout d'abord à remercier mes encadrants : Christophe, qui m'a pris sous son aile dès le Master et qui m'a accordé sa confiance en me confiant un stage puis cette thèse. Tu m'as énormément appris, bien sûr scientifiquement mais aussi culturellement (il faut dire qu'on part de loin), professionnellement et humainement. J'ai particulièrement aimé parler musique avec toi, je suis très heureux d'avoir enfin trouvé quelqu'un qui partage mes goûts pour la musique parisienne mais aussi la brit pop et j'en passe. Je suis content de t'avoir fait découvrir plus d'un groupe/artiste, et que tu m'aies également ouvert à beaucoup de nouveautés (vive les voix féminines !). Il faut quand même préciser que j'ai dû faire preuve de beaucoup de résilience notamment pour garder mes cheveux longs (Monsieur est accro aux ciseaux !). Merci aussi à Lazhar, notre chef et spécialiste toucans, qui m'a mis le pied à l'étrier en m'accueillant le premier au laboratoire quand j'étais encore un bébé, et qui m'a fait attraper le virus de la recherche ! On s'est bien amusé et je retiendrai de toi cette phrase : « Toujours faire les choses sérieusement mais ne pas se prendre au sérieux ». J'ai hésité avec « à fond la fourme ! » mais ça claquait moins. Merci aussi à Taco, qui était l'encadrant non-officiel de cette thèse et qui a toujours été présent quand on avait besoin de lui, notamment lors du séjour de mon chef outre-Atlantique. Je te suis très reconnaissant de m'avoir consacré autant de temps et apporté beaucoup scientifiquement. Enfin, merci à Stéphanie, qui est arrivée dans cette maison de fous mais qui a tenu bon face à l'opresseur de sacs à mains et autres accessoires de mode. On ne t'a pas épargnée avec ce sujet qui a tourné très fort à la physico et pourtant tu t'es accrochée et tu m'as soutenu tout le long de ma thèse, merci à toi.

Cette thèse a été principalement réalisée à l'IMMM dans l'équipe PCI, que je tiens à remercier pour leur accueil chaleureux pendant presque 5 ans. Merci notamment à Lingsam, qui a daigné laisser mes genoux intacts ; Justine, même si je me suis pris quelques oufballs dans la tronche ; Yuwen, avec qui on s'est beaucoup serré les coudes ; Elise, alias Pipo la pie, avec qui on n'a jamais réussi à avoir une conversation de moins d'une heure ; Marisol, avec qui on a passé de bonnes soirées ; David et Hien aussi (on boit bien avec les plasmiciens !) ; Gireesh, contre qui j'ai dû LUTTER pour qu'il range ses affaires ; Rémy, mon compagnon d'armes de Master ; mais aussi Noémie, Toutoune, Ahmad, João, Clémence, Inès, Cécile, Toto, Viet, Julien et j'en oublie sûrement. Merci aussi à Cyrille, Frédérick et Boris pour leur aide sur les manips et leur sympathie, Fabienne que j'ai souvent embêtée pour l'administratif, et Frédéric qui m'a beaucoup aidé avec les TP. Merci enfin à Olivier et Erwan pour nos discussions riches et variées.



Merci aux stagiaires que j'ai encadrés pendant ma thèse, à savoir Mathieu, Camille, Clément et Khalil. J'ai pris beaucoup de plaisir à travailler avec vous, j'espère que vous avez appris des choses et apprécié le temps passé au labo.

Je ne me suis pas cantonné à PCI. Merci donc à Anthony pour le TEM, François et Sandy pour la WAXS, Héloïse pour les ATG, Danielle, Elodie et Maxime pour l'administratif et les copains doctorants Wenhao, Juliette, Valentine, Meryem, Wafa et Antoine.

Merci aussi aux membres de la cellule de site de l'ED avec qui j'ai beaucoup appris. Un merci tout particulier à Geoffroy, qui m'a beaucoup aidé et qui fait beaucoup pour les doctorants du Mans de manière générale.

Cette thèse a été réalisée en collaboration avec MOLTECH-Anjou, dans le cadre du programme SPEED (Smart sustainable PolymErs and procEss Development) qui visait à développer la recherche dans le domaine des polymères via une collaboration entre deux laboratoires de la région Pays de la Loire. A titre personnel, j'ai adoré passer du temps à MOLTECH, que je remercie pour leur accueil. Merci particulièrement à Clément, avec qui il n'est pas possible de ne pas s'entendre !

Merci aussi à Marc Schmutz, notre microscopiste attitré qui nous a fait beaucoup avancer sur la fin de la thèse, à qui on doit la découverte majeure de cette thèse, et qui s'est beaucoup investi dans ce travail. Merci à Fabrice Cousin qui m'avait appris la SANS en début de thèse lors des FAN du LLB, et qui m'a ensuite appris la SAXS et permis d'en faire sur des échantillons, et avec qui il a été très agréable de discuter tant de science que de sujets plus vastes. Merci également à Fabienne Gauffre, Thierry Aubry et François Ganachaud avec qui nous avons eu de riches échanges, y compris dans le cadre de mon CSI pour les deux premiers. Merci à toutes ces personnes d'avoir accepté de faire partie de mon jury et d'avoir jugé mon travail.

Enfin je remercie mon entourage pour leur soutien pendant ce marathon : Papa, Bibu, Bilout', Loulou, Mamée, Papy, Jacques, et toute la famille, et puis les copains : Florent, Tomtom, Dmytro, Lélé, Samy, Gwelloné, Cédric, Antonio Grimauli...

Des bisous.





# Table of contents

General introduction .....	1
Chapter 1. State of the art .....	7
1) Buckminsterfullerene .....	7
a. General aspects .....	7
i. History .....	7
ii. Chemical structure .....	8
b. C <sub>60</sub> in organic medium .....	9
i. Apolar organic solvents .....	9
ii. Polar organic solvents .....	11
iii. Reactivity with aliphatic amines .....	12
2) Dispersion in water .....	13
a. Emulsification-evaporation .....	13
b. Nanoprecipitation .....	17
i. Ouzo effect .....	17
ii. Rate-controlled injection methods .....	21
iii. Dialysis method .....	23
c. Other methods .....	24
3) Stabilisation of fullerene nanoparticles in water .....	25
a. Stability origin .....	25
b. Stabilisation by surface active agents .....	27
i. Molecular surfactants .....	28
ii. Amphiphilic or hydrophilic polymers .....	30
c. Chemical modification .....	38
i. Hydrophilic functions grafting .....	38
ii. Covalent binding to polymers .....	41
4) Properties of fullerene aggregates in water .....	42
a. Chemical and biological properties .....	42
b. Physical properties .....	45
5) Hydrogels formed by self-assembly of polysoaps .....	49
a. General features of hydrogels .....	49
b. Reinforcement strategies .....	52
i. Topological gels .....	52
ii. Double or interpenetrated networks .....	53
iii. Ionic gels .....	54
iv. Nanocomposite gels .....	56

c. Nanocarbon-containing hydrogels .....	59
d. Cationic polysoaps based on polystyrene backbones.....	61
References .....	67
Chapter 2. Materials and methods.....	85
1) Amphiphilic polymer synthesis .....	85
a. Precursor synthesis.....	85
i. Experimental protocol .....	85
ii. Characterization.....	86
b. Functionalization by a tertiary amine .....	89
i. Experimental protocol .....	89
ii. Characterization.....	89
iii. 75C12 aqueous solutions .....	90
2) Preparation of C <sub>60</sub> aqueous colloidal suspensions .....	92
a. Mother solutions in organic solvents.....	92
b. Dispersion of C <sub>60</sub> in water by emulsification-evaporation .....	93
c. Freeze-drying/re-dispersion.....	94
d. Ouzo effect.....	94
3) Chemical composition.....	95
a. UV-visible spectroscopy .....	95
b. Thermogravimetric analysis (TGA).....	97
c. Analytical centrifugation .....	97
4) Scattering techniques .....	99
a. Generalities on scattering techniques.....	99
b. Static Light Scattering (SLS) .....	101
c. Dynamic Light Scattering (DLS) .....	102
d. Small-Angle X-Ray Scattering (SAXS) .....	103
e. Wide-Angle X-Ray Scattering/Diffraction (WAXS/WAXD).....	104
5) Microscopy .....	105
a. Transmission electron microscopy .....	105
i. Dried TEM .....	105
ii. Cryo-TEM .....	105
b. Confocal Laser Scanning Microscopy (CLSM) .....	105
c. Raman scattering and fluorescence .....	105
6) Rheology .....	106
a. Flow measurements.....	106
b. Dynamic rheology .....	107
c. Rheological study of 75C12 in water .....	108

References .....	111
Chapter 3. Self-Assembly in water of C <sub>60</sub> fullerene into isotropic nanoparticles or nanoplatelets mediated by a cationic amphiphilic polymer.....	115
1) Preparation of aqueous C <sub>60</sub> colloidal suspensions .....	115
a. Emulsification-evaporation process .....	115
b. UV-visible light absorption of C <sub>60</sub> dispersed in water .....	120
c. Concentration of C <sub>60</sub> in water .....	123
d. Stability of the particles dispersions.....	125
2) Characterization of the particles.....	128
a. Size and molar mass of the C <sub>60</sub> particles.....	128
b. Morphology of the C <sub>60</sub> particles .....	133
3) Discussion .....	137
a. Mechanism of C <sub>60</sub> particles formation .....	137
b. Morphology and size of the C <sub>60</sub> particles .....	139
Conclusion.....	141
References .....	142
Chapter 4. Structure and physical properties of C <sub>60</sub> nanoplatelets .....	145
1) Size of the nanoplatelets.....	145
a. Influence of $\Phi_{org}$ on the nanoplatelets size .....	145
b. Size of the nanoplatelets .....	149
2) Internal structure.....	150
a. Structure in SAXS .....	150
b. Raman scattering .....	152
c. Wide Angle X-Ray diffraction.....	154
3) Formation of nanoplatelets with other stabilizers.....	157
a. Other XCn polymers.....	157
b. De-formulation of cationic polymers .....	159
4) Fluorescence of C <sub>60</sub> nanoplatelets .....	162
Conclusions .....	164
References .....	165
Chapter 5. Nanocomposite hydrogels functionalized by C <sub>60</sub> nanoplatelets: effect on the mechanical properties .....	169
1) Elaboration and characterization of the nanocomposite hydrogels.....	169
a. Composition of the fullerene/polymer composite powders .....	169
b. Preparation of the nanocomposite hydrogels.....	170
c. Structure of the nanocomposite hydrogels .....	171
2) Rheological properties of the nanocomposite hydrogels .....	173
a. Stiffness and dynamics of the networks.....	173

b. Non-linear mechanical properties .....	177
Conclusions .....	179
References .....	180
Chapter 6. C <sub>60</sub> aqueous colloidal suspensions by Ouzo effect .....	183
1) Solutions of C <sub>60</sub> in n-butylamine .....	183
a. Choice of the co-solvent .....	183
b. Interactions between C <sub>60</sub> and n-butylamine .....	184
2) Elaboration of Ouzo C <sub>60</sub> particles .....	188
a. Ouzo region mapping .....	188
b. Stability upon ageing .....	189
c. Characterization of the particles .....	192
i. Morphology .....	192
ii. Influence of the volume fraction of C <sub>60</sub> solution .....	193
iii. Influence of fullerene concentration .....	197
3) Stabilization by 75C12 .....	198
a. Effect on the state diagram and stability .....	198
b. Effect on the size of the particles .....	200
Conclusions .....	203
References .....	205
General conclusion .....	209
References .....	212







## General introduction

This PhD project was about a marriage between two worlds.

On one hand, Buckminsterfullerene ( $C_{60}$ ) is the most common member of the fullerenes family, which are the zero-dimensional allotropic forms of carbon. Fullerenes have been discovered in 1985 by Curl, Smalley and Kroto, who received the Nobel Prize in Chemistry in 1996 for this discovery. These cages only made of carbon atoms possess many  $\pi$ -electrons, which provides them a high potential for applications in optics, optoelectronics, and medicine. For the latter in particular,  $C_{60}$  needs to be dispersed in water, which is a challenge due to its high hydrophobicity. Several strategies have been used to do so. The first one is to chemically modify  $C_{60}$  by grafting hydrophilic functions on its surface which allows a high increase of its dispersibility in water. However, a main drawback is that such modifications affect the conjugation of the molecule, thus reducing its functionality for applications. Also, chemical modification can be tedious and difficult to scale-up. The second strategy is the solvent-shifting method:  $C_{60}$  is dissolved in an organic solvent in which it is soluble and then transferred to water thanks to either emulsification-evaporation if the solvent is not miscible with water, or nanoprecipitation if it is. Generally, another compound is added as a stabilizer. It can be a host molecule, like cyclodextrin, that allows to molecularly dissolve  $C_{60}$  in low extents in water, a surfactant or an amphiphilic polymer. With the two latter stabilizers, aggregates are typically obtained, with concentrations up to one gram per liter. This relatively low concentration hinders the potential of  $C_{60}$ . Consequently,  $C_{60}$  is less considered with respect to carbon nanotubes and graphene, respectively the one- and two-dimensional allotropic forms of carbon which have been discovered more recently, which attracted more interest than fullerenes. However, fullerenes are already very useful in the design of organic photovoltaics. The overcoming of obstacles like the concentration in water and the design of novel materials based on fullerenes would therefore certainly open new doors and pave a new way for fullerenes.

On the other hand, polysoaps  $XC_n$  are amphiphilic macromolecules that consist, in this work, of a poly(styrene) backbone of which  $X\%$  units carry surfactant-like units based on a quaternary ammonium group as the polar head and bearing a long alkyl side chain with  $n$  carbon atoms. When these polymers are solubilized in water, they self-assemble into micelles of various morphologies depending on their chemical structure: lamellas for  $35\text{mol}\% < X < 55\text{mol}\%$  and worm-like micelles for  $65\text{mol}\% < X < 80\text{mol}\%$ . In both cases, at higher concentration, above a percolation concentration, physical hydrogels are formed that display viscoelastic properties. Hydrogels based on polymeric cylindrical micelles are more homogeneous and dynamic than hydrogels based on lamellas. However, their stiffness is low compared to that of chemical gels

obtained by covalent cross-linking of hydrophilic polymer chains. There is thus a need for their reinforcement.

Polysoaps being amphiphilic, they can also be used as stabilizers for hydrophobic compounds. They have already been used in the past to stabilize quantum dots or latexes in water. They can therefore be considered as good candidates for the dispersion and stabilization of  $C_{60}$  particles in water. The presence of aromatic units in the structures of both compounds is an opportunity to create strong interactions by  $\pi$ -stacking in combination with the more classical hydrophobic ones.  $C_{60}$  particles can then be considered as fillers for the design of nanocomposite hydrogels where the matrix is the polysoap, as their potential strong attractive interactions could reinforce mechanically the networks. Moreover, hydrogels containing fullerenes are very rare and the functionality of  $C_{60}$  could be exploited in a new way thanks to these materials.

This thesis is divided in six chapters.

In the first chapter, a state-of-the-art will introduce as precisely as possible  $C_{60}$  fullerene from the point of view of its chemical structure, reactivity and solubility. Then, the various methods used to disperse hydrophobic nanoparticles in general, but also in the specific case of  $C_{60}$ , will be described. We will review the various explanations for the origin of the stability of the particles of  $C_{60}$  in water both with and without any added stabilizer. We will then focus on the actual applications of  $C_{60}$  in aqueous medium, and will establish the link between its chemistry and aggregation state with its physical and biological properties. The chapter will end with a description of hydrogels, the strategies to reinforce their mechanical properties, the integration on nanocarbons in hydrogels matrixes, and the specific case of hydrogels formed by XCn polysoaps.

In the second chapter, we will present the materials and methods used during this work. The synthesis of 75C12, the polysoap that was used throughout this work, will be detailed, then preparation of  $C_{60}$  aqueous colloidal suspensions will be described. The various characterization techniques for assessing the chemical composition and the aggregation state of  $C_{60}$  will be presented, as well as rheology that was used for studying the mechanical properties of the nanocomposite hydrogels.

In the third chapter, we will present the emulsification-evaporation method we used to produce  $C_{60}$  nanoparticles in water in presence of 75C12. First, we will explain the characterizations of emulsions prior to the evaporation with confocal microscopy. Then, the various processing conditions that were tested will be given, and the quantification of  $C_{60}$  concentration by UV-visible absorption spectroscopy will be detailed. We will show that depending on the processing conditions, various morphologies of  $C_{60}$  nanoparticles were obtained. The use of chloroform

allowed the co-solubilization of  $C_{60}$  and 75C12, which lead to isotropic nanoparticles of  $C_{60}$  stabilized by 75C12, with a tunable size depending on the polymer concentration. When carbon disulfide was used instead of chloroform, the concentration of  $C_{60}$  dispersed in water was increase up to 8 g/L, which is the highest value ever obtained for neat  $C_{60}$  in water. Additionally, cryo-transmission electron microscopy (cryo-TEM) observations highlighted the peculiar morphology of  $C_{60}$  that self-assembled into nanoplatelets. The stability upon ageing in the presence or not of salt will be shown. Ultimately, the mechanism for the formation of such particles will be discussed.

In the fourth chapter, we will focus on the nanoplatelets obtained with the emulsification-evaporation method. We will give more details on their morphology, thanks to combined light and X-Ray scattering experiments, in addition to cryo-TEM pictures, and discuss the possibilities to tune their size with the processing parameters. Their crystal structure has been studied by X-Ray diffraction, and their interactions with 75C12 will be discussed based on Raman scattering and fluorescence experiments. We will then discuss the possibility to extend our method, for producing dispersions of  $C_{60}$  particles in water, to other stabilizers such as other  $XC_n$  polysoaps, poly(styrene sulfonate) and surfactants with a chemical structure close to the one of 75C12.

In the fifth chapter, we will present the elaboration of nanocomposite hydrogels of 75C12 containing  $C_{60}$  nanoparticles by freeze-drying of the aqueous colloidal suspensions followed by their re-suspension. Their composition was measured by absorption spectroscopy and thermogravimetric analysis. The dispersion state of the  $C_{60}$  nanoparticles was studied by light scattering and cryo-TEM. The influence of the addition of  $C_{60}$  nanoparticles on the rheological properties of the hydrogels will then be discussed in terms of both dynamics and stiffness of the nanocomposite network. The non-linear mechanical properties, *i.e.* the behavior of the network under high strains will also be presented.

In the sixth and last chapter, the Ouzo effect will be presented as an alternative method to produce aqueous colloidal suspensions of  $C_{60}$  fullerene. It consists of the fast addition of water onto a solution of  $C_{60}$  in a polar organic co-solvent. The choice of an appropriate co-solvent, that is a solvent that displays a high solubility for  $C_{60}$  and that is miscible with water, will be discussed. The solvent that was chosen was n-butylamine. We will discuss the reactivity between this compound and  $C_{60}$ , then we will display the state diagram of  $C_{60}$ /n-butylamine/water ternary mixture. The stability of the Ouzo particles was studied by both macroscopic observations and analytical centrifugation. The morphology and size of the particles was assessed by TEM, light scattering and analytical centrifugation. To vary the size of the particles, two parameters were varied: the fullerene concentration in n-butylamine and

the volume fraction of these mother solutions in the final mixture. The influence of the dialysis step used to purify the mixtures from n-butylamine will be discussed. Ultimately, we added 75C12 in the formulation by solubilizing it in the water that is added to C<sub>60</sub> in n-butylamine. The influence of 75C12 on the size of the particles and their stability will be discussed.

Last we will conclude and give perspectives for this work.

# Chapter 1. State of the art

1) Buckminsterfullerene .....	7
a. General aspects.....	7
i. History.....	7
ii. Chemical structure.....	8
b. C <sub>60</sub> in organic medium .....	9
i. Apolar organic solvents .....	9
ii. Polar organic solvents .....	11
iii. Reactivity with aliphatic amines.....	12
2) Dispersion in water .....	13
a. Emulsification-evaporation .....	13
b. Nanoprecipitation.....	17
i. Ouzo effect .....	17
ii. Rate-controlled injection methods .....	21
iii. Dialysis method .....	23
c. Other methods .....	24
3) Stabilisation of fullerene nanoparticles in water .....	25
a. Stability origin .....	25
b. Stabilisation by surface active agents .....	27
i. Molecular surfactants.....	28
ii. Amphiphilic or hydrophilic polymers .....	30
c. Chemical modification .....	38
i. Hydrophilic functions grafting .....	38
ii. Covalent binding to polymers .....	41
4) Properties of fullerene aggregates in water.....	42
a. Chemical and biological properties.....	42
b. Physical properties .....	45
5) Hydrogels formed by self-assembly of polysoaps .....	49
a. General features of hydrogels .....	49
b. Reinforcement strategies.....	52
i. Topological gels.....	52
ii. Double or interpenetrated networks .....	53
iii. Ionic gels.....	54
iv. Nanocomposite gels .....	56
c. Nanocarbon-containing hydrogels.....	59
d. Cationic polysoaps based on polystyrene backbones.....	61
References .....	67



## Chapter 1. State of the art

In this chapter, an overview of literature will be given. In the first part, C<sub>60</sub> fullerene will be presented as well as the processes commonly used to disperse it in water. In the second part, the stabilisation mechanisms of C<sub>60</sub> in water will be discussed and a non-exhaustive list of surfactant and polymers used for its stabilisation will be given. Also, some insight will be given in the chemical modification of C<sub>60</sub>, still with the perspective of transferring it to aqueous medium. In the third part, the main applications of C<sub>60</sub> and its derivatives in water will be detailed according to the preparation process, the structure and the efficiency in the given applications. In the last part, hydrogels will be presented and the specific case of hydrogels reinforced by nanocarbons will be detailed. A special focus on the cationic polymer used in this work will close this chapter.

### 1) Buckminsterfullerene

#### a. General aspects

##### i. History

Fullerenes are molecular cages made of pure carbon. They are indeed cited as one of the allotropic forms of carbon, along with graphite, diamond, nanotubes and graphene. The existence of such compounds was only theoretical until they have been first discovered experimentally in 1985 by Harold Kroto, Robert Curl and Richard Smalley, who have received the Nobel Prize of Chemistry in 1996 for this discovery.<sup>1</sup> It took few years for the researchers to really study these molecules, because of the lack of large-scale production. In 1991, Krätschmer *et al.* first described a production process leading to approximately 100 mg.<sup>2</sup> This process allowed the beginning of many studies on the fullerenes. However, the powder obtained from this method was a mixture of many fullerenes: mainly C<sub>60</sub> fullerene, along with a non-negligible part of C<sub>70</sub>, and traces of other fullerenes. A further purification of the soot was thus necessary to obtain pure molecules. Industrial production of fullerene became possible in the middle of the 2000s thanks to the Japanese company Frontier Carbon Corporation, which was able to produce gram-scale of C<sub>60</sub>.<sup>3</sup>

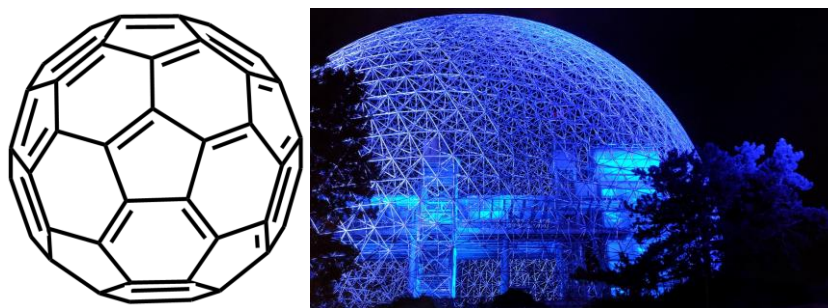
In our work, we will focus only on C<sub>60</sub>, as it is still today the most common and cheapest fullerene. Its purification is often undergoing through chromatographic separation over alumina column or by sublimation, and it can be bought in tens of grams quantities with a purity exceeding 99%.



*ii. Chemical structure*

$C_{60}$  fullerene is composed of 12 pentagons and 20 hexagons, and no pentagons are connected to each other, forming the shape of a truncated icosahedron. In this molecule, each carbon atom is bound to three other carbon atoms, with two single bonds and one double bond. Two types of carbon-carbon bonds can be distinguished: bonds between two 6-member rings are 1.40 Å long, while bonds between 5-member rings and 6-member rings are 1.46 Å long.<sup>4</sup> 6-member rings are aromatic, while 5-member rings are anti-aromatic. Overall, because of pentagonal cycles,  $C_{60}$  cannot be considered as aromatic and does not respect the Hückel rule, which stipulates that an aromatic molecule must possess  $4n+2$   $\pi$  electrons, with  $n$  a natural whole number, as it has a total of 60 of them.

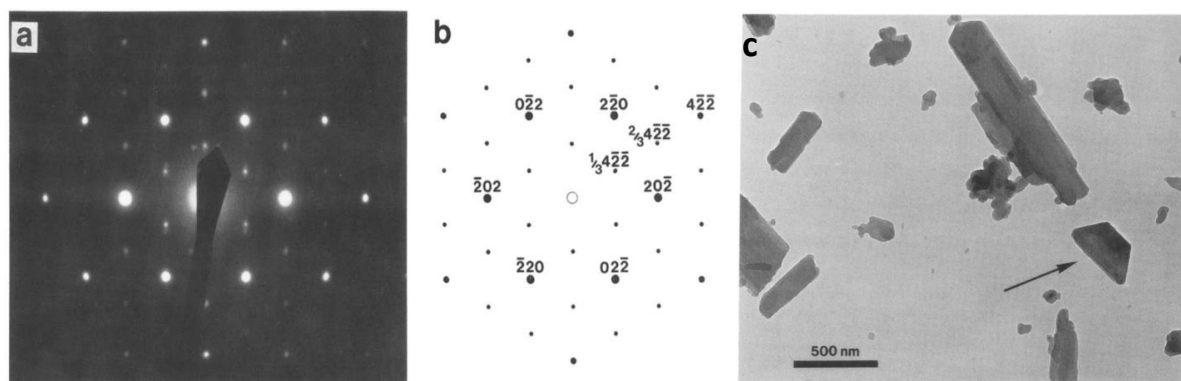
$C_{60}$  fullerene is also named Buckminsterfullerene in homage to Richard Buckminster Fuller, a famous architect who built geodesic domes. Among them is the one of Montreal Biosphere on Île-de-Sainte-Hélène in Montreal, which is 76 meters tall. The resemblance between fullerenes, especially  $C_{60}$ , and this building is indeed marking (Figure 1.1).



**Figure 1.1.** On the left, chemical structure of Buckminsterfullerene. On the right, the geodesic dome of Montreal Biosphere conceived by Richard Buckminster Fuller.

Overall diameter of  $C_{60}$  is 7.09 Å, but in solid state the distance between two  $C_{60}$  is 10.02 Å, which corresponds to its Van der Waals diameter.<sup>2</sup>

$C_{60}$  crystals were first described by Krätschmer *et al.* They stated that the crystals adopted a close packed hexagonal geometry. However, a debate led to the final conclusion by Harris *et al.* in 1992 that they form a face-centred cubic structure (fcc) as shown by the assignment of the diffraction pattern spots (Figure 1.2). Some forbidden spots (in the 422 direction) are attributed to defects in this organisation. These defects are typical in fcc structures where twin-accelerated growth occurs. This phenomenon leads to formation of platelets and rods with a size below the micron, as it was evidenced by bright-field microscopy pictures (Figure 1.2c).<sup>5</sup>

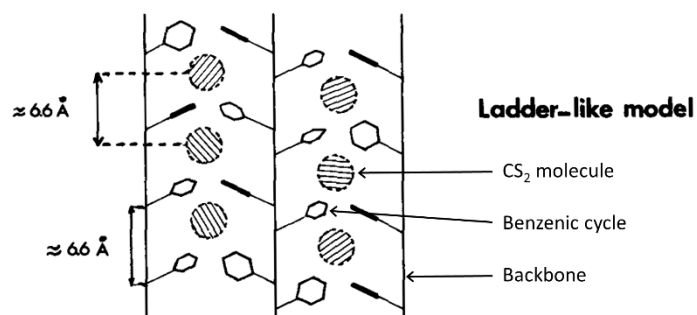


**Figure 1.2.** a) Diffraction pattern of  $C_{60}$  microcrystals, b) assignment of the spots to the fcc structure and c) bright-field microscopy image of the analysed crystals.<sup>5</sup>

### b. $C_{60}$ in organic medium

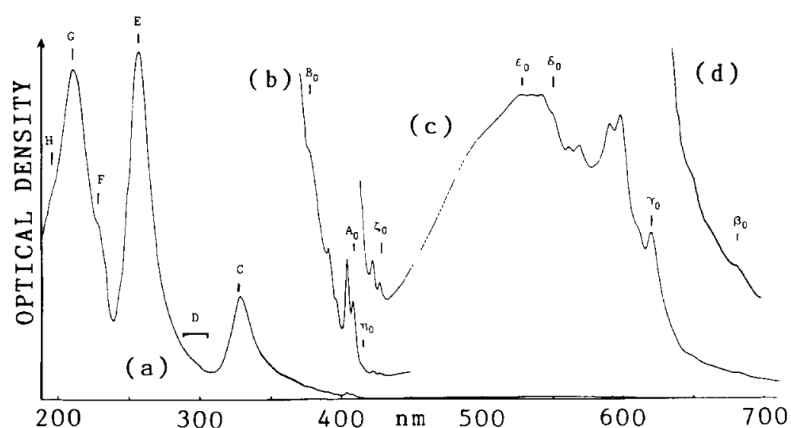
#### i. Apolar organic solvents

$C_{60}$  is not soluble in water. Since its structure comprises aromatic units, it displays some affinity with aromatic apolar solvents in the order naphthalenes >> benzenes. In these solvents, its solubility is high, on a g/L scale. For example, it is soluble at 33 g/L in 1-methylnaphtalene and at 2.8 g/L in toluene.<sup>6</sup> When halides such as chloride atoms are added to the aromatic cycles, solubility increases such as in the case of 1-chloronaphtalene, leading to 51 g/L solubility. However, non-aromatic haloalkanes such as chloroform or dichloromethane solubilise it in a lesser extent (respectively 0.16 and 0.26 g/L). The best solvent is 1,1,2,2-tetrachloroethane, where the solubility reaches 5.3 g/L. Alkanes, without halides, poorly solubilise  $C_{60}$ , but solubility increases when increasing the number of carbon atoms (going from 5 mg/L for n-pentane to 0.167 g/L for n-tetradecane<sup>7</sup>). Other peculiar solvents can solubilise  $C_{60}$  such as 2-methylthiophene, which is aromatic, and carbon disulfide ( $CS_2$ ). The latter is also known to solubilize carbon nanotubes (CNTs). Molecular dynamics indeed showed that a layer of  $CS_2$  forms around CNTs.<sup>8</sup> To explain this, one could consider  $CS_2$  interactions with other compounds containing aromatic cycles. It was shown for example that atactic polystyrene forms gels in  $CS_2$ . This was attributed to the formation of ladders in which the arms are the polystyrene chains and the rungs are  $CS_2$  molecules. It is suggested that each sulfur atom interacts with one aromatic cycle of polystyrene, thus creating bridges between two of them (Figure 1.3).<sup>9, 10</sup> Indeed, nematic organisation was demonstrated by small angle neutron scattering studies.<sup>11</sup> The same thing may happen between fullerene and  $CS_2$ .



**Figure 1.3.** Ladder-like model of the conformation of polystyrene-carbon disulfide complexes.<sup>10</sup>

In apolar organic solvents, C<sub>60</sub> solutions appear pink to dark purple depending on their concentration. Absorption spectra always display the same absorption maxima in terms of wavelength, no matter the solvent. In n-hexane, three maxima can be found respectively at 227, 257 and 328 nm in UV domain, followed by a maximum at 408 nm in the purple. These absorptions result from electronic transitions of the type  $X^1T_{1u}-1^1A_g$ , with X ranging from 1 to 9. In visible domain, absorption is much lower and a series of maxima can be found from 420 to 660 nm (Figure 1.4).<sup>12</sup> Few shifting of the peaks happens when another apolar solvent is used, but the global spectra are similar and absorption coefficients do not vary much.<sup>13</sup>



**Figure 1.4.** (a) UV-visible absorption spectrum of C<sub>60</sub> in n-hexane. (b), (c) and (d) are magnifications of (a), respectively x20, x200 and x1000.<sup>12</sup>

Even though C<sub>60</sub> is molecularly solubilised in the solvents listed above, aggregation can occur upon ageing as demonstrated by Dattani *et al.*<sup>14</sup> Indeed, under visible light, oxidation could be highlighted by formation of epoxy cycles on the surface of C<sub>60</sub> as evidenced by Fourier-transform infrared and mass spectroscopy (FTIR and MS, respectively). Dynamic light scattering (DLS) measurements displayed a relaxation corresponding to aggregates with a hydrodynamic radius around 100 nm. Their scattering intensity went up with irradiation time.

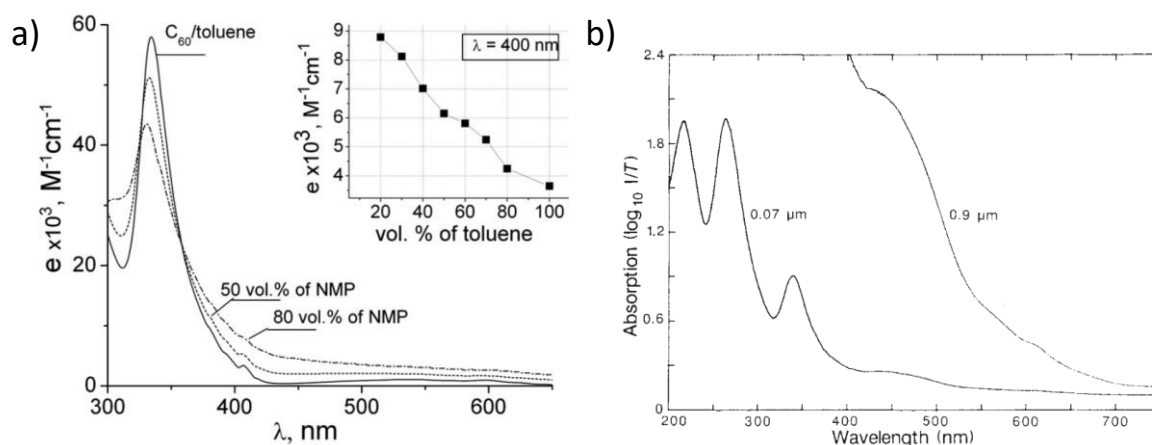
In the dark, same aggregation occurred as well but it was much slower. The clusters had a form factor corresponding to fractal aggregates with fractal dimension up to  $df=2.1$ .<sup>14</sup> The two main mechanisms for aggregation of particles in solution that exist are Reaction- and Diffusion-Limited Cluster Aggregation (RLCA and DLCA, respectively). The fractal dimensions resulting from RLCA and DLCA are respectively 2.1 and 1.8.<sup>15</sup> This means that RLCA leads to denser aggregates, which seems to be the case for fullerene solutions upon ageing. Please note that the study was made on saturated solutions of  $C_{60}$  in toluene. Similar observations could be made in  $CS_2$  solutions by Small-Angle Neutron Scattering (SANS), both saturated and unsaturated.<sup>16</sup> It is therefore important to work on fresh samples and to protect them from light.

Finally, a temperature dependency of the solubility was reported by Ruoff *et al.* A maximum solubility was observed in apolar organic solvents near room temperature.<sup>17</sup>

## *ii. Polar organic solvents*

$C_{60}$  is poorly soluble in most polar organic solvents, such as ethanol, acetone, THF, acetonitrile... Two exceptions should be however considered: electron donor solvents such as anisole and N-methylpyrrolidone (NMP). Indeed,  $C_{60}$  has been widely described as a good electron acceptor because of its non-aromatic structure. It can undergo six oxidations in total, which are reversible as demonstrated by cyclic voltammetry measurements.<sup>18</sup>

$C_{60}$  aggregation state is not the same in polar solvents as in apolar ones. Indeed, Mchedlov-Petrosyan *et al.* demonstrated by DLS measurements that large clusters were formed when  $C_{60}$  was transferred from toluene to NMP.<sup>19</sup> UV-visible spectroscopy displayed solvatochromism consisting in a bathochromic shift when NMP was added,<sup>20</sup> and absorption in visible region became more intense and broader. The spectra indeed looked like the spectra of films of bulky  $C_{60}$  (Figure 1.5).

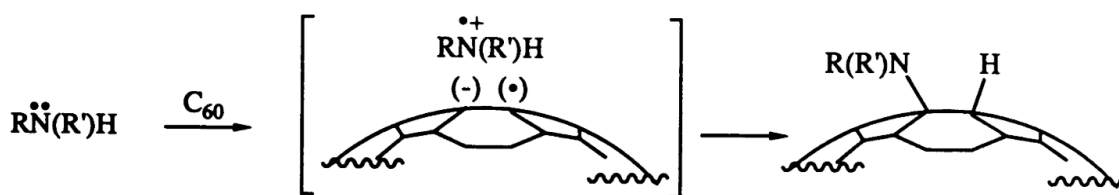


**Figure 1.5.** a) Molar absorption coefficient of  $\text{C}_{60}$  in toluene-NMP mixtures.<sup>20</sup> b) Absorption spectra of  $\text{C}_{60}$  films of two different thicknesses.<sup>2</sup>

### iii. Reactivity with aliphatic amines

Aliphatic amines are the only polar organic compounds able to solubilize  $\text{C}_{60}$  above 1 g/L. The most efficient one is n-butylamine (3.6 g/L<sup>21</sup>), and in general, primary amines are better  $\text{C}_{60}$  solvents than secondary ones. Tertiary amines are poor solvents for  $\text{C}_{60}$ . Aniline or quinoline are not better solvents for  $\text{C}_{60}$  than the previously cited amines, despite their aromatic nature.

Actually in the specific case of amines a chemical reaction can occur. Amines react with  $\text{C}_{60}$  through a nucleophilic addition on a carbon-carbon double bond, leading to grafting of the amine on one carbon, the other one receiving a proton of the amine (Figure 1.6). This reaction can occur as many times as the nitrogen of the amine carries hydrogen atoms which inhibits tertiary amines to react with  $\text{C}_{60}$ .



**Figure 1.6.** Nucleophilic addition of amines on  $\text{C}_{60}$  molecules.<sup>22</sup>

Nakamura *et al.* showed the formation of regioselective penta-adducts at room temperature, catalyzed by visible light, in toluene. High yields were achieved especially for cyclic amines, like piperazines. Indeed, pyrrolidine can solubilise  $\text{C}_{60}$  up to 47 g/L.<sup>21</sup> However, in these conditions n-butylamine didn't react.<sup>23</sup> Another example reports on the addition of secondary amines leading to penta- or hexa-adducts but with lower yields.<sup>24</sup> Methylamine has been shown to react instantly with  $\text{C}_{60}$  in toluene. This reaction is highlighted by a change of color from

purple to yellow and MS showed that adducts could be obtained up to  $n=18$  but with a majority of  $n=1,2$  and 6. In these conditions, FTIR displays N-H bond characteristic band, contrary to the product of reaction with dimethylamine where a single addition is possible. For n-butylamine, when 2 equivalents were added in toluene, selective monoaddition was achieved.<sup>25</sup> Temperature is once again of importance since when it is increased, solubility of  $C_{60}$  in n-butylamine decreases.<sup>26</sup>

Wudl *et al.* reported that n-propylamine successfully added on  $C_{60}$  when the latter was directly dissolved in it, leading to a mixture of adducts with a maximum of twelve additions per  $C_{60}$  molecule as shown by MS. Mixtures obtained by reaction of  $C_{60}$  with n-propylamine, ethylene diamine and morpholine were soluble in slightly acid water. However, adduct resulting from reaction with dodecylamine was insoluble in water.<sup>22</sup>

During reactions,  $C_{60}$  goes through an intermediate radical anion state that can be followed by spectrophotometry. Indeed, the radical anion species absorb in near-infrared. This kind of measurement shows what type of amines react with  $C_{60}$ , which is not the case for aniline and long alkyl chain amines like dioctylamine.<sup>27</sup>

Qiao *et al.* showed that dissolution of  $C_{60}$  in amines is accompanied by an increase of absorbance (because of the increase of concentration). In diethylamine, 3 days are needed to reach a steady state. They also showed that the electron transfer rate was decreased when increasing temperature. For tertiary amines, spectroscopy evidenced the formation of electron-transfer complexes through donor-acceptor interactions.<sup>28</sup>

In conclusion, amines can react with fullerene which will be of prior importance regarding chapter 6.

## 2) Dispersion in water

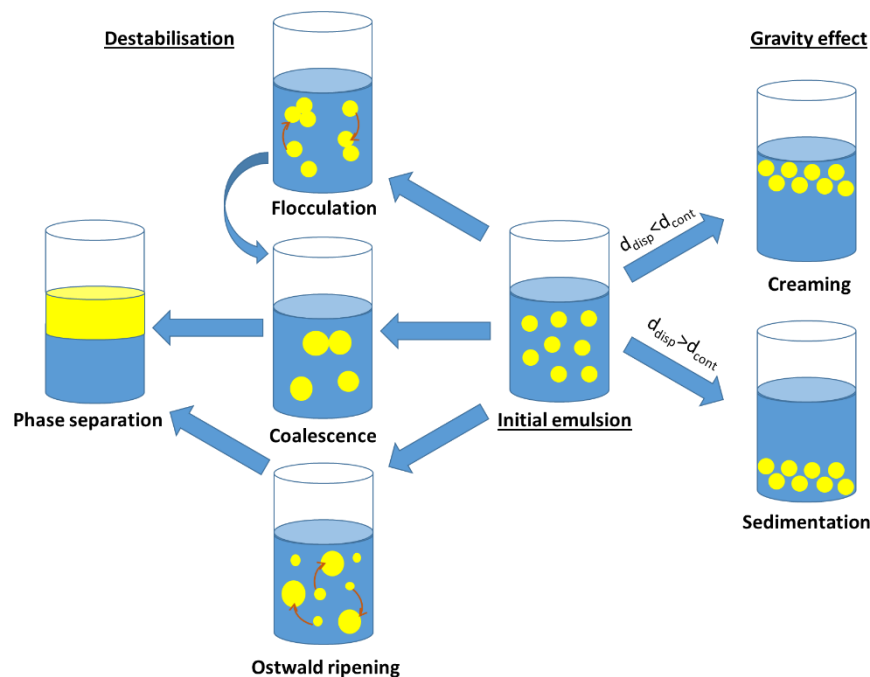
The different dispersion processes described in literature are summarized here. In particular, we will discuss the application of the processes to the dispersion of  $C_{60}$  in water. More general information will be given and control over the size will be discussed for each technique.

### a. Emulsification-evaporation

Emulsions are systems consisting in two (or more) immiscible liquids with one dispersed as droplets in the other. Typically, they are obtained by mixing water with an organic apolar compound. A very famous example of emulsion in daily life is milk, which consists in droplets of fat dispersed in water and stabilized by proteins such as micellar casein. In emulsion science, the main challenges are the control of droplets size and their stabilization. Indeed,

thermodynamically these systems are metastable, which means that their stability is mainly kinetically driven. Droplets can undergo different destabilization mechanisms as detailed in Figure 1.7:

- Coalescence is the fusion of two droplets which were in contact with each other. This contact can be induced by simple Brownian motion (natural diffusion), by flocculation or by hydrodynamic diffusion (either by action of gravity or by an external flow).
- Ostwald ripening is the diffusion of dispersed phase from one small droplet to a bigger one.
- Flocculation results from attractive forces between two droplets which leads to their sticking. It does not lead to complete phase separation by itself, however it favours coalescence.
- Creaming and sedimentation are not always considered as true destabilisation as droplets size is unchanged, however the droplets move to the top in the first case and to the bottom in the second case under gravity because of the density difference between dispersed and continuous phase. They eventually lead to contacts between droplets, thus favouring the other destabilisation mechanisms.



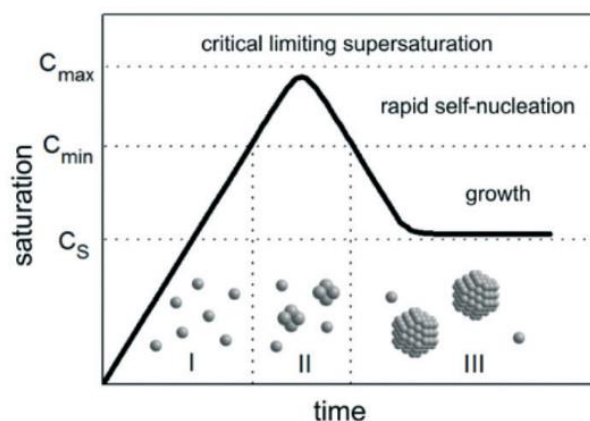
**Figure 1.7.** Destabilisation mechanisms for emulsions.

To prevent destabilisation, a continuous stirring can be applied to maintain the initial state of the emulsion, or surface agents such as surfactant molecules or polymers can be added to the emulsion. The surface agents can however not prevent creaming or sedimentation. The continuous phase should then increase in viscosity or even turn into a gel (emulgel).



Three types of emulsions are distinguished by IUPAC: macroemulsions where droplets are bigger than 1  $\mu\text{m}$ , miniemulsions where their diameter ranges between 50 nm and 1  $\mu\text{m}$ , and microemulsions for which their diameter is below 50 nm. Stirring is one of the parameters to control droplet size. For macroemulsions, magnetic or mechanical stirring are used whereas ultrasonication is used for mini and microemulsions. In all cases a surfactant is used, however for mini- and microemulsion extra compounds are sometimes added. Co-surfactants are typically polar organic compounds (like pentanol) and are used to decrease surface tension and so does the size of droplets. Co-stabilizers are very hydrophobic compounds (like hexadecane) that cannot diffuse through water and are used to prevent Ostwald ripening. However, these compounds are used to help at stabilising emulsions, but if a continuous stirring is applied, again they are not needed. In general, it is not possible to continuously stir with ultrasounds, because the process is very energetic and overheats the sample.

Emulsification-evaporation process is commonly used for dispersing colloidal particles in solution. First, an oil-in-water emulsion is formed with oil droplets consisting of organic solvent containing the solute that have to be dispersed. Then, the organic solvent is evaporated. At this step, the concentration of solute increases in the organic solvent with time, because the total volume decreases upon solvent evaporation. According to the model of LaMer,<sup>29</sup> supersaturation conditions are reached which leads to the formation of many nuclei within a short time (Figure 1.8). Thus, the concentration of molecularly solubilized solute decreases. Then, particles grow until the concentration goes down to saturation value. Once the solvent is fully evaporated, the solid particles are suspended in water.



**Figure 1.8.** Evolution of concentration of individual solute (solid line) with time during a dispersion process.  $C_s$  is the saturation,  $C_{\max}$  is the concentration at which the energy of nucleation becomes lower than the energy of individual dispersion,  $C_{\min}$  is the value starting which growth occurs by Ostwald ripening.<sup>29</sup>



Different emulsification-evaporation processes are distinguished, which depends on the stirring conditions (either magnetic or ultrasound), presence or not of one or more surfactants and co-surfactants... For example, polymer latexes can be produced by mini-emulsion polymerization, which imply ultrasounds. It is also possible to take an already prepared polymer, and to disperse it, as in the case of ethyl cellulose and poly(lactic acid) (PLA). They were dissolved in ethyl acetate, then mixed with water thanks to a microfluidics device, and the solvent was evaporated under vacuum.<sup>30</sup> Generally speaking, the size of the particles can be tuned by formulation parameters such as concentration, surfactant or polymer addition or volume fraction of oil...

Emulsification-evaporation was first transposed to C<sub>60</sub> by Andrievsky *et al.*<sup>31</sup> They proposed to dissolve C<sub>60</sub> in toluene followed by ultrasonic treatment in absence of surfactant. MS measurements showed that no chemical modification was induced by this process even though it is highly energetic.

The successful dispersion was attributed to the formation of methyl benzoate ions from ultrasonic treatment of toluene, which would be responsible of electrostatic stabilization of C<sub>60</sub> in water.<sup>32, 33</sup> This can be true for samples in the absence of surfactant molecules or polymers, however the same process was also used with chloroform in presence of SDS or in carbon disulfide with functionalised C<sub>60</sub> and was still efficient.<sup>34, 35</sup> Please note that this process gave access to solutions with only several mg/L concentration in absence of any stabilizers.

Andrievsky *et al.* showed in 1999 that C<sub>60</sub> particles formed by sonication in water from toluene have a polycrystalline nature by Selected Area Electron Diffraction (SAED) from TEM images. In this specific case, small particles of a few tens of nm in diameter, very polydisperse, were formed. However, since the sample has been dried it is difficult to know which are the primary particles and therefore hard to conclude whether particles are mono- or polycrystals.<sup>36</sup> The crystalline nature of the aggregates was contradicted by Cid *et al.* who showed TEM images of particles prepared by the same method and concluded that they are amorphous. However, no proof like a SAED pattern was given so far.<sup>37</sup>

Additional SANS data were given by Avdeev *et al.* on these particles. They first concluded that particles were very polydisperse, and slightly anisotropic. For their structure, two models were proposed. In the first one, dense crystals surrounded by a thin solvated shell are proposed. The second one corresponds to a dense packing of C<sub>60</sub> single molecules surrounded by 24 molecules of water. The possibility of complexation of C<sub>60</sub> by water molecules will be discussed in the fourth part of this chapter. Furthermore, the authors stated that a non-negligible part of the particles were very small, with a diameter of only 1 or 2 nm, corresponding to individual fullerene molecules.<sup>38</sup>

The crystalline nature has been highlighted by Prylutskyy *et al.* from spectroscopic data since forbidden electronic transitions typical of the crystalline state agreed with experimental data obtained in the visible domain. They came to the conclusion that fractal aggregates were formed with a fractal dimension of about 1.8 (in line with DLCA, see section 1.1.b.i) and whose building blocks were made of 13 molecules of  $C_{60}$  organized in a crystal displaying a  $T_h$  symmetry.<sup>39</sup>

Gigault *et al.* investigated further these fractal objects. An asymmetric flow field-flow fractionation (AF4) combined with static light scattering detection allowed the analysis of  $C_{60}$  aggregates sorted by size. It is claimed that fractal aggregates were obtained only for the largest ones based on TEM images on dried samples rather than in solution. Finally, the description of dense objects such as fractals does not seem appropriate, and increasing the fractal dimension up to almost 3 would indicate very dense objects, which microscopy does not seem to show.<sup>40</sup>

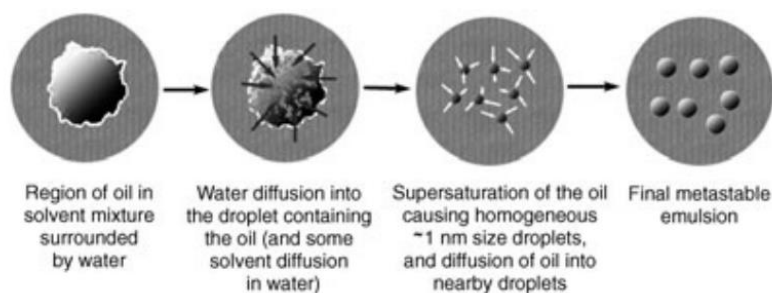
### b. Nanoprecipitation

Nanoprecipitation consists in the mixing of a solution of the solute in a good solvent with a bad solvent. From this mixture supersaturation occurs as for emulsification-evaporation but this time by decreasing of the solvent quality, leading to nucleation-growth mechanism. Two main preparation paths can be distinguished: injection of one solution in the other, or dialysis of the solution against bad solvent. In the first case, several factors can impact the final size of particles: addition rate, volume fractions of each solution, concentration of the mother solution in good solvent, stirring speed...

#### i. Ouzo effect

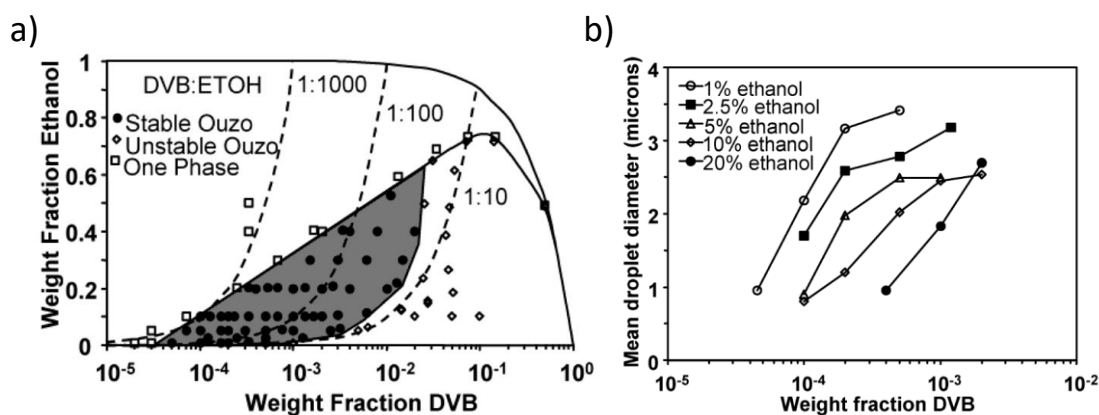
The simplest nanoprecipitation process is called Ouzo effect. It consists in a fast addition of a bad solvent to the solute solution, without stirring except slight handshaking. This phenomenon was named after the Greek Aperitif Ouzo. A large volume of water is traditionally added on top of it, turning the initially transparent solution into a cloudy one. Actually, Ouzo consists in an ethanol-water mixture in which hydrophobic compounds, the aroma, are dissolved. When this mixture is diluted in water, the continuous medium shifts to higher polarity, thus dramatically decreasing the solvent quality of the aroma. According to the model of LaMer,<sup>29, 41</sup> a supersaturation then occurs, resulting in the nucleation of very small droplets of aroma which grow through coalescence until reaching a metastable state within a few seconds (Figure 1.9). This type of emulsion can remain metastable for several days without the help of any stabilizer. This phenomenon can actually be extended to many ternary mixtures consisting on water, a hydrophobic compound (like aroma in Ouzo) and a good solvent of this compound that is miscible with water that is basically an organic polar solvent (e.g. ethanol in Ouzo).

Another attempt to explain the supersaturation phenomenon is the so-called Marangoni effect. The interfacial tension between organic polar solvent and water actually induces turbulences causing penetration of the first into the second one. Then, droplets would form. However, it was shown that preparation path itself has no influence on the final result. Mixing a solution in good solvent with bad solvent, or a solution in a mixture of good and bad solvent with bad solvent yield the same results.<sup>42</sup>



**Figure 1.9.** Steps of emulsion formation during Ouzo effect.<sup>41</sup>

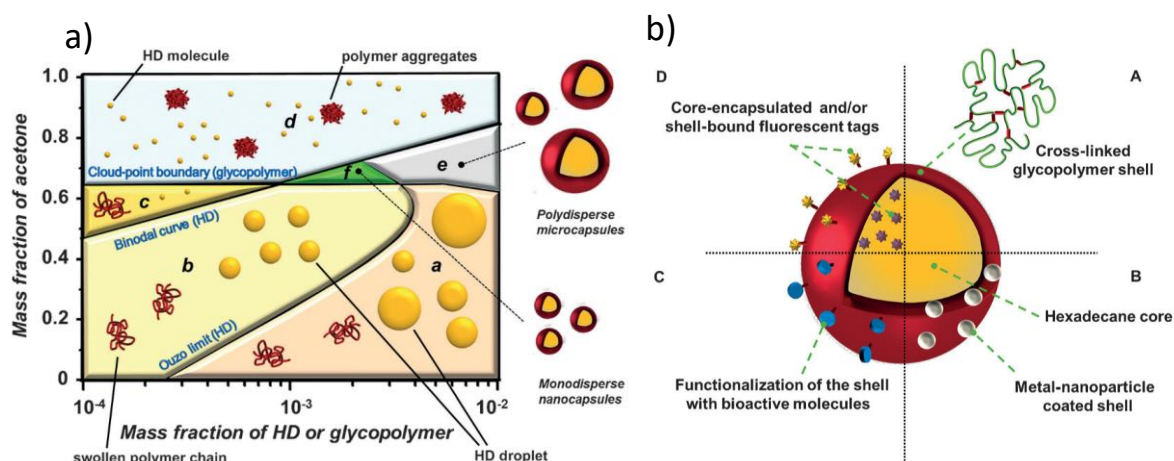
Katz and Vitale studied a ternary mixture composed of water, ethanol and divinylbenzene (DVB). They showed that the Ouzo effect (characterized by visual determination of turbidity) depends on two factors for a given ternary mixture: volume fraction of water and solute concentration in a polar solvent.<sup>43</sup> It is then possible to draw phase diagrams of these systems with only two axes corresponding to these parameters, instead of ternary phase diagrams. Three regions were distinguished: stable and unstable Ouzo regions and monophasic solution. Ouzo appears when ethanol fraction is not too high, so that the solvent quality is bad enough to induce nucleation of DVB droplets. In addition, when DVB concentration is too high, the system becomes unstable because of emulsions destabilisation processes described previously. The border separating Ouzo and monophasic regions is then a binodal, and the border separating stable and unstable Ouzo is called the Ouzo limit (Figure 1.10a). Finally, the size of the droplets has been shown to increase with increasing DVB concentration, but to decrease when increasing the volume fraction of the ethanol solution. The latter observation can be counter-intuitive because the overall DVB concentration in the final mixture increases when volume fraction of ethanol solution increases, but again, solvent quality increases because there is more good solvent in the mixture, so the interfacial tension decreases (Figure 1.10b). To conclude, a good way for achieving a large concentration of hydrophobic compound without affecting the stability of the system is to find the balance between water and polar solvent in the mixture.



**Figure 1.10.** a) Ouzo phase diagram of a ternary mixture of water-ethanol-DVB at room temperature. Gray zone is the stable Ouzo region. b) Evolution of the droplets size with respect to DVB concentration in the mother solution for different volume fractions of ethanol in the mixture.<sup>43</sup>

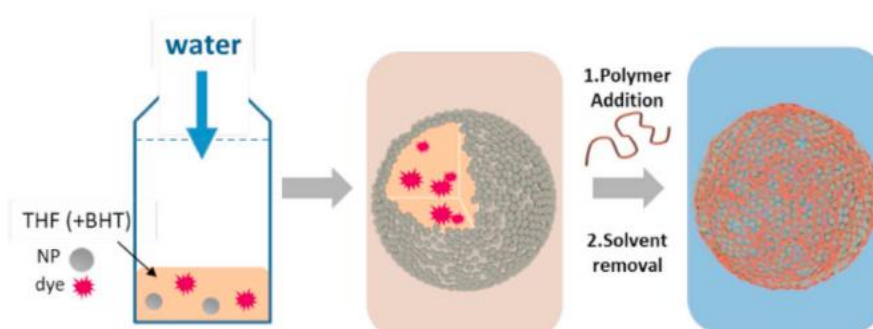
Later, the process was generalized to many other systems, including solid hydrophobic compounds. Ouzo effect can therefore be used to obtain colloidal dispersions. Same rules as the ones given before were valid for polymers like poly(methyl methacrylate) (PMMA), PLA or poly( $\epsilon$ -caprolactone) (PCL) with acetone as polar solvent.<sup>42</sup> It is important to note that one of the main advantages of this technique is the narrow dispersity of the particle size, though the latter increases when concentration is increased.<sup>44</sup> In the absence of surfactants, the formation of monodisperse colloidal particles of PMMA in water required to work at a very low concentration of particles.<sup>44</sup>

Nanocapsules can also be obtained by Ouzo effect. To this extent, a hydrophobic solvent or a drug is added to the formulation, and the polymer needs to be hydrophilic. The oil (e.g. hexadecane) is dissolved in polar organic solvent such as acetone and the polymer is dissolved in water. It is there necessary to find a region in the phase diagram where the oil will co-precipitate with polymer. This region is the cross over between Ouzo region for the oil and phase separation region for the polymer (Figure 1.11a). Eventually, core-shell structures are obtained with the oil forming the nucleus surrounded by polymer. Within the co-precipitation region, the size of nanocapsules can be controlled by the formulation of the mixture. After forming these structures, polymer is cross-linked to maintain the capsule structure after removal of acetone. Finally, these nanocapsules can display various functionality (optical or magnetic, for example) as chromophore or inorganic nanoparticles such as gold or iron oxide can be grafted on the polymer surface during the process (Figure 1.11b).<sup>45, 46</sup>



**Figure 1.11.** a) Phase diagram of hexadecane and glycopolymer in water/acetone mixtures. b) Schematic illustration of the functionalization possibilities for nanocapsules *via* Ouzo effect.<sup>45</sup>

The group of Fabienne Gauffre used Ouzo effect to form inorganic nanocapsules thanks to the ternary mixture water/THF/butylhydroxytoluene (BHT). Inorganic iron oxide nanoparticles functionalized with octylamine were also in the mixture and spontaneously formed the nanocapsules. A polymer was subsequently added to crosslink the nanoparticles and retain the hollow structure even after solvent removal (Figure 1.12). The polymer was either poly(acrylic acid) (PAA) or a diblock poly(acrylic acid)-b-poly(ethylene oxide) (PAA-b-PEO), chosen for its ability to complex with iron oxide *via* its carboxylic acid functions. The concept was extended to gold nanoparticles and quantum dots as well as hybrids of the previously cited inorganic particles.<sup>47</sup> These capsules named hybridosomes® were able to encapsulate a hydrophobic dye when it was added to the original formulation, with internal concentration up to 170 g/L and yields exceeding 80%.<sup>48</sup>



**Figure 1.12.** Schematic representation of Ouzo-induced formation of hybrid inorganic nanoparticles (NP)-polymer nanocapsules in water. Dashed line represents the amount of water added.<sup>48</sup>

Deguchi *et al.* used Ouzo effect to produce aqueous colloidal C<sub>60</sub> suspensions. Since C<sub>60</sub> does not display good solubility in polar solvents, one of the least bad solvents which was chosen

was tetrahydrofuran (THF).  $C_{60}$  fullerene's solubility is only 9 mg/L in this solvent as long as it is distilled prior to use and that dissolution is performed under argon. UV-visible spectrum of  $C_{60}$  in THF shows that it is dissolved molecularly as it displays similar spectrum as in toluene or  $CS_2$ . The final concentration in water is at best 9 mg/L with this method. However, since it is easy to process and does not require any specific equipment, this method became very popular, especially in biomedical sciences as it will be discussed further.<sup>49</sup>

The group of François Ganachaud succeeded thanks to Ouzo effect to entrap carbon nanotubes (CNTs) in PMMA particles. They first dispersed CNTs in water with the help of a surfactant, then they quickly added a solution of PMMA in acetone to induce the formation of nanoparticles. TEM images highlighted the good dispersion state of CNTs in the PMMA particles, even after thermal annealing. This shows that Ouzo is an effective method to form composite materials containing nanocarbons.<sup>50</sup>

An alternative use of this process was the successive transfers with decreasing solvent qualities. First,  $C_{60}$  was dissolved in toluene, then THF, acetone and water were respectively added to the solution. Solvents were subsequently evaporated under reduced pressure.<sup>51</sup> Other authors used a similar sequence going from hexane to water, however since  $C_{60}$  is soluble in hexane to much lower extents, the resulting suspensions is then very diluted.<sup>52</sup>

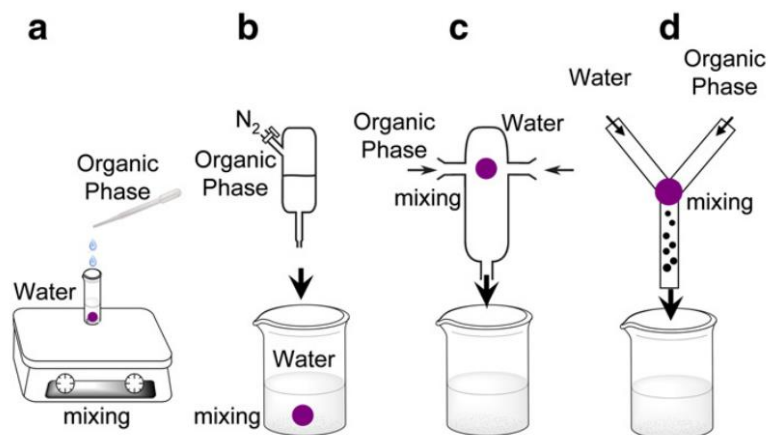
## *ii. Rate-controlled injection methods*

Bad solvent addition rate is a key parameter for controlling the size of the nanoparticles obtained by nanoprecipitation methods. Ouzo effect is, within these techniques, a specific case where this addition rate is maximum. A variety of devices has been developed to modulate this rate (Figure 1.13). The simplest process aside from Ouzo is the other extreme in terms of addition rate: namely drop-wise addition. The addition rate can be simply controlled by pressure-driven injection, or by a syringe-pump device. Please note that in these two cases, the receiving container which is already filled with bad solvent is continuously stirred to ensure a good homogenization (Figures 1.13a and b). The stirring energy itself is one more parameter influencing nanoparticles size. Indeed, increasing stirring rate leads to particles of decreasing size.<sup>53</sup>

Last, flash nanoprecipitation (FNP) consists in quickly premixing the two phases together in a chamber, where basically an Ouzo effect occurs, before their addition to a large amount of continuous phase. In this way, the amount of bad solvent during precipitation can be lowered and smaller particles are obtained as explained in section 1.2.b.i. The chamber can have different geometries as shown in Figures 1.13c and d. The mixing conditions (size of the chamber, mixing rate) determine the number of nucleus formed during the supersaturation step, and then the features of the final nanoparticles.<sup>54</sup> As for Ouzo effect, increasing



concentration of solute in the mother solution yields bigger nanoparticles.<sup>55</sup> However, the main difference between Ouzo and FNP lies in the type of regime where the mixing process occurs, respectively laminar or turbulent. It was shown experimentally that the latter yields smaller particles than the first.<sup>42</sup>

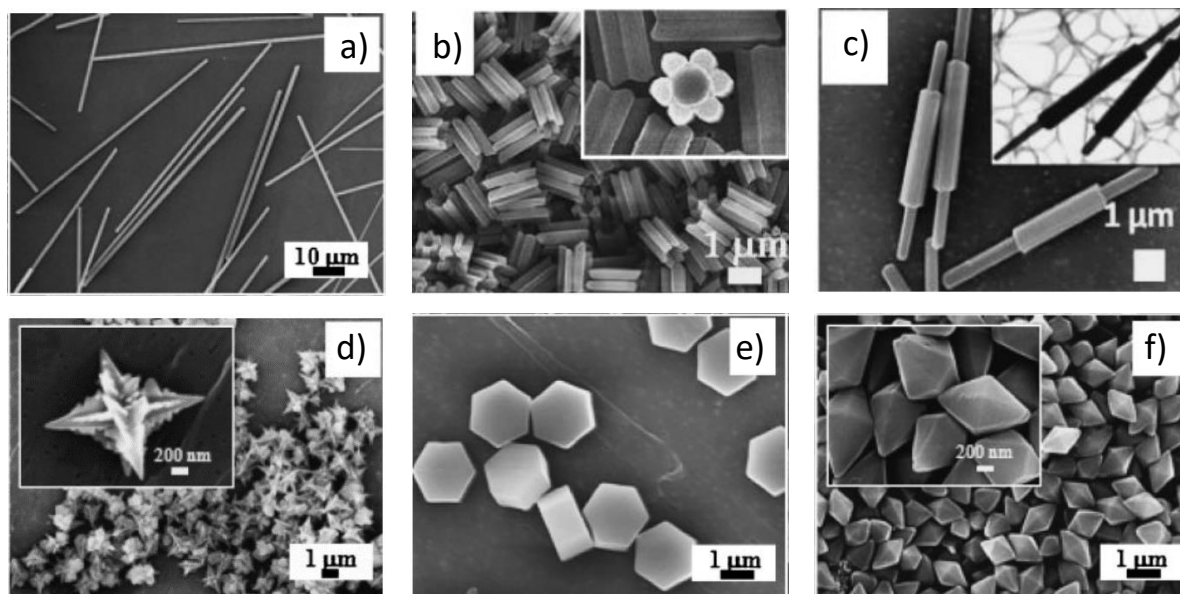


**Figure 1.13.** Different rate of injection for nanoprecipitation methods. a) drop-wise addition, b) pressure-driven injection, c) T-junction and d) Y-junction impinging jet mixers. Purple circles symbolize the area where the mixing of the two solutions is occurring.<sup>42</sup>

Drop-wise FNP was used for the formation of  $C_{60}$  nanoparticles in water. Fortner *et al.* obtained a variety of nanoparticle sizes by modulating the pH of water and the rate of organic phase addition. When the latter was increased, smaller particles were produced.<sup>56</sup> The morphology of the nanoparticles produced by FNP will be discussed in the section 1.3.b.

Many studies report formation of  $C_{60}$  nanocrystals by precipitation from a good apolar solvent (e.g. xylene, toluene, carbon disulfide...) to a bad polar solvent (e.g. acetone, ethanol...). 1D objects were first obtained from m-xylene added to a cetyltrimethylammonium bromide (CTAB) solution in isopropanol. Depending on the initial concentration of  $C_{60}$ , rods were obtained if initial  $C_{60}$  concentration was low, whereas when it was high, depletion induced hollow structures.<sup>57</sup> These nanocrystals have an optical signature slightly different from that of  $C_{60}$  films, and in Raman spectroscopy the vibration bands are similar to the ones of pure  $C_{60}$ .<sup>58</sup> Irradiation with light induced the growth of the nanowhiskers leading to nanocrystals with a section of about 200 nm and up to 10  $\mu$ m in length.<sup>59</sup> Masuhara *et al.* have prepared micro objects of various shapes ranging from simple spheres to square-based bipyramids, including sticks, hexagonal plates, stars or pastry rolls (Figure 1.14). This variety of shapes was obtained by adjusting the qualities of the good and bad solvents used, as well as their quantities and concentrations. It has been also shown that both injection and aging temperatures have an influence on the final shape and size of the microcrystals. This can be attributed to the change in solvent quality for both nucleation and growth processes.<sup>60, 61</sup> This study proves that this

method can give access to a great variety of particles in terms of both shapes and sizes, giving access to a broad diversity of potential applications. According to Park *et al.* the geometry of the assemblies depends on the type of good solvent used. A 3D solvent like  $\text{CCl}_4$  gives hexagonal platelets, a 2D solvent like m-xylene gives 1D objects and a 1D solvent like n-hexane gives 0D objects, *i.e.* isotropic particles.<sup>62</sup>



**Figure 1.14.**  $\text{C}_{60}$  microcrystals obtained by precipitation a) from m-xylene to isopropanol and aged at  $0^\circ\text{C}$ , b) at  $20^\circ\text{C}$ , c) at  $80^\circ\text{C}$ , d) from toluene to isopropanol, e) from p-xylene to n-propanol, f) from carbon disulfide to isopropanol.<sup>60</sup>

### iii. Dialysis method

Nanoprecipitation can also be achieved by dialysis: solutions of a hydrophobic solute in a polar organic solvent are poured in a dialysis membrane. Then dialysis is performed against water in order to replace the organic solvent. In general, this method gives access to particles with bigger sizes than other nanoprecipitation methods.<sup>63</sup>

For  $\text{C}_{60}$  fullerene, dialysis was used by first dissolving  $\text{C}_{60}$  in NMP. This solvent was chosen as saturation occurs at nearly 1 g/L.<sup>6</sup> Dialysis against water yielded maximum concentration of 0.17 g/L with the help of a polymer, poly(vinylpyrrolidone) (PVP). Absorption spectrum of the resulting suspension was similar to the one obtained via other dispersion methods, showing that no chemical modification of  $\text{C}_{60}$  occurred.<sup>64</sup>

Tomchuck *et al.* prepared  $\text{C}_{60}$  particles by dialysis method. They characterized them with both SAXS and SANS, which displayed similar results. A slope in  $q^{-2.9}$  for the scattering intensity was obtained, indicating a very dense structure. Please note that a slope of  $q^{-3}$  is theoretically impossible, but can reflect high polydispersity. The polydispersity was confirmed by the presence of a smooth Porod regime at high  $q$  values with a slope of  $q^{-4}$ . Another interesting



point of this work is that background noise is much more important in SANS than in SAXS. This shows that C<sub>60</sub> particles have a high electron density. As for SANS, the high noise is not surprising because the contrast of C<sub>60</sub> in D<sub>2</sub>O is very low (their scattering length densities are respectively 5.501 and 6.397x10<sup>-10</sup> cm<sup>-2</sup>).<sup>65</sup>

### c. Other methods

Emulsification-evaporation and nanoprecipitation are the two main processes used in literature to disperse C<sub>60</sub> in water. However, several other ones have been attempted and are presented in this part.

The most common process apart from the ones already discussed is the prolonged stirring (over several weeks) of solid C<sub>60</sub> in water. Prior to this, it was necessary to mill the initial powder. This is a way to avoid any use of organic solvent. However, this method leads to very low dispersion yields, with final concentrations hard to quantify because authors did not show the absorption spectroscopy results. Concentrations given in the paper are obviously overestimated because the turbidity that should be present for dispersion of such big particles is apparently not subtracted. Moreover, the absorption coefficient given is higher than other ones that can be found in literature as it will be discussed later on. Particles obtained by this method are big and polydisperse, and display morphology that clearly looks like what can be expected: that are fragments of crystals after fracture.<sup>66</sup>

Milling can also be followed by ultrasonic treatment as shown by Deguchi *et al.* This time, a surfactant (sodium dodecyl sulfate, SDS) was used to obtain reasonable concentrations and sizes of particles.<sup>67</sup> The same team also showed that particles can be obtained by trapping powder between two sliding surfaces. Particles obtained this way were unsurprisingly micrometric and polydisperse.<sup>68</sup> This method will be called mechanochemical.

Aqueous Counter Collision consists, as suggested by the name, to project two high pressure water flows against solid C<sub>60</sub> to break it into small pieces. Similarly, to particles obtain by grinding, they are big enough to be observed by optical microscopy and polydisperse.<sup>69</sup>

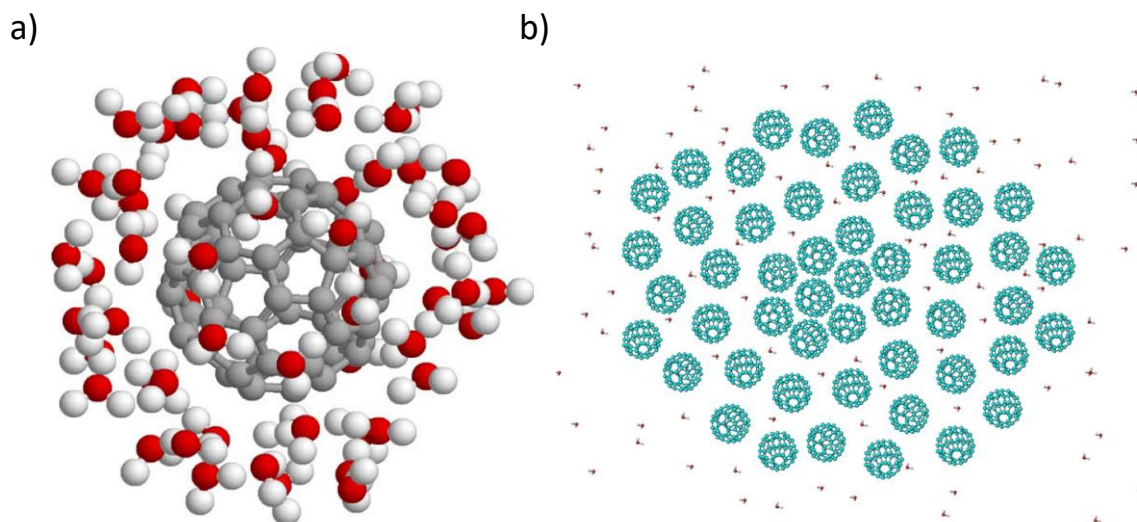
Mchedlov-Petrosyan summarizes in a review that it should be considered as a general rule that the colloids of C<sub>60</sub> are (poly)crystalline, and that suspensions as well as solutions of C<sub>60</sub> are mixtures of molecules and generally polydisperse nanoparticles.<sup>28</sup>

### 3) Stabilisation of fullerene nanoparticles in water

#### a. Stability origin

Destabilization mechanisms of emulsions presented in Figure 1.7 are also valid for colloidal suspensions.

C<sub>60</sub> fullerene nanoparticles can be dispersed in water without the help of a surfactant or polymer, up to the ppm scale. Given the hydrophobicity of C<sub>60</sub>, this is very surprising. Several possible stabilization mechanisms were given to explain this observation. A first theory was based on the interaction between C<sub>60</sub> and water. Indeed, oxygen atoms possess free electron pairs that they can share with C<sub>60</sub>, the latter being a good electron acceptor. Scharff *et al.* suggested the formation of water clathrates around C<sub>60</sub> particles thanks to theoretical quantum-chemical calculations combined with experimental data. The lowest energy water-fullerene complex was C<sub>60</sub>(H<sub>2</sub>O)<sub>60</sub> (Figure 1.15a).<sup>70</sup> Peidys *et al.* also performed theoretical calculations and showed that thermodynamic equilibrium was achieved when C<sub>60</sub> particles were more dense at their core than at their surface. The latter then would include water molecules (Figure 1.15b).<sup>71</sup>



**Figure 1.15.** a) Fullerene molecule complexed by 60 water molecules as suggested by Scharff *et al.*<sup>70</sup> b) Schematic representation of fullerene aggregates including water molecules as proposed by Peidys *et al.*<sup>71</sup>

Experimentally, several studies reported that C<sub>60</sub> particles are negatively charged at their surface in water, by zeta potential measurements. This was observed for various dispersion processes.<sup>64, 72, 73</sup> According to simulation works, this negative zeta potential could arise from the water clathrates around fullerene particles that could give a partial polarisation.<sup>74</sup>

When stability is due to electrostatic repulsions, the increase of ionic strength causes destabilisation because of their screening. Moreover, when counter-ions are multivalent, they might form bridges between particles by chelation, which causes flocculation. When stabilisation is steric, adding counter ions does not affect stability.

C<sub>60</sub> nanoparticles are unstable in saline medium as it was reported in several studies. Concentrations of NaCl as low as 10 mM were sufficient to induce reduction of zeta potential and subsequent aggregation of suspensions with only few mg/L for C<sub>60</sub> concentration.<sup>51, 75-77</sup>

Chen and Elimelech tested both monovalent (NaCl) and divalent (CaCl<sub>2</sub>) salts. Critical coagulation concentration (CCC) corresponds to minimum salt concentration at which complete destabilisation of particles is measured. Below this concentration, the amount of particle which destabilise is proportional to salt concentration following a RCLA mechanism (see section 1.1.b.i). Above this concentration, increasing ionic strength increases the destabilisation speed following a DLCA mechanism. CCC value was around 100 mM for NaCl, whereas it was only 5 mM for CaCl<sub>2</sub>. We can then conclude that C<sub>60</sub> nanoparticles are indeed negatively charged, as divalent cations effectively chelate them.<sup>78</sup> Another study by the same research group discussed aggregation in excess ionic strength. They measured a fractal dimension (df) around 2.0 for the aggregates. This is surprising because, at such high concentrations, DLCA is supposed to occur leading to aggregates with df around 1.7.<sup>79</sup>

These observations prove that fullerene particles are more stabilized by electrostatic repulsions than by the formation of water clathrates. Some authors speculated that electrostatic forces come from a partial oxidation of C<sub>60</sub> at its surface. However, the groups of Andrievsky and Andreev, who produced particles via emulsification-evaporation and dialysis methods, respectively, showed that no modification of the molar mass could then be noted by mass spectrometry.<sup>31, 80</sup>

Another team suggests hydroxylation of C<sub>60</sub> to occur during sonication. They did not use any organic solvent, but just directly sonicated powder in water. They freeze-dried the obtained particles and analysed the resulting solid. FTIR showed the apparition of a broad signal typical of C-O bonds, but also a signal from C-H bonds. The attribution to hydroxyl groups is then surprising. It is well-known that freeze-drying does not fully remove water from a sample. This signal could then be due to traces of water in the solid which was confirmed by solid state <sup>1</sup>H NMR which displayed a signal around 1 ppm even on pristine C<sub>60</sub>. The proof for hydroxylation is poor and water pollution is more likely to occur. Mass spectrometry would help at evidencing it but was not performed in this study.<sup>81</sup>

However, the oxidation occurred after long exposures to UV, and only in oxygen-containing atmosphere, leading to the degradation of photophysical properties of C<sub>60</sub>: their absorption of

UV and visible light decreasing with increasing exposure time. Both FTIR and MS spectra accounted for oxidation of  $C_{60}$ . In Static Light Scattering, scattered intensity decreases with exposure time, which can be either due to a decrease of size/molar mass or a decrease of contrast. The latter can be expected if particles are highly oxidized. TEM pictures failed at giving any complementary information as no particles could be observed.<sup>82</sup>

Apart from chemical modification of the surface, another explanation to its negative potential could be adsorption of anions. The group of François Ganachaud showed that bicarbonate ions, naturally present in water because of  $CO_2$  dissolution, tend to adsorb on hydrophobic surfaces such as air bubbles, oil droplets or hydrophobic polymer latexes. This is valid for pH values comprised between 5 and 10, where bicarbonate ions are in majority. This pH range corresponds to  $C_{60}$  dispersion studies.<sup>83</sup> For emulsification-evaporation process, Gál *et al.* showed by MS the formation of methylbenzoate ions and suggested that they form a layer around  $C_{60}$  clusters. This is interesting as it could explain why toluene in particular is a solvent of choice for this process.<sup>32</sup>

To conclude, it is now well-established that  $C_{60}$  nanoparticles in water without stabilizers are negatively charged at their surface as proved by numerous zeta potential measurements, and by their instability in saline medium. It is worth noting that this electrostatic stabilisation is observed no matter the preparation method. However, the explanation to this negative charge is still under debate and could originate from the oxidation of the surface or from anions adsorbed at the surface. The second seems more likely as no real proof of chemical modification was brought, and oxidation seems to require drastic conditions such as long time exposure to intense UV light.

#### b. Stabilisation by surface active agents

Surfactants and polymers are often used to increase the amount of  $C_{60}$  particles dispersed in water and to stabilise them. Generally speaking, these compounds form a protective layer around the dispersed phase. When suspensions are composed of hydrophobic molecules dispersed in an aqueous medium, amphiphilic polymers or molecules are ideal because their hydrophobic moieties interact with the particles, and their hydrophilic part forms a protective layer around them. Protection can be obtained thanks to electrostatic repulsions in the case of ionized stabilizers, or steric hindrance when they are neutral. However, these species must be used with parsimony. When their concentration is high, they can induce depletion forces resulting in flocculation of particles.

Here, some examples are given and specific interactions due to chemical structure of the stabilizers are discussed. To help this discussion, comparisons are made with systems used for the stabilisation of CNTs.

*i. Molecular surfactants*

One of the most effective surfactants for stabilization of  $C_{60}$  in water is Triton X-100, which forms micelles with a radius about 3 nm in water.<sup>84</sup> At low surfactant concentration, two populations could be distinguished by DLS. One population with  $R_h$  around 10 nm was attributed to surfactant micelles and the population around 50 nm was attributed to  $C_{60}$  particles. At high surfactant concentration, only one population was observed and attributed to  $C_{60}$  nanoparticles stabilized by surfactant. Interestingly, below CMC a strong absorption in visible light is seen, which is typical of solid  $C_{60}$ , whereas above CMC, UV absorption dramatically decreases and a maximum at 408 nm can be observed like encountered in organic solvents, where  $C_{60}$  is molecularly dissolved. In comparison, another surfactant, sodium dodecylbenzenesulfonate (SDBS), also displayed a decrease of  $C_{60}$  absorbance in visible, but in a lesser extent, and the maximum at 408 nm was not observed. The authors suggest that the absorption spectrum is a good way to probe the aggregation state of  $C_{60}$ , which will be discussed in the 4.c part of this chapter, and that their work highlighted the better ability for Triton X-100 to molecularly disperse  $C_{60}$  compared to an ionic surfactant.<sup>85</sup> The same group drew a comparison between cetyltrimethylammonium bromide (CTAB), sodium dodecylsulfate (SDS), Tween 65 and Brij 78, all of them being common surfactants. SDS and Brij did not allow the dispersion of  $C_{60}$  in water. CTAB helped dispersion but the resulting suspensions were unstable. Only Tween yielded stable dispersions. This work highlighted the advantages of neutral surfactants over ionic ones.<sup>86, 87</sup> Torres *et al.* also observed that neutral surfactants such as Triton X-100 or Tweens were better stabilizers as a plateau in dispersion yield was reached at lower concentration than for ionic surfactants like N-dodecyltrimethylammonium chloride (DTAC) and myristyltrimethylammonium bromide (MTAB).<sup>88</sup>

CNTs possess a chemical structure very close to the ones of fullerenes. For this reason, an interesting way to find efficient stabilizers for the latter is to check how CNTs can be stabilized in water. Since both CNTs and fullerenes contain many aromatic cycles on their surface, aromatic surfactants are very promising candidates to adsorb on them. Quaternary ammonia containing aromatic units were tested. When aromatic moieties were small, such as phenyls or naphthalenes respectively composed of one and two aromatic rings, the surfactants were not able to disperse CNTs in water. However, when aromaticity was increased to three (anthracene) or four aromatic cycles (pyrene), CNTs were dispersed, yielding colorful solutions. The deep black color of dispersion with the pyrene surfactant indicates a high CNTs concentration, although the authors did not quantify it. In the same study, fluorescence of the dispersions was studied since the surfactant displayed fluorescence in the visible region. The surfactant excess was high, since fluorescence is not impacted by CNT, however when CNTs

were centrifuged and redispersed (thus, eliminating the excess of surfactant), fluorescence was highly quenched by CNTs. Moreover, simple dialysis lead to destabilisation of CNTs, indicating that surfactant molecules were in dynamic equilibrium with the interface. The main drawback of these aromatic molecules is that they tend to aggregate with themselves via  $\pi$ -stacking as indicated by fluorescence measurements showing excimers formations. This tendency to stack means that an important amount of surfactant is not located at the interface. Also, it can be expected that at high surfactant concentration, important aggregation of these molecules might lead to destabilisation of the dispersions.<sup>89</sup>

Another study by Blanch *et al.* dealt with dispersion of CNTs by usual surfactants. They observed that a maximum CNT concentration was reached at intermediate surfactant concentration for all the systems. They attributed this behaviour to depletion, because this optimum was obtained at a constant surfactant concentration no matter the CNT concentration. This implies that stabilisation was not controlled by surfactant/CNT ratio, excluding the formation of complexes. Moreover, small ionic surfactants such as SDBS were more effective than larger and non-ionic surfactants such as Pluronic F-127 or Brij S100 for small diameter CNTs.<sup>90</sup> This statement contradicts the observations made by Lee *et al.* for fullerenes.<sup>86</sup> For larger CNTs, the tendency was very different as larger CNTs were better stabilized by PVP and Pluronics®. This shows the limitations of comparing CNTs and fullerenes, as the ability of surfactants or polymers to stabilize them seems to depend on their size.

The fate of C<sub>60</sub> particles in natural water was broadly studied in order to anticipate the environmental impact of such nanomaterials. It was largely proved that small quantities of C<sub>60</sub> (few ppm) can be dispersed in natural water thanks to the presence of natural organic matter (NOM). The latter is a complex mixture of organic compounds like humic and fulvic acids. Humic acids were proved to better stabilize C<sub>60</sub> than fulvic ones, even though both possess aromatic units in their chemical structure.<sup>66, 91</sup> Additionally, it is worth noting that the so-produced particles could go through a 20 nm pore filter, meaning that C<sub>60</sub> was well dispersed with a maximal concentration of 4 mg/L.<sup>92</sup> The same tendency was shown for CNTs.<sup>93</sup> Also, it was reported that exposure to sunlight during stirring increased the concentration of C<sub>60</sub> in water.<sup>94</sup> Absorption spectrometry study showed that the extinction coefficient decreases with exposure time. This observation corroborates the study in ref.<sup>82</sup>, indicating a possible oxidation of C<sub>60</sub> during the process. Humic acids help stabilizing C<sub>60</sub> in NaCl solutions up to 150 mM. In CaCl<sub>2</sub>, chelation of humic acid lead to destabilization even faster than in the absence of any stabilizer.<sup>79</sup>

When C<sub>60</sub> nanoparticles are stabilised by ionic surfactants, their stability in high ionic strength media is low. However, adding excess surfactant helps at increasing their stability. Their

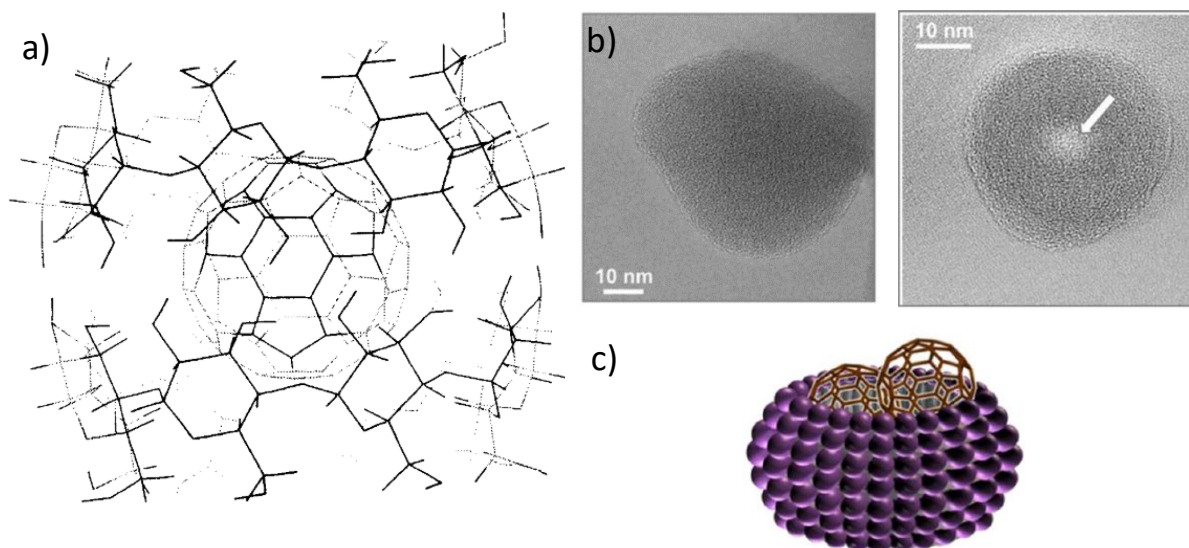


stability in saline solutions is still better when they are stabilized by neutral species such as poly(N-vinylpyrrolidone) (PVP). The interactions of  $C_{60}$  with PVP will be further discussed in the next part.<sup>95</sup>

## ii. *Amphiphilic or hydrophilic polymers*

One way to stabilize  $C_{60}$  molecules in water is to embed them in a cage. Cyclodextrins (CD) are then good candidates. They are cyclic polysaccharides with a truncated cone shape. Three sizes exist:  $\alpha$ - (cavity diameter equal to 0.45 nm),  $\beta$ - (0.70 nm) and  $\gamma$ -CD (0.85 nm). The hydrophobic cavity of these polymers is well known to encapsulate hydrophobic compounds.<sup>96</sup> Since  $C_{60}$  itself has a diameter of 0.71 nm, the  $\gamma$ -CD seems to be the more suited. It was indeed shown that it can complex  $C_{60}$  in water. Such a result published in 1992 was revolutionary because it allowed selective complexation of  $C_{60}$  from a mixture of various fullerenes. It was shown from the complex formation kinetics that a 2:1 (cyclodextrin:fullerene molar ratio) inclusion complex was formed (Figure 1.16a).<sup>97</sup> The main advantage of this inclusion complex is that  $C_{60}$  is molecularly dispersed in aqueous medium, which is very hard to achieve as stated previously. However, above approximately 60 mg/L,  $C_{60}$  tends to aggregate.<sup>98</sup> Please note that an original dispersion method was used: a  $C_{60}$  solution in toluene was mixed with an aqueous solution of  $\gamma$ -CD and the mixture was refluxed during 48h. The complex was recovered after drying. Other cyclodextrins can also be used. For example,  $\alpha$ -CD forms complexes with the cation radical of  $C_{60}$ . The complex is maintained even after reduction back to ground state.<sup>99</sup> 2-hydroxypropyl- $\beta$ -CD was used to yield  $C_{60}$  nanoparticles at a maximum concentration of 0.7 g/L processing the mechanochemical method.<sup>100</sup> Finally,  $\gamma$ -CD-grafted gold nanoparticles were physically bound by  $C_{60}$  molecules, leading to the formation of fractal aggregates.<sup>101</sup>

Calixarenes are also used as hosts for inclusion complexes, however  $C_{60}$  was aggregated with this host as shown by absorption spectroscopy.<sup>96, 102, 103</sup> Inclusion complexes were also achieved with so-called glyconanosomes which consists in cross-linked nanodisks based on an oligomer of PEG modified with sugar units and hydrophobic alkyl chains containing carbon-carbon triple bonds. These nanoparticles were able to thread onto CNTs but also to include various hydrophobic molecules such as  $C_{60}$ . However, the concentration of  $C_{60}$  was only few tens of g/L (Figures 1.16b and c).<sup>104</sup>

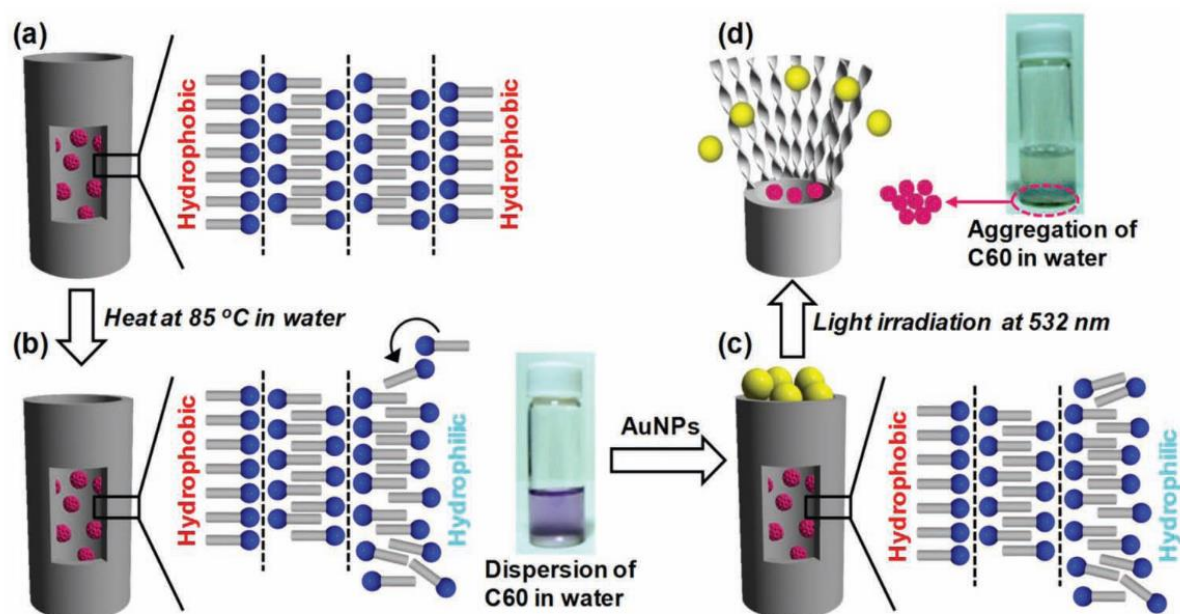


**Figure 1.16.** a) Schematic representation of the 2:1  $\gamma$ -cyclodextrin:C<sub>60</sub> inclusion complex.<sup>97</sup> b) TEM images of glyconanosomes without (left) and with (right) C<sub>60</sub>. c) Schematic representation of the glyconanosome/fullerene inclusion complex.<sup>104</sup>

Beside molecular dispersion, the elaboration of C<sub>60</sub> nanoparticles with peculiar morphologies is also reported because of the wide range of possibilities as we discussed in section 1.2.b.ii. However, for now we discussed only the formation of microcrystals by solvent exchange methods, but it is also possible to induce nanostructuration through interaction with the stabilizer. For example, fullerene nanocylinders were obtained thanks to an amylose-iodine complex that formed a helix structure capable of roping around C<sub>60</sub> molecules. It was possible to remove iodine by addition of ascorbic acid after formation of the nanowhiskers, leaving only amylose to stabilise them.<sup>105</sup>

Ishikawa *et al.* designed a glycolipid that displays various self-assemblies depending on the solvent. In water, it forms nanosheets, in alcohols nanotubes and in toluene helices. The glycolipid was dispersed in methanol and mixed with C<sub>60</sub> in toluene, the mixtures were freeze-dried and redispersed in water. The mixtures still display the formation of nanotube but local structure at the interface was modified by a flip-flop mechanism to put hydrophilic moieties on the outer side of the nanotube. C<sub>60</sub> were thus trapped inside the nanotubes and dispersed molecularly in water as evidenced from the purple color of the resulting solutions. The concentration was equal to 0.5 g/L. Finally, gold nanoparticles were also incorporated in the nanotubes and irradiation in the visible region induced local heating because of the gold nanoparticles, unfolding the nanotubes and releasing the C<sub>60</sub> molecules that aggregated and destabilized from solution (Figure 1.17).<sup>106</sup>





**Figure 1.17.** Schematic description of the encapsulation of C<sub>60</sub> inside glycolipid nanocylinders followed by their release triggered by photothermally induced unfolding of the nanotubes.<sup>106</sup>

Other polysaccharides than cyclodextrins or amylose were used to disperse C<sub>60</sub> in water. When pullulan was functionalized by a cholesterol, the resulting self-assemblies in water were able to stabilize C<sub>60</sub> nanoparticles obtained by Ouzo nanoprecipitation from pyridine.<sup>107</sup>

Bartocci *et al.* reported stabilisation of C<sub>60</sub> in water by co-milling with a specific peptide. The latter was containing hydrophilic moieties thanks to quaternary ammonium functions and « functional ligands » with a pendant phenyl group. According to the authors, the highest concentration was 1.3 g/L. However, the only proof that they give is thermogravimetric analysis (TGA) where the peptide degrades at the same temperature as C<sub>60</sub>. However, the concentration must be high since the samples display a dark color. Finally, without any solvent, high-speed vibration milling yielded higher concentrations than manual grinding, itself being better than sonication with a horn tip.<sup>108</sup> Another team also successfully dispersed C<sub>60</sub> in water with different phenyl-containing peptides. Interestingly, C<sub>60</sub> concentration was in all cases higher when dispersion was processed in basic medium than at neutral pH. At low pH, almost no C<sub>60</sub> was dispersed. The peptide that gave the highest concentration for the dispersion at pH 12 was different from the one at pH 7. Although pK<sub>a</sub> values are not given in this work, it can be expected that final concentration depends on the ionization degree of the peptide.<sup>109</sup>

Another approach is to use synthetic polymers with a proper chemical structure *i.e.* amphiphilic displaying preferential specific interactions with C<sub>60</sub> such as  $\pi$ -stacking or donor-acceptor interactions. As we previously discussed, C<sub>60</sub> complexes with nitrogen-containing species because of nitrogen's ability to share a pair of electrons. In this way, donor-acceptor complexes

are formed, C<sub>60</sub> being the acceptor. This explains why poly(N-vinylpyrrolidone) (PVP) was widely used to stabilize C<sub>60</sub> nanoparticles in water.<sup>95, 110-115</sup> One can wonder if PVP is physically or chemically bound to C<sub>60</sub>, because of the propensity of amines to graft onto C<sub>60</sub> molecules. UV-visible absorption spectra of modified C<sub>60</sub> are very different from the ones of pristine fullerene, since the three characteristic maxima in UV region are lost. In the case of PVP-stabilised C<sub>60</sub>, these maxima are clearly observed, so chemical reaction can be excluded.<sup>73</sup> Actually, PVP being an amide, is less reactive than amines, and the nitrogen atom of PVP repeating unit does not carry a hydrogen atom, which is a prerequisite to react with C<sub>60</sub> as it was discussed in the section 1.1.b.iii. PVP is also a common stabilizer for CNTs, along with poly(styrene sulfonate) (PSS).<sup>116</sup>

Diblock PS-b-PDMA (poly(dimethylacrylamide)) copolymers gave access to C<sub>60</sub> dispersions in water with concentrations up to 50 mg/L.<sup>117</sup> Diblock PS-b-PDMAEMA (poly(2-dimethylamino ethylmethacrylate)) copolymers self-assemble into core-shell micelles into which C<sub>60</sub> molecules migrate.<sup>118</sup>

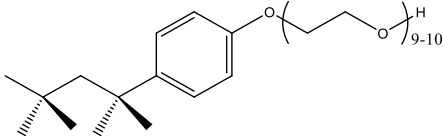
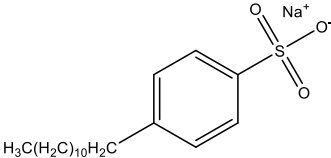
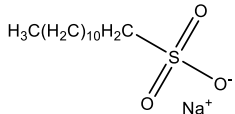
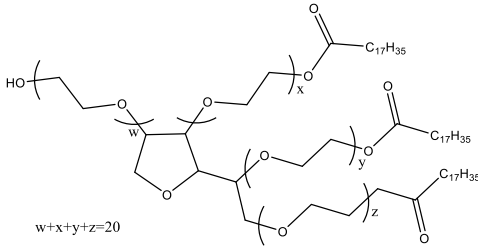

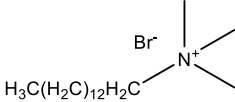
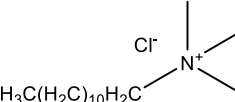
Other block copolymers that were used were Pluronic®, which are commercial PEO-b-PPO-b-PEO triblock copolymers. The central PPO (poly(propylene oxide)) block is hydrophobic and side PEO blocks are hydrophilic. These copolymers self-assemble in micelles when dispersed in water and are biocompatible. That is why they have attracted the interest of researchers seeking for C<sub>60</sub> nanoparticles for biomedical applications. Sonication of C<sub>60</sub> powder in the presence of Pluronic F-127 dispersed in water yielded reproducible spherical particles. Increasing Pluronic concentration decreased the size and dispersity of the particles until reaching a plateau that can be attributed to saturation of the surface of particles with polymer. The solutions were pale yellow-colored, indicating a low C<sub>60</sub> concentration (ppm scale). The authors also showed that the particles are stable in saline media in diluted conditions, despite a negative zeta potential.<sup>119</sup>

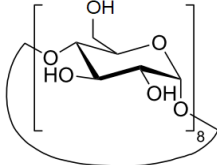
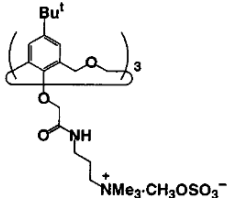
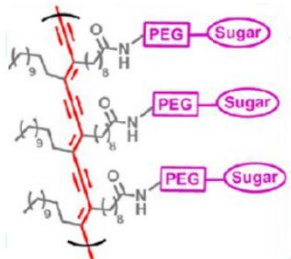
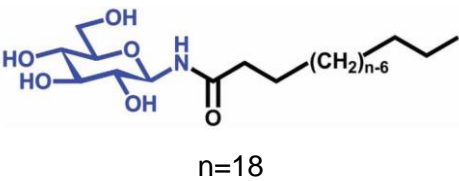
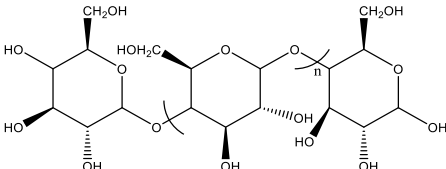
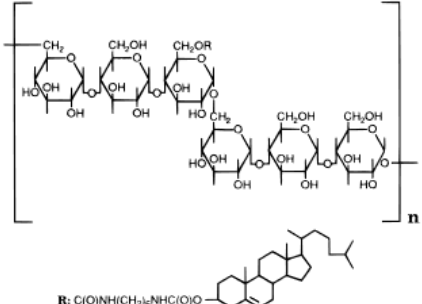
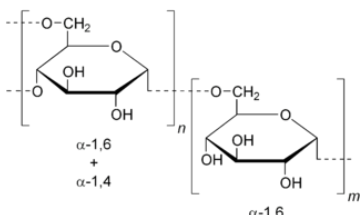
A similar example is the use of a PDMS-b-(PDMS-g-(PEO-co-PPO)), which can be assimilated to a PDMS backbone on which amphiphilic chains are grafted. Dispersion was achieved through sonication in a bath without the help of an organic solvent. The resulting particles were micrometer-sized and concentration was not higher than 25 mg/L even with 5 g/L polymer.<sup>120</sup>

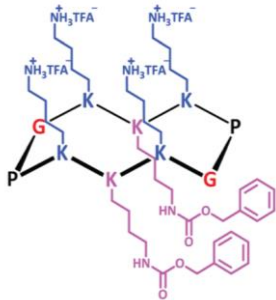
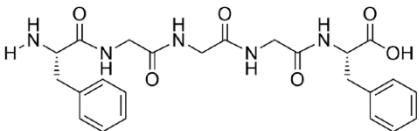
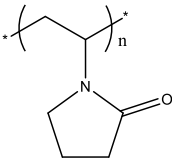
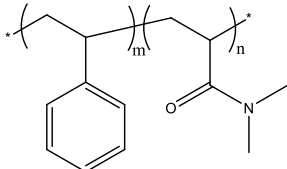
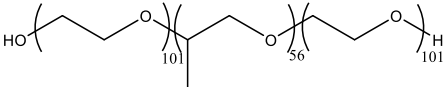
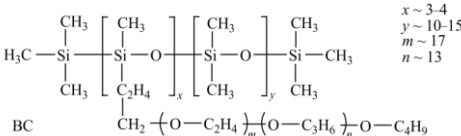
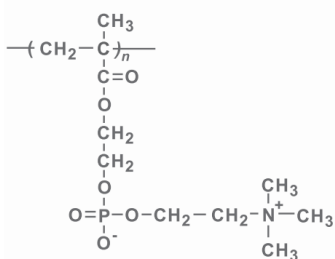
Finally, Ohata *et al.* reported complexation between C<sub>60</sub> and poly(2-(methacryloyloxy)ethyl phosphorylcholine) (PMPC), a zwitterionic polymer achieved by co-milling. A maximum concentration of C<sub>60</sub> of 0.67 g/L was obtained with only 1 g/L PMPC, corresponding to a yield of 60%. Finally, combined DLS measurements showed that particles size was independent of polymer concentration.<sup>121</sup>

A summary of surfactant molecules and polymers used for the dispersion of  $C_{60}$  molecules in water is given in Table 1.1.

**Table 1.1.** Summary of all the surfactants and polymers used for stabilisation of  $C_{60}$  and CNTs discussed in this chapter. <sup>a</sup>:  $C_{\text{surf}}$ =surfactant or polymer concentration. <sup>b</sup>:  $C_{\text{full}}$ = fullerene concentration. <sup>c</sup>: TFA=trifluoroacetic acid, P=proline, K=lysine, G=glycine. <sup>d</sup>: Proofs are lacking to claim this result. The chemical structures were either drawn or taken from cited references.

Name	Chemical structure	Dispersion method	$C_{\text{surf}}$ (g/L)	$C_{\text{full}}$ max (g/L)	Ref.
Triton X-100		Emulsification	6	$20 \cdot 10^{-3}$	88
SDBS		Emulsification	10	$5 \cdot 10^{-3}$	87
SDS		Emulsification	5	$5 \cdot 10^{-3}$	87
Tween 65		Emulsification	10	$11 \cdot 10^{-3}$	88
Brij 35/78	 Brij 35 : x=10, y=23 Brij 78 : x=16, y=20	Emulsification	10	$5 \cdot 10^{-3}$	87
MTAB		Emulsification	40	$16 \cdot 10^{-3}$	88
DTAC		Emulsification	100	$8 \cdot 10^{-3}$	88
Humic acid	Mixture of compounds	Magnetic stirring	0.1	$4 \cdot 10^{-3}$	92
Fulvic acid	Mixture of compounds	Magnetic stirring	0.1	$60 \cdot 10^{-6}$	92

$\gamma$ -cyclo-dextrine		Reflux	26	$60 \cdot 10^{-3}$	97
Calixarenes		Magnetic stirring	0.4	$0.17^d$	103
Glyco-nanosome		Ultrasonic stirring	1	Not given	104
Glycolipid	 n=18	Co-solvation, drying, re-dispersion in water	1	0.5	106
Amylose		Magnetic stirring	0.7	$90 \cdot 10^{-3}$	105
Cholesteryl pullulan	 R: C(O)NH(CH2)6NHC(O)O-	Ouzo	1	0.6	107
Dextran		Magnetic stirring	1	Not given	122

Bartocci's peptide <sup>c</sup>		Mechano-chemical	5.2	1.3 <sup>d</sup>	108
Peptidic nano-tweezer		Ultrasonic stirring	0.1	36.10 <sup>-3 d</sup>	109
PVP		Emulsification	2.3	72.10 <sup>-3 d</sup>	95
		Nanoprecipitation	120	65.10 <sup>-3</sup>	110
PS-b-PDMA		Nanoprecipitation / Dialysis	0.5	47.10 <sup>-3 d</sup>	117
Pluronic F-127		Ultrasonic stirring	10	Few mg/L	119
PDMS-b-(PDMS-g(PEO-co-PPO))		Ultrasonic stirring	5	Not given	120
PMPC		Mechano-chemical	1	0.67	121

By simple view of the Table 1.1, one can understand the difficulty to determine which method or which stabilizer is more appropriate for C<sub>60</sub> dispersion in water. Indeed, each study involves one or few stabilizers, with its very own preparation path. A lack of consistency between all these works prevents rigorous comparison in order to draw links between stabilizer chemical

structure and its affinity to  $C_{60}$ . Also, many studies do not clearly explain how the final fullerene concentration is measured. However, some conclusions can be drawn.

First, the few works in which  $C_{60}$  concentration dispersed in water is higher than 0.5 g/L involved various dispersion method, mechano-chemical ones seeming to be the most efficient. However, it should be tempered by the lack of studies about the stability of the resulting dispersions. Emulsification seems to be less efficient as the highest concentration reached is 72 mg/L with PVP.<sup>95</sup> Although, it is worth noting that reaching a high fullerene concentration is not a target for many works, and only few of them wished at increasing it. We can then believe that the optimisation of the processing conditions would help at increasing the yield for the dispersion of fullerene. Finally, each dispersion process can lead to a variety of objects, inducing dramatic consequences on the physical or biological properties of the particles.

It appears that a prerequisite for the stabilizers is an amphiphilic nature. For example, a cholesterol-bearing pullulan allows the dispersion of up to 0.5 g/L of  $C_{60}$ ,<sup>107</sup> while dextran, which is a branched analogue of pullulan, without chemical modification was unable to yield stable particles.<sup>122</sup> Furthermore, Iyer *et al.* showed that in the case of amylose, it was necessary to create a hydrophobic cavity thanks to the starch-iodine complex to trap  $C_{60}$ .<sup>105</sup> In the same way, cyclodextrines or calixarenes are able to disperse  $C_{60}$  thanks to their hydrophobic cavity. For PVP even though the possibility to form donor-acceptor complexes with  $C_{60}$  is beneficial, only few tens of mg/L in water can be reached because of the lack of amphiphilic properties. It can then be concluded that hydrophobic interactions are of major importance for dispersing  $C_{60}$  in water.

The role of aromatic moieties in the dispersion is unclear. Indeed, SDBS did not display better dispersion properties than SDS. However, Tomonari *et al.* showed with CNTs that several aromatic cycles might be needed to induce  $\pi$ -stacking, as dispersion was achieved for pyrene- and anthracene-containing surfactants, but not for the naphthalene and phenyl analogues.<sup>89</sup> One could note that all the stabilizers giving access to  $C_{60}$  concentrations above 0.5 g/L contain nitrogen atoms. It is therefore tempting to conclude that donor-acceptor interactions are also a prerequisite for achieving dispersion of high concentration. However, Ohata *et al.* dispersed a high amount of  $C_{60}$  using PMPC, in which nitrogen is present in a quaternary ammonium function, which means that nitrogen does not possess any free electron pair to share for donor-acceptor interactions with  $C_{60}$ .

To conclude, systematic studies are still needed to better understand the influence of the dispersion process and the chemical structure of the stabilizer on the dispersion state of  $C_{60}$  in water. However, the best stabilizers were amphiphilic and showed an ability to form

hydrophobic cavities able to host fullerene molecules. Donor-acceptor and  $\pi$ -stacking interactions might also help at dispersing  $C_{60}$ , but their importance is still not well-established.

### c. Chemical modification

As we already briefly discussed,  $C_{60}$  is an electrophilic molecule. Despite its apparent symmetry, all its carbon atoms are not equivalent, which means that chemistry can lead to its regioselective modifications. Fullerene can then be considered as a platform on which functional groups can be attached, and a control over their orientation in space is possible. Also, since  $C_{60}$  is a good electron acceptor, attaching electron donor groups on it is a way to induce self-assembly for the design of functional materials such as organogels.<sup>123</sup> Chemistry is also a tool for optimizing the properties of fullerene and improve its processability such as its solubility in water, either by covalently modifying  $C_{60}$  with hydrophilic functions or by attaching it to water-soluble polymers.

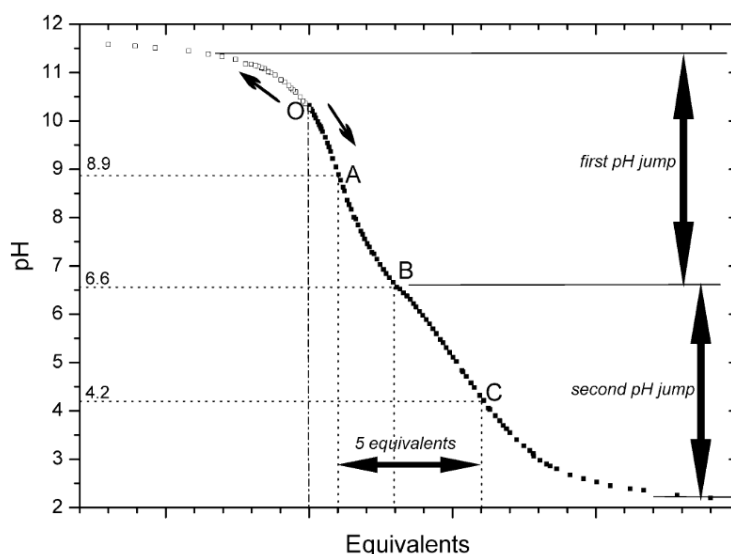
#### i. Hydrophilic functions grafting

We already showed that amines react with  $C_{60}$  by nucleophilic addition. Here we give some examples of various hydrophilic derivatives of  $C_{60}$ , and some derivatives that can undergo original self-assemblies.

The most common water-soluble fullerene derivatives are  $C_{60}(OH)_x$ , known as fullerols or fullerenols. Some of them are commercially available. Their synthesis proceeds through the reaction of  $C_{60}$  with NaOH<sup>124</sup> or after mixing it with nitric and sulfuric acid.<sup>125</sup> The first method leads to fullerols containing up to 24 hydroxyl functions, whereas the second one is limited to 12 functions. Kokubo *et al.* showed that the latter derivatives could react with hydrogen peroxide giving access to up to 40 hydroxyl groups. While  $C_{60}(OH)_{12}$  is not soluble in water,<sup>126-128</sup>  $C_{60}(OH)_{22-24}$  is highly soluble (250 g/L) at neutral pH and room temperature according to Semenov *et al.*<sup>124</sup> These very high values contradict the work of Kokubo *et al.* who reported solubilities of 17 and 59 g/L for  $C_{60}(OH)_{36}$  and  $C_{60}(OH)_{40}$ , respectively.<sup>126</sup> The stability of these species in water is achieved through increase of both their polarity and electrostatic repulsions. Since fullerols have a chemical structure close to phenol, it can be expected to display pH sensitivity. No pKa values are reported for fullerols but Brant *et al.* showed that electrophoretic mobility of  $C_{60}(OH)_{20-24}$  displays increased values with increasing pH. Furthermore, fullerol was more aggregated in acidic conditions than in basic ones (approximately one decade of difference for  $R_h$  between pH 6.0 and 10.8).<sup>129</sup> Vleno *et al.* reported titration of  $C_{60}(OH)_{36}$  and showed that high ionization was reached for pH higher than 12. The titration curve also highlights that the hydroxyl groups are not equivalent since two pH jumps can be seen between pH 2 and 12 (Figure 1.18).<sup>130</sup> In total, 10 protons are labile, going from  $C_{60}(OH)_{29}(O^-)_7$  at pH 2 to  $C_{60}(OH)_{19}(O^-)_{17}$  at pH 12. This means that fullerols are always ionized no matter the pH.



Also, the same study shows that aggregation occurs in PBS buffer solution, which is possibly due to the high ionic strength of the medium. Interestingly, Kokubo *et al.* underlined the inability of fullerols to crystallize contrary to pure  $C_{60}$ .<sup>126</sup>

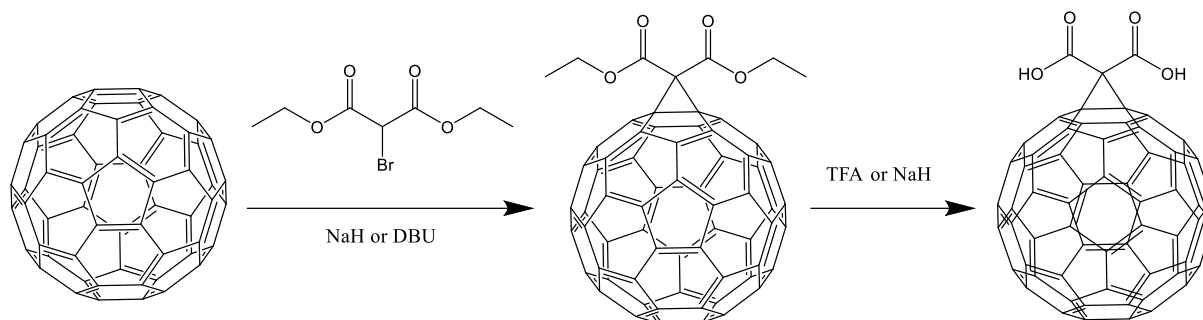


**Figure 1.18.** Titration curve of  $C_{60}(OH)_{36}$  by HCl (open symbols) and NaOH (close symbols).<sup>130</sup>

A second hydrophilic derivative for  $C_{60}$  is malonic  $C_{60}$ . Its polarity is significantly increased with respect to neat  $C_{60}$  since two carboxylic groups are grafted on one carbon-carbon double bond. Its synthesis proceeds in two steps (Figure 1.19). The first one consists in a Bingel reaction. This reaction yields mono- or poly-adducts (up to 6 adducts) that can be separated by chromatography.<sup>131</sup> For each number of adducts, several isomers can be obtained because there are many reactive sites. For example, Cheng *et al.* showed that three main regioisomers could be obtained for the bis-adduct.<sup>132</sup> The second step is an acidolysis of the ester derivative by trifluoroacetic acid (TFA). Ester functions are then converted into carboxylic functions. Acidolysis is preferred to saponification in basic conditions, as NaOH tends to attack  $C_{60}$  leading to the grafting of hydroxyl groups on it.<sup>133</sup> Otherwise, a non-hydroxide base like NaH can be used.<sup>134</sup> In any case, the number of carboxylic acids depends on the first step. As for fullerols, the more  $C_{60}$  is functionalized, the best is the solubility in water. This way, mono-adduct is only moderately soluble above pH 9 while tris-adduct is very soluble even at pH 7. However, all malonic fullerenes are insoluble in acidic solutions. The stability is thus only ensured by electrostatic repulsions.<sup>134</sup> Guldi showed that the mono-adduct's aggregation is prevented when it is encapsulated in  $\gamma$ -cyclodextrin or micelles of surfactants (Triton X-100 or cetyltrimethylammonium chloride, CTAC).<sup>135</sup> It was suggested that aggregation was due to insufficient coverage of  $C_{60}$  with hydrophilic functions, thus promoting aggregation of the « naked » regions. If more functions are added, this aggregation could be prevented.<sup>136</sup> The tris-adduct displays a solubility which depends on temperature (250 g/L at 20°C and 450 g/L



at 60°C) but tends to aggregate when concentration is increased. Above saturation, hydrated crystals are formed at low temperature and dry ones at high temperature.<sup>137</sup>



**Figure 1.19.** Two-steps synthesis path for the production of malonic fullerenes. For clarity only the mono-adduct is shown.<sup>132</sup>

Based on the Bingel reaction, a dendrofullerene was developed by the group of Hirsch: the solubility was 8.7 g/L in PBS buffer at pH 7.4, and 65 g/L at pH 10. The main advantage of this modification is the huge increase of solubility whilst keeping the optical properties of fullerene since a monoaddition is at play. However, the synthesis is much tedious than previous methods.<sup>138</sup>

In the Prato reaction, sarcosine reacts with a carbonyl-containing molecule to generate ylide, an intermediate zwitterionic specie that grafts onto  $C_{60}$  by nucleophilic addition. An N-methylpyrrolidine is formed. The two groups on the carbon in  $\alpha$  of the amine are the groups that were surrounding the carbonyl of the original reactant. Interestingly, addition of iodomethane results in a nucleophilic addition on N-methylpyrrolidone, yielding quaternary ammoniums. Highly soluble derivatives were thus obtained for bis-adducts, with saturation concentrations up to 15 g/L in water and comparable values in PBS buffer solutions.<sup>139</sup> Prato reaction was used to add pendant oligo(ethylene oxide) chains to  $C_{60}$  molecules. Interestingly, their number and topology modify the self-assemblies. Indeed, different chemistries gave access to nanosheets, vesicles, nanotubes or rods. To make these derivatives soluble in water, it was necessary to ionize the amine. Concentrations up to 1 g/L could be reached with these derivatives.<sup>140</sup> When a porphyrin was added, hollow cylinders were obtained. However, no solubility data were given for the porphyrin derivative.<sup>141</sup> In the same way, a quaternary ammonium carrying a  $C_{12}$  alkyl chain was grafted onto  $C_{60}$  by Prato reaction. Nanowhiskers along with small platelets were formed when they were solubilized in water.<sup>142, 143</sup> By analogy to the reaction of  $C_{60}$  with sarcosine for Prato reaction,  $C_{60}$  was functionalized with glycine. The obtained derivative was soluble up to 15 g/L (in terms of  $C_{60}$  only), with a very simple one-step synthesis.<sup>144</sup>

Nakamura and his group have developed a chemistry that gives access to C<sub>60</sub> penta-adducts. In addition to the many applications in organic solvents, such as the formation of self-assemblies to form networks (organogels), this specific addition has enabled the development of amphiphilic “conical” derivatives, with a hydrophobic head (the C<sub>60</sub>) and several hydrophilic arms at the termination. Otherwise, it is also possible to generate a cyclopentadienyl carbanion on the C<sub>60</sub>. Thus if hydrophobic arms are grafted, vesicles can be formed because the hydrophilic part is between two hydrophobic parts. When they are single benzene rings, spherical aggregates with R<sub>h</sub> equal to 17 nm are formed, and solubility reaches 6 g/L.<sup>145</sup> An interesting observation is that unlike conventional surfactants such as CTAB or SDS, these derivatives do not position themselves at the water/air interface (formation of bubbles) but partition selectively at the water/oil interface in emulsions. One of the applications of these vesicles in materials science is their decoration by complexation with functionalized ethylene oxide gold nanoparticles, leading to the growth of the latter on the surface of the vesicles. Thus, the plasmon resonance energy is changed so that the maximum absorption wavelength is shifted from 510 to 544 nm. These objects showed thermal decomposition under the effect of a green laser.<sup>146</sup> When alkyl chains are composed of 8 to 20 carbon atoms, self-assemblies in the form of vesicles are obtained, according to LS data. The vesicle shape was justified by an R<sub>g</sub>/R<sub>h</sub> ratio close to 1 and a comparison with the aggregation number measured by SLS. Numerical modeling showed that the vesicles are bilayers, since their thickness corresponds to 2 of these molecules.<sup>145, 147</sup>

If the adducts are comprising aromatic cycles, their rigidity leads to self-assemblies as shuttlecocks that self-assemble together to form 1D self-assemblies. Thus, liquid crystals are formed in dodecane.<sup>148</sup>

## ii. Covalent binding to polymers

Many studies attempted to disperse C<sub>60</sub> in water by formation of covalent bonds between C<sub>60</sub> and hydrophilic polymer chains. Various chemical paths are possible: C<sub>60</sub> can be grafted onto the monomer which is subsequently polymerized or directly on a polymer chain. Both options give access to polymer chains containing C<sub>60</sub>, with a possibility to vary the amount of C<sub>60</sub>. The second option gives access to C<sub>60</sub>-terminated polymer chains. In this case, obviously the amount of C<sub>60</sub> per polymer chain is much lower.<sup>149</sup>

A copolymer was obtained by copolymerization of N-vinylpyrrolidone (NVP) and a C<sub>60</sub> vinyl monomer obtained by Prato reaction. NVP was chosen by the authors for its affinity with C<sub>60</sub> as we already discussed. The resulting polymer was highly soluble in water, and allowed dispersion of up to 5.6 g/L C<sub>60</sub> in water.<sup>150</sup>

Samal *et al.* entrapped bis-p-aminophenyl (BPE) in  $\gamma$ -CD, then added  $C_{60}$ . The diamine reacted with  $C_{60}$  (see section 1.1.b.iii), and an alternating copolymer  $C_{60}$ -alt-BPE was obtained. It was soluble in water at a concentration bigger than 10 g/L according to the authors, and displayed modified absorbance spectra.<sup>151</sup>

$C_{60}$  mono-substituted by PNIPAM chains was obtained in two ways. The first involved NIPAM RAFT-polymerization ended by an addition of the radical onto the fullerene. The second consisted in a click reaction between an azide-terminated PNIPAM chain and  $C_{60}$ . As a result, thermoresponsive  $C_{60}$  particles with a diameter of about 100 nm were obtained. Above Lower Critical Solubility Temperature (LCST) of PNIPAM, it became hydrophobic and particles destabilized but could be resuspended at room temperature. Data on the method of solubilization or on the solubility were inconsistent.<sup>152, 153</sup> Likewise,  $\epsilon$ -caprolactone chains were functionalized with  $C_{60}$  by click chemistry,<sup>154</sup> as well as cellulose nanocrystals (CNC).<sup>155</sup>

Among polysaccharides, chitosan possesses an amine function. and is also biocompatible. However, a common solvent for these two species is difficult to find. High molar mass chitosan is soluble only in acidic water while fullerene is rather soluble in nonpolar organic solvents. Two overcoming ways are proposed in the literature: either use an oligo(chitosan)<sup>156</sup>, or use an ethylene glycol-functionalized chitosan.<sup>157, 158</sup> In these two conditions, it is soluble in dimethylsulfoxide (DMSO), which is miscible with toluene and benzene. For the second case, Kwag *et al.* proved that  $C_{60}$  was successfully added to the amine. It is also possible to graft  $C_{60}$  on a pendant hydroxyl group by addition of a strong base like LiOH as shown by Kim *et al.* This reaction can then be extended to many other polysaccharides, one example being hyaluronic acid.<sup>159</sup>

#### 4) Properties of fullerene aggregates in water

The aim of this part is to describe some of the physical and biological properties of  $C_{60}$  in terms of possible applications. Chemical, biological and opto-electronical properties of  $C_{60}$  will be reviewed. More particularly, the influence of physical features such as aggregation state and crystallinity on these properties will be discussed.

##### a. Chemical and biological properties

Fullerene is often described as a “free-radical sponge”: it is very reactive toward radicals. It means that it can be used as an additive in a formulation to protect another specie from reaction with radicals, thanks to its electrophilic nature.<sup>160</sup> For example, a hydrophilic  $C_{60}$  derivative showed impressive free radical scavenging properties, since at a concentration of 0.15 g/L it

can destroy  $\text{OH}^\cdot$  radicals by almost 98% as shown by RPE measurements.<sup>140</sup> Radical scavenging ability can be improved by chemical modification: bis-adduct of malonic acid deactivates 100 times more effectively  $^1\text{O}_2$ .<sup>161</sup> Guldi *et al.* probed the effect of aggregation state of  $\text{C}_{60}$  over its radical scavenging ability by complexing it with  $\gamma$ -CD. They observed an increase in the Reactive Oxygen Species (ROS) quenching,<sup>162</sup> but they came to the conclusion that the radical scavenging mainly came from  $\gamma$ -CD itself.<sup>163</sup> A comparative study by the same authors concluded that malonic bis-adducts outperformed tris- and more adducts as well as pure  $\text{C}_{60}$  and mono-adduct with  $\gamma$ -CD, fullerol  $\text{C}_{60}(\text{OH})_{18}$  and an hexa-sulfonic acid derivative in terms of radical scavenging ability.<sup>136</sup> In addition, the tris-adduct malonic derivatives have neuroprotective activity towards toxic agents that are not sensitive to more common “free radical scavengers”.<sup>164</sup> This feature makes  $\text{C}_{60}$  a promising candidate for antioxidant applications such as in cosmetics, where commercial products are already available.<sup>120</sup>

On the other hand, when  $\text{C}_{60}$  is exposed to intense visible or UV light, it is excited to the singlet then triplet state which can react with dioxygen to produce singlet oxygen  $^1\text{O}_2$ , a powerful oxidant species with cytotoxic properties. Other ROS are produced such as peroxides,  $\text{OH}^\cdot$ . Its use in photodynamic therapy for the treatment of tumours,<sup>109, 165, 166</sup> as well as cytotoxic agent can then be considered. Regarding toxicity in environmental conditions, several studies conclude to the non-toxicity of neat  $\text{C}_{60}$  but rather to the toxicity of the species with which it can interact (such as THF as a processing solvent).<sup>167-169</sup> Gadofullerenes were produced to follow the location of  $\text{C}_{60}$  particles by Magnetic Resonance Imaging (MRI) during the phototherapy while not inhibiting the generation of ROS.<sup>170, 171</sup>

Belousova *et al.* stated that when particles were obtained via emulsification method, two types could be distinguished: small amorphous particles along with bigger crystalline ones. It seems that amorphous particles generate more  $^1\text{O}_2$  than crystalline particles. However, it is difficult to conclude if it is due to the larger total surface of these small particles, or to porosity in their structure.<sup>172</sup> Another explanation could be that in crystals, triplet-triplet annihilation might occur.<sup>173</sup> Lyon *et al.* compared particles obtained by the emulsification and Ouzo methods, as well as particles obtained by magnetic stirring and by complexation with PVP. The 4 methods give particles significantly different in morphology, but the particles obtained from emulsification and magnetic stirring displayed the same behavior. Particles obtained by emulsification are spherical, particles with PVP appear to be spherical too. Particles obtained by simple agitation are more toxic than those obtained by sonication or in presence of PVP. By far the most toxic are those that have been nanoprecipitated from THF. Since the Ouzo particles are not smaller than the others, their toxicity is likely to be related to the presence of residual THF. Toxicity decreases with increasing size, the specific surface being then a key

parameter to consider as well regarding the toxicity.<sup>174</sup> The antibacterial activity of these particles on *E. Coli* bacteria is comparable to that of SDS and better than that of nickel, but less good than silver.<sup>175</sup> but again the cytotoxicity may be due to traces of THF.<sup>176</sup> Production of  $^1\text{O}_2$  was observed when  $\text{C}_{60}$  was well-dispersed in surfactant micelles, but not when it was aggregated. However, ROS production in micellar solutions was less effective than in organic solvent, maybe because fullerenes were still not dispersed at the molecular state.<sup>85, 87</sup>

Chemical modification of fullerene to make it more soluble in water resulted in the reduction of its production capacity of ROS.<sup>177</sup> Since radicals originate from C=C double bonds,<sup>178</sup> when their number decreases,  $\text{C}_{60}$  will lose its conjugation and its ability to produce ROS.<sup>179</sup> It is very likely that it is also due to its increased radical scavenging ability, as for  $\text{OH}^\cdot$  radical quenching, better results were obtained with the mono- than with the bis-adduct.<sup>132</sup>

Rose bengal is a kind of gold standard for photosensitizers. With its respect, a fullerol derivative has been reported to display a higher oxygen consumption (associated with the production of singlet oxygen) in the UV domain. However, the associated quantum yield was still lower than the one of rose Bengal in the visible region.  $\text{C}_{60}$  remains though an interesting photosensitizer for applications where the excitation wavelength is located in UV region.<sup>180</sup> In addition, generation of the anion radical by reduction is increasingly difficult when fullerene is functionalized by malonic acid, and like with fullerols, photophysical properties are also affected. Finally, the generation of  $^1\text{O}_2$  via the triplet state of the fullerene is greatly reduced, hence the lower cytotoxicity is likely.<sup>181</sup> To conclude, compromise has to be met between solubility and functionality for fullerols regarding their temper as ROS generator. When considering quaternary ammonium derivatives obtained via Prato reaction, an increase of the production of  $^1\text{O}_2$  was observed.<sup>173</sup> As for toxicity, various fullerene derivatives have been studied. A penta-adduct of carboxylates is toxic while mono-adducts of various polar functions and  $\text{C}_{60}$ -PVP complexes displayed no toxicity. It can be expected then that the toxicity comes from the carboxylates and not from the fullerene moiety.<sup>182</sup> Antibacterial films are often obtained from  $\text{C}_{60}$  solutions in polar solvents such as ethanol. Prato derivatives allow an increase in the solubility of  $\text{C}_{60}$  in polar solvents to build these films.<sup>183</sup> A PVP polymer along with a fullerene-grafted polyacrylate showed an increasing ROS production with increasing  $\text{C}_{\text{full}}$  until reaching a plateau at high  $\text{C}_{\text{full}}$ . Please note that ROS measurement is made by visible spectroscopy with a fluorescent probe. Since  $\text{C}_{60}$  absorbs in visible at high concentration, the plateau might not be real but due to quenching of the absorbance.<sup>150</sup>

$^1\text{O}_2$  production is also useful for the cleavage of DNA.<sup>184</sup> On top of that, Prato derivatives possessing quaternary ammonium can complex with negatively charged DNA strands.<sup>185</sup>

Singlet oxygen production can be used in applications other than medical ones such as the oxidation of organic molecules in fine chemistry.<sup>186</sup> However, the use of such species in aqueous media has not been widespread so far.<sup>187</sup> Another use of singlet producing species is photo-decontamination, in particular of air-water interfaces (degradation of ibuprofen or bisphenol A). However, this aspect has not been explored for fullerene.<sup>188</sup>

C<sub>60</sub> displays specific interactions with HIV protease.<sup>189</sup> C<sub>60</sub> has an antiviral activity in general, especially when in the form of hydrophilic derivatives. The position of the various functions has a direct influence on its antiviral activity.<sup>184</sup> Conversely, unmodified C<sub>60</sub> has more activity against "enveloped viruses", which was attributed to the generation of singlet oxygen. This effect is indeed enhanced in the presence of light and oxygen.<sup>184, 190</sup>

C<sub>60</sub> is also able to complex with albumins from bovines and humans, resulting in conformation changes. However, for the moment little is understood and therefore controlled because the interactions depend on the size of particles and the nature of proteins.<sup>191-193</sup>

Finally, C<sub>60</sub> forms complexes with aromatic active ingredients, opening new doors for controlled delivery systems: three examples were reported with doxorubicin, methylene blue and proflavin. Complexation was proven by spectroscopy: at low concentrations and aggregation of fullerene by stacking on molecules of interest was evidenced by an increase in absorbance in the visible domain and an increase of scattered intensity in SLS. In addition, free enthalpy energy calculations show that the interactions are dominated by Van der Waals bonds and to a lesser extent by hydrophobic ones. Despite the positive charge provided by the ammonium functions of the molecules studied and the negative zeta potential observed on the surface of the naked C<sub>60</sub> aggregates, the electrostatic interactions are very weak according to theoretical computations of the free enthalpy.<sup>194</sup>

### b. Physical properties

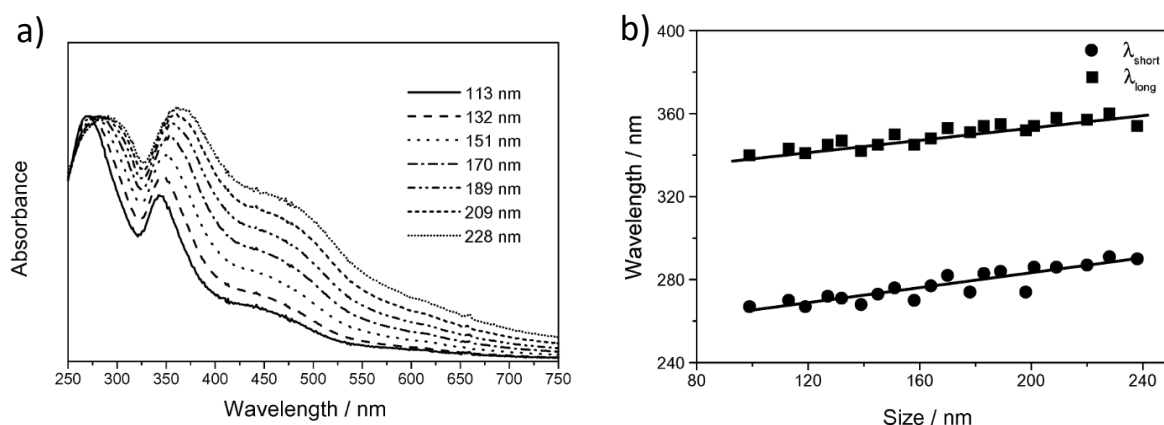
As it was briefly discussed in the first part of this chapter, C<sub>60</sub> significantly absorbs light, especially in the UV domain but also in the visible region when it is aggregated. Many studies gave insight on absorbance's dependence over particles size. Most of them dealt with its influence over the position of the maxima in UV region.

Bensasson *et al.* first reported the influence of aggregation state on the absorbance in both UV and visible regions. They took as extremes C<sub>60</sub> solutions in good apolar solvents like toluene for the most dispersed state, and C<sub>60</sub> film as the most aggregated ones. They showed that when the aggregation state of C<sub>60</sub> increases, the more intense are maximum wavelengths of both UV maxima around 260 and 340 nm. Also, they showed that the absorbance (noted A) ratios  $A_{260}/A_{330}$  and  $A_{330}/A_{450}$  both decrease with increasing aggregation state. Still, no discussion is made about the absolute values. In other words, it is not indicated whether it is



the absorbance in visible and at 330 nm that goes up when C<sub>60</sub> aggregates, or if it is the absorbance at 260 nm that decreases.<sup>13</sup>

Kato *et al.* sorted C<sub>60</sub> particles by size with the help of an AF4 device equipped with a multi-angle light scattering detector. After such a sorting, UV-visible absorbance spectra were collected (Figure 1.20a). As particle size increases, for a constant absorption at 260 nm, the absorption at 340 nm increases, as well as in all visible range. It should be noted that the absorbance does not seem to go to zero at high wavelengths, which can be attributed to slight turbidity of the solutions. This is not surprising considering the sizes of the particles. However, turbidity cannot explain the changes in absorbance. Indeed, it is theoretically proportional to  $\lambda^{-4}$ . It is therefore higher at lower wavelengths, so it should increase the absorbance of the 260 nm peak more than the 340 nm peak. In addition, both absorbance peaks in UV are shifted to higher wavelengths. When the maxima values are plotted against size, a linear law can be drawn for both of them (Figure 1.20b).<sup>195</sup>



**Figure 1.20.** a) Absorption spectra of particles sorted by size ( $R_h$  indicated in legend), normalized on the 260 nm maximum. b) Evolution of maximum absorption wavelength vs  $R_h$ .<sup>195</sup>

Gigault *et al.* also used AF4 to observe C<sub>60</sub> particles of various sizes (between 30 and 250 nm) obtained by emulsification method. The  $A_{450}/A_{340}$  ratio increases with increasing particle size accordingly to Kato's report. Indeed, the absorbance increases in the visible when the C<sub>60</sub> aggregates, but the effect may also be related to the turbidity of the system given the sizes. Moreover, once again no detail was given on absolute values, it is difficult to know if both absorbances go up with a steeper increase in visible region, or if only absorbance in visible goes up.<sup>196</sup>

From all these observations, Deguchi *et al.* suggested a linear law between maximum wavelength for the peak around 340 nm and size of the particles as a tool for size prediction based on absorption spectra. It is also clear from this study that as C<sub>60</sub> aggregates, the absorbance at 260 nm decreases and the absorption in visible region increases. For the 340

nm peak, absolute absorbance does not vary much with size.<sup>67</sup> Chang *et al.* fail at finding such a universal linear law.<sup>197</sup> One parameter that could influence their results is the dispersity of the particles. Indeed, Kato *et al.* used AF4 so the particles should be more monodisperse in their study. Additionally, these three studies all used different methods to produce C<sub>60</sub> particles: Kato used both emulsification and Ouzo methods, Deguchi used manual grinding followed by suspension in water and Chang used prolonged magnetic stirring. It is likely that preparation method has an influence on the spectrum, for example because of the presence of solvent traces. For this last reason, the band at 220 nm was never studied because most organic solvents absorb at this wavelength, which corresponds to the electronic transition  $\sigma \rightarrow \sigma^*$ .

Chemical modification of C<sub>60</sub> has consequences on its optical properties. First, refractivity is impacted. The refractive index increment of C<sub>60</sub>/PMPC particles was found equal to 0.72 mL/g for a 2:3 C<sub>60</sub>:PMPC complex (in weight). Since PMPC itself has a dn/dc equal to 0.14 mL/g<sup>198</sup>, a very high dn/dc of 1.59 mL/g can be calculated for C<sub>60</sub> alone. This high refractivity is usual for carbon allotropes. For example, diamond and graphite have refractive indexes of respectively 2.4 and 2.7 at room temperature. A C<sub>60</sub>(OH)<sub>22-24</sub> fullerol had a dn/dc of 0.24 mL/g at 25°C. It can be extrapolated that for the solid, the refractive index is much lower than for pristine C<sub>60</sub>. For absorption properties, this fullerol displayed no absorption maximum in visible nor in UV region.<sup>124</sup> The loss of absorbance through functionalization is observed for a C<sub>60</sub>(OH)<sub>36</sub>, the absorbance at 260 nm is the only one to be maintained but it does not follow the Beer-Lambert law and is only observed at some intermediate concentrations.<sup>130</sup>

C<sub>60</sub> is widely used in nonlinear optics as an optical limiter in organic solvents like toluene. Optical limitation consists in allowing only part of the light to go through a medium. All photons above a critical value of transmittance are absorbed. In water, researchers have designed particles stabilized by an amphiphilic polymer. At equal transmittance in the visible with toluene, or at much lower concentration (since C<sub>60</sub> absorbs much more in aggregated than in molecular state), optical limitation is similar to a solution in toluene. If a large amount of C<sub>60</sub> in water is reached, very good optical limiting properties can therefore be expected.<sup>199</sup> When C<sub>60</sub> is trapped in  $\gamma$ -CD aqueous solutions, its optical limitation is slightly lower than the one it has in toluene at the same concentration. This, together with the previous observations, suggest that fullerene should be aggregated to efficiently exploit its optical limitation abilities. Also, it showed better optical limitation than CNTs regarding picosecond pulses, although both are comparable for longer, *i.e.* nanosecond pulses.<sup>200</sup>

Despite its conjugations C<sub>60</sub> displays poor fluorescence. The emission maximum is located between 650 and 800 nm in organic solvents. The presence of oxygen has little influence on fluorescence as well as the nature of the organic<sup>201</sup> or the excitation wavelength.<sup>202</sup> In water,



encapsulated  $C_{60}$  display fluorescence at shorter wavelengths (maximum at 530 nm) but generally at lower intensities than in an organic solvent.<sup>102</sup> The functionalization of fullerene modifies its photoluminescence, both on the emission spectra, similarly to absorption, and on the quantum yields that increase for derivatives such as Prato or malonic ones.<sup>203</sup> Nakamura *et al.* grafted phenyl rings onto  $C_{60}$  in order to form deca- and octa- adducts. Deca-adducts showed bigger extent of fluorescence than octa-, and OLED devices made with one deca- and two octa- emitted lights of three different colors.<sup>204</sup> Water-soluble Brettreich's dendrofullerene shows a sharper fluorescence spectrum than pure  $C_{60}$  in toluene but the quantum yield is similar. This opens up possibilities of photoinduced oxidation, for example with iodine.<sup>205</sup>

$C_{60}^{3-}$  anions were generated by electrolysis in tetrabutylammonium electrolyte solution: monodisperse nanoparticles with a diameter of less than 10 nm were obtained. These particles were highly fluorescent. Irradiation was applied at 365 nm and particles emitted in the blue region. As the excitation wavelength was increased, the wavelength of emission was also increased and emission intensity decreased.<sup>206</sup> This type of particles could be called « fullerene quantum dots », by analogy with graphene ones exhibiting.<sup>207</sup>

Amine-functionalized  $C_{60}$  are also fluorescent. Fluorescence increases with reaction time. Absorption is mainly located in UV and violet-blue regions, while emission occurs between green and red wavelengths. The amines that increase fluorescence the most are primary ones. The longer the alkyl chain, the more fluorescent fullerene is in toluene ( $C_{12} > C_7 > C_4 > C_3 > C_2$ ). Fluorescence intensity is in general dependent on the aggregation state. Indeed, if molecules aggregate, quenching mechanisms can occur because of spatial proximity between the molecules. This means that a possible influence of the solvent quality on these different adducts could be an explanation to the modification of intensity.<sup>208</sup>

$C_{60}$  is also able to quench fluorescent systems. Fluorescence quenching is a dissipation of the emitted fluorescence that cannot be explained by absorbance alone. In general, it is due to energy transfers such as Förster resonance energy transfer (FRET), where a first dye emits in the absorption region of a second one, which itself emits at a higher wavelength. Basically this is a donor-acceptor interaction. For example, poly[2-methoxy-5-(2-ethyl-hexyloxy)-1,4-phenylene-vinylene] (MEH-PPV), a semi-conducting conjugated polymer, is quenched by a common  $C_{60}$  derivative, phenyl  $C_{61}$  butyric acid (PCBM) in ortho-dichlorobenzene (o-DCB).<sup>209</sup> It is also quenched by pristine  $C_{60}$  in benzene.<sup>210</sup>

This ability to form complexes with donors is valuable in organic electronics. Indeed, PCBM is very used in photovoltaic devices as the acceptor of the p-n junctions, generally along with poly(3-hexylthiophene) (P3HT) as donor.<sup>211</sup> In general, such layers are formed by co-solvation in an organic solvent and deposited by spin-coating. Formation of PCBM nanoparticles in water

to form such films allows a better control of the latter's structure in comparison to direct deposition from an organic solvent. Also, the process becomes eco-friendlier because the organic solvent used to disperse the particles can be more easily recovered for recycling.<sup>34, 212, 213</sup> Another advantage of preparing these dispersion is that inks are obtained, that can be directly imprinted on films.<sup>214</sup>

For applications in polymer solar cell fabrication, printing of the P3HT:PCBM layer is achieved by inkjet. To have homogeneous layers, a relatively volatile solvent is needed to be evaporated easily. If it is too volatile, layers tend to blister. Water therefore looks like a good compromise for this application. Finally, a low viscosity is necessary so that the drops correctly overlap once deposited. It is then of importance to develop inks of low-viscosity.<sup>215</sup>

## 5) Hydrogels formed by self-assembly of polysoaps

The rich variety of fullerene properties, especially in aqueous medium, is still hindered by its lack of solubility and/or stability. Integrating fullerenes in a hydrogel matrix would address the second problem and could lead to new functionalities of these materials. Here, general features about hydrogels and their reinforcement strategies are given. A focus will be made on hydrogels containing fullerene (and more generally, nanocarbons). Finally, the family of polymers that were used throughout the present study will be presented.

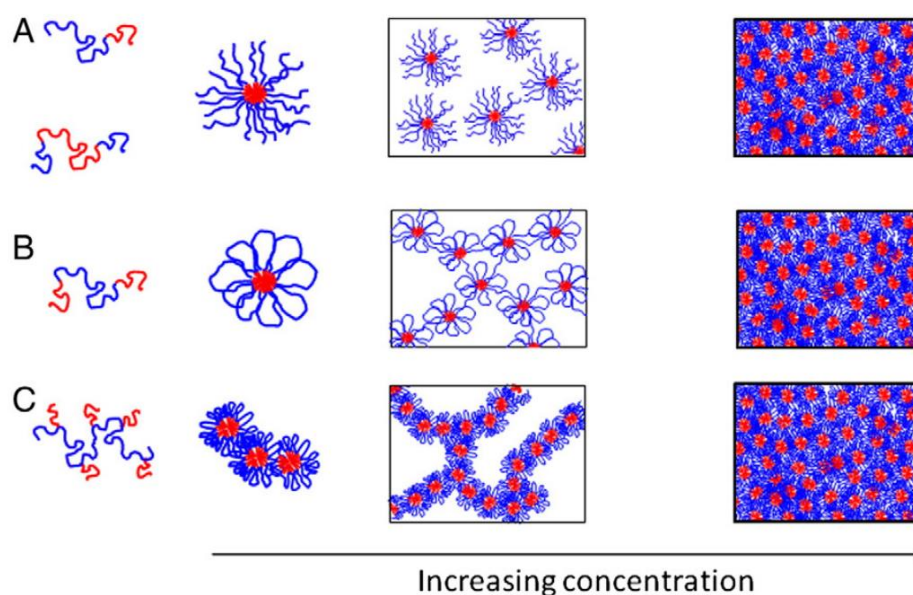
### a. General features of hydrogels

Hydrogels are materials that do not flow under their own weight even though they are mainly containing water, up to 95 wt%. They result from the formation of a network swollen by water. This network is constituted by an interconnected solid matrix. Two types of gels can be distinguished: chemical and physical gels.

Chemical gels result from covalent crosslinking of polymer chains. The solid matrix is then a crosslinked polymer network, and the crosslinks are permanent. Chemical hydrogels necessitate the use of hydrophilic polymers, because they need to swell in water. Crosslinking can be obtained by adding a crosslinking agent during the course of polymerization. This agent is generally a molecule containing several functions that can react during the chain polymerization process, like bisacrylamide for radical polymerizations. Otherwise, gelation can be generated in situ by adding polymerizable functions to the polymer chains and triggering polymerization by an initiator.<sup>216</sup>

Physical gels result from networks which crosslinks are temporary. The latter are obtained by weak interactions such as hydrogen or ionic bonds,  $\pi$ -stacking, hydrophobic or donor-acceptor

interactions. For example, alginates display gelation when they are chelated by calcium divalent ions. The most common hydrogel formation path is the use of an amphiphilic copolymer. Typically, amphiphilic copolymers self-assemble in water by hydrophobic interactions, and the micelles that they form may percolate at high concentrations to form large-scale networks. Block copolymer architecture is generally chosen to control the self-assembly. Diblocks possessing one hydrophilic and one hydrophobic block self-assemble in water to form micelles. The formation of a network is thus dictated by the interactions between the hydrophilic moieties of the micelles. In most cases, a network is obtained when concentration is increased to the point where micelles are in contact with each other. Triblock copolymers possessing hydrophobic side blocks and a central hydrophilic block can form flower-like micelles, and bridges can be formed between two micelles core provided micelles are close enough, *i.e.* concentration is high enough. The consequence is that a much lower polymer concentration is required to form networks. Finally, multi-sticker copolymers form objects with less defined structure but the multiplicity of the associating points on one single polymer chain conducts to enhanced connectivity as for triblocks (Figure 1.21).<sup>217</sup>



**Figure 1.21.** Schematic representation of micelles and networks formed by amphiphilic diblock (A), triblock (B) and multi-sticker (C) copolymers.<sup>217</sup>

One of the most interesting features of physical gels is that the hydrophobicity of the block(s) can be triggered by an external stimulus by using functional monomers. For example, PNIPAM becomes hydrophobic when it is heated above its LCST. Using these monomer units allows the design of “smart” hydrogels that can undergo reversible sol-gel transitions with the appropriate stimulus.<sup>218, 219</sup>

To form physical gels, the matrix is not necessarily polymeric, because particles or molecules can also form this kind of network. In the first case, particles that are able to bind to each other can form networks. For example, silica particles can form it thanks to hydrogen bonding. In the second case, two molecules can associate via weak interactions like donor-acceptor ones. These assemblies are named supramolecular polymers, and if two different molecules are used, alternated copolymers are obtained.

Physical bonds are temporary. It means that providing the hydrophobicity of the associative blocks is not too high, once in a while, a hydrophobic block can be extracted from a crosslink to either come back, either go to another crosslink.<sup>220</sup> The consequence is that these gels, described as “living”, can be at thermodynamic equilibrium and behave as viscoelastic fluids. From the rheological point of view, it can be observed that they behave like liquids at low frequencies and like elastic solids at high frequencies (hydrophobic blocks have no time to relax on this time scale). One consequence of this behaviour is the ability of these materials to self-heal after breakage. Another is their ability to adopt a change in shape to adapt to their container. If the hydrophobic blocks are very hydrophobic, the lifetime of the crosslinks becomes incommensurably long and no relaxation can be seen anymore. The system is “dead”. However, dynamics can be reactivated by making the hydrophobic blocks hydrophilic through an external stimulus.

Chemical gels behave this way too, as the extraction is impossible since the bonds are covalent. The relaxation time can then be considered infinite, and no sol-gel transition can be obtained. Therefore, these materials display rather poor self-healing properties.

The mechanical properties of chemical and physical gels are very different. They are often investigated by dynamic rheology. “Dead” gels are characterized by a purely elastic response to stress. A loss modulus  $G''$ , related to the viscous behaviour of the material, can be measured but it is much lower than the storage modulus  $G'$ . On the other hand, “living” gels behave as viscoelastic liquids. Their response to stress depends on the frequency of the applied stress. At high frequency, the gels behave as solid because the polymer chains do not have enough time to relax. At low frequency, relaxation occurs, so they behave as liquids: they flow.

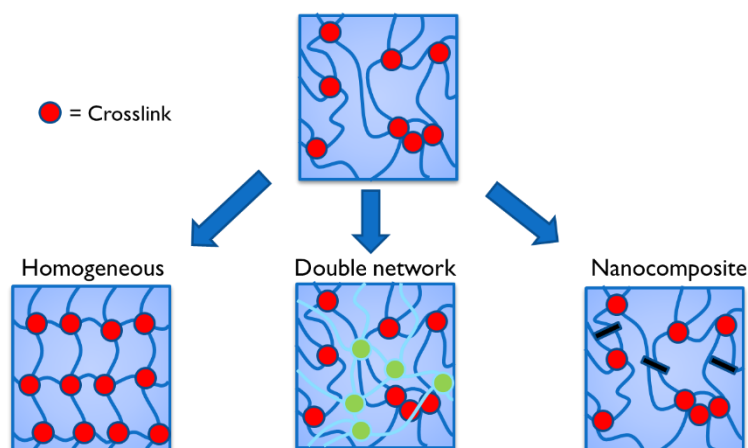
Concerning the deformability of gels, at low stress values, they behave elastically, meaning they deform proportionally to the stress and the strain value is ruled out by the elastic modulus of the material. They go back to their initial state once the applied force is stopped. This is the linear regime. Beyond a certain value, defects in the network start to appear. The strain is no longer proportional to the load, and cracks form until breakage of the gel. The resistance of a gel can be addressed regarding both rupture stress and strain. In general, chemical gels possess high elastic moduli, so they can handle important stress. However, they don't deform

much before breaking. For example, a poly(2-acrylamido-2-methylpropanesulfonic acid) (PAMPS) hydrogel at 8 wt% polymer concentration broke at 0.4 MPa. Its strain at rupture was only 41%.<sup>221</sup> On the other hand, “living” physical gels are more deformable, but only resist to low loads. A 4 wt% telechelic fluoroalkylene end-capped PEO gel broke at a nearly 300% strain, but the associated strain was only 400 Pa.<sup>222</sup>

To summarize, “dead” hydrogels comprise both chemical and frozen physical gels. They can handle high loads but cannot elongate much and their potential damages are irreversible. “Living” hydrogels are weak but dynamic physical gels. They can handle only low stresses, but can deform more and recover from damages. It is of importance to find ways to reinforce these systems to take the best from both worlds. The main strategies will now be detailed.

### b. Reinforcement strategies

Three main strategies are employed to reinforce gels as described in Figure 1.22.



**Figure 1.22.** Main strategies for the reinforcement of hydrogels.

#### i. Topological gels

As we discussed earlier, rupture under strain is favoured by the presence of defects in the network. The first strategy consists in working on the chemistry to design a perfectly homogeneous network. The most famous example in this category is the topological gel. Okumura and Ito presented in 2001 a novel gel made of PEO chains surrounded by eight-shaped crosslinks, namely polyrotaxanes. These crosslinks are actually two  $\alpha$ -CD bound together. Since the two  $\alpha$ -CD are surrounding different PEO chains, they act as crosslinks. The latter are physical and can slip along the PEO chains. This gives high connectivity while keeping a dynamic network. Defects are much harder to create since the network is at thermodynamic equilibrium.<sup>223</sup> These gels were strained up to 2000% before rupture.<sup>224</sup>

ii. *Double or interpenetrated networks*

Gong *et al.* first reported in 2001 a double network (DN) hydrogel. They built up a poly(acrylamide) (PAAm) network by allowing it to polymerize within an already prepared PAMPS network. The resulting hydrogel possessed improved mechanical properties. The corresponding PAAm and PAMPS single networks broke respectively at 0.8 and 0.4 MPa stress, with a strain of 84% and 41%, whereas the DN broke at 17.2 MPa, with a strain of 92%. It should be noted that this DN gel should also have an improved modulus, as the stress improves more with strain than for single networks at low deformations.<sup>221</sup> Actually, this is the main strength of these gels: they can reach very high fracture stresses. On the other hand, Tanaka *et al.* showed that they are much less deformable than other reinforced hydrogels (*i.e.* topological and nanocomposite gels). This unique feature makes these gels that still mostly contain water (at least 60 vol%) the most promising candidates for the synthesis of biomaterials with similar mechanical properties as cartilage.<sup>224</sup>

Sun *et al.* showed another way by interpenetrating a physical and a chemical network. The first was alginate crosslinked by  $\text{Ca}^{2+}$  chelation, and the second was a PAAm network. Both networks were connected by condensation of carboxyl groups of alginate with amide groups from PAAm. Three types of crosslinks can thus be distinguished: ionic bonds exclusive to the alginate network, covalent bonds exclusive to the PAAm network, and covalent bonds in common for both networks. Since both weak and strong crosslinks are present in the system, it can be pictured as a sacrificial physical network of alginate that is able to self-heal after fracture and protects the covalent PAAm network. The healing was however long and incomplete after 1 day.<sup>225</sup>

Other preparation paths exist aside from the previously discussed, which are simultaneous non-interfering polymerizations, and selective crosslinking of a linear polymer solubilized in a network. It is also possible to use non-crosslinked linear chains that physically interact with the matrix. So-obtained semi-interpenetrated networks also possess improved mechanical properties.<sup>226</sup> It can be seen as a double network, but only one is chemical and the second one is physical. This is particularly interesting in the regard of recovery abilities, as it is well known that physical gels recover better than chemical ones after high deformation, and can even self-heal after fracture. The physical network can thus be pictured as a sacrificial network that breaks first under stress to reform afterwards. This way, the integrity of the chemical network is maintained.

In the same spirit, to combine advantages of both “dead” and “living” gels, it is possible to add self-associative polymers to a network with a similar chemical structure to form a common network with both dynamic and covalent crosslinks. For example, Nicol *et al.* used triblock

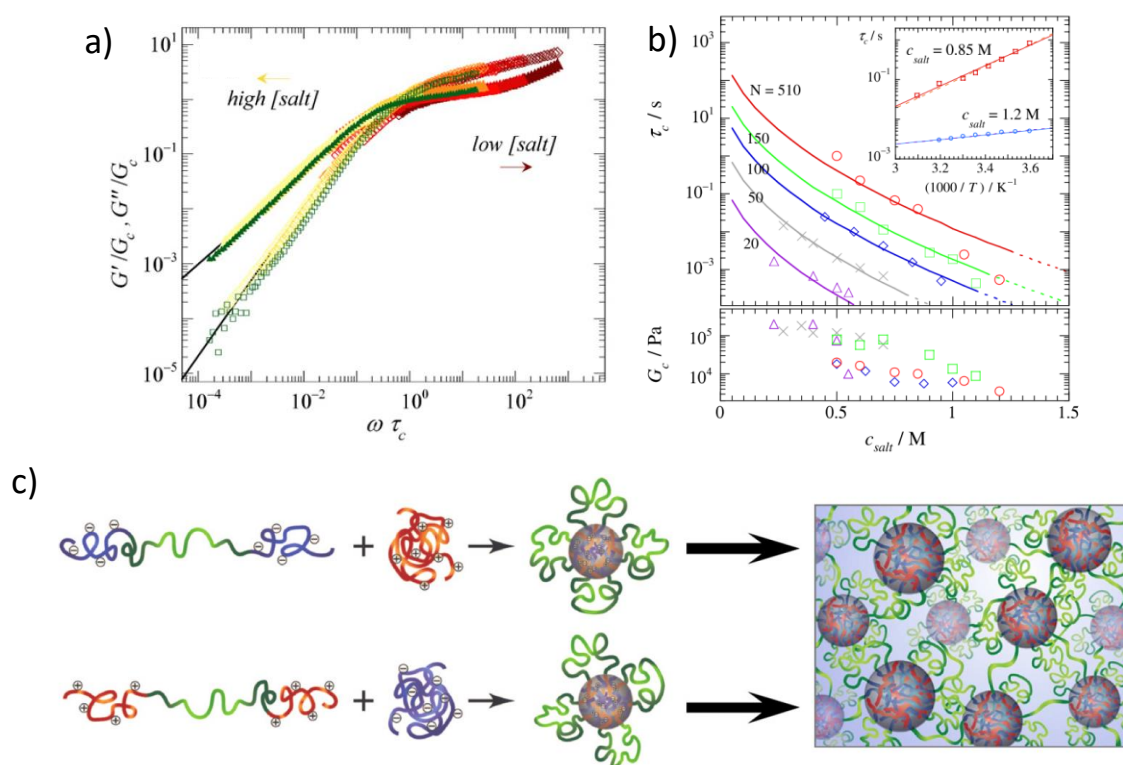


copolymers with a central PEO block and acrylic side blocks. When these blocks were poly(methacryloyloxyethyl acrylate), the polymer (tPEO) formed flower-like micelles. With a sufficient concentration, these micelles formed bridges and a physical gel was obtained. The presence of alkenes on the acrylic blocks allowed a subsequent polymerization, giving birth to a chemical network. Mixing tPEO with a similar polymer with poly(isobutyryloxyethyl acrylate) side blocks (IEI), that is basically the non-crosslinkable analogue of tPEO, lead to the formation of a common physical network. The subsequent crosslinking gave birth to a network possessing both dynamic and covalent bonds. The addition of IEI did not have a major effect on the elastic modulus. However, at a constant tPEO concentration, increasing the content of IEI enhanced the deformability of the gels. The fracture stress was then always similar, around 3 kPa, but the fracture strain increased from 120% to 350% for a 5% tPEO gel without and with 8 wt% IEI.<sup>227</sup>

### iii. Ionic gels

As we briefly discussed, gelation can be triggered by creation of ionic bonds between polymer chains, generally by a multivalent ion, like  $\text{Ca}^{2+}$ , thus forming a network (for example, with alginate). In 2015, Lin *et al.* reported chemical gels of PAAm copolymerized with PAA. The addition of  $\text{Fe}^{3+}$  ions in the network induced the formation of supplementary ionic bonds, thus creating very strong gels. In these systems, the toughness was essentially controlled by the AA/PAAm molar ratio. For example, when the latter was increased, the rupture stress increased from 3.3 to 5.9 MPa, and the associated strain went from 850 to 750%. Increasing this ratio further did not increase the fracture stress much, but dramatically decreased the rupture strain. These gels displayed self-healing abilities, although it took several hours.<sup>228</sup> Still, the recovery was complete which was better than results obtained with DN gels designed by Sun *et al.*

As for the tPEO/IEI micelles presented earlier, it is also possible to form a single network with two different polymers by using two oppositely charged polyelectrolytes. When they are solubilized together, they form coacervates leading to phase separation. However, if at least one of them carries a neutral hydrophilic block, complex coacervate core micelles (C3Ms) can be formed.<sup>229</sup> Their size and morphology is controlled mainly by the size and ratio of the neutral block with respect to the charged one in the diblock. In addition, their formation is highly impacted by ionic strength. Indeed, at high ionic strength, the coacervate core liquefies as the salt acts as a plasticizer.<sup>230</sup> An attempt to explain this is that many counter-ions are condensed on the charged units (so-called Manning effect) and it is not possible for the polyelectrolyte of opposite charge to remain adsorbed on each other, as the equilibrium shifts highly in favour of small ions to maximize entropy.



**Figure 1.23.** a) Master curve of frequency sweeps of a PDMAEMA/PAA (block length is  $N=500$  for both) physical network at  $20^\circ\text{C}$  and  $\gamma=2\%$  with various salt (KCl) concentrations. b) Salt concentration dependency of relaxation time and elastic modulus for different block lengths. Inset is an Arrhenian plot of temperature dependency for  $c_{salt}=0.8$  and  $1.2$  M for  $N=500$ .<sup>231</sup> c) Schematic representation of flowerlike C3Ms and networks formed by a homo-polyelectrolyte with a telechelic polyelectrolyte of opposite charge.<sup>232</sup>

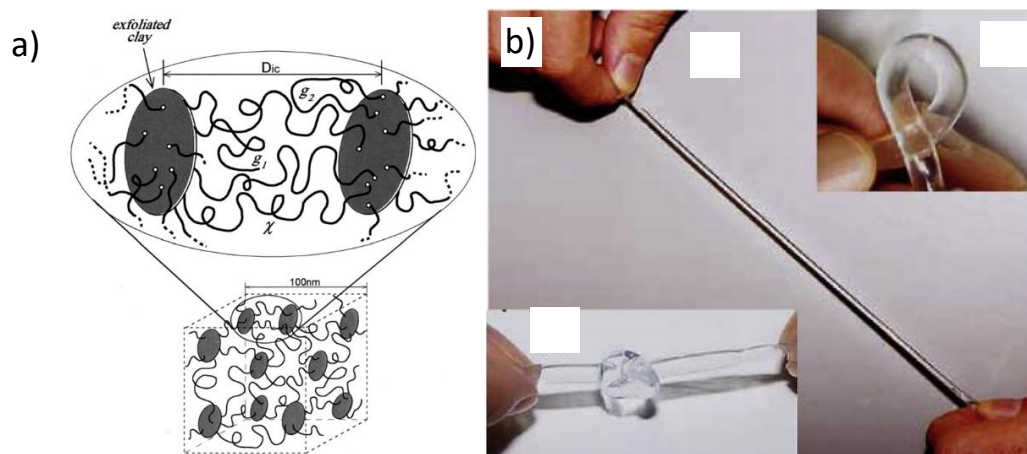
Spruijt *et al.* reported in 2010 the formation of networks where crosslinks are coacervates constituted of poly(dimethylaminoethylmethacrylate) (PDMAEMA) and PAA. Interestingly, as for C3M formation, the dynamics of the network are very affected by salt concentration. At low ionic strength, hydrogels with very high relaxation times were obtained. When it increased, relaxation time dropped until reaching a liquid behaviour (Figure 1.23a). A master curve was built from frequency sweeps at various ionic strengths, showing a universal behaviour where only time-scale is affected by salt concentration (Figure 1.23b). This was explained by the arrhenian character of the gels. The latter was decreased when salt concentration increased, meaning that the energy barrier to cross was diminished. Both block lengths were varied and an increased block length lead to an increased relaxation time.<sup>231</sup> The use of telechelic triblocks with a central neutral block and side charged blocks instead of diblocks could even lead to flowerlike C3Ms which spontaneously formed networks at much lower concentrations than their diblock analogues (Figure 1.23c).<sup>232</sup>



Sun *et al.* designed networks based on a similar concept, where cationic and anionic monomers were copolymerized at high concentration with equimolar quantities. The network thus possessed both covalent and ionic crosslinks. These gels had high fracture stresses, up to 2 MPa, with a strain of 700%. They were able to self-heal, with a nearly complete recovery after only 30 min.<sup>233</sup>

#### iv. Nanocomposite gels

Nanocomposite (NC) hydrogels are networks reinforced by nanoparticles that are dispersed in the matrix and that physically interact with it. Under stress, they act as dissipaters. Haraguchi and Takehisa first reported such systems in 2002.<sup>234</sup> They performed PNIPAM polymerization and chemical crosslinking in a colloidal suspension of clay nanoplatelets. Briefly, the initiator was selectively adsorbed on the clay and monomer was added. Then polymerization was conducted, and resulted in the formation of transparent hydrogels, in contrast with traditional chemical gels of PNIPAM that are turbid (Figure 1.24). This indicates a better homogeneity of the microstructure. Also, the gels did swell in a large excess of water without dissolving, indicating that the crosslinks are permanent. Interestingly, if an organic crosslinker, N,N'-Methylenebisacrylamide (BIS), was added to the initial mixture, it was overcoming the clay particles as a crosslinker and a standard hydrogel was obtained. Thus, physical interactions of PNIPAM chains with the particles are not enough to induce a reinforcement, but more selectively an interaction with the initiator does. These hydrogels could elongate up to 1400%. Increasing the amount of clay particles induced an increase in modulus (from 1.5 kPa with 1 wt% particles up to 10 kPa with 5 wt% particles) and fracture stress (from 40 to 110 kPa), but a lowering in fracture strain (from 1400% to 800%).<sup>234</sup> It also decreases their ability to swell, as for organic-crosslinked gels with increasing crosslinker contents.<sup>235</sup> Nishida *et al.* provided experimental proof by 2D SAXS patterns that the high deformability arises from anisotropic alignment of the clay nanoplatelets in a perpendicular direction to the stress, allowing the polymer chains to stretch. The rupture happens when polymer chains cannot stretch anymore. These gels were able to self-heal after fracture because of the reversible character of the bonds between polymer chains and clay. 2D SAXS shows that the initial state recovery coincides with the moment when the clay nanoplatelets are not aligned anymore.<sup>236</sup> The use of a clay that can swell in water and that can be exfoliated, such as smectites (e.g. hectorite, montmorillonite), is a prerequisite. The type of clay has an influence on the final mechanical properties of the hydrogels, presumably due to their selective interactions with the initiator. In addition, it was observed that monomers containing amide give gels with better mechanical properties than other monomers, probably because of their ability to form hydrogen bonds with clay particles. Aside from transparency, these gels also displayed different physical properties than their organic analogues, such as birefringence or increase in contact angle with water.<sup>235</sup>



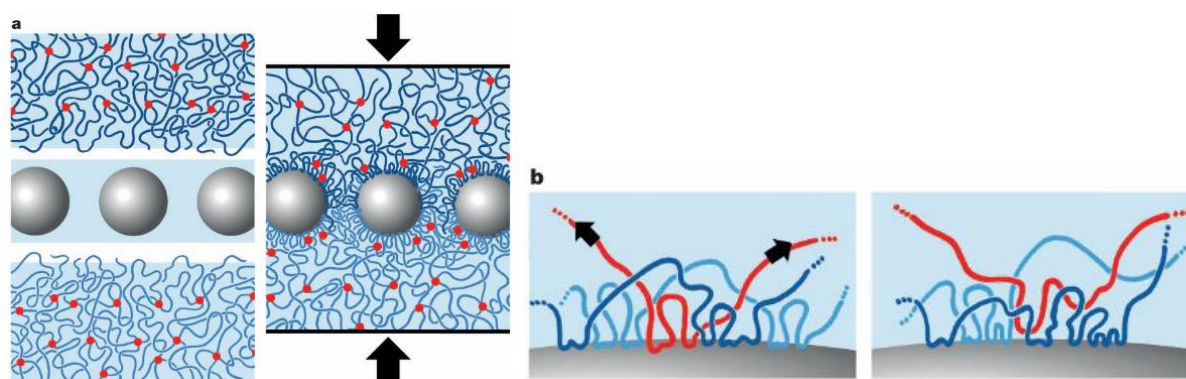
**Figure 1.24.** a) Schematic illustration of Haraguchi hydrogels with clay nanoplatelets separated where the distance between two crosslinks is determined by clay concentration. b) Pictures showing the high deformability and transparency of such hydrogels.<sup>235</sup>

Similar systems were obtained by Lin *et al.* in 2010 who replaced clay by silica nanoparticles. They used PDMA as polymer matrix, as it strongly interacts with silica. Contrary to Haraguchi's case, an organic crosslinker was at first necessary. Indeed, the physical interactions between the polymer chains and the particles are so strong that the preparation of a concentrated sample (*i.e.* in the semi-dilute regime) becomes an issue. In situ polymerization in the presence of silica nanoparticles therefore yielded gels with enhanced fracture stress (up to 500 kPa) and elastic modulus (up to 180 kPa). Impressively, the elastic modulus of the latter gel was two times higher than for the control even though it contained only 1.5 vol% particles. However, the fracture strain was not affected much.<sup>237</sup> In contrast, similar but non-chemically crosslinked hydrogels proposed by Carlsson *et al.* showed better swelling and deformation, which was originating from a better energy dissipation. However, the elastic modulus was lower which could be compensated by increasing the concentration of particles. At best, a 20-fold modulus was obtained while still maintaining a deformability over 1000%.<sup>238</sup> The authors noted that PDMA and PNIPAM could effectively bind to silica, probably through hydrogen bonding, but not PAAm, for example.

Suzuki *et al.* showed the effect of particles size on the microstructure. They tested three different sizes, ranging from 4 nm to 14 nm. Interestingly, the smallest particles gave the toughest gels. Time-resolved DLS during polymerization process showed the progressive formation of aggregates. Contrast-variation SANS measurements displayed the fractal aggregation of silica particles (with  $df=2.1$ , indicating a dense aggregation). Polymer formed thicker layers on the bigger particles, but a higher aggregation state was displayed for the smaller particles. This formation of a polymer network templated by the particles might be the explanation of the reinforcement.<sup>239</sup> Since silica particles are isotropic, contrary to clay, the

elongation mechanism might be completely different. 2D SANS experiments in contrast-matching to selectively measure the contribution of silica to the scattered intensity showed the alignment of the silica particles in the direction of the elongation under high strains.<sup>240</sup>

Marcellan and Leibler therefore suggested that silica particles solutions could be used as a glue to connect polymer networks. The adhesion mechanism is pictured in Figure 1.25. This opens application of these hybrid systems in tissue engineering.<sup>241</sup>



**Figure 1.25.** Schematic illustration of the adhesion mechanism of two polymer networks via silica particles. The latter are positioned at the interface and connect the networks by adsorption of polymer chains on them (a). The system is dynamic, so that when a polymer chain is detaching from the surface of a particle, it is quickly replaced by another (b).<sup>241</sup>

Haraguchi's group pushed the concept even further by combining both silica and clay particles in the same PNIPAM network (which showed its ability to interact with both particles). Please note that silica was introduced as TEOS followed by polycondensation, giving birth to a network of silica, and not as particles as in the previous case. The resulting gels were very stiff, giving access to even higher moduli and fracture stresses (at best 3.6 MPa and 1.8 kPa, respectively, vs 0.2 MPa and 0.6 MPa for the non-silicated hydrogel). However, the swelling and elongation abilities were dramatically decreased (less than 100% for the previous gel, vs 1000% for the non-silicated gel). To conclude, combination of both silica and clay allowed to reach moduli and fracture stresses comparable to the ones of DN hydrogels, but through the sacrifice of deformability.<sup>242</sup>

Here we focused on hydrogen-bonding interactions between particles and network. Obviously, other interactions can be imagined for NC gels. Nanocarbons give the possibility to form hydrophobic or  $\pi$ -stacking interactions with appropriate networks. Some examples are given below, with a specific focus on C<sub>60</sub> fullerene-containing hydrogels.

### c. Nanocarbon-containing hydrogels

Wakai *et al.* reported the first hydrogels containing C<sub>60</sub> fullerene. They used difunctional azo-PEG chains (with a molar mass of 4000 g/mol) that turned into bis-radicals once heated. These radicals successfully added to C<sub>60</sub> molecules. The C-C bonds that were attacked by radicals were bis-adducts, thus forming networks consisting in PEG chains crosslinked by C<sub>60</sub> molecules. Since several additions can occur on one single C<sub>60</sub> molecule, the latter can be considered as a multifunctional crosslinker. The hydrogels generated this way swelled in THF, methanol and water in which the swelling ratio was the highest (570%). They also had enhanced mechanical properties, as the increase of C<sub>60</sub> content led to increase of fracture stress up to 350 kPa, and similarly to Haraguchi gels, the swelling decreased as the amount of C<sub>60</sub> increased. Finally, the thermal stability of PEG was enhanced thanks to the presence of C<sub>60</sub>.<sup>243</sup>

Zhang *et al.* recently reported hydrogels obtained by the co-assembly of a small peptide, Fmoc-FF, and a tris-acid Prato adduct of fullerene. The peptide formed a fibrillar network on which fullerene particles adsorbed. The NC hydrogel was slightly reinforced compared to the peptide-only network, as the elastic modulus was increased 4 times. No effect was observed on the nonlinear mechanical properties. These hydrogels were able to generate <sup>1</sup>O<sub>2</sub> and to accelerate wound healing under irradiation.<sup>244</sup> Two other papers report the formation of hydrogels containing C<sub>60</sub>, but did not give many details on the benefits of C<sub>60</sub> on their physical properties. Mba *et al.* synthesized a supramolecular gelator possessing telechelic Fmoc groups that can promote  $\pi$ -stacking interactions. TEM images showed a tendency of C<sub>60</sub> to deposit on the fibrillar network formed by this gelator, although since it was dried there are no proofs that it also happens in the wet state.<sup>245</sup> Sugikawa *et al.* delivered C<sub>60</sub> onto a gelatin chemical gel by transfer from  $\gamma$ -CD. The UV-visible absorption spectra of the gels displayed very large absorption bands, suggesting a high dispersity of the particles.<sup>246</sup>

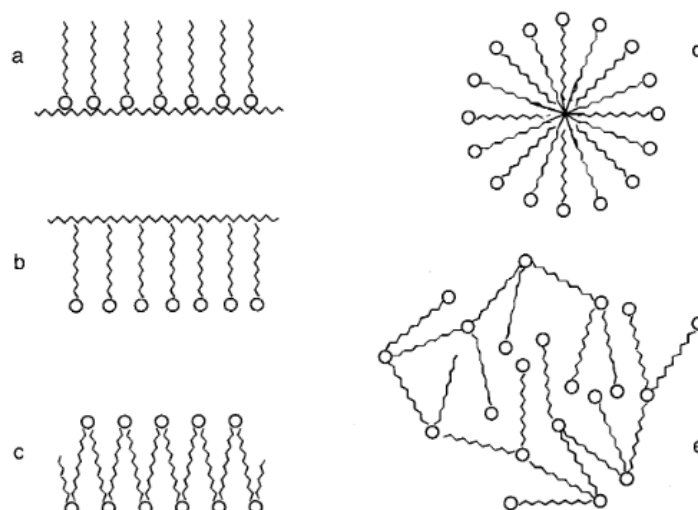
Other nanocarbons were more widely used for the design of NC hydrogels. CNTs were incorporated in poly(methacrylic acid) (PMAA) networks. The deswelling of a gel containing 0.5 g/L CNTs under electrical field was doubled compared to the control, and its electrical resistivity was significantly decreased. This allows applications for electrical-triggered delivery.<sup>247</sup> Loading a PNIPAM hydrogel with CNTs allowed the LCST transition to be sharper and reduced its response time which makes these systems suitable as actuators.<sup>248</sup> Mottet *et al.* dispersed CNTs in a surfactant aqueous solution that was transferred in an alginate hydrogel. They increased the Newtonian viscosity of the alginate by nearly two decades. The hydrogels were conductive thanks to the presence of CNTs.<sup>249</sup>

Still in alginate hydrogels, graphene oxide (GO) was incorporated, enhancing the mechanical properties, especially when alginate concentration was low. At 1 wt% alginate, without GO, Newtonian liquids were obtained. With 3 g/L GO, weak hydrogels with a 30 Pa elastic modulus were obtained. The main increase in mechanical strength is achieved by the addition of a divalent salt that crosslinks the gel *via* ionic bonds. These gels were stable even in saline conditions. GO brings superoleophobicity, as the contact angle with an oil was much increased in its presence. Thus, these materials can be used in marine media to form protective layers against oils.<sup>250</sup> Actually, graphene is able to form hydrogels by itself. Hydrothermal reduction of a graphene oxide suspension in water conducted to the formation of networks containing only 2.6 wt% graphene. The mechanical properties of these materials were impressive, with a modulus of 500 kPa, and a yield stress of 12 kPa. The fracture strain was however very low, around 10 wt%. These materials are therefore not deformable. However, they display interesting conductive properties, as well as thermal stability.<sup>251</sup> GO was used as a nanofiller in poly(vinyl alcohol) (PVA) gels. Only 1 wt% GO increased the tensile stress from 1.5 to 3.5 MPa, as well as the rupture deformation, from 100 to 165%. The compressive strength was slightly lower, and less affected by GO particles, going from 1.0 to 1.35 MPa.<sup>252</sup>

As we showed in the section 1.5.b.iv, reinforcement supposes a high multi-functionality of the crosslinkers, which is presumably better achieved with larger particles such as CNTs or graphene. They cannot then be challenged by C<sub>60</sub> in the field of mechanical reinforcement. Still, for now they displayed less impressive reinforcing abilities than inorganic nanoparticles such as silica or clay. Their use relies more on the functionality, such as high electrical conductivity or superoleophobicity, giving access to smart materials in another manner than copolymer networks that are generally mechanically weak. For specific optical and biological applications, C<sub>60</sub> would still be of high interest to develop such materials. Generally speaking, the nanocarbon-containing NC hydrogels found in the literature are mostly chemical gels. The few physical network-forming polymers are unable to interact via  $\pi$ -stacking or hydrophobic interactions. These interactions are the most promising for these materials, and are still underexploited for the reinforcement of hydrogels.

#### d. Cationic polysoaps based on polystyrene backbones

The concept of polysoap was first introduced by Lachewsky.<sup>253</sup> It refers to polymers in which repeating units contain a surfactant. These polymers, contrary to many amphiphilic polymers, can self-assemble through intramolecular interactions and not intermolecular ones. Many chemical structures can be imagined to incorporate surfactants in a polymer (Figure 1.26).



**Figure 1.26.** Various macromolecular architectures of polysoaps: a) head type, b) tail-end type, c) main-chain type, d) star type, e) hyperbranched type. The circles represent polar heads, and zigzags represent apolar tails.<sup>254</sup>

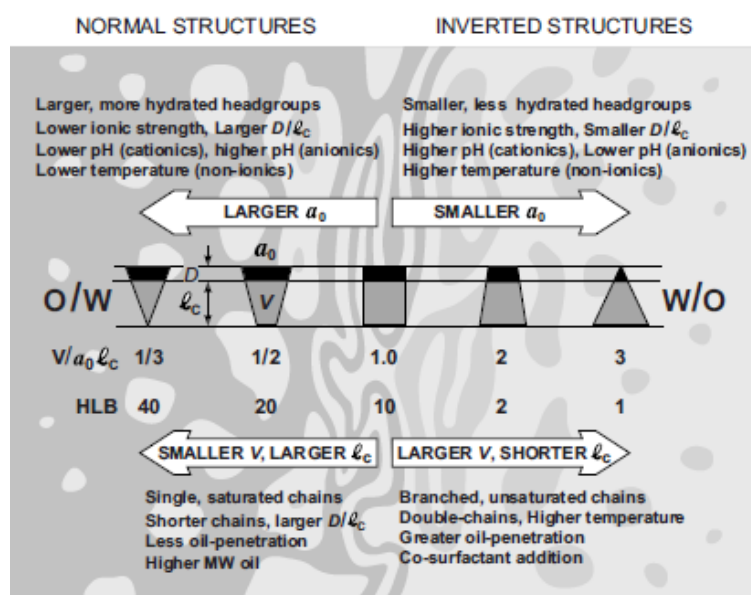
The geometry of the micelles, for molecular surfactants, depends on the packing parameter  $p$ , defined by Eq.1.1:

$$p = \frac{V}{a_0 l_c} \quad \text{Eq. 1.1}$$

With  $V$  the volume occupied by the alkyl chain,  $a_0$  the optimal area occupied by the polar head on the micelle's surface, and  $l_c$  the length of the alkyl chain in its maximal extensibility.

As it is summarized on Figure 1.27, the self-assemblies are thus mainly controlled by the length of the alkyl chain for a single polar head. If the contribution of the alkyl chain overcomes the one of the polar head, inverted micelles are thus obtained. For this reason, for common surfactants, the packing parameter is directly linked to the hydrophilic/hydrophobic balance (HLB).







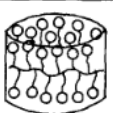
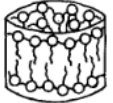


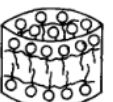
**Figure 1.27.** Summary of the chemical structure's influence on the surfactant micelles geometry.<sup>255</sup>

For ionic surfactants, the ionic strength is also an important parameter. Indeed, when it increases, the counter-ions go closer to the polar head, thus reducing the repulsions between them. Then,  $a_0$  decreases so  $p$  increases. For example, CTAB forms spherical micelles in water, but in highly saline solutions, giant worm-like micelles are formed. At high surfactant concentration, these cylinders entangle, inducing a steep increase of viscosity until forming networks. Physical gels that behave like viscoelastic liquids are formed.<sup>256</sup> The dynamics are related to the exchange of surfactants in micelles, so they depend on factors like ionic strength, but also on temperature. Indeed, this exchange supposes the overpass of an energy barrier. This activation energy relies on an Arrhenian law for these systems, following Eq. 1.2:

$$\tau \propto \exp\left(-\frac{E_a}{RT}\right) \quad \text{Eq. 1.2}$$

With  $\tau$  the relaxation time,  $E_a$  the activation energy in J/mol,  $R$  the gas constant equal to 8.314 J/K/mol, and  $T$  the temperature in K.

The architecture has dramatic consequences on the solubility and the self-assemblies of the polysoaps, because of its impact on the flexibility of chains. For example, head type polysoaps are generally insoluble in water because the polar head cannot go on the outside, as it is surrounded by apolar chains. On the contrary, tail-end type polymers possess more available polar heads, so their solubility in water is higher. In addition, for the same reason, head type polysoaps can only form reverse micelles (*i.e.* a polar core surrounded by an apolar shell) whereas tail-end type form direct micelles in water (Figure 1.28).<sup>253, 257</sup>

POLYMER \ MICELLES					
	SPHERICAL	CYLINDRICAL	DISC LIKE	INVERSE CYLINDRICAL	INVERSE SPHERICAL
TYPE A					
TYPE B					
TYPE C					

**Figure 1.28.** Various self-assemblies that can be obtained with different polysoap architectures.<sup>257</sup>

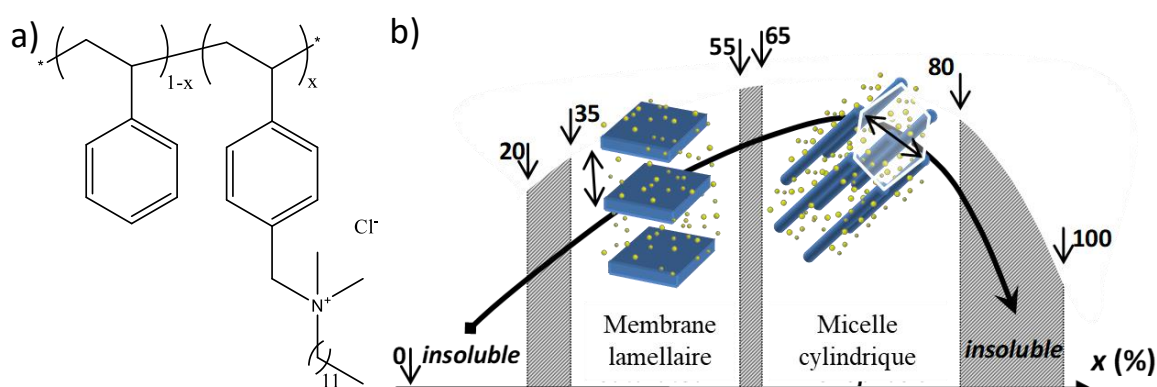
One way to increase the flexibility of the chains is to introduce spacers between the surfactant units. Two types of spacers can be distinguished: main-chain and side-chain spacers. For example, for head-type polysoaps, main-chain spacers decrease the density of polar heads on the backbone, giving to the polymer the possibility to form direct micelles. The HLB varies depending on the polarity of the spacers, and so does  $p$ . So, introducing spacers is a powerful method to tune the self-assemblies of polysoaps.<sup>253</sup>

This is the philosophy of polystyrene-based polysoaps. Surfactant units based on quaternary ammonia are grafted on a PS backbone. The phenyl plays the role of a side-chain spacer. In 1990, Aoyagi *et al.* designed « surfmers », or surfactant monomers which are surfactants with a polymerizable group. They grafted tertiary amines with two methyl groups and one longer alkyl chain on vinylbenzyl chloride (VBC), yielding p-vinylbenzyl dimethylalkylammonium chloride monomers. We will further call these units as  $C_n$ , with  $n$  the number of carbons in the alkyl chain. A subsequent polymerisation gave access to polymers with  $M_w$  up to 32 kg/mol.<sup>258</sup> Cochin *et al.* prepared similar polymers with C8, C12 and C16 alkyl chains with molar masses ranging from 300 to 3000 kg/mol.<sup>259</sup> Fluorescence and conductivity measurements were used to determine the CMC of the surfmers, which decreased with increasing alkyl chain length. The aggregation number of these micelles increased linearly with concentration, whereas for the C12 polysoap, it remained constant at low concentration and only increased linearly above 0.1 M.<sup>260</sup> After polymerization, only the C16 polysoap displayed hydrophobic domains. Its size was the double of the size of the C8 polysoap, but the  $R_g/R_h$  was close to 2 for both, although it is slightly higher for C16. Such a high ratio is beyond the theoretical value for swollen polymers in a good solvent (1.86), which would be unlikely for such hydrophobic structures. It is thus very likely that it is due to the growth of anisotropic micelles. C16 may form slightly longer



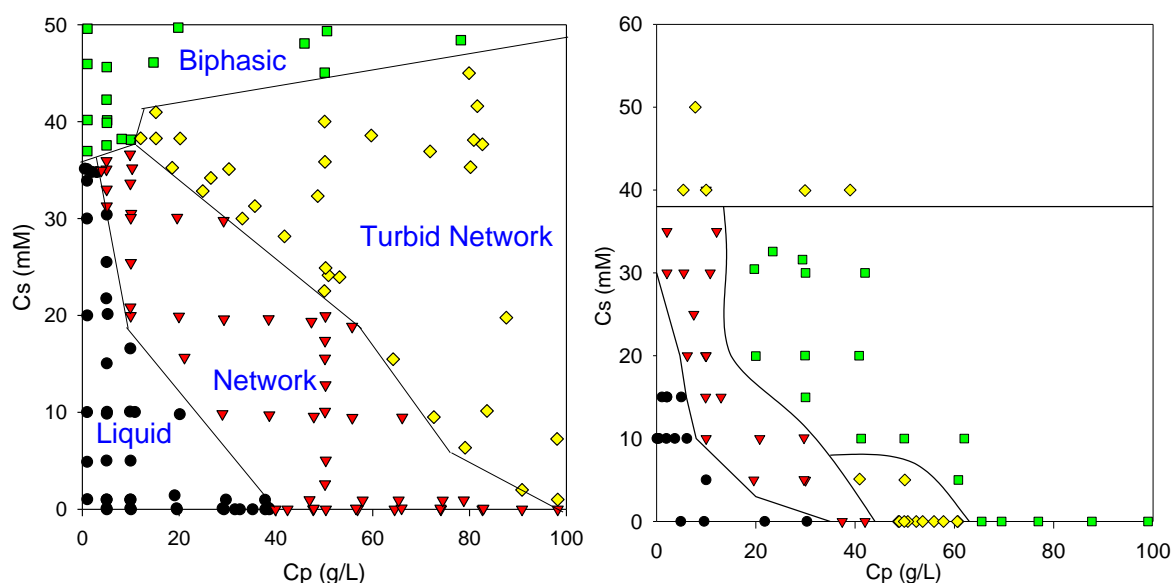
micelles than C8, which would explain the difference of  $R_g/R_h$  ratio.<sup>260</sup> It formed worm-like micelles in water as evidenced by cryo-TEM pictures. When their concentration was increased, the worms started connecting and formed aggregates.<sup>261</sup>

In 1997, Rouault *et al.* came up with the idea of forming the surfactant units after polymerization instead of before. Basically, this is a change from a grafting *through* to a grafting *to* technique. They prepared homopolymers of VBC (with  $M_n=15$  kg/mol) that they further functionalized with a C12 amine. The so-prepared polymers were only soluble when they were partially functionalized, between 40 and 80 mol% of the repeating units. This is a proof, for the most functionalised polymers, that main-chain spacers are necessary to make polysoaps water-soluble. These polysoaps were able to form gels beyond a percolation concentration. At high concentration, these gels were birefringent, indicating the formation of nematic structure, so anisotropic assemblies. Additionally, the heating of these gels lead to a drop of viscosity at low concentrations and to phase separation at high concentrations (close to 10 wt%).<sup>262</sup> This was due to the hydrolysis of the remaining VBC units at high temperature, leading to crosslinking between these units and irreversible destabilization. To counter this, Chassenieux *et al.* grafted triethylamine on the remaining VBC functions. They also copolymerized VBC together with styrene, and functionalized all the VBC functions with a C16 amine. This way, two copolymers with 55 mol% spacer units were obtained, with in the first case hydrophilic spacers and in the second case hydrophobic ones. The second one gave much more viscous solutions, and gels were obtained with only 0.3 wt% polymer concentration.<sup>263</sup> These styrene-containing copolymers were further studied by Limouzin-Morel *et al.* It was determined that the key parameter for the geometry of the assemblies was the molar ratio between styrene and soap units. Vesicles were obtained for 35 mol% cationic units, lamellas between 40 and 55%, and cylinders between 65 and 80% (Figure 1.29).<sup>264</sup>



**Figure 1.29.** a) Chemical structure of the polysoaps based on styrene and VBC units, with  $X$  the molar percentage of cationic units. b) Self-assemblies obtained in water.<sup>265</sup>

The length of the alkyl chain was the only factor that influence the spacing of the lamellas and the diameter of the cylinders. The concentration did not affect the internal structure of both lamellas and cylinders.<sup>264</sup> Dutertre *et al.* established the phase diagram of a 80 mol% polymer with a C12 pendant chain by macroscopic observations. The polymer formed gels above 4 wt%. When NaCl was added, the attractive forces were much increased and gels could be formed with only 0.5 wt% polymer with 35 mM NaCl. Above 40 mM NaCl, phase separation was observed no matter the polymer concentration. At high salt and polymer concentrations, the gels became turbid, indicating high heterogeneity of the microstructure.<sup>266</sup> In contrast, similar polymers with 45 mol% cationic units never formed transparent gels. The turbid gels that they formed were very brittle in comparison with the ones formed by the cylindrical micelles. The critical coagulation concentration was the same for both polymers (Figure 1.30). (not published)



**Figure 1.30.** Phase diagrams of C12 styrene-based polysoaps with 80 mol% (left) and 45 mol% (right) cationic units. Cs and Cp are salt and polymer concentrations, respectively.<sup>265</sup>

Cryo-TEM pictures show that at low concentration, small spherical micelles are formed. The worm-like micelles are observed starting at 5 g/L polymer. This is confirmed by SLS, which shows that the spherical micelles in dilute regime are unimers. In the presence of NaCl, even at polymer concentrations as low as 0.01 g/L, the polymer is already aggregated. SANS measurements indicated that the addition of salt interestingly did not affect the internal structure but did increase the length of the worm-like micelles. To conclude on both SANS and phase diagrams observations, adding salt has the same consequences on the structuration as the addition of polymer. The increase of the alkyl chain length induced an increased aggregation.<sup>266</sup> Dynamic rheology measurements of the hydrogels formed by the C12 polymer

with 80 mol% cationic units were conducted. The viscosity increased sharply near the percolation concentration. After formation of gels, the elastic modulus increased rapidly with increasing concentration but then settled to a logarithmic law. On the other hand, the relaxation time also increased near the percolation point but reached a plateau afterwards. In saline conditions, the percolation was reached at much lower polymer concentrations, in good agreement with the macroscopic observations. The elastic modulus of the gels in saline medium was higher than in pure water no matter the polymer concentration. The plateau for the relaxation time remained identical. The rheological measurements therefore confirm the previous assumptions. The temperature has a classical influence on the rheology of these giant micelles networks, with an Arrhenian behaviour. When the alkyl chain length was increased, the percolation concentration was greatly reduced. The most impressive impact is on relaxation time. The latter was increased by two decades from C12 to C14, and by three decades from C14 to C16. The C16 gels are therefore much less dynamic, and the relaxation can only be observed at high temperature (80°C). It can be speculated that the relaxation time is related to the microstructure, as both are influenced by the same parameter (alkyl chain length, temperature), and unaffected by the same ones (salt and polymer concentration).<sup>267</sup>

To conclude, polysoaps derived from styrene with a quaternary ammonium function form giant micelles which geometry depends on the molar ratio of cationic units. The introduction of hydrophobic spacers allowed these giant micelles to form networks, thus giving birth to physical hydrogels. The microstructure is determined by the length of the alkyl chain length, and addition of salt favoured the percolation without impacting the structure. These polymers already have applications, such as stabilization of polymer latexes,<sup>268, 269</sup> and encapsulation of quantum dots both in solution<sup>270, 271</sup> and in nanocomposite bulk materials.<sup>272-274</sup> In the case of stabilisation in solution, there are two possibilities. Either the surfmers are positioned at the interface and subsequently polymerized or the polysoaps are directly used in solution. The latter strategy has been chosen for the present work to disperse and stabilize C<sub>60</sub> fullerene particles in water. The chemical structure of this polysoap opens the door to potential hydrophobic and  $\pi$ -stacking interactions with C<sub>60</sub>, and offers the possibility to design nanocomposite hydrogels where the colloidal stabilizer is the network itself.

## References

1. Kroto, H. W.; Heath, J. R.; O'Brien, S. C.; Curl, R. F.; Smalley, R. E., C60 : Buckminsterfullerene. *Nature* **1985**, 318 (6042), 162-163.
2. Krätschmer, W.; Lamb, L. D.; Fostiropoulos, K.; Huffman, D. R., Solid C60: a new form of carbon. *Nature* **1990**, 347 (6291), 354-358.
3. Takehara, H.; Fujiwara, M.; Arikawa, M.; Diener, M. D.; Alford, J. M., Experimental study of industrial scale fullerene production by combustion synthesis. *Carbon* **2005**, 43 (2), 311-319.
4. Hedberg, K.; HEDBERG, L.; BETHUNE, D. S.; BROWN, C. A.; DORN, H. C.; JOHNSON, R. D.; DE VRIES, M., Bond Lengths in Free Molecules of Buckminsterfullerene, C60, from Gas-Phase Electron Diffraction. *Science* **1991**, 254 (5030), 410-412.
5. Harris, P. J. F.; Douthwaite, R. E.; Stephens, A. H. H.; Turner, J. F. C., The structure and growth of C60 platelets. *Chemical Physics Letters* **1992**, 199 (6), 631-634.
6. Ruoff, R. S.; Tse, D. S.; Malhotra, R.; Lorents, D. C., Solubility of fullerene (C60) in a variety of solvents. *The Journal of Physical Chemistry* **1993**, 97 (13), 3379-3383.
7. Boucher, D.; Howell, J., Solubility Characteristics of PCBM and C60. *The Journal of Physical Chemistry B* **2016**, 120 (44), 11556-11566.
8. Kholmurodov, K.; Aru, G.; Yasuoka, K., Molecular dynamics simulations of the interaction of carbon nanotube and a carbon disulfide solvent. *Natural Science* **2010**, 2 (8), 902-910.
9. Francois, J.; Gan, J. Y.; Guenet, J. M., Sol-gel transition and phase diagram of the system atactic polystyrene-carbon disulfide. *Macromolecules* **1986**, 19 (11), 2755-2760.
10. Guenet, J.-M.; Klein, M., Structures in polystyrene solutions: Their origins and their implications on physical gelation. *Makromolekulare Chemie. Macromolecular Symposia* **1990**, 39 (1), 85-98.
11. Guenet, J. M., Neutron scattering investigation of the chain trajectory in thermoreversible gels. *Macromolecules* **1987**, 20 (11), 2874-2878.
12. Leach, S.; Vervloet, M.; Desprès, A.; Bréheret, E.; Hare, J. P.; John Dennis, T.; Kroto, H. W.; Taylor, R.; Walton, D. R. M., Electronic spectra and transitions of the fullerene C60. *Chemical Physics* **1992**, 160 (3), 451-466.
13. Bensasson, R. V.; Bienvenue, E.; Dellinger, M.; Leach, S.; Seta, P., C60 in model biological systems. A visible-UV absorption study of solvent-dependent parameters and solute aggregation. *The Journal of Physical Chemistry* **1994**, 98 (13), 3492-3500.
14. Dattani, R.; Gibson, K. F.; Few, S.; Borg, A. J.; DiMaggio, P. A.; Nelson, J.; Kazarian, S. G.; Cabral, J. o. T., Fullerene oxidation and clustering in solution induced by light. *Journal of Colloid and Interface Science* **2015**, 446, 24-30.
15. Lin, M. Y.; Lindsay, H. M.; Weitz, D. A.; Ball, R. C.; Klein, R.; Meakin, P., Universality in colloid aggregation. *Nature* **1989**, 339 (6223), 360-362.
16. Avdeev, M. V.; Tropin, T. V.; Aksenov, V. L.; Rosta, L.; Kholmurodov, M. T., Formation of fullerene clusters in carbon disulfide: Data on small-angle neutron scattering and molecular dynamics. *Journal of Surface Investigation. X-ray, Synchrotron and Neutron Techniques* **2008**, 2 (6), 819.
17. Ruoff, R. S.; Malhotra, R.; Huestis, D. L.; Tse, D. S.; Lorents, D. C., Anomalous solubility behaviour of C60. *Nature* **1993**, 362 (6416), 140-141.
18. Xie, Q.; Arias, F.; Echegoyen, L., Electrochemically-reversible, single-electron oxidation of C60 and C70. *Journal of the American Chemical Society* **1993**, 115 (21), 9818-9819.
19. McHedlov-Petrosyan, N. O.; Kamneva, N. N.; Al-Shuuchi, Y. T. M.; Marynin, A. I.; Shekhovtsov, S. V., The peculiar behavior of fullerene C60 in mixtures of 'good' and polar solvents: Colloidal particles in the toluene-methanol mixtures and some other systems. *Colloids and Surfaces A: Physicochemical and Engineering Aspects* **2016**, 509, 631-637.

20. Kyzyma, O. A.; Kyrey, T. D.; Avdeev, M. V.; Korobov, M. V.; Bulavin, L. A.; Aksenov, V. L., Non-reversible solvatochromism in N-methyl-2-pyrrolidone/toluene mixed solutions of fullerene C60. *Chemical Physics Letters* **2013**, 556, 178-181.
21. Semenov, K. N.; Charykov, N. A.; Keskinov, V. A.; Piartman, A. K.; Blokhin, A. A.; Kopyrin, A. A., Solubility of Light Fullerenes in Organic Solvents. *Journal of Chemical & Engineering Data* **2010**, 55 (1), 13-36.
22. Wudl, F.; Hirsch, A.; Khemani, K. C.; Suzuki, T.; Allemand, P. M.; Koch, A.; Eckert, H.; Srdanov, G.; Webb, H. M., Survey of Chemical Reactivity of C60, Electrophile and Dieno-polarophile Par Excellence. In *Fullerenes*, American Chemical Society: 1992; Vol. 481, pp 161-175.
23. Isobe, H.; Tomita, N.; Nakamura, E., One-Step Multiple Addition of Amine to [60]Fullerene. Synthesis of Tetra(amino)fullerene Epoxide under Photochemical Aerobic Conditions. *Organic Letters* **2000**, 2 (23), 3663-3665.
24. Li, Y.; Gan, L., Selective Addition of Secondary Amines to C60: Formation of Penta- and Hexaamino[60]fullerenes. *The Journal of Organic Chemistry* **2014**, 79 (18), 8912-8916.
25. Seshadri, R.; Govindaraj, A.; Nagarajan, R.; Pradeep, T.; Rao, C. N. R., Addition of amines and halogens to fullerenes C60 and C70. *Tetrahedron Letters* **1992**, 33 (15), 2069-2070.
26. Letcher, Solubility of buckminsterfullerene in tetrahydrofuran, thiophene, tetrahydro-thiophene, 1,2-dichlorobenzene, 1,2,4-tri-chlorobenzene and n-butylamine **1995**.
27. Cataldo, F.; Iglesias-Groth, S.; Manchado, A., On the Radical Anion Spectra of Fullerenes C60 and C70. *Fullerenes, Nanotubes and Carbon Nanostructures* **2013**, 21 (6), 537-548.
28. McHedlov-Petrosyan, N. O., Fullerenes in Liquid Media: An Unsettling Intrusion into the Solution Chemistry. *Chemical Reviews* **2013**, 113 (7), 5149-5193.
29. Polte, J., Fundamental growth principles of colloidal metal nanoparticles – a new perspective. *CrystEngComm* **2015**, 17 (36), 6809-6830.
30. Desgouilles, S.; Vauthier, C.; Bazile, D.; Vacus, J.; Grossiord, J.-L.; Veillard, M.; Couvreur, P., The Design of Nanoparticles Obtained by Solvent Evaporation : A Comprehensive Study. *Langmuir* **2003**, 19 (22), 9504-9510.
31. Andrievsky, G. V.; Kosevich, M. V.; Vovk, O. M.; Shelkovsky, V. S.; Vashchenko, L. A., On the production of an aqueous colloidal solution of fullerenes. *Journal of the Chemical Society, Chemical Communications* **1995**, (12), 1281-1282.
32. Gal, M.; Kolivoska, V.; Kavan, L.; Bulickova, J.; Pospisil, L.; Hromadova, M.; Zukalova, M.; Sokolova, R.; Kielar, F., On the Stability of Fullerene C-60 in Aqueous Medium. *Fullerenes Nanotubes and Carbon Nanostructures* **2012**, 20 (8), 737-742.
33. Pospisil, L.; Gal, M.; Hromadova, M.; Bulickova, J.; Kolivoska, V.; Cvacka, J.; Novakova, K.; Kavan, L.; Zukalova, M.; Dunsch, L., Search for the form of fullerene C-60 in aqueous medium. *Physical Chemistry Chemical Physics* **2010**, 12 (42), 14095-14101.
34. Holmes, N. P.; Marks, M.; Kumar, P.; Kroon, R.; Barr, M. G.; Nicolaidis, N.; Feron, K.; Pivrikas, A.; Fahy, A.; Mendaza, A. D. d. Z.; Kilcoyne, A. L. D.; Müller, C.; Zhou, X.; Andersson, M. R.; Dastoor, P. C.; Belcher, W. J., Nano-pathways: Bridging the divide between water-processable nanoparticulate and bulk heterojunction organic photovoltaics. *Nano Energy* **2016**, 19, 495-510.
35. Kim, Y. J.; Loeffler, T. D.; Chen, Z.; Sankaranarayanan, S. K. R. S., Promoting Noncovalent Intermolecular Interactions Using a C60 Core Particle in Aqueous PC60s-Covered Colloids for Ultraefficient Photoinduced Particle Activity. *ACS Applied Materials & Interfaces* **2019**, 11 (42), 38798-38807.
36. Andrievsky, G. V.; Klochkov, V. K.; Karyakina, E. L.; McHedlov-Petrosyan, N. O., Studies of aqueous colloidal solutions of fullerene C60 by electron microscopy. *Chemical Physics Letters* **1999**, 300 (3), 392-396.
37. Cid, A.; Moldes, O. A.; Diniz, M. S.; Rodriguez-Gonzalez, B.; Mejuto, J. C., Redispersion and Self-Assembly of C-60 Fullerene in Water and Toluene. *Acs Omega* **2017**, 2 (5), 2368-2373.



38. Avdeev, M. V.; Khokhryakov, A. A.; Tropin, T. V.; Andrievsky, G. V.; Klochkov, V. K.; Derevyanchenko, L. I.; Rosta, L.; Garamus, V. M.; Priezzhev, V. B.; Korobov, M. V.; Aksenov, V. L., Structural features of molecular-colloidal solutions of C-60 fullerenes in water by small-angle neutron scattering. *Langmuir* **2004**, *20* (11), 4363-4368.
39. Prylutsky, Y. I.; Durov, S. S.; Bulavin, L. A.; Adamenko, I. I.; Moroz, K. O.; Geru, I. I.; Dihor, I. N.; Scharff, P.; Eklund, P. C.; Grigorian, L., Structure and Thermophysical Properties of Fullerene C60 Aqueous Solutions. *International Journal of Thermophysics* **2001**, *22* (3), 943-956.
40. Gigault, J.; Grassl, B., Improving the understanding of fullerene (nC60) aggregate structures: Fractal dimension characterization by static light scattering coupled to asymmetrical flow field flow fractionation. *Journal of Colloid and Interface Science* **2017**, *502*, 193-200.
41. Ganachaud, F.; Katz, J. L., Nanoparticles and Nanocapsules Created Using the Ouzo Effect: Spontaneous Emulsification as an Alternative to Ultrasonic and High-Shear Devices. *ChemPhysChem* **2005**, *6* (2), 209-216.
42. Lepeltier, E.; Bourgaux, C.; Couvreur, P., Nanoprecipitation and the Ouzo effect : Application to drug delivery devices. *Advanced Drug Delivery Reviews* **2013**, *71*, 86-97.
43. Vitale, S. A.; Katz, J. L., Liquid Droplet Dispersions Formed by Homogeneous Liquid-Liquid Nucleation : The Ouzo Effect. *Langmuir* **2003**, *19* (10), 4105-4110.
44. Aubry, J.; Ganachaud, F.; Cohen Addad, J.-P.; Cabane, B., Nanoprecipitation of Polymethylmethacrylate by Solvent Shifting:1. Boundaries. *Langmuir* **2009**, *25* (4), 1970-1979.
45. Yan, X.; Delgado, M.; Fu, A.; Alcouffe, P.; Gouin, S. G.; Fleury, E.; Katz, J. L.; Ganachaud, F.; Bernard, J., Simple but Precise Engineering of Functional Nanocapsules through Nanoprecipitation. *Angewandte Chemie International Edition* **2014**, *53* (27), 6910-6913.
46. Yan, X.; Sivignon, A.; Alcouffe, P.; Burdin, B.; Favre-Bonté, S.; Bilyy, R.; Barnich, N.; Fleury, E.; Ganachaud, F.; Bernard, J., Brilliant glyconanocapsules for trapping of bacteria. *Chemical Communications* **2015**, *51* (67), 13193-13196.
47. Sciortino, F.; Casterou, G.; Eliat, P.-A.; Troadec, M.-B.; Gaillard, C.; Chevance, S.; Kahn, M. L.; Gauffre, F., Simple Engineering of Polymer–Nanoparticle Hybrid Nanocapsules. *ChemNanoMat* **2016**, *2* (8), 796-799.
48. Goubault, C.; Sciortino, F.; Mongin, O.; Jarry, U.; Bostoën, M.; Jakobczyk, H.; Burel, A.; Dutertre, S.; Troadec, M.-B.; Kahn, M. L.; Chevance, S.; Gauffre, F., The Ouzo effect: A tool to elaborate high-payload nanocapsules. *Journal of Controlled Release* **2020**, *324*, 430-439.
49. Deguchi, S.; Alargova, R. G.; Tsujii, K., Stable Dispersions of Fullerenes, C60 and C70, in Water. Preparation and Characterization. *Langmuir* **2001**, *17* (19), 6013-6017.
50. Lucas, P.; Vaysse, M.; Aubry, J.; Mariot, D.; Sonnier, R.; Ganachaud, F., Finest nanocomposite films from carbon nanotube-loaded poly(methyl methacrylate) nanoparticles obtained by the Ouzo effect. *Soft Matter* **2011**, *7* (12), 5528-5531.
51. Brant, J.; Lecoanet, H.; Wiesner, M. R., Aggregation and deposition characteristics of fullerene nanoparticles in aqueous systems. *Journal of Nanoparticle Research* **2005**, *7* (4-5), 545-553.
52. Hilburn, M. E.; Murdianti, B. S.; Maples, R. D.; Williams, J. S.; Damron, J. T.; Kuriyavar, S. I.; Ausman, K. D., Synthesizing aqueous fullerene colloidal suspensions by new solvent-exchange methods. *Colloids and Surfaces a-Physicochemical and Engineering Aspects* **2012**, *401*, 48-53.
53. Martínez Rivas, C. J.; Tarhini, M.; Badri, W.; Miladi, K.; Greige-Gerges, H.; Nazari, Q. A.; Galindo Rodríguez, S. A.; Román, R. Á.; Fessi, H.; Elaissari, A., Nanoprecipitation process: From encapsulation to drug delivery. *International Journal of Pharmaceutics* **2017**, *532* (1), 66-81.
54. Saad, W. S.; Prud'homme, R. K., Principles of nanoparticle formation by flash nanoprecipitation. *Nano Today* **2016**, *11* (2), 212-227.
55. Zhang, C.; Pansare, V. J.; Prud'homme, R. K.; Priestley, R. D., Flash nanoprecipitation of polystyrene nanoparticles. *Soft Matter* **2012**, *8* (1), 86-93.

56. Fortner, J. D.; Lyon, D. Y.; Sayes, C. M.; Boyd, A. M.; Falkner, J. C.; Hotze, E. M.; Alemany, L. B.; Tao, Y. J.; Guo, W.; Ausman, K. D.; Colvin, V. L.; Hughes, J. B., C-60 in water: Nanocrystal formation and microbial response. *Environmental Science & Technology* **2005**, 39 (11), 4307-4316.
57. Ji, H.-X.; Hu, J.-S.; Tang, Q.-X.; Song, W.-G.; Wang, C.-R.; Hu, W.-P.; Wan, L.-J.; Lee, S.-T., Controllable Preparation of Submicrometer Single-Crystal C60 Rods and Tubes Through Concentration Depletion at the Surfaces of Seeds. *The Journal of Physical Chemistry C* **2007**, 111 (28), 10498-10502.
58. Jin, Y.; Curry, R. J.; Sloan, J.; Hatton, R. A.; Chong, L. C.; Blanchard, N.; Stolojan, V.; Kroto, H. W.; Silva, S. R. P., Structural and optoelectronic properties of C60 rods obtained via a rapid synthesis route. *Journal of Materials Chemistry* **2006**, 16 (37), 3715-3720.
59. Kobayashi, K.; Tachibana, M.; Kojima, K., Photo-assisted growth of C60 nanowhiskers from solution. *Journal of Crystal Growth* **2005**, 274 (3), 617-621.
60. Masuhara, A.; Tan, Z.; Kasai, H.; Nakanishi, H.; Oikawa, H., Fullerene Fine Crystals with Unique Shapes and Controlled Size. *Japanese Journal of Applied Physics* **2009**, 48 (5), 050206.
61. Tan, Z.; Masuhara, A.; Kasai, H.; Nakanishi, H.; Oikawa, H., Multibranched C60Micro/Nanocrystals Fabricated by Reprecipitation Method. *Japanese Journal of Applied Physics* **2008**, 47 (2), 1426-1428.
62. Park, C.; Song, H. J.; Choi, H. C., The critical effect of solvent geometry on the determination of fullerene (C60) self-assembly into dot, wire and disk structures. *Chemical Communications* **2009**, (32), 4803-4805.
63. Zhang, C.; Chung, J. W.; Priestley, R. D., Dialysis Nanoprecipitation of Polystyrene Nanoparticles. *Macromolecular Rapid Communications* **2012**, 33 (20), 1798-1803.
64. Andreev, S.; Purgina, D.; Bashkatova, E.; Garshev, A.; Maerle, A.; Andreev, I.; Osipova, N.; Shershakova, N.; Khaitov, M., Study of Fullerene Aqueous Dispersion Prepared by Novel Dialysis Method: Simple Way to Fullerene Aqueous Solution. *Fullerenes Nanotubes and Carbon Nanostructures* **2015**, 23 (9), 792-800.
65. Tomchuk, A. A.; Shershakova, N. N.; Andreev, S. M.; Turetskiy, E. A.; Ivankov, O. I.; Kyzyma, O. A.; Tomchuk, O. V.; Avdeev, M. V., C60 and C60-arginine aqueous solutions: In vitro toxicity and structural study. *Fullerenes, Nanotubes and Carbon Nanostructures* **2020**, 28 (4), 245-249.
66. Duncan, L. K.; Jinschek, J. R.; Vikesland, P. J., C-60 colloid formation in aqueous systems: Effects of preparation method on size, structure, and surface, charge. *Environmental Science & Technology* **2008**, 42 (1), 173-178.
67. Deguchi, S.; Mukai, S.-a.; Yamazaki, T.; Tsudome, M.; Horikoshi, K., Nanoparticles of Fullerene C60 from Engineering of Antiquity. *The Journal of Physical Chemistry C* **2010**, 114 (2), 849-856.
68. Deguchi, S.; Mukai, S.-a.; Sakaguchi, H.; Nonomura, Y., Non-Engineered Nanoparticles of C-60. *Scientific Reports* **2013**, 3.
69. Kawano, Y.; Kondo, T., Preparation of Aqueous Carbon Material Suspensions by Aqueous Counter Collision. *Chemistry Letters* **2014**, 43 (4), 483-485.
70. Scharff, P.; Risch, K.; Carta-Abelmann, L.; Dmytruk, I. M.; Bilyi, M. M.; Golub, O. A.; Khavryuchenko, A. V.; Buzaneva, E. V.; Aksenov, V. L.; Avdeev, M. V.; Prylutsky, Y. I.; Durov, S. S., Structure of C60 fullerene in water : spectroscopic data. *Carbon* **2004**, 42 (5), 1203-1206.
71. Peidys, D. A.; Hernandez Santiago, A. A.; Evstigneev, M. P., The interplay of enthalpic/entropic factors in nanoparticles' aggregation in solution: The case of fullerene C60. *Journal of Molecular Liquids* **2020**, 318, 114043.
72. Brant, J.; Lecoanet, H.; Wiesner, M. R., Aggregation and Deposition Characteristics of Fullerene Nanoparticles in Aqueous Systems. *Journal of Nanoparticle Research* **2005**, 7 (4), 545-553.
73. Uchida, K.; Tamura, A.; Fukushima, N.; Yajima, H., Dependence of the dispersion behavior of 60 fullerene in aqueous media on the chain length of poly(N-isopropylacrylamide) as a dispersing agent. *Colloid and Polymer Science* **2011**, 289 (1), 73-78.

74. Choi, J. I.; Snow, S. D.; Kim, J.-H.; Jang, S. S., Interaction of C-60 with Water: First-Principles Modeling and Environmental Implications. *Environmental Science & Technology* **2015**, 49 (3), 1529-1536.
75. Bouchard, D.; Ma, X.; Issacson, C., Colloidal Properties of Aqueous Fullerenes: Isoelectric Points and Aggregation Kinetics of C-60 and C-60 Derivatives. *Environmental Science & Technology* **2009**, 43 (17), 6597-6603.
76. Chen, K. L.; Elimelech, M., Aggregation and deposition kinetics of fullerene (C-60) nanoparticles. *Langmuir* **2006**, 22 (26), 10994-11001.
77. Chen, K. L.; Elimelech, M., Relating Colloidal Stability of Fullerene (C-60) Nanoparticles to Nanoparticle Charge and Electrokinetic Properties. *Environmental Science & Technology* **2009**, 43 (19), 7270-7276.
78. Chen, K. L.; Elimelech, M., Aggregation and Deposition Kinetics of Fullerene (C60) Nanoparticles. *Langmuir* **2006**, 22 (26), 10994-11001.
79. Meng, Z.; Hashmi, S. M.; Elimelech, M., Aggregation rate and fractal dimension of fullerene nanoparticles via simultaneous multiangle static and dynamic light scattering measurement. *Journal of Colloid and Interface Science* **2013**, 392, 27-33.
80. Andreev, S. M.; Purgina, D. D.; Bashkatova, E. N.; Garshev, A. V.; Maerle, A. V.; Khaitov, M. R., Facile preparation of aqueous fullerene C60 nanodispersions. *Nanotechnologies in Russia* **2014**, 9 (7), 369-379.
81. Labille, J.; Masion, A.; Ziarelli, F.; Rose, J.; Brant, J.; Villieras, F.; Pelletier, M.; Borschneck, D.; Wiesner, M. R.; Bottero, J.-Y., Hydration and Dispersion of C-60 in Aqueous Systems: The Nature of Water-Fullerene Interactions. *Langmuir* **2009**, 25 (19), 11232-11235.
82. Lee, J.; Cho, M.; Fortner, J. D.; Hughes, J. B.; Kim, J.-H., Transformation of Aggregate C-60 in the Aqueous Phase by UV Irradiation. *Environmental Science & Technology* **2009**, 43 (13), 4878-4883.
83. Yan, X.; Delgado, M.; Aubry, J.; Gribelin, O.; Stocco, A.; Boisson-Da Cruz, F.; Bernard, J.; Ganachaud, F., Central Role of Bicarbonate Anions in Charging Water/Hydrophobic Interfaces. *The Journal of Physical Chemistry Letters* **2018**, 9 (1), 96-103.
84. Paradies, H. H., Shape and size of a nonionic surfactant micelle. Triton X-100 in aqueous solution. *The Journal of Physical Chemistry* **1980**, 84 (6), 599-607.
85. Lee, J.; Yamakoshi, Y.; Hughes, J. B.; Kim, J.-H., Mechanism of C60 Photoreactivity in Water: Fate of Triplet State and Radical Anion and Production of Reactive Oxygen Species. *Environmental Science & Technology* **2008**, 42 (9), 3459-3464.
86. Lee, J.; Fortner, J. D.; Hughes, J. B.; Kim, J.-H., Photochemical Production of Reactive Oxygen Species by C60 in the Aqueous Phase During UV Irradiation. *Environmental Science & Technology* **2007**, 41 (7), 2529-2535.
87. Lee, J.; Kim, J.-H., Effect of Encapsulating Agents on Dispersion Status and Photochemical Reactivity of C60 in the Aqueous Phase. *Environmental Science & Technology* **2008**, 42 (5), 1552-1557.
88. Torres, V. M.; Posa, M.; Srdjenovic, B.; Simplício, A. L., Solubilization of fullerene C60 in micellar solutions of different solubilizers. *Colloids and Surfaces B: Biointerfaces* **2011**, 82 (1), 46-53.
89. Tomonari, Y.; Murakami, H.; Nakashima, N., Solubilization of Single-Walled Carbon Nanotubes by using Polycyclic Aromatic Ammonium Amphiphiles in Water—Strategy for the Design of High-Performance Solubilizers. *Chemistry – A European Journal* **2006**, 12 (15), 4027-4034.
90. Blanch, A. J.; Lenehan, C. E.; Quinton, J. S., Optimizing Surfactant Concentrations for Dispersion of Single-Walled Carbon Nanotubes in Aqueous Solution. *The Journal of Physical Chemistry B* **2010**, 114 (30), 9805-9811.
91. Li, X.; Ding, G.; Zhang, J.; Wang, Y.; Li, W.; Wang, C.; Li, R.; Yang, Z., Generation and properties of aqu/nC(60): the combined effects of humic acid, sunlight, and agitation intensity. *Environmental Science and Pollution Research* **2020**.
92. Terashima, M.; Nagao, S., Solubilization of 60 fullerene in water by aquatic humic substances. *Chemistry Letters* **2007**, 36 (2), 302-303.



93. Wang, X.; Tao, S.; Xing, B., Sorption and Competition of Aromatic Compounds and Humic Acid on Multiwalled Carbon Nanotubes. *Environmental Science & Technology* **2009**, *43* (16), 6214-6219.
94. Li, Q.; Xie, B.; Hwang, Y. S.; Xu, Y., Kinetics of C-60 Fullerene Dispersion in Water Enhanced by Natural Organic Matter and Sunlight. *Environmental Science & Technology* **2009**, *43* (10), 3574-3579.
95. McHedlov-Petrosyan, N. O.; Klochkov, V. K.; Andrievsky, G. V., Colloidal dispersions of fullerene C-60 in water: some properties and regularities of coagulation by electrolytes. *Journal of the Chemical Society-Faraday Transactions* **1997**, *93* (24), 4343-4346.
96. Ariga, K.; Kunitake, T., *Supramolecular chemistry-fundamentals and applications: advanced textbook*. Springer Science & Business Media: 2006.
97. Andersson, T.; Nilsson, K.; Sundahl, M.; Westman, G.; Wennerström, O., C60 embedded in  $\gamma$ -cyclodextrin: a water-soluble fullerene. *Journal of the Chemical Society, Chemical Communications* **1992**, (8), 604-606.
98. Wang, H. M.; Wenz, G., Molecular solubilization of fullerene C(60) in water by  $\gamma$ -cyclodextrin thioethers. *Beilstein journal of organic chemistry* **2012**, *8*, 1644-1651.
99. Zhang, Y.; Liu, W.; Gao, X.; Zhao, Y.; Zheng, M.; Li, F.; Ye, D., The first synthesis of a water-soluble  $\alpha$ -cyclodextrin/C-60 supramolecular complex using anionic C-60 as a building block. *Tetrahedron Letters* **2006**, *47* (48), 8571-8574.
100. Iohara, D.; Hirayama, F.; Higashi, K.; Yamamoto, K.; Uekama, K., Formation of Stable Hydrophilic C60 Nanoparticles by 2-Hydroxypropyl- $\beta$ -cyclodextrin. *Molecular Pharmaceutics* **2011**, *8* (4), 1276-1284.
101. Liu, J.; Alvarez, J.; Ong, W.; Kaifer, A. E., Network Aggregates Formed by C60 and Gold Nanoparticles Capped with  $\gamma$ -Cyclodextrin Hosts. *Nano Letters* **2001**, *1* (2), 57-60.
102. Shafiqul, I.; Mamoru, F.; Osamu, I.; Atsushi, I.; Tsukasa, H.; Seiji, S., Photoexcited State Properties of C60 Encapsulated in a Water-Soluble Calixarene. *Chemistry Letters* **2000**, *29* (1), 78-79.
103. Ikeda, A.; Hatano, T.; Kawaguchi, M.; Shinkai, S.; Suenaga, H., Water-soluble [60]fullerene-cationic homooxacalix[3]arene complex which is applicable to the photocleavage of DNA. *Chemical Communications* **1999**, (15), 1403-1404.
104. Assali, M.; Cid, J.-J.; Pernia-Leal, M.; Munoz-Bravo, M.; Fernandez, I.; Wellinger, R. E.; Khiar, N., Glyconanosomes: Disk-Shaped Nanomaterials for the Water Solubilization and Delivery of Hydrophobic Molecules. *Acs Nano* **2013**, *7* (3), 2145-2153.
105. Iyer, K. S.; Raston, C. L.; Saunders, M., Hierarchical aqueous self-assembly of C60 nano-whiskers and C60-silver nano-hybrids under continuous flow. *Lab on a Chip* **2007**, *7* (9), 1121-1124.
106. Ishikawa, K.; Kameta, N.; Aoyagi, M.; Asakawa, M.; Shimizu, T., Soft Nanotubes with a Hydrophobic Channel Hybridized with Au Nanoparticles: Photothermal Dispersion/Aggregation Control of C60 in Water. *Advanced Functional Materials* **2013**, *23* (13), 1677-1683.
107. Douglas, L.; Markus, N.; Mutsuo, M.; Junzo, S., Complexation of C60 Fullerene with Cholesteryl Group-Bearing Pullulan in Aqueous Medium. *Chemistry Letters* **2000**, *29* (1), 64-65.
108. Bartocci, S.; Mazzier, D.; Moretto, A.; Mba, M., A peptide topological template for the dispersion of 60 fullerene in water. *Organic & Biomolecular Chemistry* **2015**, *13* (2), 348-352.
109. Di Giosia, M.; Nicolini, F.; Ferrazzano, L.; Soldà, A.; Valle, F.; Cantelli, A.; Marforio, T. D.; Bottoni, A.; Zerbetto, F.; Montalti, M.; Rapino, S.; Tolomelli, A.; Calvaresi, M., Stable and Biocompatible Monodispersion of C60 in Water by Peptides. *Bioconjugate Chemistry* **2019**, *30* (3), 808-814.
110. Behera, M.; Ram, S., Mechanism of Solubilizing Fullerene C60 in Presence of Poly(Vinyl pyrrolidone) Molecules in Water. *Fullerenes, Nanotubes and Carbon Nanostructures* **2015**, *23* (10), 906-916.
111. Ram, M. B. S., Solubilization and stabilization of fullerene C60 in presence of poly(vinylpyrrolidone) molecules in water. **2011**.

112. Krasnou, I.; Tarabukina, E.; Melenevskaya, E.; Filippov, A.; Aseyev, V.; Hietala, S.; Tenhu, H., Rheological Behavior of Poly(vinylpyrrolidone)/Fullerene C60 Complexes in Aqueous Medium. *Journal of Macromolecular Science, Part B* **2008**, *47* (3), 500-510.
113. Kurmaz, S. V.; Obratsova, N. A.; Perepelitsina, E. O.; Anokhin, D. V.; Shilov, G. V.; Kabachkov, E. N.; Torbov, V. I.; Dremova, N. N., Synthesis and characterization of C60-based composites of amphiphilic N-vinylpyrrolidone/triethylene glycol dimethacrylate copolymers. *Polymer Composites* **2014**, *35* (7), 1362-1371.
114. Kurmaz, S. V.; Obratsova, N. A.; Perepelitsina, E. O.; Shilov, G. V.; Anokhina, D. V.; Pechnikova, E. V., New hybrid macromolecular structures of C-60 fullerene-amphiphilic copolymers of N-vinylpyrrolidone and triethylene glycol dimethacrylate. *Materials Today Communications* **2015**, *4*, 130-140.
115. Yamakoshi, Y. N.; Yagami, T.; Fukuhara, K.; Sueyoshi, S.; Miyata, N., Solubilization of fullerenes into water with polyvinylpyrrolidone applicable to biological tests. *Journal of the Chemical Society, Chemical Communications* **1994**, (4), 517-518.
116. Star, A.; Steuerman, D. W.; Heath, J. R.; Stoddart, J. F., Reversible water-solubilization of single-walled carbon nanotubes by polymer wrapping. *Angewandte Chemie International Edition* **2002**, *41* (14), 2508-2512.
117. Metanawin, T.; Tang, T.; Chen, R.; Vernon, D.; Wang, X., Cytotoxicity and photocytotoxicity of structure-defined water-soluble C60/micelle supramolecular nanoparticles. *Nanotechnology* **2011**, *22* (23), 235604.
118. Wang, X.-S.; Metanawin, T.; Zheng, X.-Y.; Wang, P.-Y.; Ali, M.; Vernon, D., Structure-defined C-60/polymer colloids supramolecular nanocomposites in water. *Langmuir* **2008**, *24* (17), 9230-9232.
119. Aich, N.; Boateng, L. K.; Flora, J. R. V.; Saleh, N. B., Preparation of non-aggregating aqueous fullerenes in highly saline solutions with a biocompatible non-ionic polymer. *Nanotechnology* **2013**, *24* (39).
120. Gataoulin, A. R.; Salina, M. S.; Bogdanova, S. A.; Galyametdinov, Y. G., Production and stabilization of fullerene dispersions in liquid media in the presence of nonionic surfactants. *Russian Journal of Applied Chemistry* **2013**, *86* (11), 1656-1662.
121. Ohata, T.; Ishihara, K.; Iwasaki, Y.; Sangsuwan, A.; Fujii, S.; Sakurai, K.; Ohara, Y.; Yusa, S.-i., Water-soluble complex formation of fullerenes with a biocompatible polymer. *Polymer Journal* **2016**, *48* (10), 999-1005.
122. Biby, T. E.; Prajitha, N.; Ashtami, J.; Sakthikumar, D.; Maekawa, T.; Mohanan, P. V., Toxicity of dextran stabilized fullerene C60 against C6 Glial cells. *Brain Research Bulletin* **2020**, *155*, 191-201.
123. Oishi, K.; Ishi-i, T.; Sano, M.; Shinkai, S., Unexpected Discovery of a Novel Organic Gel System Comprised of [60]Fullerene-containing Amphiphiles. *Chemistry Letters* **1999**, *28* (10), 1089-1090.
124. Semenov, K. N.; Charykov, N. A.; Keskinov, V. N., Fullerenol Synthesis and Identification. Properties of the Fullerenol Water Solutions. *Journal of Chemical & Engineering Data* **2011**, *56* (2), 230-239.
125. Chiang, L. Y.; Swirczewski, J. W.; Hsu, C. S.; Chowdhury, S. K.; Cameron, S.; Creegan, K., Multi-hydroxy additions onto C60 fullerene molecules. *Journal of the Chemical Society, Chemical Communications* **1992**, (24), 1791-1793.
126. Kokubo, K.; Matsubayashi, K.; Tategaki, H.; Takada, H.; Oshima, T., Facile synthesis of highly water-soluble fullerenes more than half-covered by hydroxyl groups. *ACS Nano* **2008**, *2* (2), 327-333.
127. Kokubo, K.; Shirakawa, S.; Kobayashi, N.; Aoshima, H.; Oshima, T., Facile and Scalable Synthesis of a Highly Hydroxylated Water-Soluble Fullerenol as a Single Nanoparticle. *Nano Research* **2011**, *4* (2), 204-215.
128. Kokubo, K.; Yamakura, S.; Nakamura, Y.; Ueno, H.; Oshima, T., Radical-scavenging Ability of Hydrophilic Carbon Nanoparticles: From Fullerene to Its Soot. *Fullerenes Nanotubes and Carbon Nanostructures* **2014**, *22* (1-3), 250-261.

129. Brant, J. A.; Labille, J.; Robichaud, C. O.; Wiesner, M., Fullerol cluster formation in aqueous solutions: Implications for environmental release. *Journal of Colloid and Interface Science* **2007**, 314 (1), 281-288.
130. Vilen, B.; Marcoux, P. R.; Lekka, M.; Sienkiewicz, A.; Fehér, T.; Forró, L., Spectroscopic and Photophysical Properties of a Highly Derivatized C60 Fullerol. *Advanced Functional Materials* **2006**, 16 (1), 120-128.
131. Camps, X.; Hirsch, A., Efficient cyclopropanation of C60 starting from malonates. *Journal of the Chemical Society, Perkin Transactions 1* **1997**, (11), 1595-1596.
132. Cheng, F.; Yang, X.; Zhu, H.; Sun, J.; Liu, Y., Synthesis of oligoadducts of malonic acid C60 and their scavenging effects on hydroxyl radical. *Journal of Physics and Chemistry of Solids* **2000**, 61 (7), 1145-1148.
133. Kraft, A.; Stangl, J.; Krause, A.-M.; Müller-Buschbaum, K.; Beuerle, F., Supramolecular frameworks based on [60]fullerene hexakisadducts. *Beilstein Journal of Organic Chemistry* **2017**, 13, 1-9.
134. Lamparth, I.; Hirsch, A., Water-soluble malonic acid derivatives of C60 with a defined three-dimensional structure. *Journal of the Chemical Society, Chemical Communications* **1994**, (14), 1727-1728.
135. Guldi, D. M., Capped Fullerenes: Stabilization of Water-Soluble Fullerene Monomers As Studied by Flash Photolysis and Pulse Radiolysis. *The Journal of Physical Chemistry A* **1997**, 101 (21), 3895-3900.
136. Guldi, D. M.; Asmus, K.-D., Activity of water-soluble fullerenes towards OH-radicals and molecular oxygen. Dedicated to Joe Silverman at the occasion of his 75th birthday. *Radiation Physics and Chemistry* **1999**, 56 (4), 449-456.
137. Semenov, K. N.; Charykov, N. A.; Murin, I. V.; Pukhareno, Y. V., Physico-chemical properties of the C60-tris-malonic derivative water solutions. *Journal of Molecular Liquids* **2015**, 201, 50-58.
138. Brettreich, M.; Hirsch, A., A highly water-soluble dendro[60]fullerene. *Tetrahedron Letters* **1998**, 39 (18), 2731-2734.
139. Bosi, S.; Feruglio, L.; Milic, D.; Prato, M., Synthesis and Water Solubility of Novel Fullerene Bisadduct Derivatives. *European Journal of Organic Chemistry* **2003**, 2003 (24), 4741-4747.
140. Chen, M.; Zhou, S.; Guo, L.; Wang, L.; Yao, F.; Hu, Y.; Li, H.; Hao, J., Aggregation Behavior and Antioxidant Properties of Amphiphilic Fullerene C60 Derivatives Cofunctionalized with Cationic and Nonionic Hydrophilic Groups. *Langmuir* **2019**, 35 (21), 6939-6949.
141. Georgakilas, V.; Pellarini, F.; Prato, M.; Guldi, D. M.; Melle-Franco, M.; Zerbetto, F., Supramolecular self-assembled fullerene nanostructures. *Proceedings of the National Academy of Sciences* **2002**, 99 (8), 5075-5080.
142. Hiroto, M.; Masaharu, S.; Takamasa, S.; Naotoshi, N., Synthesis, Aggregate Structure and Electrochemical Properties of a Water-Soluble Fullerene-Bearing Ammonium Amphiphile. *Chemistry Letters* **1999**, 28 (8), 815-816.
143. Nakashima, N.; Ishii, T.; Shirakusa, M.; Nakanishi, T.; Murakami, H.; Sagara, T., Molecular Bilayer-Based Superstructures of a Fullerene-Carrying Ammonium Amphiphile: Structure and Electrochemistry. *Chemistry - A European Journal* **2001**, 7 (8), 1766-1772.
144. Jiang, G.; Yin, F.; Duan, J.; Li, G., Synthesis and properties of novel water-soluble fullerene-glycine derivatives as new materials for cancer therapy. *Journal of Materials Science: Materials in Medicine* **2015**, 26 (1), 24.
145. Masaya, S.; Noriaki, N.; Motoki, T.; E., H. U.; Hiroyuki, I.; Eiichi, N.; Shui-Quin, Z.; Benjamin, C., Pentaorgano[60]fullerene R5C60-. A Water Soluble Hydrocarbon Anion. *Chemistry Letters* **2000**, 29 (9), 1098-1099.
146. Harano, K.; Nakamura, E., Interfacial Chemistry of Conical Fullerene Amphiphiles in Water. *Accounts of Chemical Research* **2019**, 52 (8), 2090-2100.
147. Zhou, S.; Burger, C.; Chu, B.; Sawamura, M.; Nagahama, N.; Toganoh, M.; Hackler, U. E.; Isobe, H.; Nakamura, E., Spherical Bilayer Vesicles of Fullerene-Based Surfactants in Water: A Laser Light Scattering Study. *Science* **2001**, 291 (5510), 1944-1947.

148. Sawamura, M.; Kawai, K.; Matsuo, Y.; Kanie, K.; Kato, T.; Nakamura, E., Stacking of conical molecules with a fullerene apex into polar columns in crystals and liquid crystals. *Nature* **2002**, 419 (6908), 702-705.
149. Yao, Z.; Tam, K. C., Stimuli-Responsive Water-Soluble Fullerene (C60) Polymeric Systems. *Macromolecular Rapid Communications* **2011**, 32 (23), 1863-1885.
150. Iwamoto, Y.; Yamakoshi, Y., A highly water-soluble C 60–NVP copolymer: a potential material for photodynamic therapy. *Chemical communications* **2006**, (46), 4805-4807.
151. Samal, S.; Choi, B.-J.; Geckeler, K. E., The first water-soluble main-chain polyfullerene. *Chemical Communications* **2000**, (15), 1373-1374.
152. Tamura, A.; Uchida, K.; Yajima, H., Reversible temperature-dependent dispersion-aggregation transition of poly(N-isopropylacrylamide)- 60 Fullerene conjugates. *Chemistry Letters* **2006**, 35 (3), 282-283.
153. Zhou, G.; Harruna, I. I.; Zhou, W. L.; Aicher, W. K.; Geckeler, K. E., Nanostructured Thermosensitive Polymers with Radical Scavenging Ability. *Chemistry – A European Journal* **2007**, 13 (2), 569-573.
154. Stoilova, O.; Jérôme, C.; Detrembleur, C.; Mouithys-Mickalad, A.; Manolova, N.; Rashkov, I.; Jérôme, R., New Nanostructured Materials Based on Fullerene and Biodegradable Polyesters. *Chemistry of Materials* **2006**, 18 (20), 4917-4923.
155. Herreros-López, A.; Carini, M.; Da Ros, T.; Carofiglio, T.; Marega, C.; La Parola, V.; Rapozzi, V.; Xodo, L. E.; Alshatwi, A. A.; Hadad, C.; Prato, M., Nanocrystalline cellulose-fullerene: Novel conjugates. *Carbohydrate Polymers* **2017**, 164, 92-101.
156. Li, Q.; Liu, C.; Li, H., Induction of Endogenous Reactive Oxygen Species in Mitochondria by Fullerene-Based Photodynamic Therapy. *Journal of Nanoscience and Nanotechnology* **2016**, 16 (6), 5592-5597.
157. Kwag, D. S.; Oh, N. M.; Oh, Y. T.; Oh, K. T.; Youn, Y. S.; Lee, E. S., Photodynamic therapy using glycol chitosan grafted fullerenes. *International Journal of Pharmaceutics* **2012**, 431 (1), 204-209.
158. Kim, S.; Lee, D. J.; Kwag, D. S.; Lee, U. Y.; Youn, Y. S.; Lee, E. S., Acid pH-activated glycol chitosan/fullerene nanogels for efficient tumor therapy. *Carbohydrate Polymers* **2014**, 101, 692-698.
159. Kwag, D. S.; Park, K.; Oh, K. T.; Lee, E. S., Hyaluronated fullerenes with photoluminescent and antitumoral activity. *Chemical Communications* **2013**, 49 (3), 282-284.
160. Krusic, P. J.; Wasserman, E.; Keizer, P. N.; Morton, J. R.; Preston, K. F., Radical Reactions of C60. *Science* **1991**, 254 (5035), 1183-1185.
161. Bensasson, R. V.; Brettreich, M.; Frederiksen, J.; Göttinger, H.; Hirsch, A.; Land, E. J.; Leach, S.; McGarvey, D. J.; Schönberger, H., Reactions of e-aq, co2•-, ho, o2•- and o2(1δg) with a dendro[60]fullerene and c60[c(cooh)2]n (n = 2–6)11Senior Research Fellow in Chemistry, Keele University. *Free Radical Biology and Medicine* **2000**, 29 (1), 26-33.
162. Guldi, D. M.; Hungerbuehler, H.; Asmus, K.-D., Unusual redox behavior of a water soluble malonic acid derivative of C60: evidence for possible cluster formation. *The Journal of Physical Chemistry* **1995**, 99 (36), 13487-13493.
163. Priyadarsini, K.; Mohan, H.; Mittal, J.; Guldi, D.; Asmus, K.-D., Pulse radiolysis studies on the redox reactions of aqueous solutions of. gamma.-cyclodextrine/C60 complexes. *The Journal of Physical Chemistry* **1994**, 98 (38), 9565-9569.
164. Dugan, L. L.; Turetsky, D. M.; Du, C.; Lobner, D.; Wheeler, M.; Almlı, C. R.; Shen, C. K.-F.; Luh, T.-Y.; Choi, D. W.; Lin, T.-S., Carboxyfullerenes as neuroprotective agents. *Proceedings of the National Academy of Sciences* **1997**, 94 (17), 9434-9439.
165. Tabata, Y.; Murakami, Y.; Ikada, Y., Photodynamic Effect of Polyethylene Glycol–modified Fullerene on Tumor. *Japanese Journal of Cancer Research* **1997**, 88 (11), 1108-1116.
166. Tokuyama, H.; Yamago, S.; Nakamura, E.; Shiraki, T.; Sugiura, Y., Photoinduced biochemical activity of fullerene carboxylic acid. *Journal of the American Chemical Society* **1993**, 115 (17), 7918-7919.



167. Gao, J.; Llana, V.; Youn, S.; Silvera-Batista, C. A.; Ziegler, K. J.; Bonzongo, J.-C. J., Aqueous suspension methods of carbon-based nanomaterials and biological effects on model aquatic organisms. *Environmental Toxicology and Chemistry* **2012**, 31 (1), 210-214.
168. Jia, G.; Wang, H.; Yan, L.; Wang, X.; Pei, R.; Yan, T.; Zhao, Y.; Guo, X., Cytotoxicity of Carbon Nanomaterials : Single-Wall Nanotube, Multi-Wall Nanotube, and Fullerene. *Environmental Science & Technology* **2005**, 39 (5), 1378-1383.
169. Kyzyma, O. A.; Avdeev, M. V.; Bolshakova, O. I.; Melentev, P.; Sarantseva, S. V.; Ivankov, O. I.; Korobov, M. V.; Mikheev, I. V.; Tropin, T. V.; Kubovcikova, M.; Kopcansky, P.; Korolovych, V. F.; Aksenov, V. L.; Bulavin, L. A., State of aggregation and toxicity of aqueous fullerene solutions. *Applied Surface Science* **2019**, 483, 69-75.
170. Tóth, É.; Bolskar, R. D.; Borel, A.; González, G.; Helm, L.; Merbach, A. E.; Sitharaman, B.; Wilson, L. J., Water-Soluble Gadofullerenes: Toward High-Relaxivity, pH-Responsive MRI Contrast Agents. *Journal of the American Chemical Society* **2005**, 127 (2), 799-805.
171. Liu, J.; Ohta, S.-i.; Sonoda, A.; Yamada, M.; Yamamoto, M.; Nitta, N.; Murata, K.; Tabata, Y., Preparation of PEG-conjugated fullerene containing Gd<sup>3+</sup> ions for photodynamic therapy. *Journal of Controlled Release* **2007**, 117 (1), 104-110.
172. Belousova, I. M.; Belousov, V. P.; Kiselev, V. M.; Murav'eva, T. D.; Kislyakov, I. M.; Sirotkin, A. K.; Starodubtsev, A. M.; Kris'ko, T. K.; Bagrov, I. V.; Ermakov, A. V., Structural and Optical Properties of Solid-Phase Singlet Oxygen Photosensitizers Based on Fullerene Aqueous Suspensions. *Optics and Spectroscopy* **2008**, 105 (5), 711-719.
173. Snow, S. D.; Lee, J.; Kim, J.-H., Photochemical and Photophysical Properties of Sequentially Functionalized Fullerenes in the Aqueous Phase. *Environmental Science & Technology* **2012**, 46 (24), 13227-13234.
174. Lyon, D. Y.; Adams, L. K.; Falkner, J. C.; Alvarez, P. J. J., Antibacterial Activity of Fullerene Water Suspensions : Effects of Preparation Method and Particle Size. *Environmental Science & Technology* **2006**, 40 (14), 4360-4366.
175. Lyon, D. Y.; Alvarez, P. J. J., Fullerene Water Suspension (nC(60)) Exerts Antibacterial Effects via ROS-Independent Protein Oxidation. *Environmental Science & Technology* **2008**, 42 (21), 8127-8132.
176. Markovic, Z.; Todorovic-Markovic, B.; Kleut, D.; Nikolic, N.; Vranjes-Djuric, S.; Misirkic, M.; Vucicevic, L.; Janjetovic, K.; Isakovic, A.; Harhaji, L.; Babic-Stojic, B.; Dramicanin, M.; Trajkovic, V., The mechanism of cell-damaging reactive oxygen generation by colloidal fullerenes. *Biomaterials* **2007**, 28 (36), 5437-5448.
177. Bensasson, R. V.; Berberan-Santos, M. N.; Brettreich, M.; Frederiksen, J.; Göttinger, H.; Hirsch, A.; Land, E. J.; Leach, S.; McGarvey, D. J.; Schönberger, H.; Schröder, C., Triplet state properties of malonic acid C60 derivatives C60[C(COOR)2]<sub>n</sub>; R = H, Et; n = 1–6. *Physical Chemistry Chemical Physics* **2001**, 3 (21), 4679-4683.
178. Yang, X. L.; Fan, C. H.; Zhu, H. S., Photo-induced cytotoxicity of malonic acid [C60]fullerene derivatives and its mechanism. *Toxicology in Vitro* **2002**, 16 (1), 41-46.
179. Prat, F.; Stackow, R.; Bernstein, R.; Qian, W.; Rubin, Y.; Foote, C. S., Triplet-State Properties and Singlet Oxygen Generation in a Homologous Series of Functionalized Fullerene Derivatives. *The Journal of Physical Chemistry A* **1999**, 103 (36), 7230-7235.
180. Pickering, K. D.; Wiesner, M. R., Fullerol-Sensitized Production of Reactive Oxygen Species in Aqueous Solution. *Environmental Science & Technology* **2005**, 39 (5), 1359-1365.
181. Guldi, D. M.; Prato, M., Excited-State Properties of C60 Fullerene Derivatives. *Accounts of Chemical Research* **2000**, 33 (10), 695-703.
182. Bobylev, A. G.; Okuneva, A. D.; Bobyleva, L. G.; Fadeeva, I. S.; Fadeev, R. S.; Salmov, N. N.; Podlubnaya, Z. A., Study of cytotoxicity of fullerene C60 derivatives. *Biophysics* **2012**, 57 (5), 572-576.
183. Mateo-Alonso, A.; Sooambar, C.; Prato, M., Synthesis and applications of amphiphilic fulleropyrrolidine derivatives. *Organic & Biomolecular Chemistry* **2006**, 4 (9), 1629-1637.
184. Bakry, R.; Vallant, R. M.; Najam-ul-Haq, M.; Rainer, M.; Szabo, Z.; Huck, C. W.; Bonn, G. n. K., Medicinal applications of fullerenes. *International journal of nanomedicine* **2007**, 2 (4), 639-649.

185. Cassell, A. M.; Scrivens, W. A.; Tour, J. M., Assembly of DNA/Fullerene Hybrid Materials. *Angewandte Chemie International Edition* **1998**, 37 (11), 1528-1531.
186. Ghogare, A. A.; Greer, A., Using Singlet Oxygen to Synthesize Natural Products and Drugs. *Chemical Reviews* **2016**, 116 (17), 9994-10034.
187. Carofiglio, T.; Donnola, P.; Maggini, M.; Rossetto, M.; Rossi, E., Fullerene-Promoted Singlet-Oxygen Photochemical Oxygenations in Glass-Polymer Microstructured Reactors. *Advanced Synthesis & Catalysis* **2008**, 350 (17), 2815-2822.
188. Díez-Mato, E.; Cortezón-Tamarit, F. C.; Bogialli, S.; García-Fresnadillo, D.; Marazuela, M. D., Phototransformation of model micropollutants in water samples by photocatalytic singlet oxygen production in heterogeneous medium. *Applied Catalysis B: Environmental* **2014**, 160-161, 445-455.
189. Friedman, S. H.; DeCamp, D. L.; Sijbesma, R. P.; Srdanov, G.; Wudl, F.; Kenyon, G. L., Inhibition of the HIV-1 protease by fullerene derivatives: model building studies and experimental verification. *Journal of the American Chemical Society* **1993**, 115 (15), 6506-6509.
190. Nakamura, E.; Tokuyama, H.; Yamago, S.; Shiraki, T.; Sugiura, Y., Biological Activity of Water-Soluble Fullerenes. Structural Dependence of DNA Cleavage, Cytotoxicity, and Enzyme Inhibitory Activities Including HIV-Protease Inhibition. *Bulletin of the Chemical Society of Japan* **1996**, 69 (8), 2143-2151.
191. Fu, X.; Fang, Y.; Zhao, H.; Liu, S., Size-dependent binding of pristine fullerene (nC(60)) nanoparticles to bovine/human serum albumin. *Journal of Molecular Structure* **2018**, 1166, 442-447.
192. Abdulmalik, A.; Hibah, A.; Zainy, B. M.; Makoto, A.; Daisuke, I.; Masaki, O.; Kaneto, U.; Fumitoshi, H., Preparation of soluble stable C-60/human serum albumin nanoparticles via cyclodextrin complexation and their reactive oxygen production characteristics. *Life Sciences* **2013**, 93 (7), 277-282.
193. Wu, H.; Lin, L.; Wang, P.; Jiang, S.; Dai, Z.; Zou, X., Solubilization of pristine fullerene by the unfolding mechanism of bovine serum albumin for cytotoxic application. *Chemical Communications* **2011**, 47 (38), 10659-10661.
194. Evstigneev, M. P.; Buchelnikov, A. S.; Voronin, D. P.; Rubin, Y. V.; Belous, L. F.; Prylutsky, Y. I.; Ritter, U., Complexation of C60 Fullerene with Aromatic Drugs. *ChemPhysChem* **2013**, 14 (3), 568-578.
195. Kato, H.; Nakamura, A.; Takahashi, K.; Kinugasa, S., Size effect on UV-Vis absorption properties of colloidal C60 particles in water. *Physical Chemistry Chemical Physics* **2009**, 11 (25), 4946-4948.
196. Gigault, J.; Mignard, E.; Hadri, H. E.; Grassl, B., Measurement Bias on Nanoparticle Size Characterization by Asymmetric Flow Field-Flow Fractionation Using Dynamic Light-Scattering Detection. *Chromatographia* **2017**, 80 (2), 287-294.
197. Chang, X.; Vikesland, P. J., UV-vis Spectroscopic Properties of nC60 Produced via Extended Mixing. *Environmental Science & Technology* **2011**, 45 (23), 9967-9974.
198. Kikuchi, M.; Terayama, Y.; Ishikawa, T.; Hoshino, T.; Kobayashi, M.; Ogawa, H.; Masunaga, H.; Koike, J.-i.; Horigome, M.; Ishihara, K.; Takahara, A., Chain dimension of polyampholytes in solution and immobilized brush states. *Polymer Journal* **2012**, 44 (1), 121-130.
199. Mountrichas, G.; Pispas, S.; Xenogiannopoulou, E.; Aloukos, P.; Couris, S., Aqueous dispersions of C-60 fullerene by use of amphiphilic block copolymers: Preparation and nonlinear optical properties. *Journal of Physical Chemistry B* **2007**, 111 (17), 4315-4319.
200. Xie, R.-H., Nonlinear Optics of fullerenes and carbon nanotubes. 2004; p 34.
201. Catalan, J.; Elguero, J., Fluorescence of fullerenes (C60 and C70). *Journal of the American Chemical Society* **1993**, 115 (20), 9249-9252.
202. Sun, Y. P.; Wang, P.; Hamilton, N. B., Fluorescence spectra and quantum yields of buckminsterfullerene (C60) in room-temperature solutions. No excitation wavelength dependence. *Journal of the American Chemical Society* **1993**, 115 (14), 6378-6381.
203. Kozák, O.; Sudolská, M.; Pramanik, G.; Cígler, P.; Otyepka, M.; Zbořil, R., Photoluminescent Carbon Nanostructures. *Chemistry of Materials* **2016**, 28 (12), 4085-4128.

204. Matsuo, Y.; Sato, Y.; Hashiguchi, M.; Matsuo, K.; Nakamura, E., Synthesis, Electrochemical and Photophysical Properties, and Electroluminescent Performance of the Octa- and Deca(aryl)[60]fullerene Derivatives. *Advanced Functional Materials* **2009**, *19* (14), 2224-2229.
205. Texier, I.; Berberan-Santos, M. N.; Fedorov, A.; Brettreich, M.; Schönberger, H.; Hirsch, A.; Leach, S.; Bensasson, R. V., Photophysics and Photochemistry of a Water-Soluble C60 Dendrimer: Fluorescence Quenching by Halides and Photoinduced Oxidation of I. *The Journal of Physical Chemistry A* **2001**, *105* (45), 10278-10285.
206. Yifeng, E.; Bai, L.; Fan, L.; Han, M.; Zhang, X.; Yang, S., Electrochemically generated fluorescent fullerene[60] nanoparticles as a new and viable bioimaging platform. *Journal of Materials Chemistry* **2011**, *21* (3), 819-823.
207. Zhang, M.; Bai, L.; Shang, W.; Xie, W.; Ma, H.; Fu, Y.; Fang, D.; Sun, H.; Fan, L.; Han, M.; Liu, C.; Yang, S., Facile synthesis of water-soluble, highly fluorescent graphene quantum dots as a robust biological label for stem cells. *Journal of Materials Chemistry* **2012**, *22* (15), 7461-7467.
208. Qiao, J. L.; Gong, Q. J.; Du, L. M.; Jin, W. J., Spectroscopic study on the photoinduced reaction of fullerene C60 with aliphatic amines and its dynamics — strong short wavelength fluorescence from the adducts. *Spectrochimica Acta Part A: Molecular and Biomolecular Spectroscopy* **2001**, *57* (1), 17-25.
209. Wang, J.; Wang, D.; Moses, D.; Heeger, A. J., Dynamic quenching of 5-(2'-ethyl-hexyloxy)-p-phenylene vinylene (MEH-PPV) by charge transfer to a C60 derivative in solution. *Journal of Applied Polymer Science* **2001**, *82* (10), 2553-2557.
210. Lin, H.; Weng, Y.; Huang, H.; He, Q.; Zheng, M.; Bai, F., Photoinduced partial charge transfer between conjugated polymer and fullerene in solutions. *Applied Physics Letters* **2004**, *84* (16), 2980-2982.
211. Dang, M. T.; Hirsch, L.; Wantz, G., P3HT:PCBM, Best Seller in Polymer Photovoltaic Research. *Advanced Materials* **2011**, *23* (31), 3597-3602.
212. Vaughan, B.; Williams, E. L.; Holmes, N. P.; Sonar, P.; Dodabalapur, A.; Dastoor, P. C.; Belcher, W. J., Water-based nanoparticulate solar cells using a diketopyrrolopyrrole donor polymer. *Physical Chemistry Chemical Physics* **2014**, *16* (6), 2647-2653.
213. Zappia, S.; Scavia, G.; Ferretti, A. M.; Giovanella, U.; Vohra, V.; Destri, S., Water-Processable Amphiphilic Low Band Gap Block Copolymer:Fullerene Blend Nanoparticles as Alternative Sustainable Approach for Organic Solar Cells. *Advanced Sustainable Systems* **2018**, *2* (3).
214. Andersen, T. R.; Larsen-Olsen, T. T.; Andreasen, B.; Böttiger, A. P. L.; Carlé, J. E.; Helgesen, M.; Bundgaard, E.; Norrman, K.; Andreasen, J. W.; Jørgensen, M.; Krebs, F. C., Aqueous Processing of Low-Band-Gap Polymer Solar Cells Using Roll-to-Roll Methods. *ACS Nano* **2011**, *5* (5), 4188-4196.
215. Aernouts, T.; Aleksandrov, T.; Girotto, C.; Genoe, J.; Poortmans, J., Polymer based organic solar cells using ink-jet printed active layers. *Applied Physics Letters* **2008**, *92* (3), 033306.
216. Kadam, V.; Nicolai, T.; Nicol, E.; Benyahia, L., Structure and Rheology of Self-Assembled Telechelic Associative Polymers in Aqueous Solution before and after Photo-Cross-Linking. *Macromolecules* **2011**, *44* (20), 8225-8232.
217. Chassenieux, C.; Nicolai, T.; Benyahia, L., Rheology of associative polymer solutions. *Current Opinion in Colloid & Interface Science* **2011**, *16* (1), 18-26.
218. Kirkland, S. E.; Hensarling, R. M.; McConaughy, S. D.; Guo, Y.; Jarrett, W. L.; McCormick, C. L., Thermoreversible Hydrogels from RAFT-Synthesized BAB Triblock Copolymers: Steps toward Biomimetic Matrices for Tissue Regeneration. *Biomacromolecules* **2008**, *9* (2), 481-486.
219. Charbonneau, C.; De Souza Lima, M. M.; Chassenieux, C.; Colombani, O.; Nicolai, T., Structure of pH sensitive self-assembled amphiphilic di- and triblock copolyelectrolytes: micelles, aggregates and transient networks. *Physical Chemistry Chemical Physics* **2013**, *15* (11), 3955-3964.

220. Charbonneau, C.; Chassenieux, C.; Colombani, O.; Nicolai, T., Controlling the Dynamics of Self-Assembled Triblock Copolymer Networks via the pH. *Macromolecules* **2011**, *44* (11), 4487-4495.
221. Gong, J. P.; Katsuyama, Y.; Kurokawa, T.; Osada, Y., Double-Network Hydrogels with Extremely High Mechanical Strength. *Advanced Materials* **2003**, *15* (14), 1155-1158.
222. Berret, J.-F.; S  r  ro, Y.; Winkelman, B.; Calvet, D.; Collet, A.; Viguier, M., Nonlinear rheology of telechelic polymer networks. *Journal of Rheology* **2001**, *45* (2), 477-492.
223. Okumura, Y.; Ito, K., The Polyrotaxane Gel: A Topological Gel by Figure-of-Eight Cross-links. *Advanced Materials* **2001**, *13* (7), 485-487.
224. Tanaka, Y.; Gong, J. P.; Osada, Y., Novel hydrogels with excellent mechanical performance. *Progress in Polymer Science* **2005**, *30* (1), 1-9.
225. Sun, J.-Y.; Zhao, X.; Illeperuma, W. R. K.; Chaudhuri, O.; Oh, K. H.; Mooney, D. J.; Vlassak, J. J.; Suo, Z., Highly stretchable and tough hydrogels. *Nature* **2012**, *489* (7414), 133-136.
226. Dragan, E. S., Design and applications of interpenetrating polymer network hydrogels. A review. *Chemical Engineering Journal* **2014**, *243*, 572-590.
227. Nicol, E.; Nicolai, T.; Zhao, J.; Narita, T., Photo-Cross-Linked Self-Assembled Poly(ethylene oxide)-Based Hydrogels Containing Hybrid Junctions with Dynamic and Permanent Cross-Links. *ACS Macro Letters* **2018**, *7* (6), 683-687.
228. Lin, P.; Ma, S.; Wang, X.; Zhou, F., Molecularly Engineered Dual-Crosslinked Hydrogel with Ultrahigh Mechanical Strength, Toughness, and Good Self-Recovery. *Advanced Materials* **2015**, *27* (12), 2054-2059.
229. Voets, I. K.; de Keizer, A.; Cohen Stuart, M. A., Complex coacervate core micelles. *Advances in Colloid and Interface Science* **2009**, *147-148*, 300-318.
230. Sproncken, C. C. M.; Magana, J. R.; Voets, I. K., 100th Anniversary of Macromolecular Science Viewpoint: Attractive Soft Matter: Association Kinetics, Dynamics, and Pathway Complexity in Electrostatically Coassembled Micelles. *ACS Macro Letters* **2021**, *10* (2), 167-179.
231. Spruijt, E.; Sprakel, J.; Lemmers, M.; Stuart, M. A. C.; van der Gucht, J., Relaxation Dynamics at Different Time Scales in Electrostatic Complexes: Time-Salt Superposition. *Physical Review Letters* **2010**, *105* (20), 208301.
232. Gucht, J. v. d.; Spruijt, E.; Lemmers, M.; Cohen Stuart, M. A., Polyelectrolyte complexes: Bulk phases and colloidal systems. *Journal of Colloid and Interface Science* **2011**, *361* (2), 407-422.
233. Sun, T. L.; Kurokawa, T.; Kuroda, S.; Ihsan, A. B.; Akasaki, T.; Sato, K.; Haque, M. A.; Nakajima, T.; Gong, J. P., Physical hydrogels composed of polyampholytes demonstrate high toughness and viscoelasticity. *Nature Materials* **2013**, *12* (10), 932-937.
234. Haraguchi, K.; Takehisa, T., Nanocomposite Hydrogels: A Unique Organic-Inorganic Network Structure with Extraordinary Mechanical, Optical, and Swelling/De-swelling Properties. *Advanced Materials* **2002**, *14* (16), 1120-1124.
235. Haraguchi, K., Nanocomposite hydrogels. *Current Opinion in Solid State and Materials Science* **2007**, *11* (3), 47-54.
236. Nishida, T.; Obayashi, A.; Haraguchi, K.; Shibayama, M., Stress relaxation and hysteresis of nanocomposite gel investigated by SAXS and SANS measurement. *Polymer* **2012**, *53* (20), 4533-4538.
237. Lin, W.-C.; Fan, W.; Marcellan, A.; Hourdet, D.; Creton, C., Large Strain and Fracture Properties of Poly(dimethylacrylamide)/Silica Hybrid Hydrogels. *Macromolecules* **2010**, *43* (5), 2554-2563.
238. Carlsson, L.; Rose, S.; Hourdet, D.; Marcellan, A., Nano-hybrid self-crosslinked PDMA/silica hydrogels. *Soft Matter* **2010**, *6* (15), 3619-3631.
239. Suzuki, T.; Endo, H.; Osaka, N.; Shibayama, M., Dynamics and Microstructure Analysis of N-Isopropylacrylamide/Silica Hybrid Gels. *Langmuir* **2009**, *25* (15), 8824-8832.
240. Rose, S.; Marcellan, A.; Narita, T.; Bou  , F.; Cousin, F.; Hourdet, D., Structure investigation of nanohybrid PDMA/silica hydrogels at rest and under uniaxial deformation. *Soft Matter* **2015**, *11* (29), 5905-5917.



241. Rose, S.; Prevotau, A.; Elzière, P.; Hourdet, D.; Marcellan, A.; Leibler, L., Nanoparticle solutions as adhesives for gels and biological tissues. *Nature* **2014**, 505 (7483), 382-385.
242. Li, H.-J.; Jiang, H.; Haraguchi, K., Ultrastiff, Thermoresponsive Nanocomposite Hydrogels Composed of Ternary Polymer–Clay–Silica Networks. *Macromolecules* **2018**, 51 (2), 529-539.
243. Wakai, H.; Momoi, T.; Yamauchi, T.; Tsubokawa, N., A Simple Preparation of C60-Poly(ethylene glycol) Gel and its Properties. *Polymer Journal* **2009**, 41 (1), 40-45.
244. Zhang, Y.; Zhang, H.; Zou, Q.; Xing, R.; Jiao, T.; Yan, X., An injectable dipeptide-fullerene supramolecular hydrogel for photodynamic antibacterial therapy. *Journal of Materials Chemistry B* **2018**, 6 (44), 7335-7342.
245. Mba, M.; Jiménez, A. I.; Moretto, A., Templating the Self-Assembly of Pristine Carbon Nanostructures in Water. *Chemistry – A European Journal* **2014**, 20 (14), 3888-3893.
246. Sugikawa, K.; Inoue, Y.; Kozawa, K.; Ikeda, A., Introduction of Fullerenes into Hydrogels via Formation of Fullerene Nanoparticles. *ChemNanoMat* **2018**, 4 (7), 682-687.
247. Servant, A.; Methven, L.; Williams, R. P.; Kostarelos, K., Electroresponsive Polymer–Carbon Nanotube Hydrogel Hybrids for Pulsatile Drug Delivery In Vivo. *Advanced Healthcare Materials* **2013**, 2 (6), 806-811.
248. Zhang, X.; Pint, C. L.; Lee, M. H.; Schubert, B. E.; Jamshidi, A.; Takei, K.; Ko, H.; Gillies, A.; Bardhan, R.; Urban, J. J.; Wu, M.; Fearing, R.; Javey, A., Optically- and Thermally-Responsive Programmable Materials Based on Carbon Nanotube-Hydrogel Polymer Composites. *Nano Letters* **2011**, 11 (8), 3239-3244.
249. Mottet, L.; Le Cornec, D.; Noël, J.-M.; Kanoufi, F.; Delord, B.; Poulin, P.; Bibette, J.; Bremond, N., A conductive hydrogel based on alginate and carbon nanotubes for probing microbial electroactivity. *Soft Matter* **2018**, 14 (8), 1434-1441.
250. Valentin, T. M.; Landauer, A. K.; Morales, L. C.; DuBois, E. M.; Shukla, S.; Liu, M.; Stephens Valentin, L. H.; Franck, C.; Chen, P.-Y.; Wong, I. Y., Alginate-graphene oxide hydrogels with enhanced ionic tunability and chemomechanical stability for light-directed 3D printing. *Carbon* **2019**, 143, 447-456.
251. Xu, Y.; Sheng, K.; Li, C.; Shi, G., Self-Assembled Graphene Hydrogel via a One-Step Hydrothermal Process. *ACS Nano* **2010**, 4 (7), 4324-4330.
252. Zhang, L.; Wang, Z.; Xu, C.; Li, Y.; Gao, J.; Wang, W.; Liu, Y., High strength graphene oxide/polyvinyl alcohol composite hydrogels. *Journal of Materials Chemistry* **2011**, 21 (28), 10399-10406.
253. Laschewsky, A., Molecular concepts, self-organisation and properties of polysoaps. In *Polysoaps/Stabilizers/Nitrogen-15 NMR*, Springer Berlin Heidelberg: Berlin, Heidelberg, 1995; pp 1-86.
254. Bayouhd, S.; Laschewsky, A.; Wischerhoff, E., Amphiphilic hyperbranched polyelectrolytes: a new type of polysoap. *Colloid and Polymer Science* **1999**, 277 (6), 519-527.
255. Israelachvili, J. N., *Intermolecular and surface forces*. Academic press: 2015.
256. Khatory, A.; Lequeux, F.; Kern, F.; Candau, S., Linear and nonlinear viscoelasticity of semidilute solutions of wormlike micelles at high salt content. *Langmuir* **1993**, 9 (6), 1456-1464.
257. Jahns, E.; Finkelmann, H., Lyotropic liquid crystalline phase behavior of a polymeric amphiphile polymerized via their hydrophilic ends. *Colloid and Polymer Science* **1987**, 265 (4), 304-311.
258. Aoyagi, T.; Terashima, O.; Suzuki, N.; Matsui, K.; Nagase, Y., Polymerization of benzalkonium chloride-type monomer and application to percutaneous drug absorption enhancer. *Journal of Controlled Release* **1990**, 13 (1), 63-71.
259. Cochin, D.; Zana, R.; Candau, F., Polymerization of micelle-forming monomers: Mechanistic study and characterization of the systems before and after polymerization. *Polymer International* **1992**, 30 (4), 491-498.
260. Cochin, D.; Candau, F.; Zana, R., Photopolymerization of micelle-forming monomers. 1. Characterization of the systems before and after polymerization. *Macromolecules* **1993**, 26 (21), 5755-5764.

261. Cochin, D.; Candau, F.; Zana, R.; Talmon, Y., Direct imaging of microstructures formed in aqueous solutions of polyamphiphiles. *Macromolecules* **1992**, 25 (16), 4220-4223.
262. Rouault, Y.; Iliopoulos, I.; Audebert, R., Gels of amphiphilic polyelectrolyte derivatives of poly(vinyl benzyl chloride). *Polymer Bulletin* **1997**, 39 (6), 741-746.
263. Chassenieux, C.; Fundin, J.; Ducouret, G.; Iliopoulos, I., Amphiphilic copolymers of styrene with a surfactant-like comonomer: gel formation in aqueous solution. *Journal of Molecular Structure* **2000**, 554 (1), 99-108.
264. Limouzin-Morel, C.; Dutertre, F.; Moussa, W.; Gaillard, C.; Iliopoulos, I.; Bendejacq, D.; Nicolai, T.; Chassenieux, C., One and two dimensional self-assembly of comb-like amphiphilic copolyelectrolytes in aqueous solution. *Soft Matter* **2013**, 9 (37), 8931-8937.
265. Dutertre, F. Structures et propriétés rhéologiques d'auto-assemblages de copolymères amphiphiles cationiques en peigne. 2014.
266. Dutertre, F.; Gaillard, C. d.; Chassenieux, C.; Nicolai, T., Branched Wormlike Micelles Formed by Self-Assembled Comblike Amphiphilic Copolyelectrolytes. *Macromolecules* **2015**, 48 (20), 7604-7612.
267. Dutertre, F.; Benyahia, L.; Chassenieux, C.; Nicolai, T., Dynamic Mechanical Properties of Networks of Wormlike Micelles Formed by Self-Assembled Comblike Amphiphilic Copolyelectrolytes. *Macromolecules* **2016**, 49 (18), 7045-7053.
268. Save, M.; Manguian, M.; Chassenieux, C.; Charleux, B., Synthesis by RAFT of Amphiphilic Block and Comblike Cationic Copolymers and Their Use in Emulsion Polymerization for the Electrosteric Stabilization of Latexes. *Macromolecules* **2005**, 38 (2), 280-289.
269. Manguian, M.; Save, M.; Chassenieux, C.; Charleux, B., Miniemulsion polymerization of styrene using well-defined cationic amphiphilic comblike copolymers as the sole stabilizer. *Colloid and Polymer Science* **2005**, 284 (2), 142-150.
270. Allen, C. N.; Lequeux, N.; Chassenieux, C.; Tessier, G.; Dubertret, B., Optical Analysis of Beads Encoded with Quantum Dots Coated with a Cationic Polymer. *Advanced Materials* **2007**, 19 (24), 4420-4425.
271. Shih-Yuan, L.; Mei-Ling, W.; Hsin-Lung, C., Polymer nanocomposite containing CdS–ZnS core–shell particles: Optical properties and morphology. *Journal of Applied Physics* **2003**, 93 (9), 5789-5793.
272. Hirai, T.; Watanabe, T.; Komazawa, I., Preparation of Semiconductor Nanoparticle–Polymer Composites by Direct Reverse Micelle Polymerization Using Polymerizable Surfactants. *The Journal of Physical Chemistry B* **2000**, 104 (38), 8962-8966.
273. Zhang, H.; Cui, Z.; Wang, Y.; Zhang, K.; Ji, X.; Lü, C.; Yang, B.; Gao, M., From Water-Soluble CdTe Nanocrystals to Fluorescent Nanocrystal–Polymer Transparent Composites Using Polymerizable Surfactants. *Advanced Materials* **2003**, 15 (10), 777-780.
274. Yang, Y.; Wen, Z.; Dong, Y.; Gao, M., Incorporating CdTe Nanocrystals into Polystyrene Microspheres: Towards Robust Fluorescent Beads. *Small* **2006**, 2 (7), 898-901.



## Chapter 2. Materials and methods

1) Amphiphilic polymer synthesis .....	85
a. Precursor synthesis .....	85
i. Experimental protocol .....	85
ii. Characterization .....	86
b. Functionalization by a tertiary amine .....	89
i. Experimental protocol .....	89
ii. Characterization .....	89
iii. 75C12 aqueous solutions .....	90
2) Preparation of C <sub>60</sub> aqueous colloidal suspensions .....	92
a. Mother solutions in organic solvents .....	92
b. Dispersion of C <sub>60</sub> in water by emulsification-evaporation .....	93
c. Freeze-drying/re-dispersion .....	94
d. Ouzo effect .....	94
3) Chemical composition .....	95
a. UV-visible spectroscopy .....	95
b. Thermogravimetric analysis (TGA) .....	97
c. Analytical centrifugation .....	97
4) Scattering techniques .....	99
a. Generalities on scattering techniques .....	99
b. Static Light Scattering (SLS) .....	101
c. Dynamic Light Scattering (DLS) .....	102
d. Small-Angle X-Ray Scattering (SAXS) .....	103
e. Wide-Angle X-Ray Scattering/Diffraction (WAXS/WAXD) .....	104
5) Microscopy .....	105
a. Transmission electron microscopy .....	105
i. Dried TEM .....	105
ii. Cryo-TEM .....	105
b. Confocal Laser Scanning Microscopy (CLSM) .....	105
c. Raman scattering and fluorescence .....	105
6) Rheology .....	106
a. Flow measurements .....	106
b. Dynamic rheology .....	107
c. Rheological study of 75C12 in water .....	108
References .....	111



## Chapter 2. Materials and methods

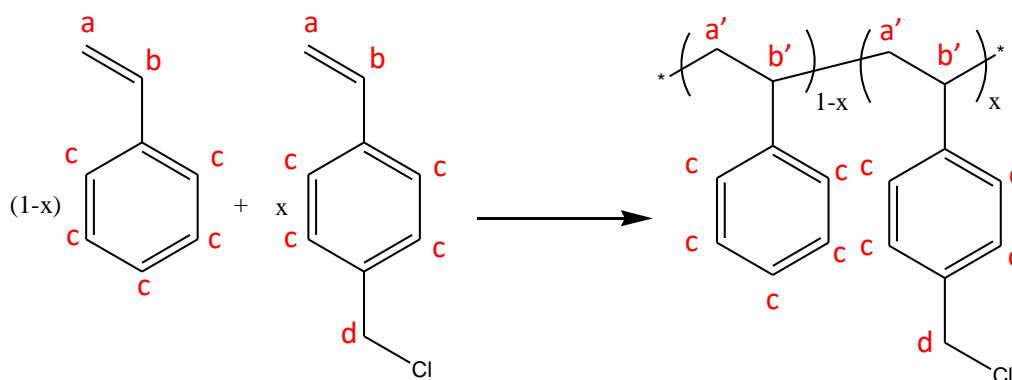
In this chapter, we will present the synthesis of the polymer and different processes used for producing fullerene nanoparticles stabilized by the said polymer as well as the nanocomposite hydrogels based on it. Finally, the various characterization techniques that have been used will be presented.

### 1) Amphiphilic polymer synthesis

The synthesis of the polymer has already been published.<sup>1</sup> First, a precursor copolymer of vinylbenzyl chloride (VBC) and styrene (Sty) was synthesized. Then, a tertiary amine was allowed to react with it to form the final cationic polymer. The experimental protocols and the characterization of the polymer are described here.

#### a. Precursor synthesis

The first step consists in a free radical copolymerization of VBC and Sty (Figure 2.1) initiated by azobisisobutyronitrile (AIBN) in toluene.



**Figure 2.1.** Synthesis of the precursor polymer. In red, indexation of protons for Figures 2.2 and 2.3.

#### i. Experimental protocol

34.149 g (224 mmol) of VBC and 6.848 g (65.8 mmol) of styrene were introduced into a three-necked round-bottom flask of 250 mL which corresponds to an initial molar fraction for VBC equal to 77 mol%. The monomers were diluted with 80 mL of toluene then the mixture was degassed by bubbling argon for 30 minutes, and brought to 65°C. 0.834 g (5.08 mmol) of AIBN were dissolved in 20 mL of toluene in a 100 mL flask and then degassed by bubbling argon for 10 minutes. This solution was then transferred into the mixture of monomers. Polymerization was stopped by cooling the mixture and opening it to air after 20 hours of reaction.

Corinne Morel-Limouzin previously determined the reactivity ratios of both monomers, respectively 0.95 and 0.62 for VBC and Sty.<sup>2</sup> The duration of the polymerization was chosen

in order to optimize the conversion without causing a major drift of the composition. It allows, according to the kinetic study reported by Wissam Moussa,<sup>3</sup> to reach a conversion of 85% that stands below 95% where the drift of composition for the copolymerization occurs.

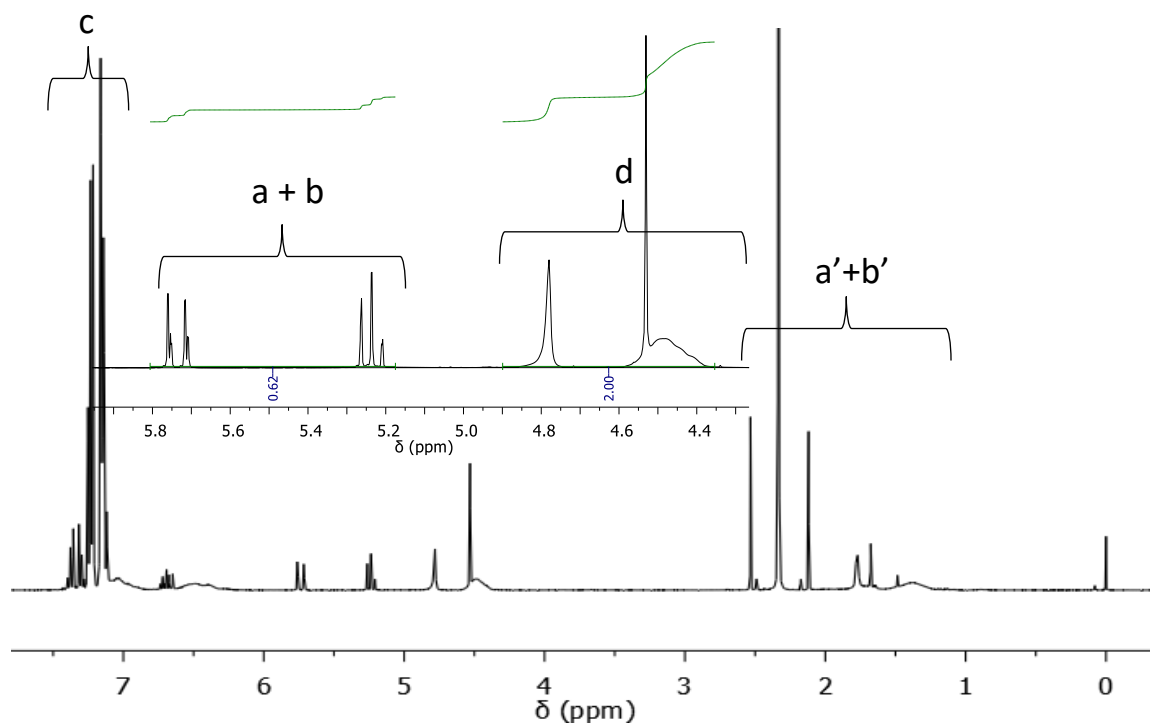
The mixture was then precipitated dropwise into 2 L of absolute methanol under vigorous stirring. The sedimented polymer was finally filtered under vacuum through a glass filter of porosity 4 and washed with 3x200 mL of absolute methanol. This operation was repeated twice in order to get rid of the excess monomer. The solid was dried in a vacuum oven at room temperature overnight. A white powder was thus isolated and ground.

## ii. Characterization

The conversion CV was computed with Eq. 2.1 from the <sup>1</sup>H NMR spectrum of the raw reaction mixture plotted in Figure 2.2. In this mixture, both polymerized and unreacted VBC are present. Basically, the conversion is the ratio between polymerized and total VBC. The remaining VBC monomer (unpolymerized) concentration [VBC]<sub>t</sub> is proportional to 77% of the integration of a vinyl proton (I<sub>a+b</sub>), the other 23% being the styrene monomers. The total VBC concentration [VBC]<sub>0</sub> is proportional to the integration of a proton of the chloromethyl group (I<sub>d</sub>):

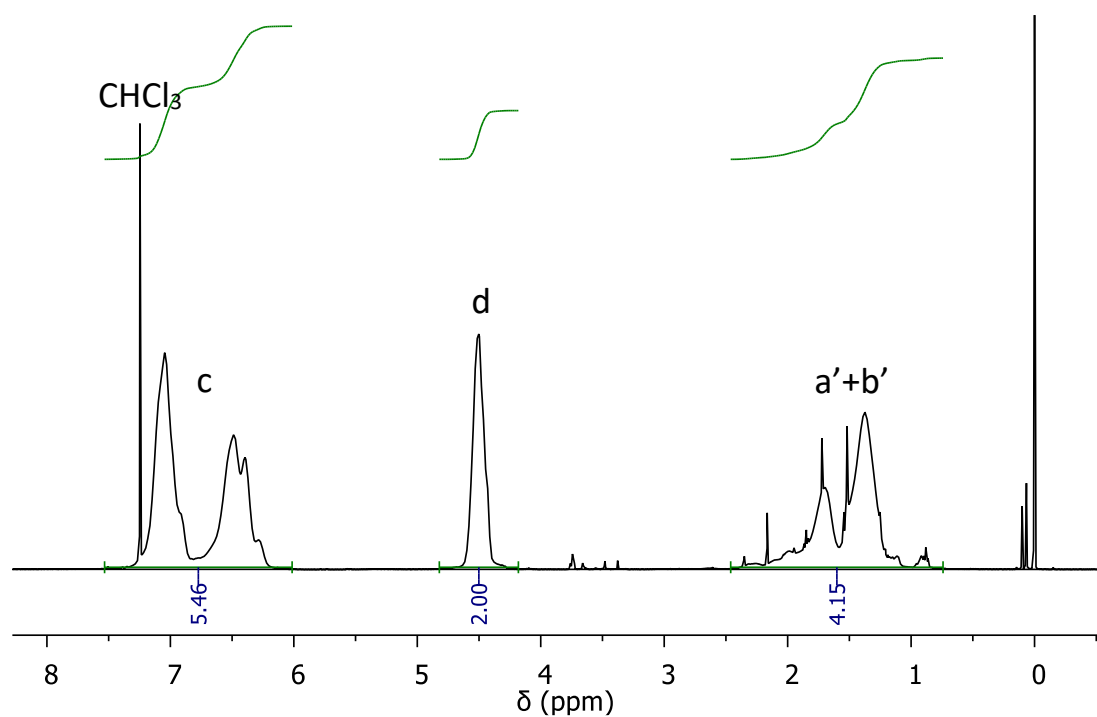
$$CV = \frac{[VBC]_0 - [VBC]_t}{[VBC]_0} = \frac{I_d - 0.77 \times I_{a+b}}{I_d} \quad \text{Eq. 2.1}$$

The conversion rate thus calculated is 85%, which corresponds to the expected value.



**Figure 2.2.**  $^1\text{H}$  NMR spectrum in  $\text{CDCl}_3$  of the raw reaction mixture after 20h polymerization. Insert is a magnification of the spectrum between 4.3 and 6 ppm. For the indexation of protons, see Figure 2.1.

The precursor was analyzed by  $^1\text{H}$  NMR in  $\text{CDCl}_3$  after precipitation as shown in Figure 2.3.



**Figure 2.3.**  $^1\text{H}$  NMR spectrum of the precursor in  $\text{CDCl}_3$  after precipitation. For the indexation of protons, see Figure 2.1.



The composition in VBC and Sty units in the purified copolymer was determined with the Eq. 2.2 to 4 from NMR spectrum in Figure 2.3:

$$I_{a'+b'} = 3(1 - x_{VBC})I_H + 3x_{VBC}I_H = 3I_H \quad \text{Eq. 2.2}$$

$$I_d = 2x_{VBC}I_H \quad \text{Eq. 2.3}$$

$$I_c = 5(1 - x_{VBC})I_H + 4x_{VBC}I_H = 5I_H - x_{VBC}I_H \quad \text{Eq. 2.4}$$

with  $I_H$  the intensity of one proton of the polymer and  $x_{VBC}$  the molar fraction of VBC units in the precursor copolymer.

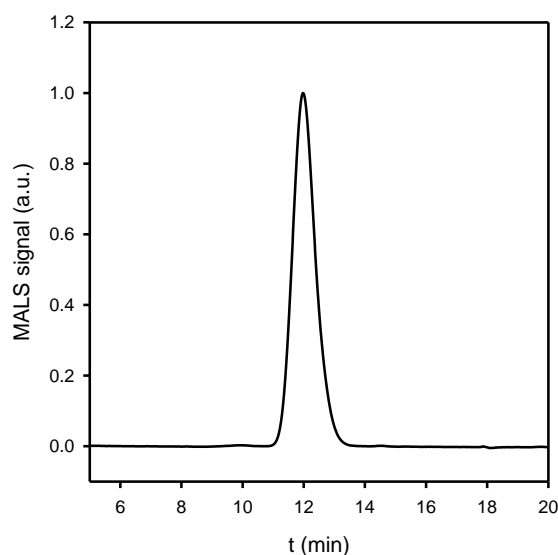
A molar fraction equal to  $75 \pm 2\%$  VBC was calculated for the precursor.

Taking conversion into consideration, the reaction yield can then be calculated with Eq. 2.5 :

$$Rdt = \frac{m_{exp}}{m_{theo} \times \tau} \times 100 \quad \text{Eq. 2.5}$$

Thus, the reaction yield was calculated to be 74%. These results are close to those obtained by Fabien Dutertre although the composition differs slightly.<sup>4</sup>

The copolymer was analyzed by SEC with THF as an eluent. The chromatogram obtained by MALS (Multi Angle Light Scattering) is plotted in Figure 2.4. using a specific refractive increment of 0.186 mL/g.

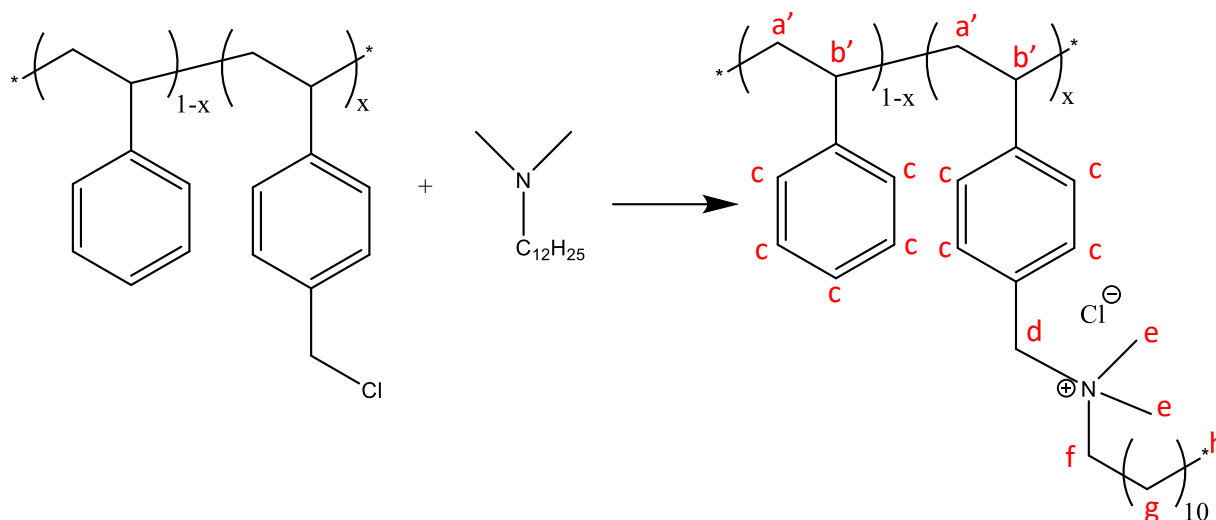


**Figure 2.4.** MALS SEC chromatogram of the precursor.

The number-averaged molar mass of the precursor  $M_n$  is then equal to 17 kg/mol and the mass-averaged molar mass  $M_w$  was estimated at 27 kg/mol, corresponding to a dispersity of 1.6.

### b. Functionalization by a tertiary amine

In the second step, an amine is grafted onto the polymer to obtain a comb structure (Figure 2.5). Here a C12 tertiary amine, N, N-dimethyldodecylamine, was grafted onto the precursor with  $x = 0.75$ . The resulting amphiphilic polymer will hereinafter be referred to as 75C12.



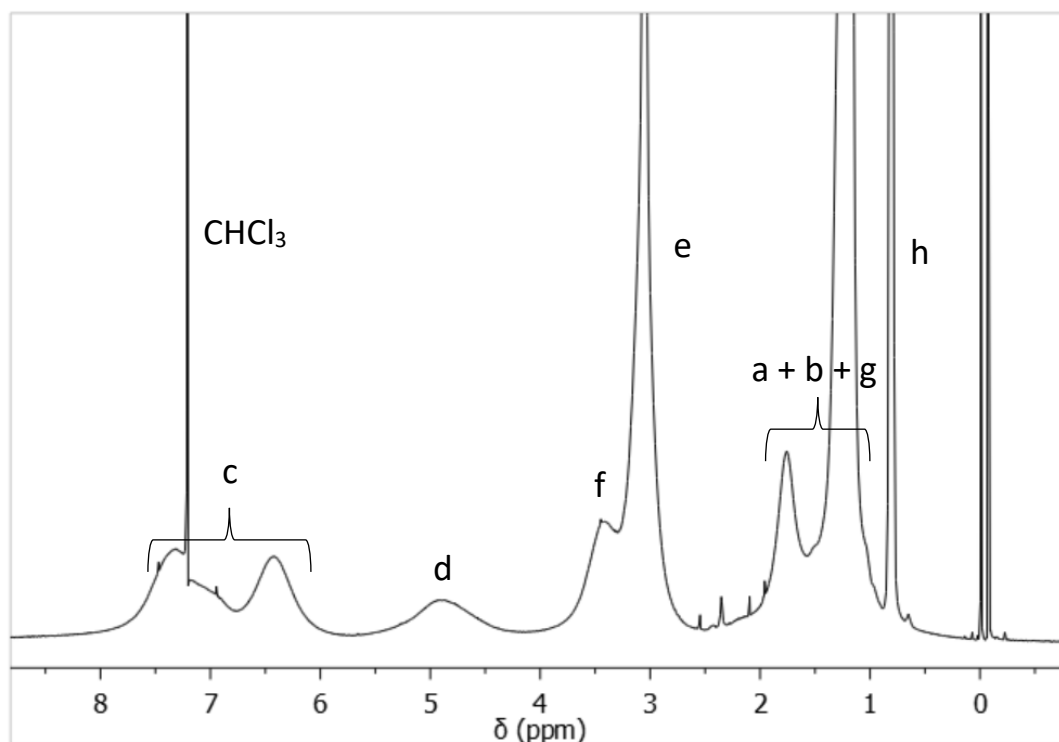
**Figure 2.5.** Synthesis of the cationic polymer 75C12. In red, indexation of protons for Figure 2.6.

#### i. Experimental protocol

25,619 g of precursor (corresponding to 137 mmol of CMS) were dissolved in 375 mL of chloroform under magnetic stirring. Once the solution was homogeneous, 58.5 g (275 mmol or 2 equivalents) of N, N-dimethyldodecylamine were added. The mixture was stirred during 5 days at room temperature. The polymer was precipitated dropwise in 4 L of diethyl ether. This was followed by filtration through a glass filter of porosity 4 and the polymer was washed with 200 mL of diethyl ether, and then dried in a vacuum oven overnight. A yield of 96%, corresponding to the percentage of VBC units derived by the amine, was obtained.

#### ii. Characterization

The amphiphilic copolymer was analyzed by  $^1\text{H}$  NMR in  $\text{CDCl}_3$  (Figure 2.6).



**Figure 2.6.**  $^1\text{H}$  NMR spectrum of 75C12 in  $\text{CDCl}_3$ . For the indexation of protons, see Figure 2.5.

The spectrum confirms the full grafting of the amine onto the precursor. Indeed, the signal at 4.5 ppm that is characteristic of the  $-\text{CH}_2\text{-Cl}$  function has disappeared and replaced by a signal at 5 ppm corresponding to the quaternary ammonium. The molar mass of 75C12 can then be computed assuming that the molar mass distribution has not been modified during the grafting reaction and the purification step.

75C12 has molar masses:  $M_n=36$  kg/mol and  $M_w=58$  kg/mol.

### iii. 75C12 aqueous solutions

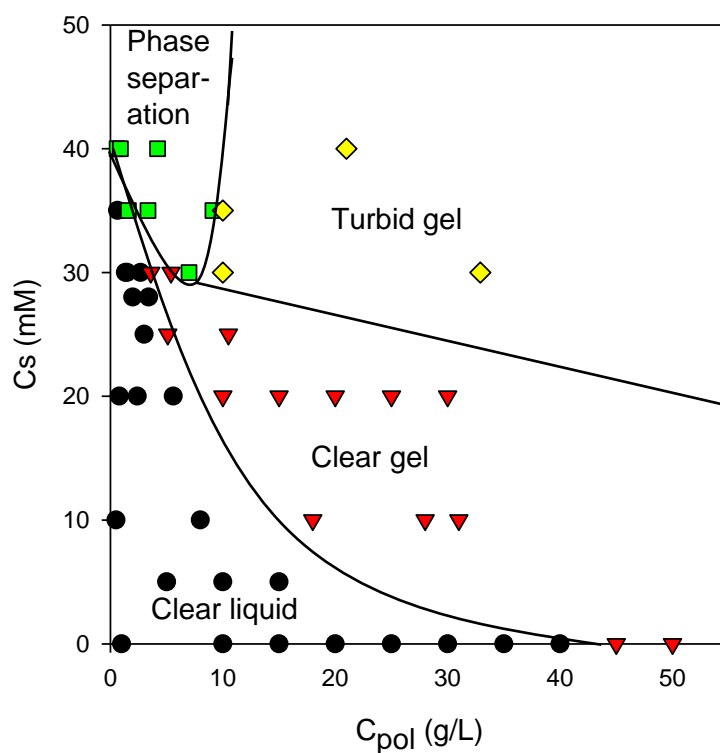
75C12 aqueous solutions are prepared with ultrapure water (Millipore) by heating them to  $80^\circ\text{C}$  in a water bath in order to rapidly reach a steady state especially when high polymer concentrations are targeted.<sup>1</sup> Solutions were also prepared in presence of salt by adding 0.1 M or 0.2 M NaCl.

75C12 solutions display four types of state as displayed in Figure 2.7: clear liquid, clear or turbid gel and two phases.



**Figure 2.7.** 75C12 aqueous solutions. From left to right: clear solution, clear gel, turbid gel and phase separation.

Therefore, a phase diagram can be established as displayed in Figure 2.8.



**Figure 2.8.** Phase diagram of 75C12 in water at 20°C.  $C_s$  is NaCl concentration.

In the absence of salt, hydrogels are obtained above  $C_{pol}=45$  g/L. In the presence of salt, this value is shifted towards lower polymer concentrations. However, adding too much salt induces phase separation or the formation of turbid, *i.e.* heterogeneous gels.

The phase diagram thus defined is very similar to that of the polymer 80C12 prepared by Fabien Dutertre.<sup>1</sup>

## 2) Preparation of C<sub>60</sub> aqueous colloidal suspensions

In this part, the preparation of stock solutions of C<sub>60</sub> in various organic solvents is explained, then the methods of dispersion by emulsification-evaporation and Ouzo effect are described. The freeze-drying-redispersion protocol is also detailed.

### a. Mother solutions in organic solvents

Stock solutions of C<sub>60</sub> in the various organic solvents were prepared by gravimetry. The solutions were systematically stirred magnetically at room temperature and protected from light for at least one night. It has been observed that milling the C<sub>60</sub> powder accelerates the solubilization, especially for solutions prepared at saturation concentration. The organic solvents used are listed in Table 2.1:

**Table 2.1.** Organic solvents used for emulsification-evaporation or Ouzo. <sup>a</sup>: T<sub>eb</sub> is the boiling point of the solvent.

Solvent	Solubility of C <sub>60</sub> (g/L)	Solubility of polymer	T <sub>eb</sub> <sup>a</sup> (°C)	Process
Chloroform	0.09	YES	61	Emulsification-evaporation
Toluene	2.6	NO	111	Emulsification-evaporation
Carbon disulfide	7.6	NO	46	Emulsification-evaporation
n-butylamine	5.0	NO	78	Ouzo

C<sub>60</sub> solubility values were determined by measuring the UV-visible absorbance spectrum of saturated solutions. They were filtered through 0.2 µm to remove non soluble fullerene. The mass absorption coefficient  $\epsilon$  (in L/g/cm) was calculated by making a calibration curve with unsaturated solutions at different concentrations and using the Beer-Lambert law as shown in Eq. 2.6:

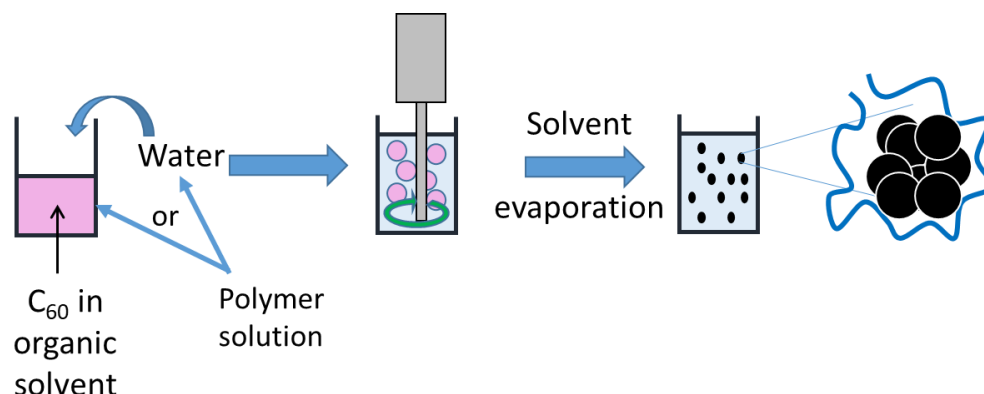
$$A = \epsilon \cdot l \cdot C \quad \text{Eq. 2.6}$$

with A the absorbance (dimensionless), l the optical path in cm and C the mass concentration in g/L.

The solubility values were obtained by measuring the absorbance of saturated solutions and using Eq. 2.6. They are in agreement with those reported by the literature.<sup>5, 6</sup>

### b. Dispersion of $C_{60}$ in water by emulsification-evaporation

A common method for preparing nanoparticles in water is to process oil-in-water emulsion. The oil phase consists of a solution of the hydrophobic component in a water-immiscible organic solvent. This solvent must subsequently be removed, generally by evaporation to obtain a colloidal suspension (Figure 2.9). The organic solvent, immiscible in water, is chosen according to criteria such as its volatility and its ability to dissolve  $C_{60}$  and possibly the polymer, as reported in table 2.1.



**Figure 2.9.** Emulsification-evaporation process applied to the dispersion of  $C_{60}$  in water in presence of an amphiphilic polymer.

The emulsions are formed by adding the solution of  $C_{60}$  in organic solvents (whose color ranges from pink to dark purple depending on the  $C_{60}$  concentration, see Figure 2.10a) to the aqueous phase. A total volume of 4 mL is prepared, with a volume fraction of the organic phase equal to 25%. An ultrasound horn tip is then immersed halfway up the aqueous phase: if the probe is too high the solution heats too little to induce the evaporation of the solvent, and if it is too low, only part of the mixture is emulsified. Ultrasounds are applied with a Vibra Cell 75115 (Bioblock Scientific, France) in a continuous mode at a frequency of 20 kHz and an amplitude of 36%, so as to have maximum dispersion energy without degrading the tip. An emulsion is instantly formed of milky appearance. Stirring is continued so as to allow the temperature of the sample to rise (75 °C reached in 5 min for a sample of 4 mL), until complete evaporation of the solvent, that is when the solution becomes clear and any organic phase is no more visible to the naked eye. Two additional minutes of stirring are systematically added for ensuring the full removal of any traces of solvents. The solutions obtained in this way have a light yellow to dark brown appearance depending on the particle concentration (Figures 2.10b and c) and are used as is.



**Figure 2.10.** a) 1 g/L  $C_{60}$  solution in toluene. b)  $C_{60}$  aqueous colloidal suspensions. From left to right, concentrations are 1 mg/L, 25 mg/L, 0.26 g/L, 1.6 g/L. c) Hydrogel with  $C_{pol}=50$  g/L and 0.8 g/L  $C_{60}$ .

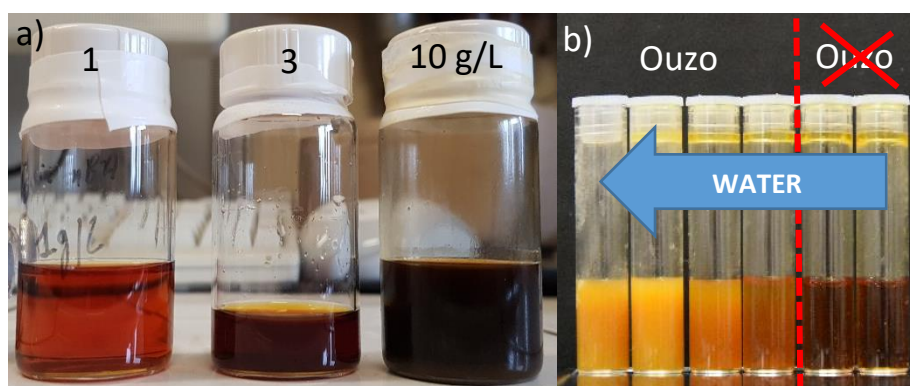
### c. Freeze-drying/re-dispersion

In order to increase the particles concentration of colloidal dispersions prepared by emulsification-evaporation, the dispersions were freeze dried as described below.

Colloidal suspensions of  $C_{60}$  in the presence of polymer were prepared as reported in part 2.b. Several batches prepared independently were then combined in a round-bottom flask that was freeze-dried using an Alpha 1-2 LD freeze-drier (Bioblock Scientific, France), at a pressure of 400 mbar and a temperature of  $-45^{\circ}\text{C}$ . The samples were brown and fluffy, the color corresponding to  $C_{60}$ . This solid is a mixture of 75C12 and  $C_{60}$  and is then re-dispersed in water.

### d. Ouzo effect

"Ouzo" nanoparticles were obtained by adding rapidly water to  $C_{60}$  solutions in n-butylamine under mild stirring. Ouzo effect is characterized by the appearance of turbidity for the solutions due to the size of the particle bigger than one hundred nanometers. The domain in which turbidity appears in the mixtures has therefore been defined as the Ouzo domain (Figure 2.11) and will be further discussed in chapter 6. After being obtained, the dispersions were dialyzed with a 1 kDa pore size against water during 24 hours in order to remove n-butylamine, the dialysis bath was renewed every hour for 3 hours. Since n-butylamine absorbs UV light, its full elimination was verified by achieving UV-visible measurements on the dialysis baths.



**Figure 2.11.** a) C<sub>60</sub> solutions in n-butylamine (from left to right, 1, 3 and 10 g/L). b) Ouzo samples with a mother solution of 2 g/L C<sub>60</sub> in n-butylamine and volume fractions of this solution equal to 50-52-60-64-66-70% from left to right. The borders of Ouzo domain are based on turbidity appearance as shown on the figure.

### 3) Chemical composition

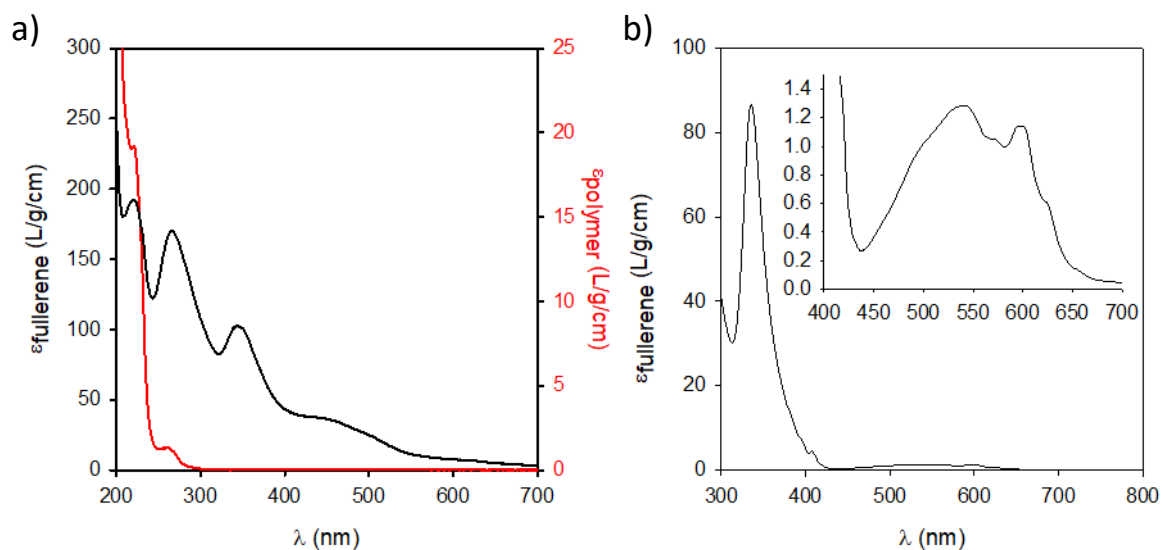
In this part, we will first discuss the methods for quantifying the amount of C<sub>60</sub> dispersed in water by UV-visible spectroscopy with the emulsification-evaporation method described in section 2.2.b. Then, the composition of the freeze-dried samples by thermogravimetric analysis will be discussed, and the analytical centrifugation technique will be presented.

#### a. UV-visible spectroscopy

Most of the samples being too concentrated for spectroscopy measurements, prior to the measurements, dilutions were systematically carried out down to 5 mg/L.

C<sub>60</sub> concentration was determined with a Cary 50 Bio spectrophotometer (Varian, UK) and a V-760 (Jasco, Japan) at 20°C. An example of the extinction coefficient  $\epsilon$  computed from the spectrum of a colloidal suspension of C<sub>60</sub> is shown in Figure 2.12a, from the Beer-Lambert law (Eq. 2.6). In order to verify the validity of  $\epsilon$ , extractions of C<sub>60</sub> with toluene were carried out according to the method described by Deguchi *et al.*<sup>7</sup> 1 mL of C<sub>60</sub> aqueous dispersion was mixed with 1 mL of 1M NaCl solution then 2 mL of toluene. Vortex-stirring (3000 rpm) was then applied until complete discoloration of the aqueous phase. For colloidal suspensions containing polymer, the absorbance of the polymer alone whose spectrum is given in Figure 2.12a has been subtracted from the raw spectrum.



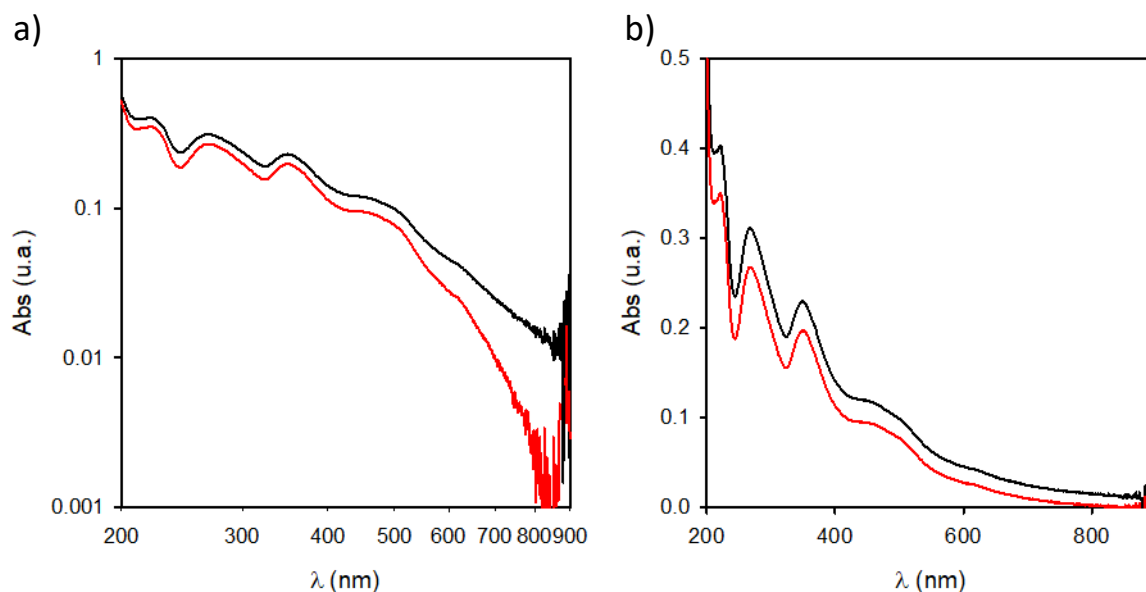


**Figure 2.12.** a) Extinction coefficients of  $C_{60}$  (black, calculated from an aqueous colloidal suspension prepared at  $C_{\text{pol}}=1$  g/L), and 75C12 (red) in water. b) Extinction coefficient of  $C_{60}$  in toluene. The insert is a magnification of the visible light region.

The spectrum of  $C_{60}$  in water (Figure 2.12a) shows broad absorption in the visible region as well as three maxima in the UV range, around 220, 260 and 340 nm, respectively.

In toluene, the absorption is much lower in the visible region, and a maximum is present at 336 nm, see Figure 2.12b. The spectrum as well as the extinction coefficient (87 L/g/cm at 336 nm) are identical to those described in the literature.<sup>8</sup> More details on UV-visible spectroscopy analysis of  $C_{60}$  aqueous suspensions will be given in chapter 3.

Some samples exhibited turbidity due to scattering by large particles. This turbidity was subtracted from the spectra by determining it at the highest wavelength. An example of spectra before and after subtraction of turbidity is shown in Figure 2.13.



**Figure 2.13.** Absorbance spectra before (black) and after (red) subtraction of the turbidity in log-log (left) or lin-lin scale (right).

### b. Thermogravimetric analysis (TGA)

Freeze dried samples prepared as described in section 2.2.c, were analyzed by TGA to determine their polymer/fullerene composition with a TGA 2 (Mettler Toledo, USA). The temperature ramps were carried out at 10°C/min from 20 to 1100°C under a flow of nitrogen at 80 mL/min on 10 mg of sample. The thermograms and their analysis will be described in Chapter 5.

### c. Analytical centrifugation

The LUMiSizer® (LUM GmbH, Germany) is a device that centrifuges samples while measuring their turbidity. This allows to quantitatively assess the stability of samples against accelerated gravity, and to speed up the destabilization process. Centrifugation can be carried out between 5g and 3600g, and turbidity is measured with an incident beam of either 470 or 865 nm wavelength. A profile is obtained for a given centrifugation time where the transmittance is displayed as function of the position in the tube, see Figure 2.14. At the start, the sample is homogeneously dispersed so the whole sample has a low transmittance. Upon centrifugation, a monodisperse dispersion (Figure 2.14a) presents a vertical front, which is the limit between a clear phase where there are no more particles and a turbid phase where particles are still dispersed. The vertical front displaces toward the top of the tube if particles cream and to the bottom if they sediment (e.g. particles sediment in Figure 2.14a). Complete destabilization leads to a clear sample all over the tube and the presence of a layer of particles at the top or the bottom of the sample. Plotting the position at which a given transmittance value is reached

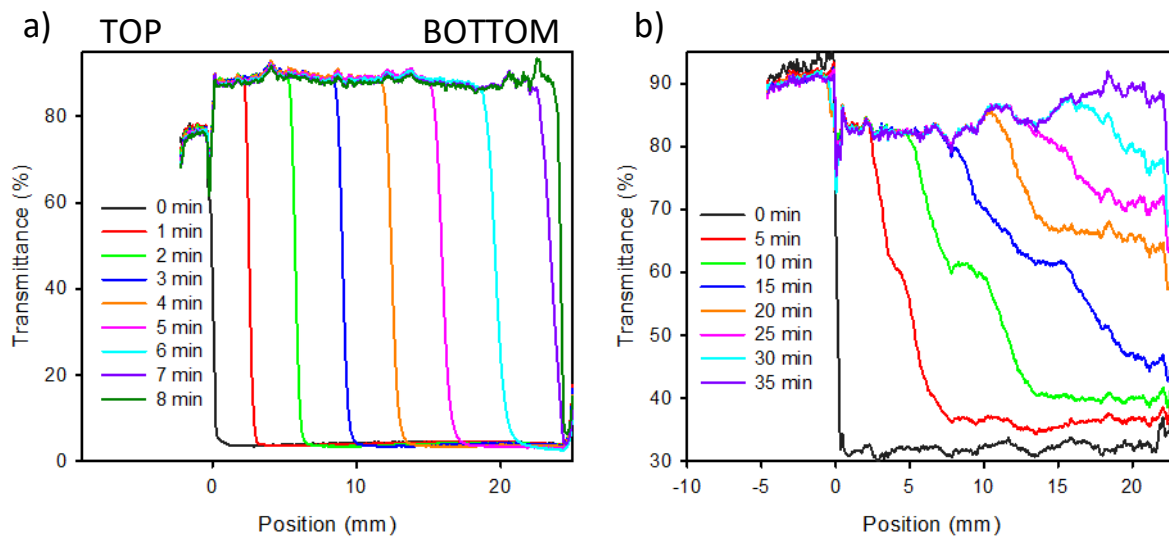
as function of time gives access to a speed that can then be linked to the particles size thanks to the Stokes law (Eq. 2.7):

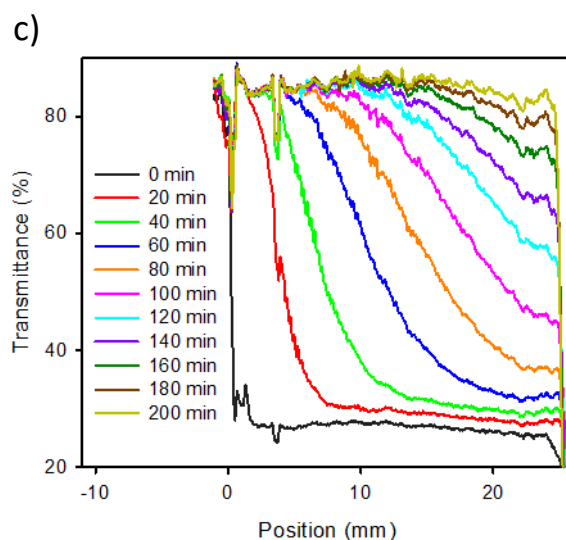
$$v = \frac{2r^2 g \Delta \rho}{9\mu} \quad \text{Eq. 2.7}$$

With  $r$  the radius of the particle (supposed spherical and homogeneous),  $g$  the gravity equal to  $9.81 \text{ m.s}^{-2}$ ,  $\Delta \rho$  the difference in density between the dispersed and continuous phases and  $\mu$  the dynamic viscosity of the continuous medium ( $1 \text{ mPa.s}$  for water).

For a bimodal dispersion, two fronts can be seen (Figure 2.14b). At low transmittance values, the bigger population can be followed while the smaller one can be followed at higher transmittance values. After some time (e.g. after 10min in Figure 2.14b), the two fronts are separated by a plateau of transmittance. At high centrifugation times (e.g. 20 min in Figure 2.14b), the first population is fully destabilized and a plateau transmittance is observed at the bottom of the tube. The size of two different populations of particles can be determined by using either transmittance at low (e.g. 50% in Figure 2.14b) or high values (e.g. 75% in Figure 2.14b) for the computation of sedimentation/creaming speed.

In the case of a polydisperse dispersion (Figure 2.14c), the profile is no more vertical but bent. Indeed, the bigger particles cream or sediment faster than the smaller ones. The sharpness of the slope therefore depends on the size dispersity. In this case, it is much harder to estimate an average size, since there is not one single speed, which will depend on the selected transmittance value. However, it is still possible to determine the stability of the sample. If destabilization only occurs by gravity effects, it is thus possible to estimate the time required at  $1g$  by using the equivalence of the product time  $\times$  gravity. For example, a sample stable for 6 minutes at  $100g$  will be stable for 600 minutes at  $1g$ .





**Figure 2.14.** Profiles at different times upon centrifugation for a) monodisperse particles, b) a bimodal sample and c) polydisperse particles. The top of the sample, *i.e.* the meniscus, is defined as the zero position, and the bottom corresponds to the brutal drop of transmittance in positive values of position. The data were furnished by the company LUM GmbH.

#### 4) Scattering techniques

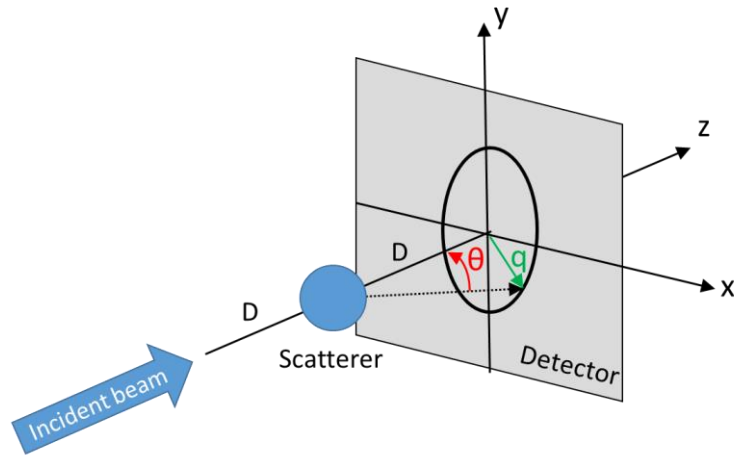
In this part, light (both static and dynamic) and X-ray scattering techniques (small and wide angles) will be presented. First, generalities will be given, then details on the theory, the equipment and data analysis of each technique will be reported.

##### a. Generalities on scattering techniques

Scattering is a phenomenon resulting from the interaction between light and matter that can be used to analyze soft matter.

This non-destructive technique allows to access to one or more characteristic lengths, such as the size of nanoparticles or the correlation length of a semi-dilute solution of polymers. It therefore complements microscopy techniques.

An experiment consists of measuring the intensity scattered by a sample when irradiated with an incident radiation of fixed wavelength and known intensity. The radiation can be visible light, X-rays or neutrons. Each radiation has its associated contrast. For light scattering, the contrast arises from the difference in refractive index between the solvent and the scatterer. In X-rays, it originates from the difference in electron density and in neutrons it originates from the difference in the diffusion length of the atoms constituting the different compounds. Detection of scattered intensity is performed on a defined scattering volume at different detection angles (Figure 2.15).



**Figure 2.15.** Simplified diagram of a scattering experiment.

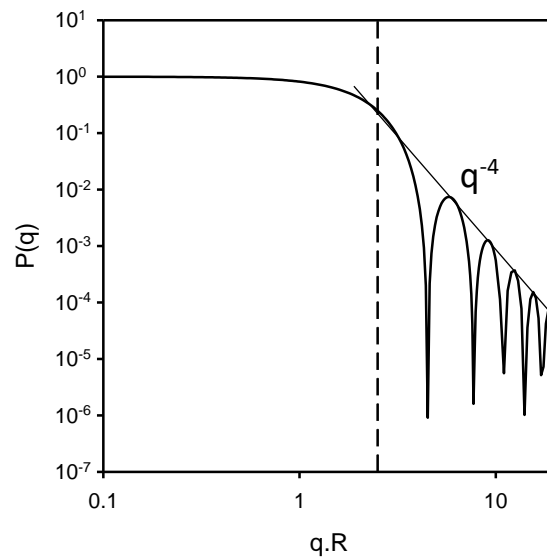
The scattered intensity  $I(q)$  depends on the wave vector  $q$ , itself related to the refractive index  $n$ , the wavelength  $\lambda$  and the detection angle  $\theta$  according to Eq. 2.8:

$$q = \frac{4n\pi}{\lambda} \sin\left(\frac{\theta}{2}\right) \quad \text{Eq. 2.8}$$

The equation shows that the wave vector is homogeneous to the inverse of a distance. It corresponds to the observation window, in the reciprocal space. This means that each detection angle corresponds to a different scale. So, if  $q^{-1}$  is smaller than the particle size, the object is observed as a whole, while if it is bigger, the internal structure is probed. The scattered intensity is the product of two contributions (Eq. 2.9):

$$I(q) = P(q) \times S(q) \quad \text{Eq. 2.9}$$

which are  $P(q)$  the form factor and  $S(q)$  the structure factor. Figure 2.16 shows the typical evolution of the form factor  $P(q)$  as a function of the wave vector  $q$  for a hard sphere.



**Figure 2.16.** Form factor of a hard sphere with a radius  $R$ .

The first part of the curve obtained at low  $q$  (left of the dashed line) is the Guinier regime. In this regime, the whole particle is observed and the form factor is approximated by Eq. 2.10:

$$\ln(P(q)) = 1 - \frac{q^2 R_g^2}{3} \quad \text{Eq. 2.10}$$

with  $R_g$  is the gyration radius of the particle.

At high  $q$ , (right of the dashed line) the Porod regime may be observed when there is a sharp interface between the scatterer and the solvent. It corresponds to oscillations of  $P(q)$  whose maxima form a power law in  $q^{-4}$ . The first minimum is found at  $qR=4.5$ , and the second at  $qR=7.7$ . When the particles are polydisperse, the dependence on  $q^{-4}$  is preserved but the oscillations vanish.

The structure factor  $S(q)$  depends on the organization of particles with respect to each other.  $S(q)$  is equal to 1 in diluted regime.

### b. Static Light Scattering (SLS)

The set-up used in this work is an ALV-5004 correlator in combination with an ALV-CGS3 goniometer. The light source is a He-Ne laser with a wavelength of 632.8 nm and the detection angles vary between 12 and 150°. Measurements were made at 20°C. Data collection is carried out with the ALV software.

In a static light scattering experiment (SLS) the scattered intensity is averaged over time and converted into a Rayleigh ratio  $R_\theta$  with Eq. 2.11 and 2.12:

$$R_s = \frac{I_s}{I_0} \quad \text{Eq. 2.11}$$

$$R_\theta = \frac{R_{\text{solution}} - R_{\text{solvent}}}{R_{\text{reference}}} \times R_{\theta, \text{reference}} \times \left( \frac{n_{\text{reference}}}{n_{\text{solvent}}} \right)^2 \quad \text{Eq. 2.12}$$

With  $I_s$  the scattered intensity for a sample  $s$ ,  $I_0$  the incident intensity,  $R_s$  the scattering ratio,  $R_{\theta, \text{reference}}$  the Rayleigh ratio of toluene which was used as reference (equal to  $1.35 \cdot 10^{-5} \text{ cm}^{-1}$ ) and  $n_s$  the refractive index. An optical constant  $K$  given by Eq. 2.13 is needed:

$$K = \frac{4\pi^2 n_{\text{reference}}^2 \left( \frac{\partial n}{\partial c} \right)^2}{\lambda^4 \mathcal{N}_A} \quad \text{Eq. 2.13}$$

With  $\mathcal{N}_A$  the Avogadro number.

From  $K$  and  $R_\theta$ , it is possible to determine the gyration radius  $R_g$ , the weight average molar mass  $M_w$  and the second virial coefficient  $A_2$  of the particle (Eq. 2.14):

$$\frac{KC}{R_\theta} = \left( \frac{1}{M_w} + 2A_2 C \right) \times \left( 1 + \frac{q^2 R_g^2}{3} \right) \quad \text{Eq. 2.14}$$

Light scattering provides access to  $R_g$  values comprised between 20 and 100 nm. Below the scattered intensity has no angular dependence, beyond it is not possible to measure a plateau intensity at low  $q$  values.

### c. Dynamic Light Scattering (DLS)

DLS is based on fluctuations of intensity over time which give access to intensity autocorrelation function  $g_2(t)$  as in Eq. 2.15:

$$g_2(t) = \langle I \rangle^2 + [g_1(t)]^2 \quad \text{Eq. 2.15}$$

With  $\langle I \rangle$  the average scattered intensity and  $g_1(t)$  the electric field autocorrelation function.  $g_1(t)$  is related to the cooperative diffusion coefficient of the particles  $D$  according to Eq. 2.16:

$$g_1(t) = \exp\left(-\frac{t}{\tau}\right) = \exp(-Dq^2 t) \quad \text{Eq. 2.16}$$

With  $\tau$  the particles relaxation time and  $D$  their cooperative diffusion coefficient. When more than one mode of relaxation is measured or for polydisperse samples, the CONTIN-REPES method allows the measurement of the relaxation time according to Eq. 2.17:<sup>9</sup>

$$g_1(t) = \int A(\tau) \exp\left(-\frac{t}{\tau}\right) = \int A(\tau) \exp(-Dq^2 t) \quad \text{Eq. 2.17}$$

The concentration once again has an influence on the measurements since the diffusion coefficient varies according to Eq. 2.18:

$$D = D_0(1 + k_D C) \quad \text{Eq. 2.18}$$



Where  $k_D$  is the dynamic second virial coefficient.

The diffusion coefficient thus determined gives access to the hydrodynamic radius  $R_h$  through the Stokes-Einstein relation given in Eq. 2.19:

$$D_0 = \frac{kT}{6\pi\eta R_h} \quad \text{Eq. 2.19}$$

With  $k$  the Boltzmann constant equal to  $1.38 \cdot 10^{-23}$  J/K,  $T$  the temperature in K and  $\eta$  the viscosity of the solvent in Pa.s.

Since the polymer has charged units, the so-called polyelectrolyte effect is observed on solutions of the polymer in water which results in the appearance of a very short time relaxation associated with the diffusion of the counterions. 5 mM NaCl is enough to screen the electrostatic interactions

#### d. Small-Angle X-Ray Scattering (SAXS)

The experiments were carried out on a Xeuss 2.0 HR Instrument (Xenocs, FR) at room temperature. The undiluted solutions were poured in a borosilicate glass capillary tube with 1.5 mm diameter. The instrument uses a microfocused Cu K $\alpha$  source with a wavelength of 1.54 Å and a PILATUS3 detector (Dectris, Switzerland). The distance between the source and the sample,  $D$ , is the same as the distance between the sample and the detector.  $D$  can be varied to obtain various  $q$  ranges as one can see from Figure 2.16. The experiments were performed at two different sample-to-detector distances, respectively 2480 mm with a collimated beam size of 0.5x0.5 mm and 540 mm with a collimated beam size of 0.8x0.8 mm to achieve a broad  $q$ -range of  $4.5 \cdot 10^{-7} \text{ m}^{-1} - 1.2 \cdot 10^{-10} \text{ m}^{-1}$ . A region of interest was selected where the intensity was the highest to minimize the noise. Image processing consisted in applying a “mask”, which is the signal of the beam without sample and that is subtracted to the signal to remove the contribution of defaults on the detector. Since the detector is planar, a 2D pattern was obtained. If the pattern is circular, then the particles are randomly oriented in the medium. If the pattern is not circular (butterfly shape, for example), it means that the objects are anisotropic and oriented in a direction. This means that depending on the direction chosen, 1D patterns (*i.e.* plots of  $I(q)$  against  $q$ ) are different.

Additionally, measurements are made for the dark, the beam (noted  $b$ ), an empty capillary ( $ec$ ), and water (the solvent). The intensity scattered ( $I_s$ ) by the sample is computed with Eq. 2.20:

$$I_s = \left[ \frac{(I_{tot} - I_{dark}) - (I_b - I_{dark})}{T_s} \right] - \left[ \frac{(I_{ec} - I_{dark}) - (I_b - I_{dark})}{T_{ec}} \right] \quad \text{Eq. 2.20}$$

With  $I_{tot}$  the total scattered intensity,  $T_s$  the transmittance of the sample and  $T_{ec}$  the transmittance of the empty capillary. A capillary tube filled with water was also measured. At

very large  $q$  values ( $q > 4 \cdot 10^{-9} \text{ m}^{-1}$ ), the scattering intensity was dominated by the water contribution. Therefore, only the data within the  $4.5 \cdot 10^7 \text{ m}^{-1} - 4 \cdot 10^{-9} \text{ m}^{-1}$  range are shown in this study.

As we discussed above in section 2.4.a, the contrast in SAXS arises from difference of electron density between the scatterer and water. Both of them having a scattering length density ( $\rho$ ) following Eq. 2.21:

$$\rho = \frac{N_A b_e}{\sum n_i M_i} \times \sum n_i Z_i \quad \text{Eq. 2.21}$$

With  $b_e$  the radius of an electron equal to  $2.85 \cdot 10^{-15} \text{ m}$ ,  $Z_i$  the atomic number of atom  $i$ ,  $n_i$  the number of atoms  $i$ ,  $M_i$  their molar mass and  $d$  the density of the compound ( $1.00 \text{ g/cm}^3$  for water and polymer and  $1.65 \text{ g/cm}^3$  for  $\text{C}_{60}$ ). The scattering length densities of  $\text{H}_2\text{O}$ , 75C12 and  $\text{C}_{60}$  are respectively  $9.5 \cdot 10^{10}$ ,  $9.8 \cdot 10^{10}$  and  $14.2 \cdot 10^{10} \text{ cm}^{-2}$ . They can then be converted into contrast factors  $K_N^2$  with Eq. 2.22:

$$K_N^2 = \left( \frac{\rho_{\text{sample}} - \rho_{\text{solvent}}}{d} \right) \cdot \frac{1}{N_A} \quad \text{Eq. 2.22}$$

With  $d$  the density of the solution, equal to  $1.00 \text{ g/cm}^3$  for dilute solutions. The scattered intensity can thus be converted into apparent molar mass  $M_{\text{app}}(q)$  with Eq. 2.23:

$$M_{\text{app}}(q) = \frac{I(q)}{K_N^2 C} \quad \text{Eq. 2.23}$$

With  $C$  the concentration of particles.

Accordingly, SAXS data can be compared to SLS data in order to obtain  $M_{\text{app}}$  over a large  $q$  range, between  $3 \cdot 10^6$  and  $3 \cdot 10^7 \text{ m}^{-1}$  for SLS and between  $5 \cdot 10^7$  and  $1 \cdot 10^{10} \text{ m}^{-1}$  for SAXS (chapter 4).

### e. Wide-Angle X-Ray Scattering/Diffraction (WAXS/WAXD)

WAXS or WAXD differ from SAXS in terms of the  $q$  range which is covered, typically between  $4 \cdot 10^9$  and  $4 \cdot 10^{10} \text{ m}^{-1}$  in this work. Measurements were conducted on a PANalytical-Empréan I X-Ray diffractometer. Freeze-dried samples were used to obtain enough contrast. The powder was introduced in a borosilicate glass capillary tube with  $1.5 \text{ mm}$  diameter. The incident beam had a wavelength of  $1.54 \text{ \AA}$  (Cu  $K\alpha$  source) and diffracted/scattered X-rays were collected in the range of  $5$  and  $60^\circ 2\theta$  using a step of  $0.0394^\circ$  (195 s per step). 6 scans of 20 min have been measured and merged to increase the statistic of the data. We used a focusing mirror in Bragg Bentano geometry in a transmission mode.

## 5) Microscopy

### a. Transmission electron microscopy

#### i. *Dried TEM*

Images were taken by Dr. Frédérick Niepceyron at IMMM with a JEM 2100 HR (Jeol, Japan). An electron gun equipped with a LaB<sub>6</sub> point fires a beam of electrons onto the sample, and a detector measures the amount of electrons passing through with a spatial response.

The samples are prepared as follows: a copper grid with a lacey carbon membrane is subjected to an air plasma treatment so as to be made more hydrophilic during the deposition of the sample. The latter is deposited with a micropipette (ca. 5  $\mu$ L) on the grid and then left to dry overnight.

#### ii. *Cryo-TEM*

Cryo-electron microscopy involves vitrifying the sample, that is, "freezing" an aqueous solution fast enough to prevent water from crystallizing.

The cryo-TEM pictures were taken by Dr. Marc Schmutz at Institut Charles Sadron (Strasbourg, France) on a Tecnai G2 sphaera (FEI) equipped with an Eagle 2K ssCCD camera (FEI). The samples were prepared as before, but instead of the drying step, they were blotted so that the solution is centered on the grid, which was then immersed in liquid ethane. A film of amorphous water was thus obtained with a thickness of ca. 200 nm. After quenching, the grid was stored in liquid nitrogen at the temperature of liquid nitrogen, *i.e.* -172°C. The grid was then placed on a Gatan 626 cryo-holder and transferred in the microscope, itself thermostated with liquid nitrogen.

### b. Confocal Laser Scanning Microscopy (CLSM)

Confocal Laser Scanning Microscopy pictures were taken with a Zeiss LSM 800 (Carl Zeiss Microscopy GmbH, Germany). One drop of a 1 g/L solution of Rhodamine B was added to the samples prior dispersion. After the latter step, one drop of emulsion was placed on a glass slide and sealed with a cover slip. We hypothesize that the chromophore preferentially labels the polymer because of the presence of rings around the droplets. Pictures of 512x512 pixels were taken with a water-immersion objective HC  $\times$  PL APO 63  $\times$  NA=1.2 and a magnification of 1. The incident laser beam had a wavelength of 548 nm and the fluorescent light was collected between 560 and 700 nm.

### c. Raman scattering and fluorescence

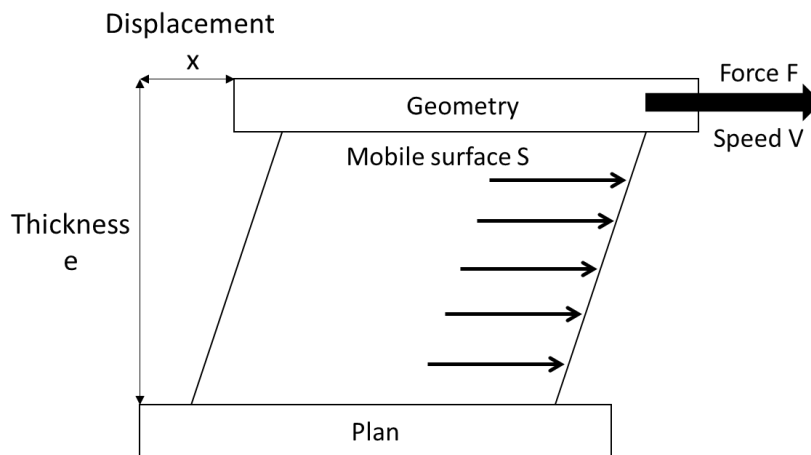
Both Raman scattering and fluorescence measurements were made by Dr. Frédéric Amiard at IMMM on an Apyron 300R Raman spectrometer (Witec, Germany) equipped with lasers of

wavelengths 532, 633 and 785 nm, a CCD detector (1650x200 px), a confocal microscope (Carl Zeiss Microscopy GmbH, Germany), a motorized table in x, y and z and a piezo-electric table with three networks (300, 600 and 1800 tr/min). Fluorescence measurements were made with the x100 objective and the 600 tr/min network. Raman scattering measurements were made with a x50 objective, the laser of 785 nm wavelength with 10 mW power and the x1800 tr/min network, with a spectral resolution of  $0.17 \text{ cm}^{-1}$ . 36 iterations were made for each spectrum.

## 6) Rheology

### a. Flow measurements

A typical rheology experiment involves placing the sample between a geometry and a plane and rotating the geometry to shear the sample and induce flow (Figure 2.17).



**Figure 2.17.** Schematic representation of a flow measurement in rheology.

The stress  $\sigma$  (Eq. 2.24), represents the distribution of the forces applied on the surface between the sample and the geometry. The strain  $\gamma$  (Eq. 2.25) is a ratio between displacement and sample thickness. The shear rate  $\dot{\gamma}$  (Eq. 2.26) is the derivative of the strain as a function of time.

$$\sigma(\text{Pa}) = \frac{F}{S} \quad \text{Eq. 2.24}$$

$$\gamma(\%) = \frac{x}{e} \times 100 \quad \text{Eq. 2.25}$$

$$\dot{\gamma}(\text{s}^{-1}) = \frac{\partial \gamma}{\partial t} = \frac{V}{e} \quad \text{Eq. 2.26}$$

The viscosity  $\eta$  (in Pa.s) of a solution or the modulus  $G$  (in Pa) of a solid can thus be determined for a solid using Eq. 2.27 and for a liquid using Eq. 2.28:

$$\sigma = \gamma G \quad \text{Eq. 2.27}$$

	$\sigma = \eta \dot{\gamma}$	Eq. 2.28
--	------------------------------	----------

For the flow viscosity, three regimes can be expected:

- Newtonian behavior :  $\eta$  is constant whatever  $\dot{\gamma}$ . In other words, the stress evolves linearly according to the latter.
- Shear-thinning :  $\eta$  decreases when  $\dot{\gamma}$  is increased.
- Shear-thickening :  $\eta$  increases when  $\dot{\gamma}$  is increased.

### b. Dynamic rheology

Dynamic rheology measurements consist in applying periodic stress to the sample. We will thus define the deformation  $\gamma(t)$  and stress  $\sigma(t)$  according to Eq. 2.29 and 2.30:

$$\gamma(t) = \gamma_0 \sin(\omega t) \quad \text{Eq. 2.29}$$

$$\sigma(t) = \sigma_0 \sin(\omega t + \delta) = \sigma_0 \sin(\omega t) \cos(\delta) + \sigma_0 \cos(\omega t) \sin(\delta) \quad \text{Eq. 2.30}$$

where  $\omega$  is the angular frequency in rad/s and  $\delta$  is the phase displacement between stress and strain. The stress can thus be divided into two terms. The term in  $\cos(\delta)$  is related to the elastic character of the material and the term in  $\sin(\delta)$  to its viscous character. Two extreme values of  $\delta$  can then simplify the equation:  $\pi/2$  for a purely viscous behavior (liquid) and 0 rad for a purely elastic behavior (solid). We can thus define two characteristics of the material:  $G'$  the storage modulus for the elastic part and  $G''$  the loss modulus for the viscous part, according to Eq. 2.31 to 33:

$$G' = \frac{\sigma_0}{\gamma_0} \cos(\delta) \quad \text{Eq. 2.31}$$

$$G'' = \frac{\sigma_0}{\gamma_0} \sin(\delta) \quad \text{Eq. 2.32}$$

$$\tan(\delta) = \frac{G''}{G'} \quad \text{Eq. 2.33}$$

Complex viscosity  $\eta^*$  can therefore be defined with Eq. 2.33:

$$|\eta^*| = \frac{1}{\omega} \sqrt{G'^2 + G''^2} \quad \text{Eq. 2.34}$$

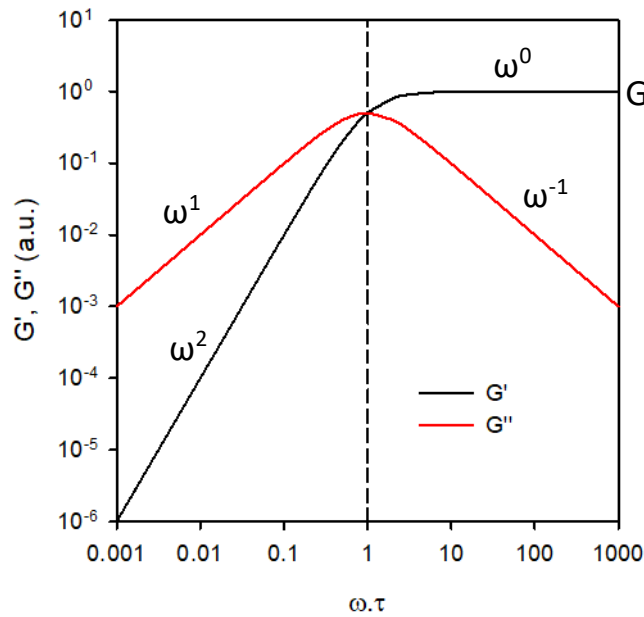
Care must be taken to perform the experiments in the linear domain, that is to say the interval of strain or stress over which the values of  $G'$  and  $G''$  are constant.

For a viscoelastic liquid with a single relaxation time, the viscoelastic moduli can be simply described by the Maxwell model given by Eq. 2.35 and 36. It reads that  $G'$  and  $G''$  depend on the applied frequency.

$$G' = G \frac{\omega^2 \tau^2}{1 + \omega^2 \tau^2} \quad \text{Eq. 2.35}$$

$$G'' = G \frac{\omega \tau}{1 + \omega^2 \tau^2} \quad \text{Eq. 2.36}$$

with  $\tau$  the relaxation time. The frequency dependence of the behavior of viscoelastic liquids can therefore be represented as in Figure 2.18:



**Figure 2.18.** Evolution of  $G'$  and  $G''$  over angular frequency according to the Maxwell model.

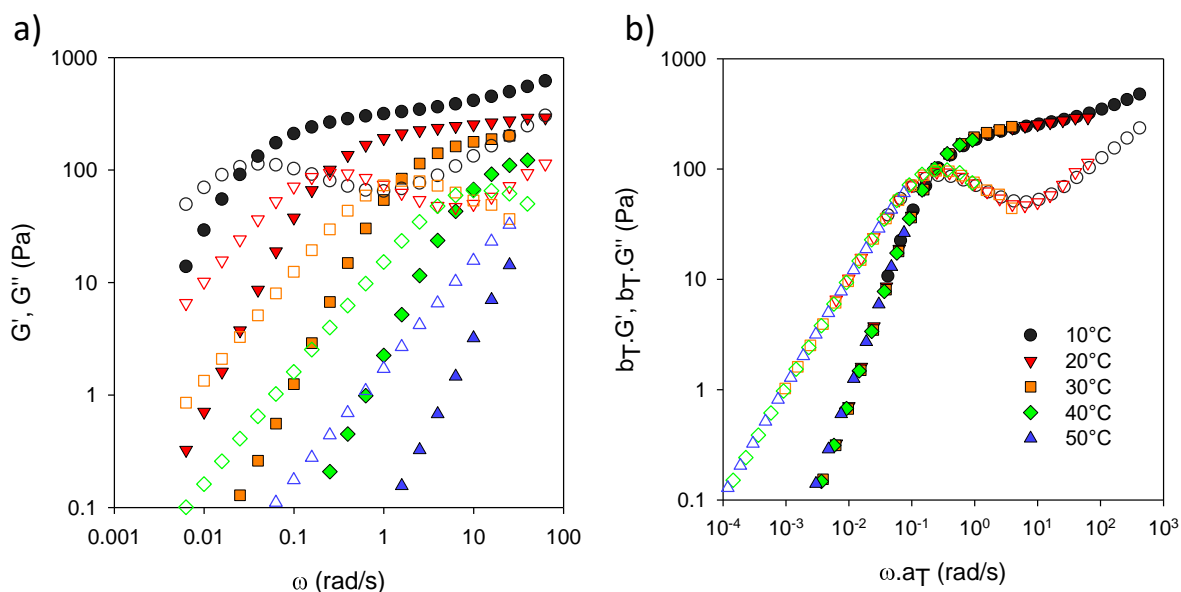
We can observe that  $G' = G''$  when  $\omega\tau = 1$ . When  $\omega\tau < 1$ , the material flows like a liquid because  $G' < G''$  and when  $\omega\tau > 1$ , the material behaves like a solid because  $G' > G''$ . In addition, at high frequencies a plateau of  $G'$  is reached. This value of  $G'$  is noted  $G$ , the elastic modulus.

### c. Rheological study of 75C12 in water

Measurements were carried out on a Discovery HR-3 rheometer (TA Instruments, USA). Three cone-plate geometries of different characteristics were used depending on the viscosity of the samples: i) 20 mm diameter, 28  $\mu\text{m}$  truncature,  $1^\circ 0' 2''$  angle, ii) 40 mm diameter, 59  $\mu\text{m}$  truncature,  $2^\circ 0' 47''$  angle, iii) 60 mm diameter, 27  $\mu\text{m}$  truncature,  $0^\circ 59' 49''$  angle. The size to pick depends on the precision needed.

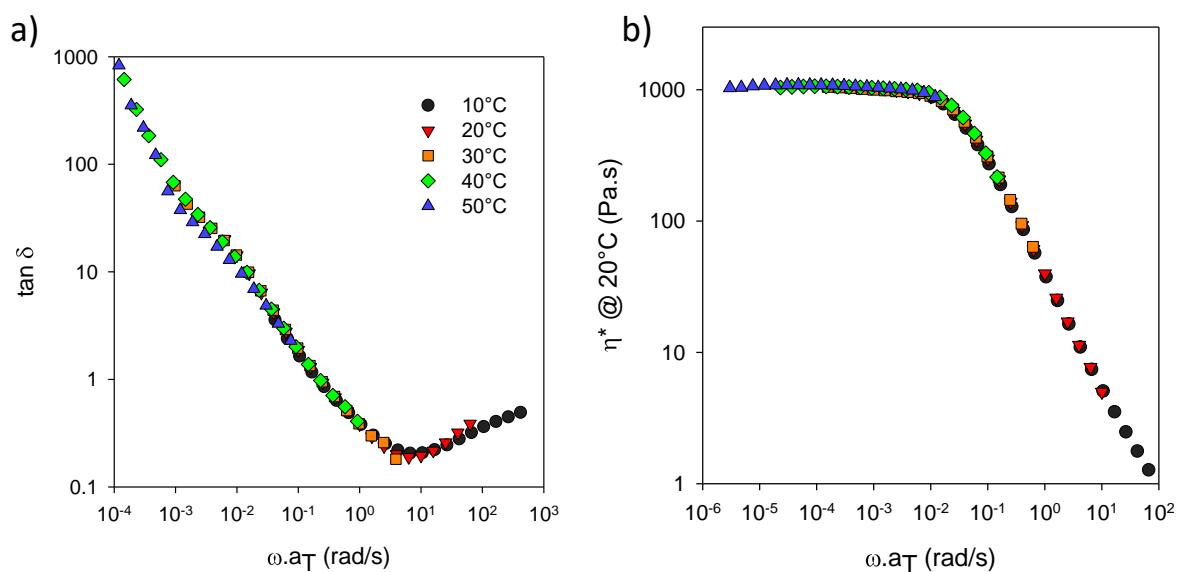
The rheological properties of polymers with a structure close to that of 75C12 were studied by Fabien Dutertre during his PhD. Here, a 50 g/L hydrogel chosen as a reference was studied. In Figure 2.19a, frequency sweeps at different temperatures are shown (a paraffin oil trap was used for measurements at high temperature to avoid water evaporation). A master curve can

be obtained by multiplying the frequency by a factor  $a_T$  and the modulus by a factor  $b_T$  (see Figure 2.19b).



**Figure 2.19.** a) Frequency sweeps at various temperatures indicated in the figure and  $\gamma=10\%$  for a hydrogel with  $C_{pol}=50$  g/L. b) Master curve with  $T_{ref}=20^\circ\text{C}$ .

The  $a_T$  factors follow an Arrhenius law, and an activation energy of 140 kJ/mol has been calculated. The  $b_T$  factors are used to correct the moduli to take thermal expansion into account. The elastic modulus of this hydrogel was 250 Pa at 20°C. The parameters  $\tan \delta$  and  $\eta^*$  are then shown after shifting in Figure 2.20.



**Figure 2.20.** Master curves of a)  $\tan \delta$  and b)  $\eta^*$  with  $T_{ref}=20^\circ\text{C}$  from data of Figure 2.19.

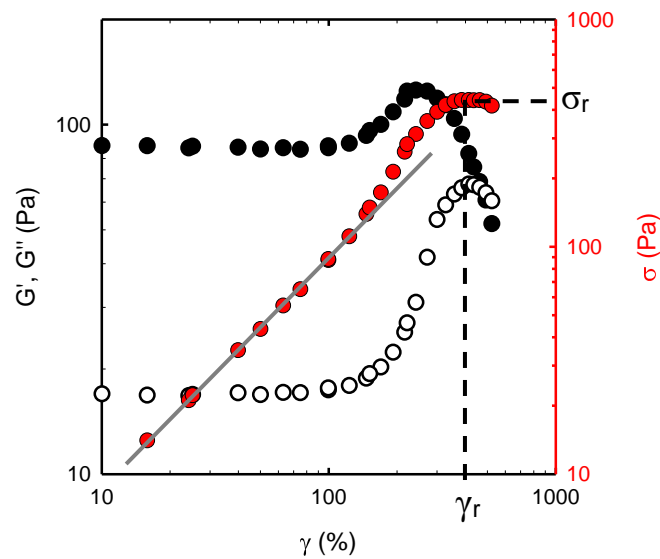


The complex viscosity of the hydrogel was 1000 Pa.s at 20°C. By analogy with flow measurements, Newtonian and then shear-thinning behaviors are observed with increasing oscillation frequency.

The non-linear behavior of these samples was also investigated. Increasing strain was applied at a fixed frequency of 10 rad/s until breakage of the hydrogel, see Figure 2.22. Typically, a linear regime is first observed: the moduli  $G'$  and  $G''$  are constant with strain, and stress evolves linearly with it (see gray line on Figure 2.22). Then, a slight shear-thickening typical for worm-like micelles<sup>10</sup> is observed most of the time before the rupture of the gel characterized by a sharp drop in  $G'$  and  $G''$ . In the present work, the rupture stress and strain, respectively noted  $\sigma_r$  and  $\gamma_r$ , were defined by the maximum value of  $\sigma$ .

Please note that since the rupture occurs in the non-linear domain, we don't use  $G'$  or  $G''$  values because Eq. 2.30 and 2.31 are not valid anymore.

Self-healing after rupture can be measured by measuring again the material in its linear domain and looking at its response over time. For 75C12-based hydrogels, the self-healing was very fast typically less than 1 minute.



**Figure 2.22.** Evolution of  $G'$ ,  $G''$  and  $\sigma$  with increasing strain for a hydrogel with  $C_{pol}=48$  g/L at  $\omega=10$  rad/s. The rupture is indicated by the dashed lines. The gray line is a guide to the eye.

## References

1. Dutertre, F.; Gaillard, C. d.; Chassenieux, C.; Nicolai, T., Branched Wormlike Micelles Formed by Self-Assembled Comblike Amphiphilic Copolyelectrolytes. *Macromolecules* **2015**, *48* (20), 7604-7612.
2. Limouzin-Morel, C.; Dutertre, F.; Moussa, W.; Gaillard, C.; Iliopoulos, I.; Bendejacq, D.; Nicolai, T.; Chassenieux, C., One and two dimensional self-assembly of comb-like amphiphilic copolyelectrolytes in aqueous solution. *Soft Matter* **2013**, *9* (37), 8931-8937.
3. Moussa, W. Etude multi-échelle de la structuration de copolymères cationiques en peigne. 2010.
4. Dutertre, F. Structures et propriétés rhéologiques d'auto-assemblages de copolymères amphiphiles cationiques en peigne. 2014.
5. Semenov, K. N.; Charykov, N. A.; Keskinov, V. A.; Piartman, A. K.; Blokhin, A. A.; Kopyrin, A. A., Solubility of Light Fullerenes in Organic Solvents. *Journal of Chemical & Engineering Data* **2010**, *55* (1), 13-36.
6. McHedlov-Petrosyan, N. O., Fullerenes in Liquid Media: An Unsettling Intrusion into the Solution Chemistry. *Chemical Reviews* **2013**, *113* (7), 5149-5193.
7. Deguchi, S.; Alargova, R. G.; Tsujii, K., Stable Dispersions of Fullerenes, C60 and C70, in Water. Preparation and Characterization. *Langmuir* **2001**, *17* (19), 6013-6017.
8. Kyzyma, O. A.; Kyrey, T. D.; Avdeev, M. V.; Korobov, M. V.; Bulavin, L. A.; Aksenov, V. L., Non-reversible solvatochromism in N-methyl-2-pyrrolidone/toluene mixed solutions of fullerene C60. *Chemical Physics Letters* **2013**, *556*, 178-181.
9. Jakeš, J., Regularized Positive Exponential Sum (REPES) Program - A Way of Inverting Laplace Transform Data Obtained by Dynamic Light Scattering. *Collection of Czechoslovak Chemical Communications* **1995**, *60* (11), 1781-1797.
10. Dutertre, F.; Benyahia, L.; Chassenieux, C.; Nicolai, T., Dynamic Mechanical Properties of Networks of Wormlike Micelles Formed by Self-Assembled Comblike Amphiphilic Copolyelectrolytes. *Macromolecules* **2016**, *49* (18), 7045-7053.



## Chapter 3. Self-Assembly in water of C<sub>60</sub> fullerene into isotropic nanoparticles or nanoplatelets mediated by a cationic amphiphilic polymer

1) Preparation of aqueous C <sub>60</sub> colloidal suspensions.....	115
a. Emulsification-evaporation process.....	115
b. UV-visible light absorption of C <sub>60</sub> dispersed in water .....	120
c. Concentration of C <sub>60</sub> in water .....	123
d. Stability of the particles dispersions .....	125
2) Characterization of the particles .....	128
a. Size and molar mass of the C <sub>60</sub> particles .....	128
b. Morphology of the C <sub>60</sub> particles .....	133
3) Discussion .....	137
a. Mechanism of C <sub>60</sub> particles formation.....	137
b. Morphology and size of the C <sub>60</sub> particles.....	139
Conclusion .....	141
References .....	142



## Chapter 3. Self-Assembly in water of C<sub>60</sub> fullerene into isotropic nanoparticles or nanoplatelets mediated by a cationic amphiphilic polymer

In this chapter, the elaboration of C<sub>60</sub> aqueous colloidal suspensions by an emulsification-evaporation process is presented. The particles are prepared in the presence of a cationic amphiphilic copolymer, 75C12, introduced in section 1.5.d and whose synthesis and characterization are described in section 2.1. First, we have studied the process of emulsification by macroscopic and confocal microscopy observations. Then after evaporation of the solvent, we have obtained dispersions of nanoparticles whose concentration was determined by UV-visible spectroscopy, their size and morphology being studied by light scattering and cryo-transmission electron microscopy (cryo-TEM). The process parameters (type of solvent, concentration of fullerene and of polymer) have been varied in a great extent and their influence on the dispersion yield and aggregation state of C<sub>60</sub> in water are discussed, as well as the stability of the particles upon ageing.

### 1) Preparation of aqueous C<sub>60</sub> colloidal suspensions

#### a. Emulsification-evaporation process

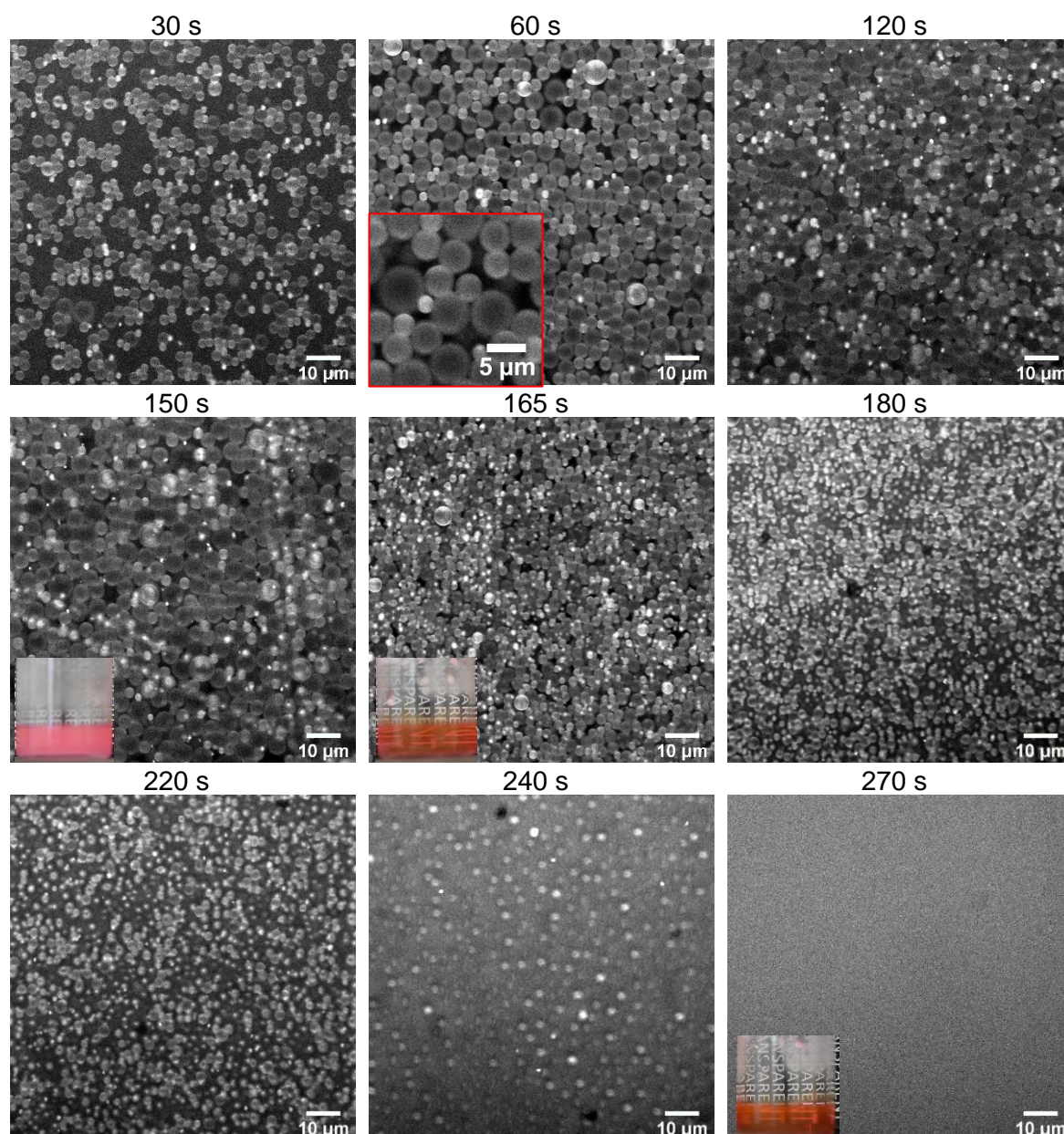
Dispersions of C<sub>60</sub> in water were prepared by modifying the emulsification-evaporation method reported for toluene/water by Andrievsky et al.<sup>1</sup> Chloroform (CHCl<sub>3</sub>) and carbon disulfide (CS<sub>2</sub>) were used instead of toluene for solubilizing C<sub>60</sub>. These solvents allow to cover a large range of solubility for C<sub>60</sub> (the limit solubility for C<sub>60</sub> being 90 mg/L, 2.8 g/L and 7.6 g/L respectively for chloroform, toluene and carbon disulfide) and display lower boiling points than toluene. The C<sub>60</sub> concentration in chloroform was set at 90 mg/L, whereas three concentrations were tested in CS<sub>2</sub> (90 mg/L, 1 g/L, 7.6 g/L). 75C12 is soluble in chloroform but not in CS<sub>2</sub> nor in toluene. For the former solvent we then tested the effect of adding 75C12 dissolved initially in the aqueous phase or in the organic phase. For the other solvents the cationic amphiphilic polymer 75C12 was added to the aqueous phase at concentrations between 1.10<sup>-3</sup> and 35 g/L. The different conditions tested here are summarized in Table 3.1. The volume fraction of the organic phase ( $\Phi_{org}$ ) was 25% when not specified, but for two methods it was varied between 10 and 75%.

**Table 3.1.** Summary of the various conditions used to disperse C<sub>60</sub> in water. <sup>a</sup>: Final concentration in water after evaporation of the organic solvent. <sup>b</sup>: saturation concentration for C<sub>60</sub> fullerene in the organic phase.

Method	Organic solvent	Polymer concentration <sup>a</sup> (g/L) / solvent	C <sub>60</sub> concentration in organic phase	Volumic fraction of organic phase
M1	Chloroform	1.10 <sup>-3</sup> to 35 / CHCl <sub>3</sub>	90 mg/L <sup>b</sup>	25%
M2		35.10 <sup>-3</sup> to 35 / H <sub>2</sub> O		
M3	Carbon disulfide	35.10 <sup>-3</sup> to 35 / H <sub>2</sub> O	90 mg/L	
M4		0.35 to 35 / H <sub>2</sub> O	1 g/L	
M5		1 to 35 / H <sub>2</sub> O	7.6 g/L <sup>b</sup>	10 to 75%
M6		35 / H <sub>2</sub> O		
M7		10 / H <sub>2</sub> O		

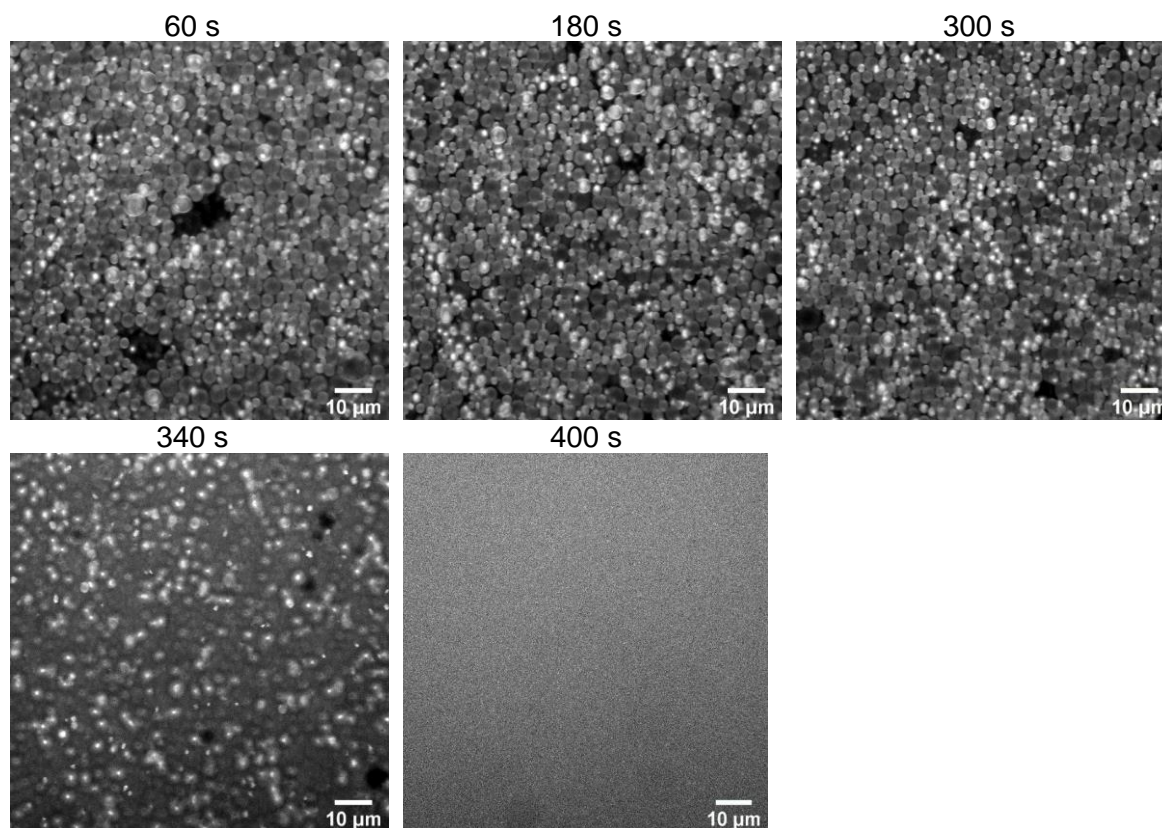
The organic and aqueous phases were mixed and emulsified with an ultrasound horn tip, as described in Chapter 2, section 2. In all cases the emulsions consisted of droplets of the organic phase embedding C<sub>60</sub> dispersed in a continuous aqueous phase. Sonication led to an increase of the temperature to about 80°C within 5 minutes and consequently to evaporation of the organic solvent. It was found that with increasing sonication time the droplet size decreased until complete evaporation of the organic solvent, which could take up to 6 min for CS<sub>2</sub> and 10 min for CHCl<sub>3</sub> (with Φ<sub>org</sub>=25%). The morphology of the emulsions was inspected using confocal laser scanning microscopy (CLSM) using Rhodamine B as a chromophore (pink color). Examples for different CS<sub>2</sub>-in-water systems are shown in Figures 3.1 to 3.5. Variations of fluorescence indicate that the partitioning of chromophore follows the order: interface>CS<sub>2</sub>>water. We attribute the rings around the droplets (e.g. insert for 60s of sonication on Figure 3.1) to selective binding of Rhodamine B to 75C12, probably because of hydrophobic interactions or π-stacking. We cannot conclude on the presence or absence of any polymer in CS<sub>2</sub>, because Rhodamine itself partitions favorably in this phase even without polymer. Figure 3.1 displays confocal images for an emulsion with C<sub>pol</sub>=1 g/L and Φ<sub>org</sub> =10%. At short sonication times droplets always have the same size (between 1 and 10 μm) but an increasing number of droplets is formed. Full emulsification is achieved after 2 min sonication. The emulsion appears milky during this time. After 165s of sonication, the emulsion appears less turbid and the droplets are smaller. Pursuing sonication leads to a continuous decrease of the size, until no more droplets can be observed. Macroscopically, the solution becomes transparent since the organic solvent has been evaporated.





**Figure 3.1.** Confocal images of  $CS_2$ -in-water emulsions with  $C_{pol}=1$  g/L and  $\Phi_{org}=10\%$  at various sonications times indicated above the pictures. Macroscopic pictures of the emulsions are shown as insert. A magnification is shown for 60s in insert.

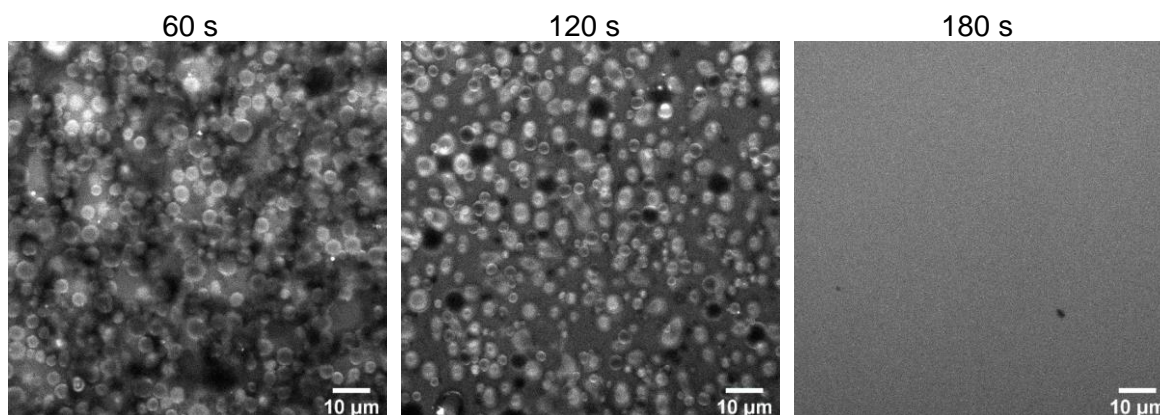
Similar observations are made with various  $\Phi_{org}$  however when increasing  $\Phi_{org}$  the time scale is shifted towards higher value because there is more solvent to emulsify and evaporate (Figure 3.2).



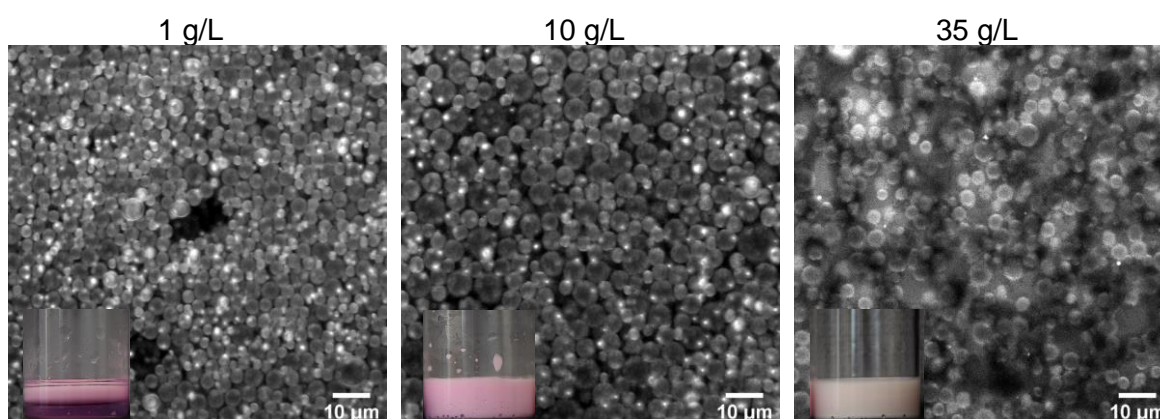
**Figure 3.2.** Confocal images of  $CS_2$ -in-water emulsions with  $C_{pol}=1$  g/L and  $\Phi_{org}=25\%$  at different sonications times indicated above the pictures.

Increasing  $C_{pol}$  has no influence on the size of the droplets, however we noted that all of the organic phase ( $\Phi_{org}=10\%$ ) was emulsified within 1 min of sonication for  $C_{pol}=10$  and 35 g/L. Additionally, the time needed to fully evaporate  $CS_2$  is lower when  $C_{pol}$  is increased (Figures 3.3 and 3.4). The emulsions with  $C_{pol}=35$  g/L are more turbid (which causes the appearance of dark domains in the picture taken after 60s of sonication, see Figure 3.3). At the macroscopic scale, the pink color is attenuated, see Figure 3.4. When more polymer is present, the rings around the droplets are more intense (Figure 3.4).



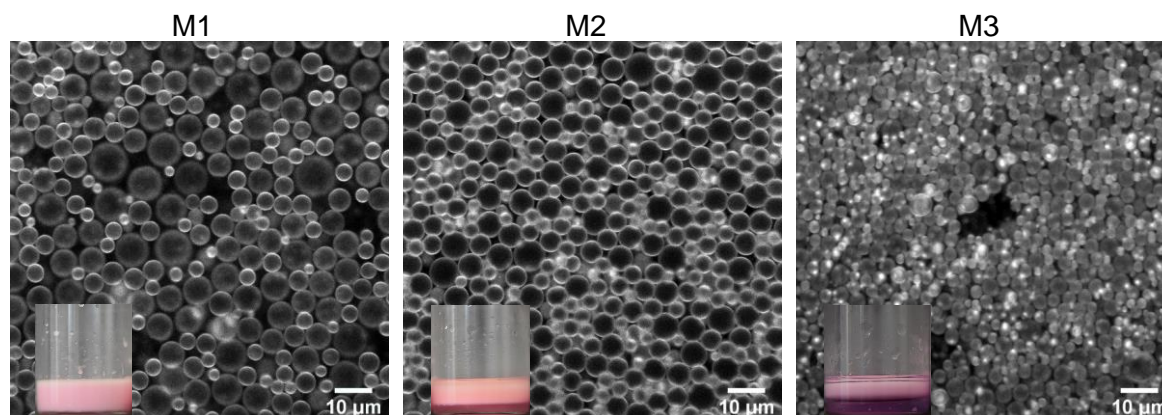


**Figure 3.3.** Confocal images of  $CS_2$ -in-water emulsions with  $C_{pol}=35$  g/L and  $\Phi_{org}=10\%$  at different sonications times indicated above the pictures.



**Figure 3.4.** Confocal images of  $CS_2$ -in-water emulsions with various  $C_{pol}$  given in the figure and  $\Phi_{org}=10\%$  after 1 minute of continuous sonication. Macroscopic pictures of the emulsions are given as inserts.

When chloroform was used instead of carbon disulfide, the Rhodamine was mainly located at the interface as the rings around the droplets are more intense, and both phases are dark (Figure 3.5). With method M1, where polymer is originally dissolved in chloroform, the excess Rhodamine was mainly partitioned in chloroform, which can be attributed again to its specific binding to 75C12. When polymer was dissolved in water, the inside of droplets was much less intense, which indicates that polymer probably does not migrate in organic phase.



**Figure 3.5.** Confocal images of M1-2-3 emulsions with  $C_{\text{pol}}=1$  g/L and  $\Phi_{\text{org}}=10\%$  after 1 minute of continuous sonication. Macroscopic pictures of the emulsions are in given as inserts.

The color of the final aqueous dispersions ranged from faintly yellow to dark brown, depending on the concentration of dispersed fullerene, see Figure 3.6. Please note that it was not possible to disperse C<sub>60</sub> in water in the absence of polymer with chloroform or carbon disulfide. However, it was possible to achieve it using toluene as previously described by Andrievsky *et al.*<sup>1</sup>

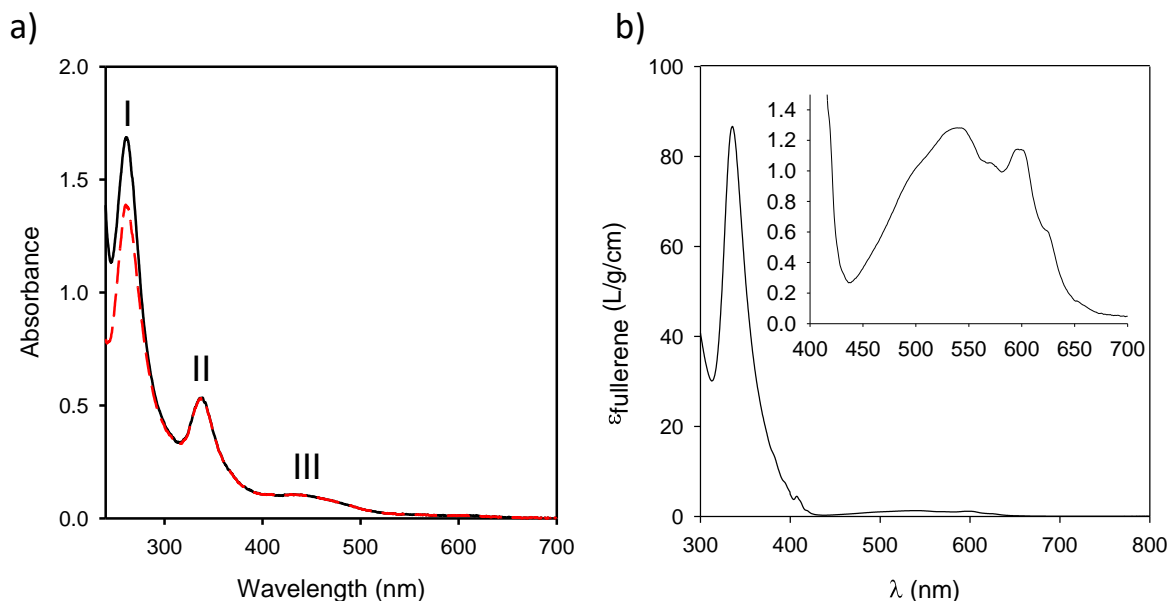


**Figure 3.6.** From left to right, colloidal suspensions with fullerene concentrations equal to 1 mg/L (without polymer), 25 mg/L (M2,  $C_{\text{pol}}=0.35$  g/L), 0.26 g/L (M4,  $C_{\text{pol}}=20$  g/L) and 1.6 g/L (M5,  $C_{\text{pol}}=10$  g/L).

### b. UV-visible light absorption of C<sub>60</sub> dispersed in water

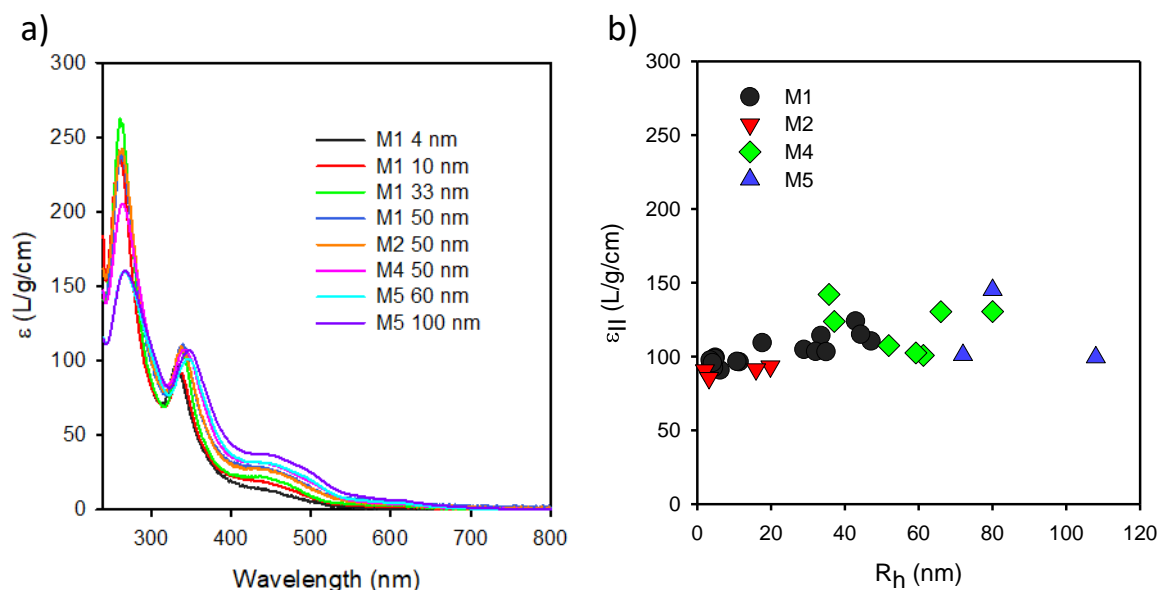
Figure 3.7a displays a typical UV-visible absorption spectrum for an aqueous dispersion of C<sub>60</sub>. In the UV region, maxima were observed at 260 nm (I) and 340 nm (II) and a broad band with low amplitude was also observed close to 440 nm (III). It should be mentioned that an absorption band was observed at 220 nm but since the polymer absorbs strongly at this wavelength, we will not consider it in the following. For the other wavelengths, the absorbance spectra have been corrected from the contribution of the polymer in order to recover the sole fullerene absorption spectrum, see Figure 3.7a. The absorption spectrum of C<sub>60</sub> dissolved in toluene is shown in Figure 3.7b and displays a single absorption peak at 336 nm. The

absorption in the visible range is much lower and it was not possible to measure absorbance below 300 nm as toluene also absorbed.



**Figure 3.7.** a) Absorption spectrum of an aqueous C<sub>60</sub> dispersion obtained from M1 with 1 g/L 75C12 before (black solid line) and after subtraction of the contribution of 75C12 (red dashed line). b) Absorption coefficient of C<sub>60</sub> in toluene. Insert is a magnification of visible light region.

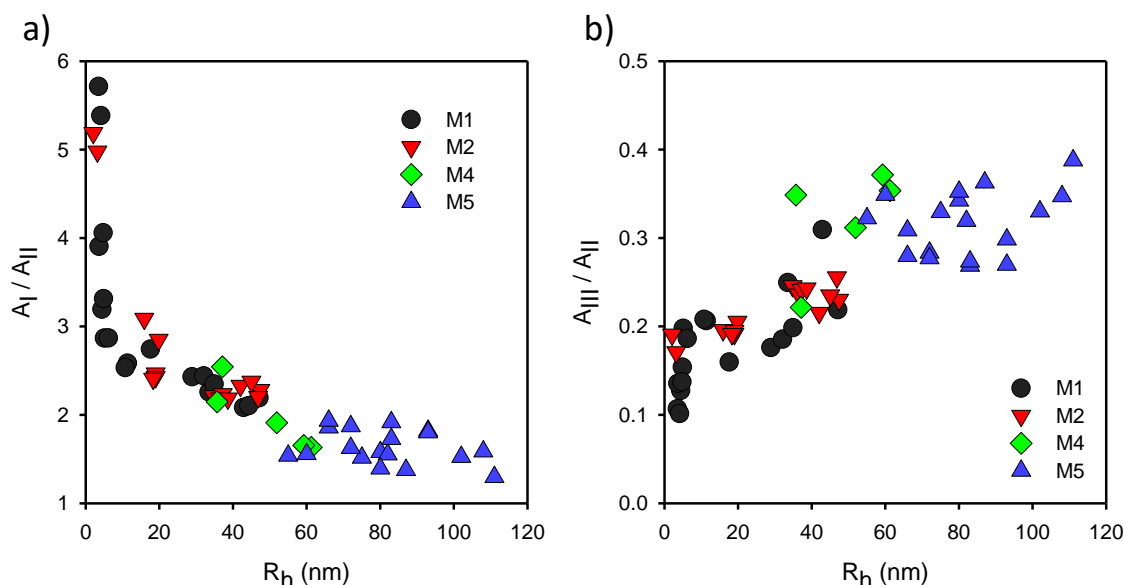
The absorption band II is used in the literature to quantify the concentration of C<sub>60</sub> dispersed in water. However, the reported values of the extinction coefficient vary a lot between different authors (Andrievsky=94.4,<sup>2</sup> Deguchi=71.2,<sup>3</sup> Scharff=5.62,<sup>4</sup> Chen=26.3<sup>5</sup> L/g/cm). Here we determined the C<sub>60</sub> concentration for a range of aqueous C<sub>60</sub> dispersions by extraction into toluene<sup>3</sup> and measuring the absorbance at 336 nm using the experimentally determined extinction coefficient  $\epsilon_{\text{tol}}=87$  L/g/cm. Knowing the C<sub>60</sub> concentration in water, the absorption spectra of the various aqueous dispersions could be expressed in terms of extinction coefficient,  $\epsilon$ , see Figure 3.8a. It was found that differences between the absorption spectra were not correlated to the way in which the suspensions were produced, but only to the size of the C<sub>60</sub> aggregates. As it will be discussed later, the average hydro-dynamic radius ( $R_h$ ) of the fullerene nanoparticles varied between 2 and 110 nm. Upon increasing this size, the absorption bands underwent a small hypsochromic shift (from 262 to 268 nm for band I and from 338 to 348 nm for band II). More important was the decrease of the amplitude of peak I and the increase of the amplitude of peak III with increasing size. The extinction coefficient of peak II varied little with the size, see Figure 3.8b.



**Figure 3.8.** a) Absorption spectra expressed in terms of the extinction coefficient for aqueous suspensions of C<sub>60</sub> aggregates with various hydrodynamic radii and prepared with different methods as indicated in figure. b) Extinction coefficient of C<sub>60</sub> in water for band II as a function of  $R_h$ .

Therefore, we have determined the concentration of C<sub>60</sub> dispersed in water by measuring the absorbance at 340 nm using the average extinction coefficient  $\epsilon = 105 \pm 15$  L/g/cm, which is close to the value reported by Andrievsky *et al.*<sup>2</sup> The UV-visible absorption spectra reported here for C<sub>60</sub> nanoparticles are similar to those reported by Kato *et al.*<sup>6</sup> who measured the effect of the particle size on the spectra of aqueous dispersions of C<sub>60</sub>. They investigated aggregates with different radii of gyration between 50 and 120 nm. Upon increasing size, they observed a weak, approximately linear, hypsochromic shift of the UV maxima I and II. They also found that the ratio of the absorbance values of I to II decreased with increasing size in agreement with the present findings. However, these authors did not correct the absorbance for the turbidity and did not relate the absorbance to the concentration of C<sub>60</sub>.

The ratio of the amplitudes of peaks I and II ( $A_I/A_{II}$ ) is shown in Figure 3.9a as a function of  $R_h$ . It decreased sharply with increasing  $R_h$  between 2 nm and 5 nm and more weakly for larger sizes. Figure 3.9b shows the ratio of the amplitudes of peaks III and II ( $A_{III}/A_{II}$ ) as a function of  $R_h$ , which increased progressively with increasing size from about 0.1 to about 0.4. There appears to be no systematic effect of the method used to disperse C<sub>60</sub> in water on these ratios which are rather correlated with the size of particles.

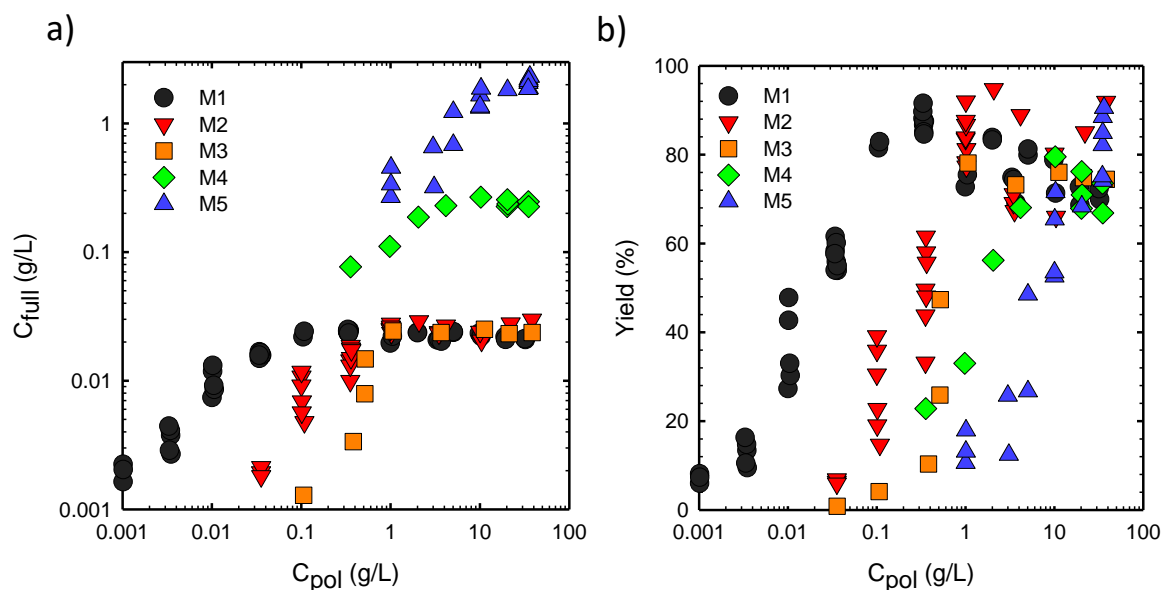


**Figure 3.9.** Ratio of the absorbance of peaks I to II (a) and of peaks III to II (b) as a function of  $R_h$  for C<sub>60</sub> particles prepared from various methods.

### c. Concentration of C<sub>60</sub> in water

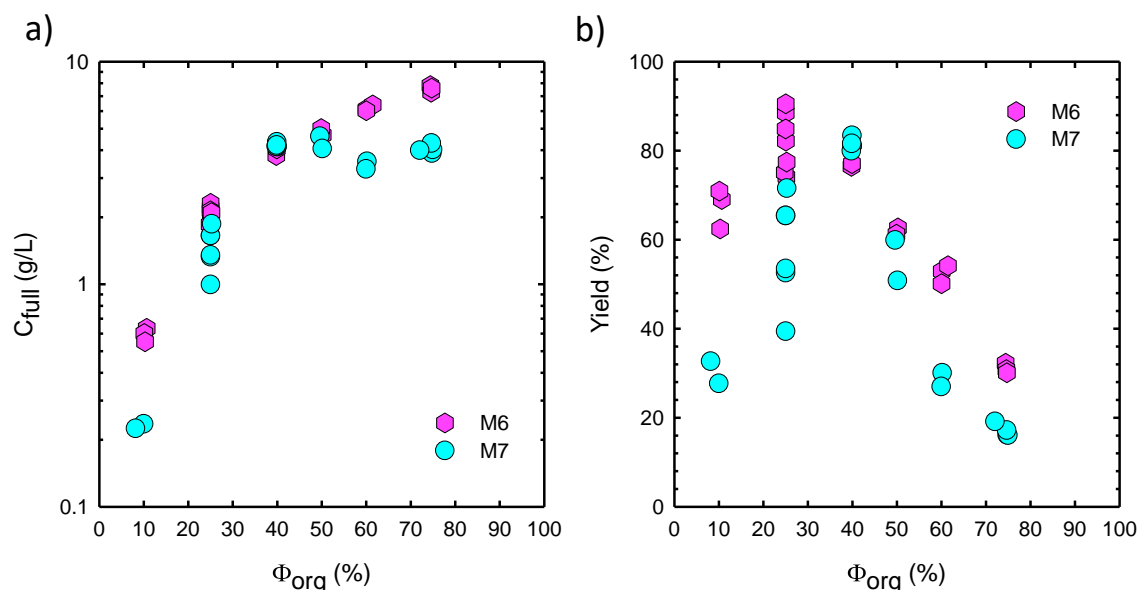
Figure 3.10a displays the concentration of C<sub>60</sub> ( $C_{full}$ ) that could be dispersed in water as a function of the concentration of 75C12 ( $C_{pol}$ ). The concentration range was limited up to 35 g/L, because at higher concentrations 75C12 forms a gel in aqueous solution (see section 1.5.d). In Figure 3.10b the same data are plotted in terms of yield defined as the ratio between  $C_{full}$  and the theoretical C<sub>60</sub> concentration if all C<sub>60</sub> in the emulsion had been effectively dispersed. The reproducibility of the results can be judged from the spread of the data shown in Figure 3.10 that were obtained in the same conditions. The amount of C<sub>60</sub> that dispersed in water increased with increasing 75C12 content until it reached a plateau value. For a given C<sub>60</sub> concentration in the organic phase (90 mg/L), the same plateau value was reached at a lower polymer concentration for chloroform than for CS<sub>2</sub> and much less polymer was needed to reach the plateau if it was dissolved in chloroform together with the C<sub>60</sub>. If more C<sub>60</sub> was dispersed in CS<sub>2</sub>, then more polymer was needed in the aqueous phase to reach the plateau. The maximum amount of C<sub>60</sub> that could be dispersed depended on the C<sub>60</sub> concentration in the organic phase, but not on the type of solvent. However, the maximum yield was found to be between 70 and 90% independent of the C<sub>60</sub> concentration whether in CHCl<sub>3</sub> or in CS<sub>2</sub>, see Figure 3.10b. At best, a fullerene concentration equal to 2.3 g/L was obtained with method M5 and  $C_{pol}$ =35 g/L.





**Figure 3.10.** Concentration (a) and yield (b) of fullerene dispersed in water as a function of the polymer concentration for fullerene nanoparticles prepared with different methods.

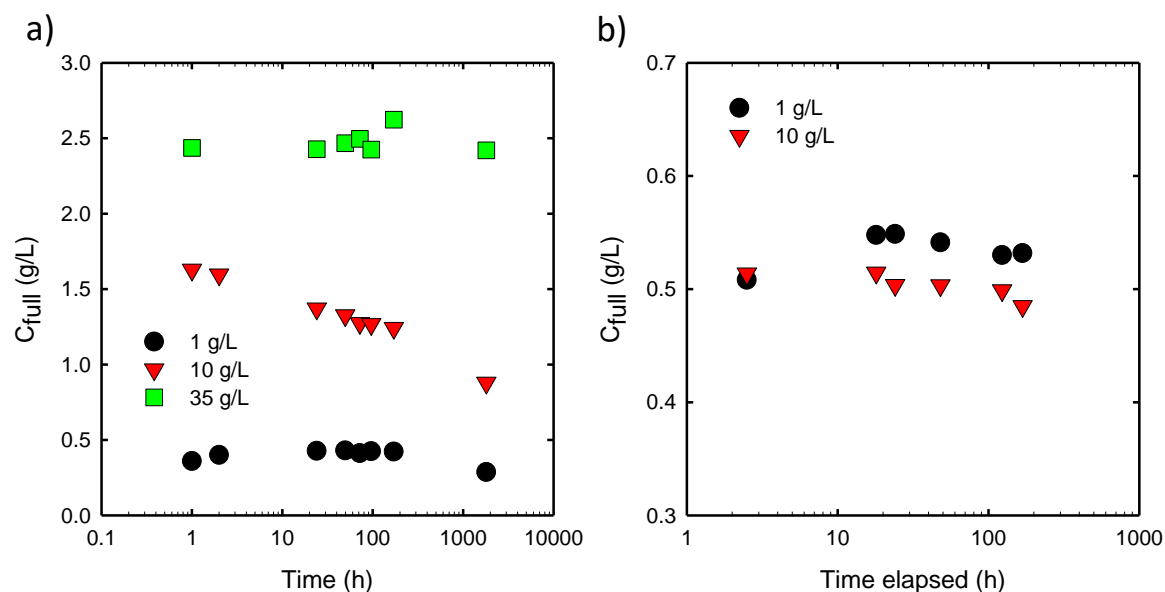
The effect of the volume fraction of the organic phase ( $\Phi_{org}$ ) was studied using saturated solutions of C<sub>60</sub> in carbon disulfide and aqueous solutions of 75C12 at fixed concentrations of 35 (M6) and 10 g/L (M7). Figure 3.11a shows that the amount of fullerene that was dispersed in the aqueous phase increased strongly with increasing  $\Phi_{org}$  up to about 40% and then either reached a plateau around 4 g/L for M7 or increased weakly up to 8 g/L at  $\Phi_{org}=75\%$  for M6. The yield increased with increasing  $\Phi_{org}$  until it reached a maximum between  $\Phi_{org}=25\%$  and 40% at  $C_{pol}=35$  g/L and closer to  $\Phi_{org}=40\%$  at  $C_{pol}=10$  g/L (see Figure 3.11b). In spite of the decreasing yield the actual concentration of fullerene in the aqueous dispersion did not decrease at higher  $\Phi_{org}$ , because the decrease of the yield was compensated by the decrease of the volume fraction of the water phase.



**Figure 3.11.** Concentration (a) and yield (b) of fullerene particles dispersed in water as function of the volume fraction of CS<sub>2</sub> for methods M6 and M7.

#### d. Stability of the particles dispersions

The extent of sedimentation of C<sub>60</sub> under gravity with time was studied by measuring the concentration of C<sub>60</sub> in the supernatant by UV-visible spectroscopy. Samples prepared from method M5 with  $C_{pol}=1$  g/L, 10 g/L and 35 g/L were studied. Figure 3.12a displays  $C_{full}$  as a function of the ageing time. During more than 2 months, samples at  $C_{pol}=1$  and 35 g/L remained very stable showing almost no sedimentation under gravity. However, at  $C_{pol}=10$  g/L,  $C_{full}$  decreased by a factor of 2 during the same ageing time. The destabilization of the sample with  $C_{pol}=10$  g/L was most likely due to slow aggregation of the particles, which was perhaps caused by their depletion induced by the polymer. Depletion may also have occurred at  $C_{pol}=35$  g/L, but the viscosity of aqueous solutions of 75C12 at 35 g/L is two orders of magnitude higher than at 10 g/L,<sup>7</sup> which slows down the process. When the dispersion at  $C_{pol}=10$  g/L was diluted from  $C_{full}=1.6$  g/L down to 0.5 g/L keeping  $C_{pol}$  constant, the dispersion remained much more stable, see Figure 3.12b showing that the destabilization rate varies with the concentration of particles for the same  $C_{pol}$ . We note that simple handshaking of the samples led to complete dispersal of the particles that have sedimented.

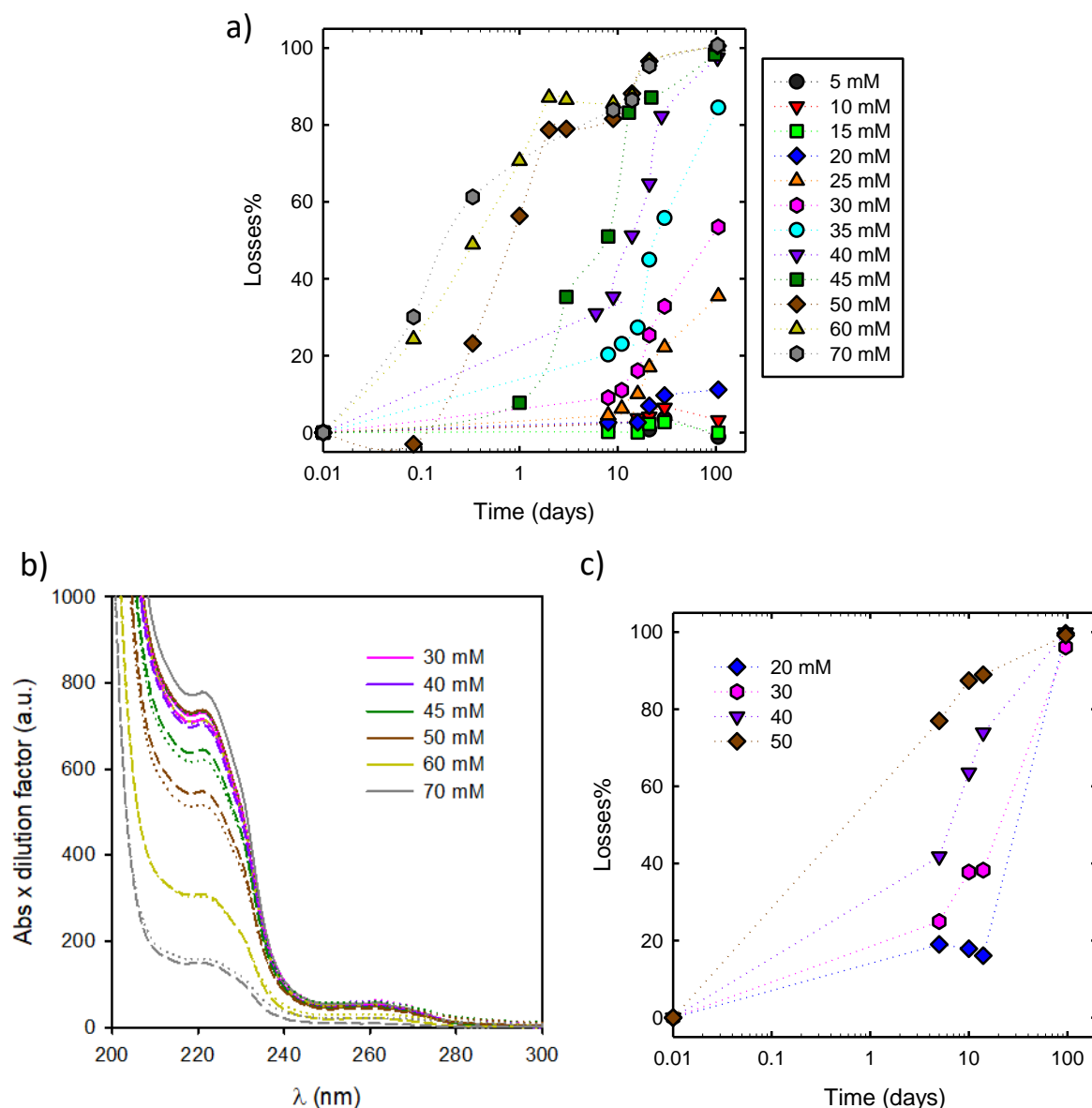


**Figure 3.12.** a) Dependence of  $C_{full}$  with time for dispersions prepared with method M5 and various polymer concentrations as indicated in the figure. b) Sample with  $C_{pol}=10$  g/L was diluted 3 times with a 10 g/L polymer solution to keep  $C_{pol}$  constant.

Investigation of the stability in saline medium is crucial for these aqueous suspensions when targeting applications where the ionic strength is an important parameter such as in biology or environmental science. An M5 sample at  $C_{pol} = 35$  g/L, which correspond to the highest  $C_{full}$  of this series of samples, *i.e.* 1.2 g/L, was diluted down to  $C_{pol}=0.04$  g/L and  $C_{full} = 1.5$  mg/L, at NaCl concentrations ( $C_s$ ) ranging from 5 to 70 mM (Figure 3.13a). The losses were defined as the percentage of concentration decrease compared to the measurement at  $t=0$ . First, the polymer itself is very sensitive to ionic strength. It was already reported elsewhere and attributed to charge screening, leading to gradual aggregation of polymer chains until eventual destabilization.<sup>8</sup> In this work, the remaining  $C_{pol}$  in supernatant was measured by UV-visible spectroscopy (Figure 3.13b). Actually, phase separation is not complete, since some polymer remains in supernatant, but it happens within a week. Indeed, no significant difference (*i.e.* more than 10%) can be seen between 1 and 2 weeks aged solutions.

However, when it comes to  $C_{60}$  colloidal suspensions, the destabilization kinetics depended much on  $C_s$ . Above 50 mM, within 1 day most of the particles sedimented. After 100 days, samples at  $C_s = 40$  and 45 mM completely sedimented and between 25 and 35 mM, destabilization was still going on. At 20 mM, however, for the sample at  $C_{full} = 1.5$  mg/L, a steady state seems to be reached after 1 month with only 10% losses. No significative destabilization can be observed at  $C_s \leq 20$  mM.

Increasing  $C_{pol}$  and  $C_{full}$  by a factor 2 affects a lot the destabilization process (Figure 3.13c). All samples  $C_s$  ranging from 20 to 50 mM were completely destabilized after 100 days. Kinetics were also affected. A sample at  $C_s = 30$  mM only took 5 days to display 25% of losses, whereas it took 3 weeks to reach this value when it was diluted 2 times. To conclude, both  $C_s$  and  $C_{full}$  affect the amount of particles destabilized, and the kinetics. This study clearly shows that stabilization of C<sub>60</sub> particles is ensured by electrostatic repulsions.



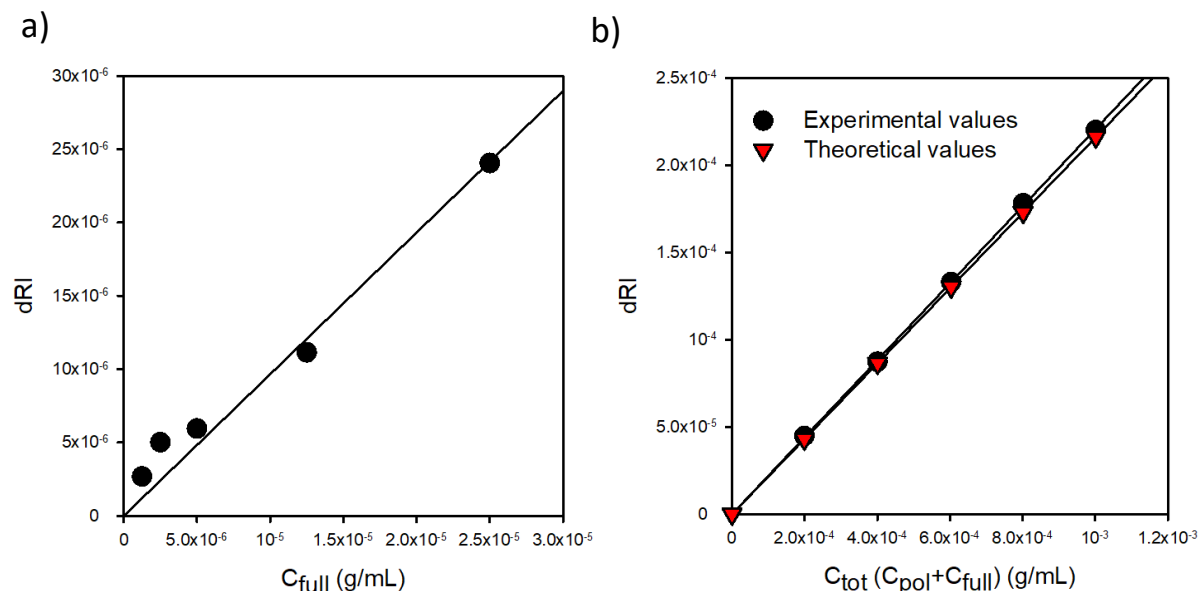
**Figure 3.13.** Percentage of losses measured from band II for an M5 sample at  $C_{pol}=35$  g/L with different NaCl concentrations indicated in legend, diluted down to  $C_{full}=$  a) 1.5 mg/L and c) 3 mg/L. b) Absorption spectra of polymer solutions at the same  $C_{pol}$  than a), at different ionic

strengths. Solid line corresponds to initial state, short-dashed line to 1 week and dotted line to 2 weeks old solutions.

## 2) Characterization of the particles

### a. Size and molar mass of the C<sub>60</sub> particles

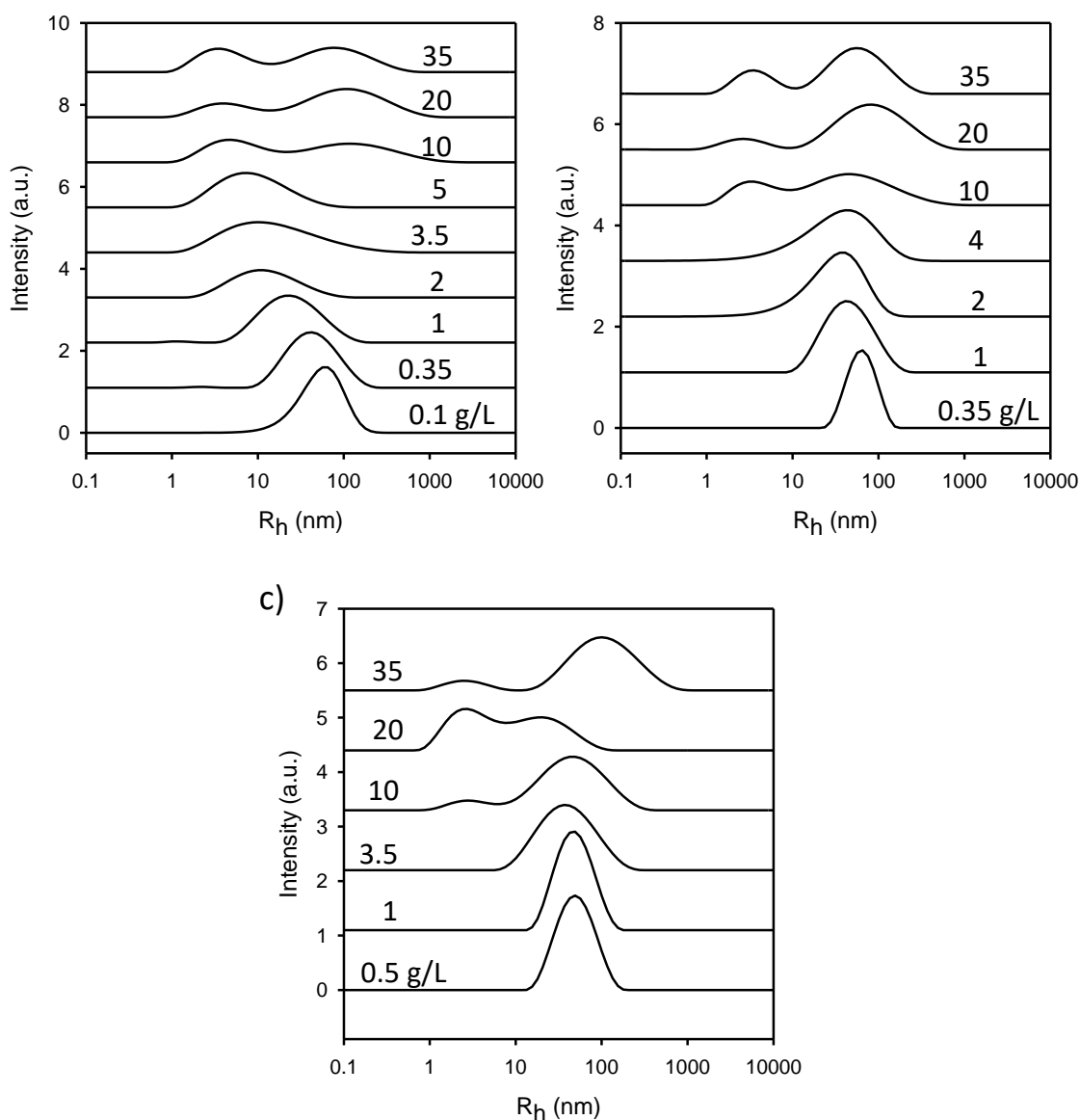
The average molar mass ( $M_w$ ), radius of gyration ( $R_g$ ) and hydrodynamic radius ( $R_h$ ) of the dispersed C<sub>60</sub> particles were determined by static and dynamic light scattering techniques, as described in section 2.4. The refractive index increments ( $dn/dC$ ) were measured using an emulsion without any polymer and fullerene treated in the same manner as a blank. Dispersions with various concentrations were analyzed. The refractive index increment ( $dn/dC$ ) of fullerene in water was determined using a sample without polymer. It was found to be equal to 1 mL/g (Figure 3.14a), which is much higher than  $dn/dC = 0.19$  mL/g reported for 75C12 in water<sup>8</sup>. For a dispersion containing both polymer and fullerene derived from M5, the measured  $dn/dC$  was equal to the weighted average of that of C<sub>60</sub> and 75C12 (Figure 3.14b). The contribution of the polymer to the scattered light compared to that of the C<sub>60</sub> particles was therefore in most cases negligible, because the contrast of the latter was 25 times higher (see section 2.4.b, Eq. 2.13).



**Figure 3.14.** Concentration-dependence of refractive index ( $dRI$ ) for samples prepared with  $C_{pol} = 0$  (a) and 35 g/L (b).

Intensity size distributions measured from DLS are displayed for M1 samples in Figure 3.15a. For low  $C_{pol}$ , a single population is observed. Upon increasing  $C_{pol}$ , the distribution of sizes broadens and shifts toward lower  $R_h$  values. For  $C_{pol} \geq 10$  g/L, two modes of relaxation were

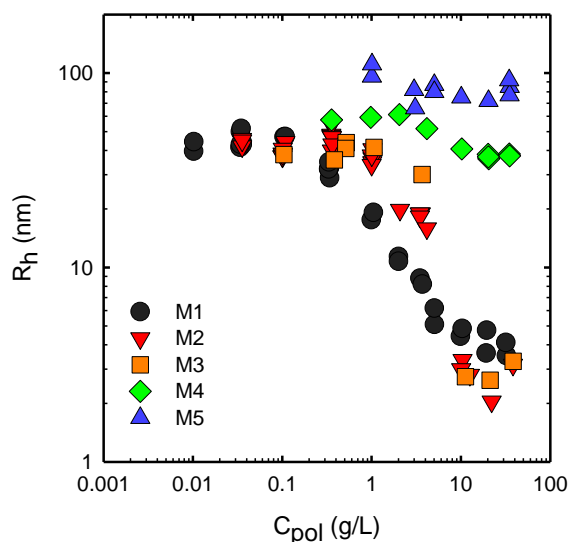
distinguished but we will only consider the fast mode of relaxation in the following. Actually, the relative amplitude and the size for the slow mode of relaxation indicate that its concentration is very small with respect to the concentration of the fast mode of relaxation. For samples prepared with polymer initially located in water (M2), the results from DLS are the same as for M1 samples (Figure 3.15b), although the shift to lower size occurs at higher  $C_{pol}$ .



**Figure 3.15.** Distribution of sizes for a) M1, b) M2 and c) M3 samples at various polymer concentrations indicated on the figures.

For dispersions prepared from chloroform, average  $R_h$  was comprised between 40 and 50 nm at low polymer concentrations whatever the initial location of the polymer (M1, M2), see Figure 3.16. This size is much larger than an individual fullerene molecule, which has a radius of 0.35 nm, indicating that aggregates were formed. Upon further increasing  $C_{pol}$ ,  $R_h$  decreased by

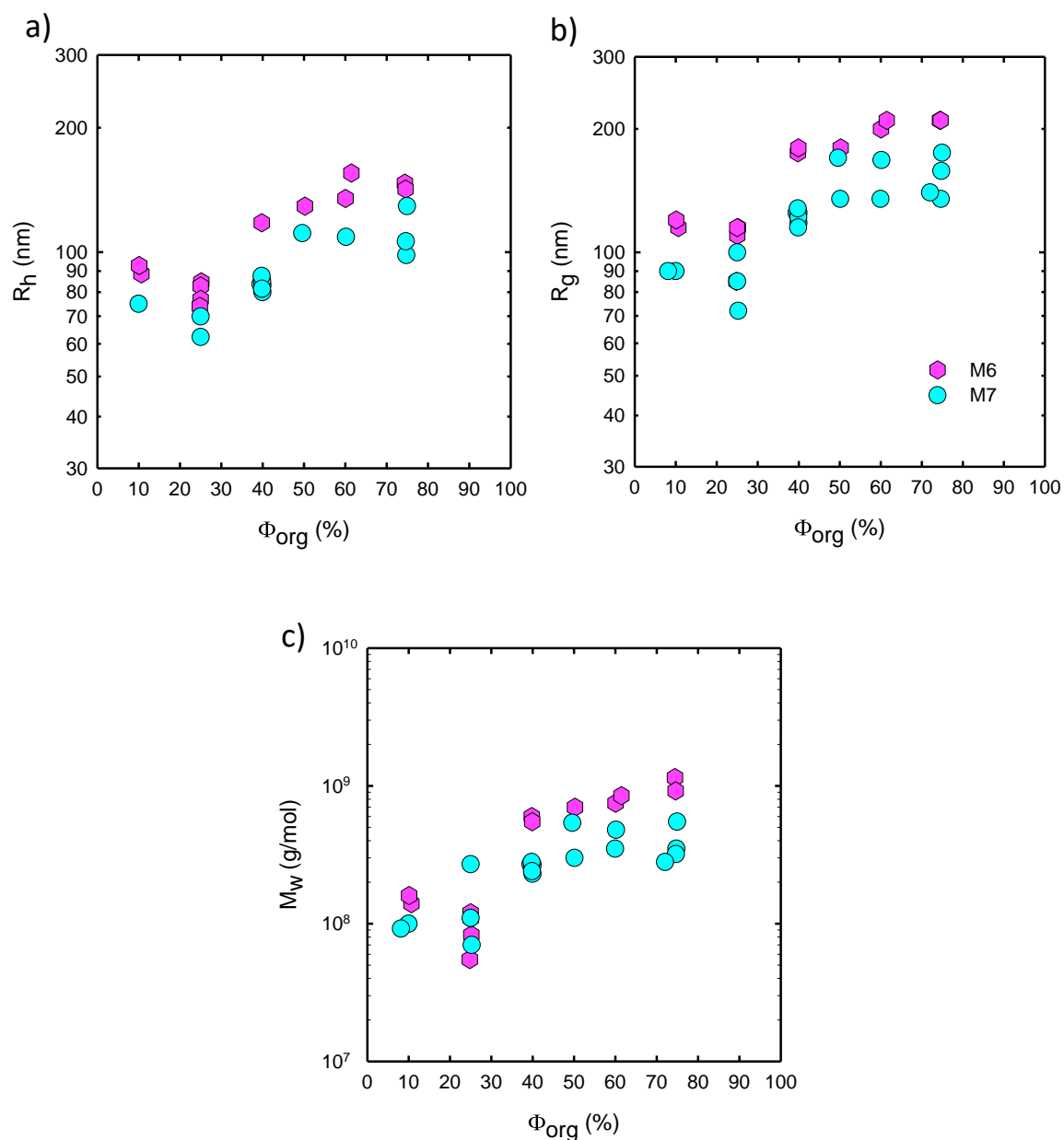
almost one order of magnitude, down to a few nanometers. It should be noted that the  $R_h$  of 75C12 in dilute aqueous solution is approximately 4 nm,<sup>8</sup> *i.e.* similar to  $R_h$  observed here at higher polymer concentrations. It is possible that at these high polymer concentrations and low particle size, the contribution of the polymers can no longer be neglected. The size of the particles in dispersions prepared from CS<sub>2</sub> at the same fullerene concentration as in chloroform (M3) also displayed a significant decrease with increasing  $C_{pol}$ , but the decrease started at higher  $C_{pol}$ . The slow relaxation mode appeared similarly as for M1 and M2 samples (Figure 3.15c). When the fullerene concentration in CS<sub>2</sub> was increased to 1 g/L (M4), the size of the particles decreased only weakly with increasing  $C_{pol}$  from about 60 nm to about 40 nm. With 7.6 g/L (M5)  $R_h$  varied between 60 nm and 100 nm, but did not depend systematically on  $C_{pol}$ .



**Figure 3.16.** Hydrodynamic radius of dispersed C<sub>60</sub> particles as a function of the polymer concentration for different methods used to prepare the dispersion as indicated in the figure.

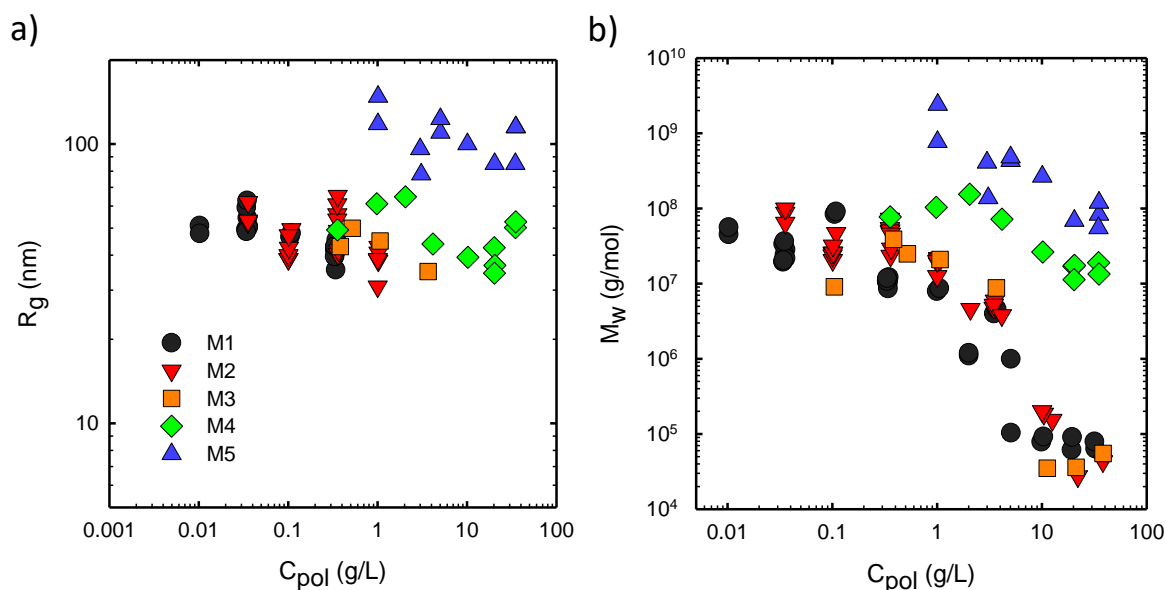
The influence of  $\Phi_{org}$  on the hydrodynamic radius of the particles is plotted in Figure 3.17a. For both polymer concentrations, the smallest sizes were observed when  $\Phi_{org} \leq 25\%$ . At higher  $\Phi_{org}$  the size increased by approximately a factor 2. Particles prepared at  $C_{pol}=35$  g/L were systematically larger than the ones prepared at  $C_{pol}=10$  g/L.  $\Phi_{org}$  influences both  $R_g$  and  $M_w$  in the same way as for  $R_h$  (Figures 3.17b and c, respectively).





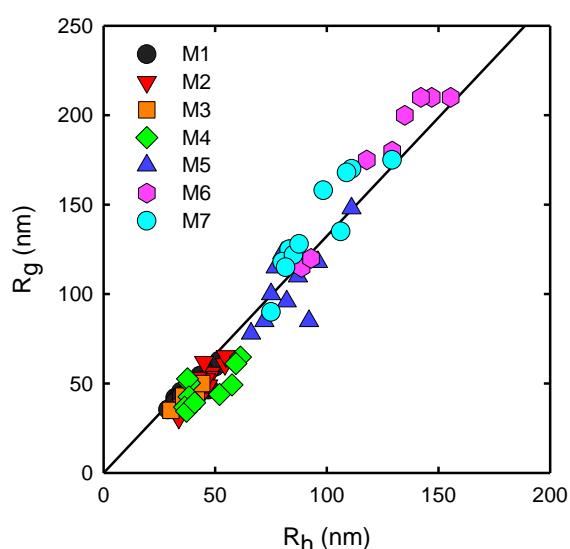
**Figure 3.17.** Hydrodynamic radius (a), gyration radius (b) and weight average molar mass (c) of fullerene particles in water as function of the volume fraction of CS<sub>2</sub> for methods M6 and M7.

Here we only discussed  $R_h$  that can be determined accurately over a wider range of particle size, but the influence of  $C_{pol}$  on both  $R_g$  and  $M_w$  is also reported in Figure 3.18.



**Figure 3.18.** a) Gyration radius and b) Weight average molar mass of M1-5 samples as determined by SLS.

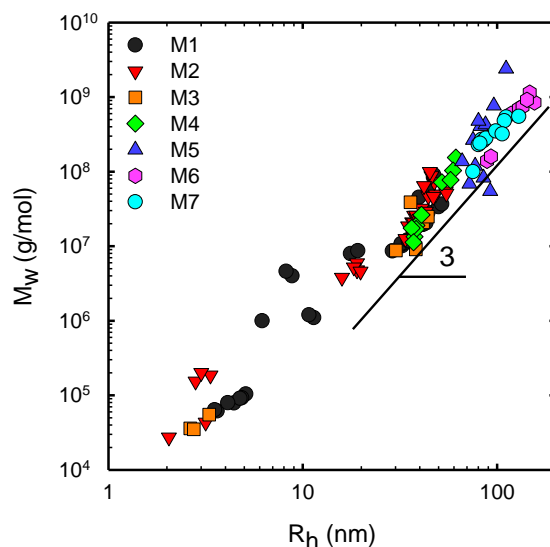
$R_g$  was found to be proportional to  $R_h$  with  $R_g/R_h \approx 1.3$ , see Figure 3.19. This ratio is much bigger than what is commonly observed for hard spheres (0.77). It is still slightly lower than 1.51, the theoretical value for a Gaussian coil. It is well known that this ratio increases when particles are elongated, and it is theoretically infinite for rods that are infinitely longer than thick. The value can then be attributed to either a low packing density of fullerenes inside the particle, or to anisotropy. Therefore, we investigated the morphology of the particles as presented in the section 3.2.b.



**Figure 3.19.** Gyration radius as a function of hydrodynamic radius.

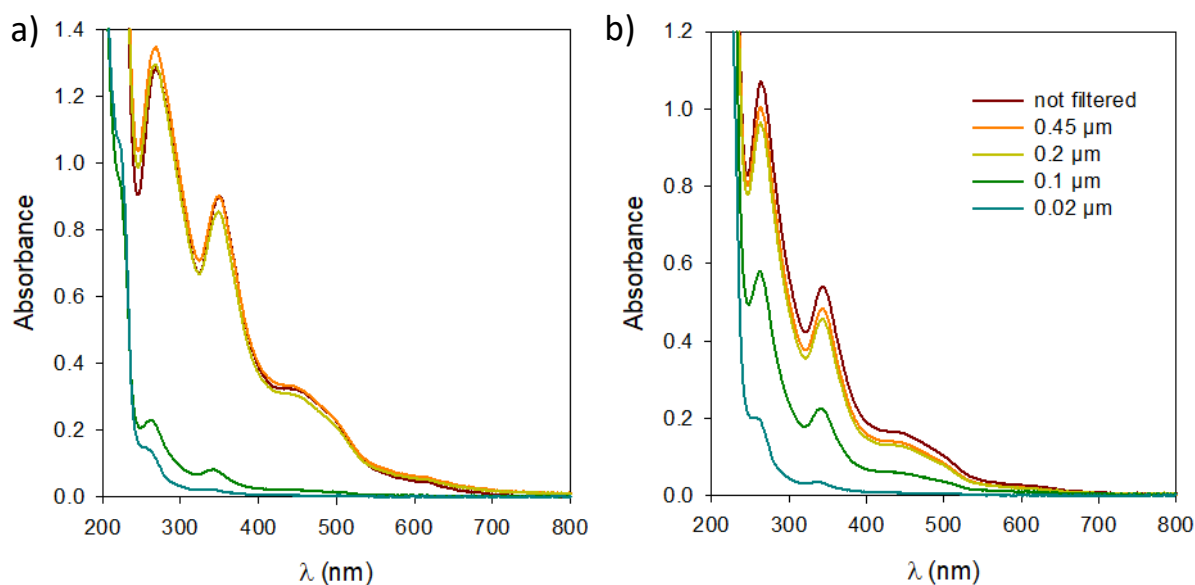
### b. Morphology of the C<sub>60</sub> particles

Figure 3.20 shows the relationship between  $M_w$  and  $R_h$  for fullerene nanoparticles prepared with various methods. Within the scatter of the data, a power law  $M_w \propto R_h^3$  was found for  $R_h > 30$  nm, which would mean that these particles had approximately the same density whatever their size. The smaller particles deviated upward from this behavior indicating that they were denser.



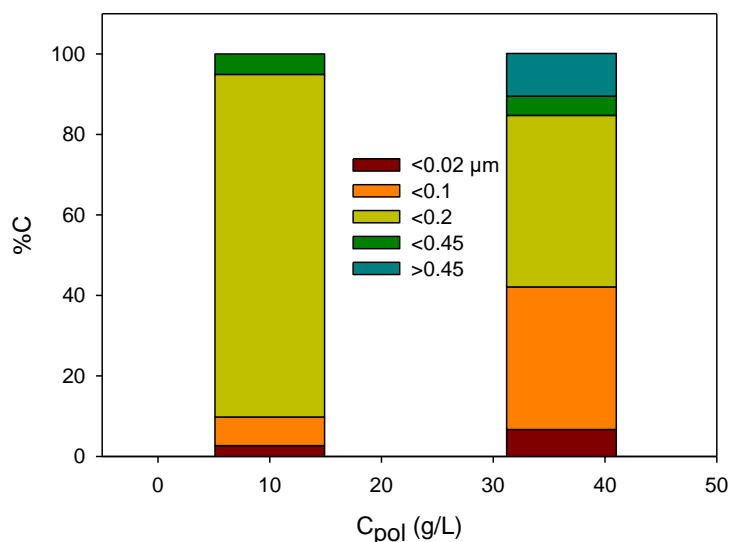
**Figure 3.20.** Weight average molar mass of fullerene particles as a function of their hydrodynamic radius.

The dispersity of the particles size has been evaluated by sequentially filtrating the samples on membranes with various porosity. After each filtration step, UV-visible absorption spectra were collected in order to determine the fullerene concentration, see Figure 3.21. For both  $C_{pol}=10$  (Figure 3.21a) and 35 g/L (Figure 3.21b), very few particles were removed by filtrating over 0.2 or 0.45  $\mu\text{m}$ . However, filtration over 0.1  $\mu\text{m}$  removed nearly all the particles for  $C_{pol}=10$  g/L, and approximately half of them for  $C_{pol}=35$  g/L. Please note that here, the polymer contribution to absorbance was not subtracted because we cannot quantify the amount of polymer before and after filtration. Of course, filtration of a polymer solution on any porosity did not remove polymer. Filtration over 0.02  $\mu\text{m}$  removed most particles in both cases, and the remaining absorption spectra look very similar to the one of 75C12 (see section 2.3.a, Figure 2.12).



**Figure 3.21.** UV-visible absorption spectra of diluted M5 samples ( $C_{pol} =$  a) 10 g/L and b) 35 g/L) before and after filtration over various pore sizes indicated in legend.

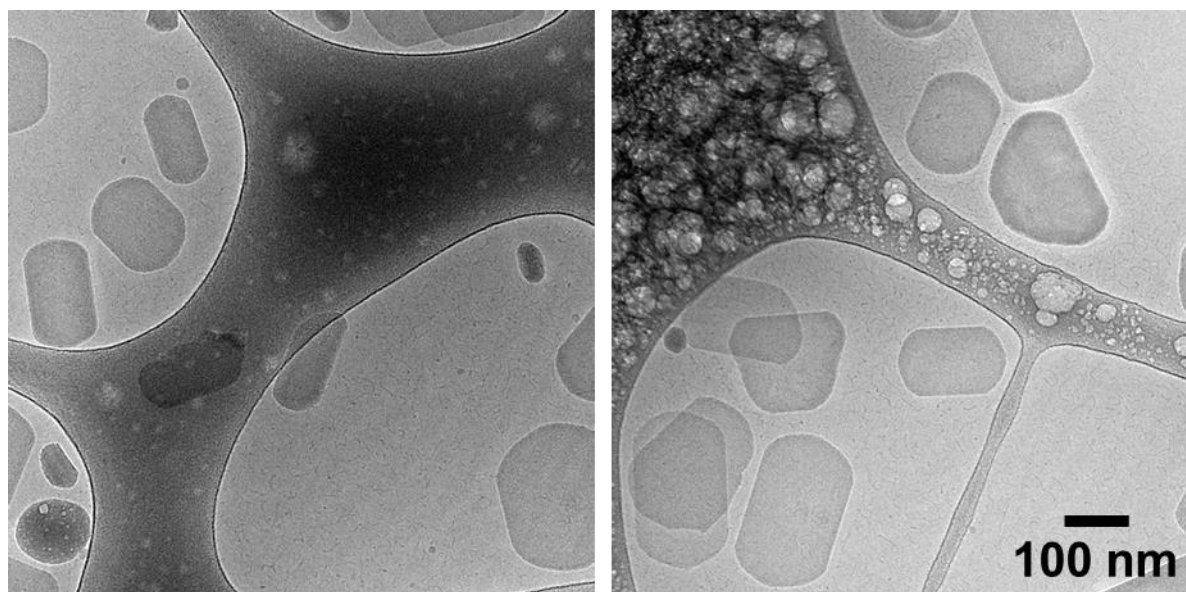
The percentage of particles removed by sequential filtrations is displayed in Figure 3.22. This percentage was estimated from the absorbance of band II, where polymer does not absorb. It results that particles prepared at  $C_{pol}=35$  g/L, were bigger in average, and more polydisperse as approximately 10% were bigger than 0.45  $\mu\text{m}$ .



**Figure 3.22.** Percentage of particles concentration after filtration over various porosities indicated in legend for two M5 samples with  $C_{pol}=10$  and 35 g/L.

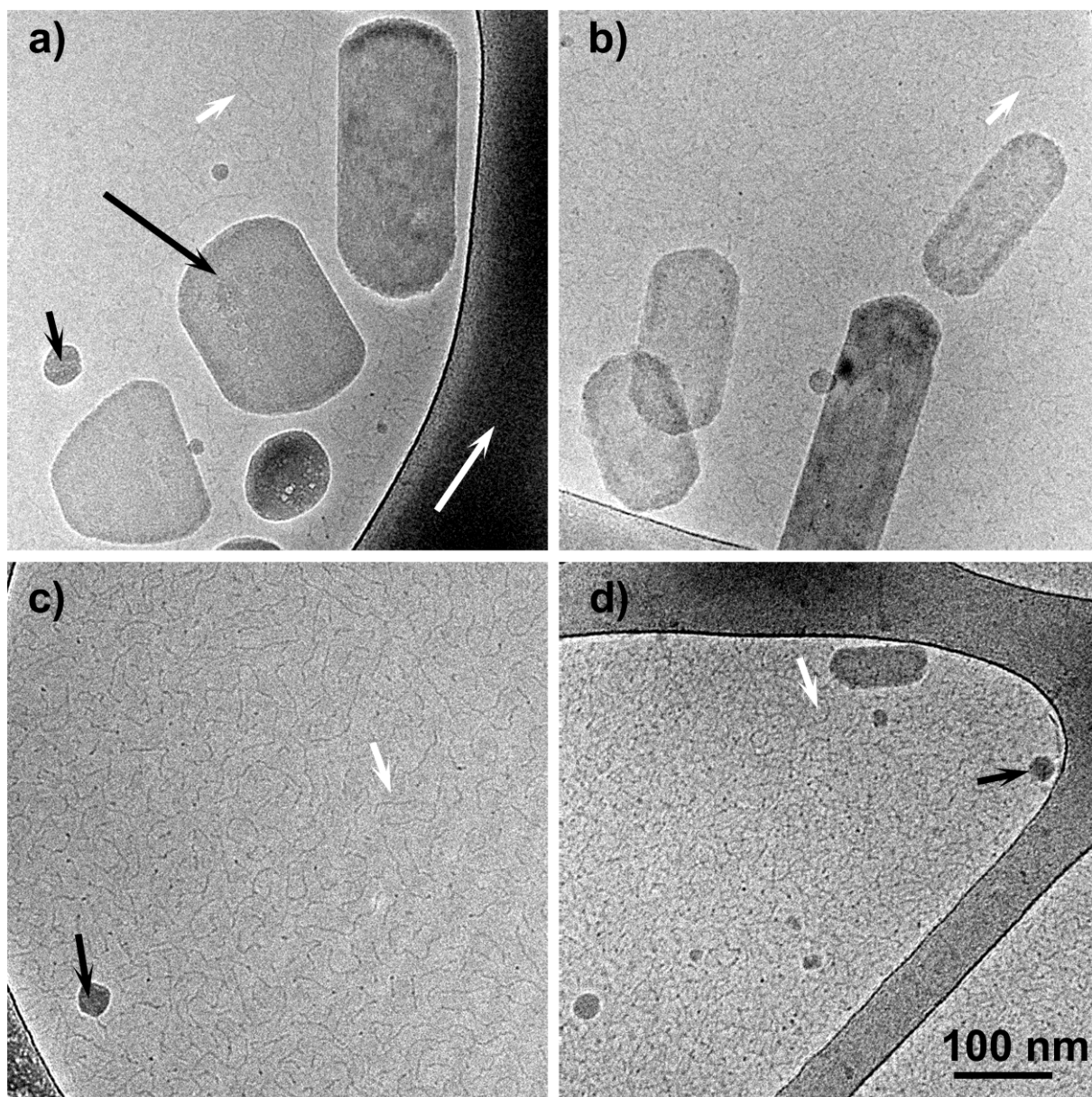
Cryo-TEM images of C<sub>60</sub> particles dispersed in water using method M5 with  $C_{pol}=10$  g/L are shown in Figures 3.23 and 3.24a. We can distinguish two kinds of structures. The first ones

indicated by the long black arrow in Figure 3.24a are thin faceted platelets displaying some crystalline order. A few particles display some twinning as in Figure 3.24b. The second kind of structures (short black arrow) are thicker objects. In a few of them, small white dots can be seen. They can either be some beam damage though the images were taken under low dose conditions or small defects in the crystal. For both cases, this could be interpreted as the presence of 75C12 macromolecules inside the structures. In the amorphous water layer, worm-like micelles (WLM) are observed at higher defocus values (short white arrow). These are the excess of 75C12 self-assembling in water.<sup>8</sup> The long white arrow corresponds to the Carbon-Formvar lacey supporting film. Similar morphologies for the fullerene nanoparticles are observed for dispersions formed with method M7 with  $C_{\text{pol}}=35$  g/L and  $\Phi_{\text{org}}=75\%$  (Figure 3.24b). The free 75C12 forming WLM are less visible as the images are taken at a lower defocus value than Figure 3.24c for example. When  $\Phi_{\text{org}}$  was decreased from 25% to 10%, only a low number of isotropic objects are seen (short black arrow in Figure 3.24c). The majority of objects are the WLM (white short arrow in Figure 3.24c). Dispersions prepared with method M4, *i.e.* starting with less fullerene, with  $C_{\text{pol}}=10$  g/L also displayed only a few small platelets together with small isotropic particles (Figure 3.24d).



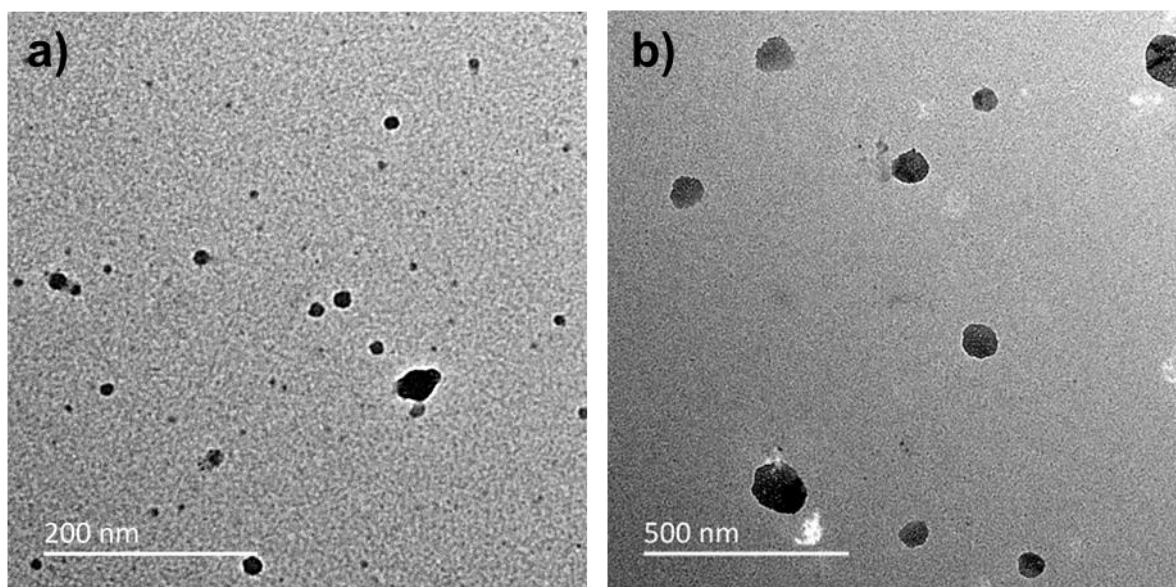
**Figure 3.23.** Cryo-TEM pictures of an M5 sample ( $C_{\text{pol}}=10$  g/L,  $\Phi_{\text{org}}=25\%$ ) at low magnification.





**Figure 3.24.** Cryo-TEM pictures for samples a) M5 ( $C_{\text{pol}}=10$  g/L,  $\Phi_{\text{org}}=25\%$ ), b) M7 ( $C_{\text{pol}}=35$  g/L,  $\Phi_{\text{org}}=75\%$ ), c) M6 ( $C_{\text{pol}}=35$  g/L,  $\Phi_{\text{org}}=10\%$ ) and d) M4 ( $C_{\text{pol}}=10$  g/L,  $\Phi_{\text{org}}=25\%$ ). Arrows are guides for the discussion. Short white arrows indicate polymeric worm-like micelles and the long white arrow shows Carbon-Formvar lacey supporting film.

A dispersion made with method M1 and  $C_{\text{pol}}=10$  g/L only contained small isotropic particles (Figure 3.25a) as did a dispersion that contained no polymer (Figure 3.25b). We can therefore conclude, in comparison with the sample prepared with method M6,  $C_{\text{pol}}=10$  g/L and  $\Phi_{\text{org}}=10\%$  (Figure 3.24c) that isotropic particles are obtained when fullerene concentration is low, whereas anisotropic objects appear when it is high.



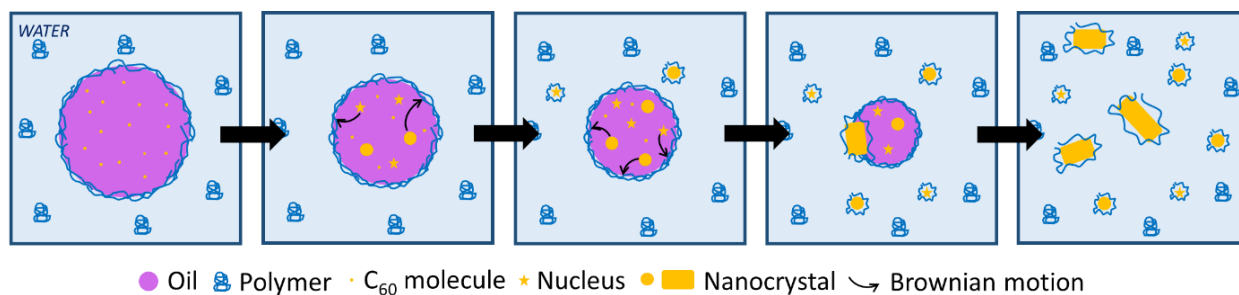
**Figure 3.25.** Dried TEM pictures of a) M1 sample ( $C_{\text{pol}}=10$  g/L,  $\Phi_{\text{org}}=25\%$ ) and b) particles prepared without any stabilizer.

### 3) Discussion

#### a. Mechanism of C<sub>60</sub> particles formation

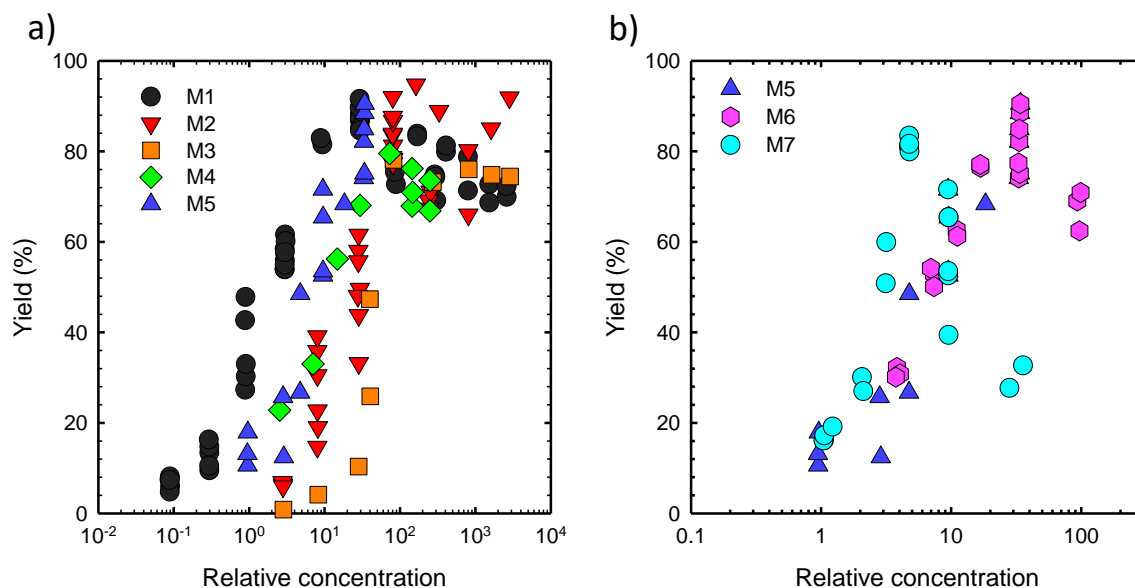
We propose the following mechanism for the formation of aqueous dispersions of C<sub>60</sub> particles in the presence of an amphiphilic polymer, see Scheme 3.1. Fullerene is initially dissolved molecularly in the solvent. A fraction of the solvent is dispersed in the form of droplets in the aqueous phase by ultrasonication, which also heats the emulsions causing evaporation of the solvent. When the solvent evaporates, the concentration of fullerene exceeds its limit of solubility leading to nucleation and growth of C<sub>60</sub> particles. As the droplets are orders of magnitude larger than particles (see Figures 3.1 to 3.5), it is clear that many nuclei are formed in each droplet and grow into particles. When the particles come in contact with the polymer, either inside the droplet or at the solvent/water interface, the latter binds to the particles. The layer of polymer covering the particles inhibits further growth and allows the particles to disperse in the aqueous phase.





**Scheme 3.1.** Schematic overview of the mechanism of C<sub>60</sub> particles formation and dispersion by the emulsification-evaporation method in the presence of the amphiphilic polymer.

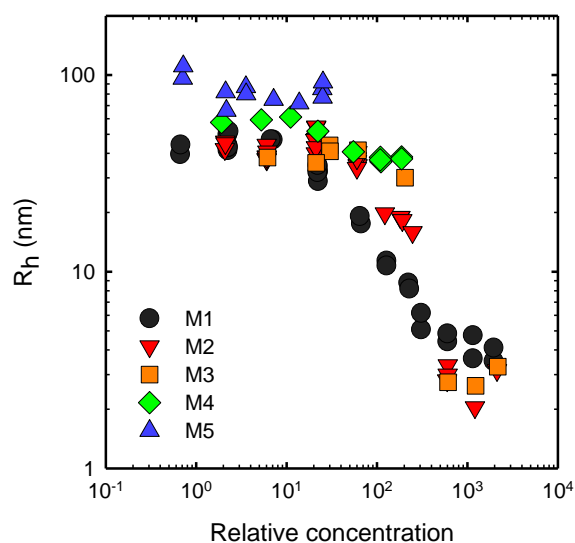
This mechanism can explain why with increasing polymer concentration, the yield of fullerene dispersion increased and the particle size decreased. In order to obtain effective coverage of the particles, the polymer concentration relative to the C<sub>60</sub> concentration is more important to consider than its absolute concentration. When plotting in Figure 3.26a the yield as a function of the relative concentration, defined as the molar ratio of 75C12 repeating units to C<sub>60</sub> molecules, rather than as a function of the total concentration shown in Figure 3.10b, the results for various dispersions superimpose better. However, dispersions obtained with the polymer dissolved in chloroform still show an increase of the yield at lower relative polymer concentrations compared to samples in which polymer was initially dissolved in water. This is possibly due to the fact that the polymer in this situation is more readily available to bind to the particles. We indeed observed that the chloroform-in-water emulsions prepared with the polymer initially dissolved in chloroform were more stable than when the polymer was first dissolved in water. In the former case, the polymer diffuses to the interface more easily. The decrease of the yield with increasing  $\Phi_{\text{org}} > 25\%$  (see Figure 3.11b) can also be explained by a decrease of the relative polymer concentration as the total amount of C<sub>60</sub> in the organic phase increased and that of 75C12 in the aqueous phase decreased. However, this cannot explain the decrease of the yield for  $\Phi_{\text{org}} < 25\%$  (see Figure 3.26b). One possibility is that a small fraction of the solvent wets the glass walls and therefore does not allow a fraction of the fullerene to disperse.



**Figure 3.26.** Yield of fullerene particles dispersion in water as function of relative concentration of 75C12 with respect to  $C_{60}$  for a) M1-5 and b) M5-7 samples.

#### b. Morphology and size of the $C_{60}$ particles

The effect of the polymer concentration on  $R_h$  also better superimposes when plotted as a function of the relative concentration, see Figure 3.27 vs. Figure 3.16. It can explain why no significant decrease of  $R_h$  was found for dispersions made with method M5, because the relative polymer concentrations tested were not high enough.  $R_h$  levelled off with decreasing  $C_{pol}$  at the same relative concentration at which the yield started to decrease, see Figure 3.26a. This suggests that larger particles that were formed at lower polymer concentrations did not disperse well leading to a decrease of the yield.



**Figure 3.27.**  $R_h$  as a function of the relative polymer concentration expressed as the molar ratio between polymer repeating units and C<sub>60</sub> for dispersions produced with methods M1-5.

The size of the particles at low relative polymer concentrations increased with increasing concentration of C<sub>60</sub> dissolved in the organic phase. We speculate that growth was faster when more C<sub>60</sub> was present so that the particles were larger before interaction with the polymer inhibited further growth.

The variety of the shape and the size dispersity of the C<sub>60</sub> particles renders it difficult to interpret the observed relationships between  $R_h$  and  $R_g$  and that between  $R_h$  and  $M_w$ . Cryo-TEM images showed that nanocrystals had formed in the shape of platelets when the dispersions were prepared with higher concentrations of fullerene.

Various shapes of C<sub>60</sub> nanocrystals have been reported in the literature so far.<sup>9-13</sup> Formation of C<sub>60</sub> nanoplatelets displaying rectangular shapes similar to what was observed in this study was reported with aerosol.<sup>9</sup> However, their contrast in TEM seems higher, indicating that the platelets were thicker. Also, when they were tilted, they displayed a hexagonal geometry, which was not seen in the current investigation. In water, nanocrystals are typically obtained when C<sub>60</sub> is precipitated from THF, which produces nanocrystals in the shape of parallelepipeds with sharp edges and high contrast in TEM.<sup>14</sup>

As far as we are aware, the particular round-edged rectangular platelet shape has not been reported in the literature and may be related to specific interactions with 75C12. As these nanocrystals are already dispersed in water, they are readily useable for potential applications. Further study is needed to elucidate the detailed structure of the nanoplatelets, their properties (which is partly done in the following chapters) and the mechanism of their formation.

## Conclusion

Aqueous dispersions of C<sub>60</sub> nanoparticles could be produced at concentrations up to 8 g/L, which is the highest concentration reported so far, at yields between 70 and 80% using an emulsification-evaporation method in the presence of an amphiphilic polymer. The size and morphology of the particles can be varied by varying the polymer and fullerene concentrations, the type of solvent or the phases volume fractions. Dispersions that are more concentrated showed nanocrystals in the form of thin elongated platelets with lengths up to a few hundreds of nm. In the next chapter, we will focus on these particles and study the possibilities to control their size, their structure and optical properties.

## References

1. Andrievsky, G. V.; Kosevich, M. V.; Vovk, O. M.; Shelkovsky, V. S.; Vashchenko, L. A., On the production of an aqueous colloidal solution of fullerenes. *Journal of the Chemical Society, Chemical Communications* **1995**, (12), 1281-1282.
2. Andrievsky, G. V.; Klochkov, V. K.; Bordyuh, A. B.; Dovbeshko, G. I., Comparative analysis of two aqueous-colloidal solutions of C<sub>60</sub> fullerene with help of FTIR reflectance and UV-Vis spectroscopy. *Chemical Physics Letters* **2002**, 364 (1), 8-17.
3. Deguchi, S.; Alargova, R. G.; Tsujii, K., Stable Dispersions of Fullerenes, C<sub>60</sub> and C<sub>70</sub>, in Water. Preparation and Characterization. *Langmuir* **2001**, 17 (19), 6013-6017.
4. Scharff, P.; Risch, K.; Carta-Abelmann, L.; Dmytruk, I. M.; Bilyi, M. M.; Golub, O. A.; Khavryuchenko, A. V.; Buzaneva, E. V.; Aksenov, V. L.; Avdeev, M. V.; Prylutskyy, Y. I.; Durov, S. S., Structure of C<sub>60</sub> fullerene in water : spectroscopic data. *Carbon* **2004**, 42 (5), 1203-1206.
5. Chen, Z.; Westerhoff, P.; Herckes, P., Quantification of C<sub>60</sub> fullerene concentrations in water. *Environmental Toxicology and Chemistry* **2008**, 27 (9), 1852-1859.
6. Kato, H.; Nakamura, A.; Takahashi, K.; Kinugasa, S., Size effect on UV-Vis absorption properties of colloidal C<sub>60</sub> particles in water. *Physical Chemistry Chemical Physics* **2009**, 11 (25), 4946-4948.
7. Dutertre, F.; Benyahia, L.; Chassenieux, C.; Nicolai, T., Dynamic Mechanical Properties of Networks of Wormlike Micelles Formed by Self-Assembled Comblike Amphiphilic Copolyelectrolytes. *Macromolecules* **2016**, 49 (18), 7045-7053.
8. Dutertre, F.; Gaillard, C. d.; Chassenieux, C.; Nicolai, T., Branched Wormlike Micelles Formed by Self-Assembled Comblike Amphiphilic Copolyelectrolytes. *Macromolecules* **2015**, 48 (20), 7604-7612.
9. Pauwels, B.; Bernaerts, D.; Amelinckx, S.; Van Tendeloo, G.; Joutsensaari, J.; Kauppinen, E. I., Multiply twinned C<sub>60</sub> and C<sub>70</sub> nanoparticles. *Journal of Crystal Growth* **1999**, 200 (1), 126-136.
10. Tan, Z.; Masuhara, A.; Kasai, H.; Nakanishi, H.; Oikawa, H., Multibranched C<sub>60</sub>Micro/Nanocrystals Fabricated by Reprecipitation Method. *Japanese Journal of Applied Physics* **2008**, 47 (2), 1426-1428.
11. Masuhara, A.; Tan, Z.; Kasai, H.; Nakanishi, H.; Oikawa, H., Fullerene Fine Crystals with Unique Shapes and Controlled Size. *Japanese Journal of Applied Physics* **2009**, 48 (5), 050206.
12. Kobayashi, K.; Tachibana, M.; Kojima, K., Photo-assisted growth of C<sub>60</sub> nanowhiskers from solution. *Journal of Crystal Growth* **2005**, 274 (3), 617-621.
13. Park, C.; Song, H. J.; Choi, H. C., The critical effect of solvent geometry on the determination of fullerene (C<sub>60</sub>) self-assembly into dot, wire and disk structures. *Chemical Communications* **2009**, (32), 4803-4805.
14. Fortner, J. D.; Lyon, D. Y.; Sayes, C. M.; Boyd, A. M.; Falkner, J. C.; Hotze, E. M.; Alemany, L. B.; Tao, Y. J.; Guo, W.; Ausman, K. D.; Colvin, V. L.; Hughes, J. B., C-60 in water: Nanocrystal formation and microbial response. *Environmental Science & Technology* **2005**, 39 (11), 4307-4316.

## Chapter 4. Structure and physical properties of C<sub>60</sub> nanoplatelets

1) Size of the nanoplatelets .....	145
a. Influence of $\Phi_{\text{org}}$ on the nanoplatelets size .....	145
b. Size of the nanoplatelets .....	149
2) Internal structure .....	150
a. Structure in SAXS .....	150
b. Raman scattering .....	152
c. Wide Angle X-Ray diffraction .....	154
3) Formation of nanoplatelets with other stabilizers .....	157
a. Other XCn polymers .....	157
b. De-formulation of cationic polymers .....	159
4) Fluorescence of C <sub>60</sub> nanoplatelets .....	162
Conclusions .....	164
References .....	165





## Chapter 4. Structure and physical properties of C<sub>60</sub> nanoplatelets

The elaboration of C<sub>60</sub> nanoplatelets was described in the previous chapter. In this chapter, we aim at giving more insight in the microstructure of the particles, thanks to cryo-transmission electron microscopy (cryo-TEM) pictures, static light and X-ray scattering (SLS and SAXS, respectively), and Raman spectroscopy. Their crystallinity will be briefly discussed based on wide-angle X-ray diffraction (WAXD) and further details on the growth mechanism during the emulsification-evaporation process will be given, based on results for the preparation of samples with a variety of amphiphilic stabilizers.

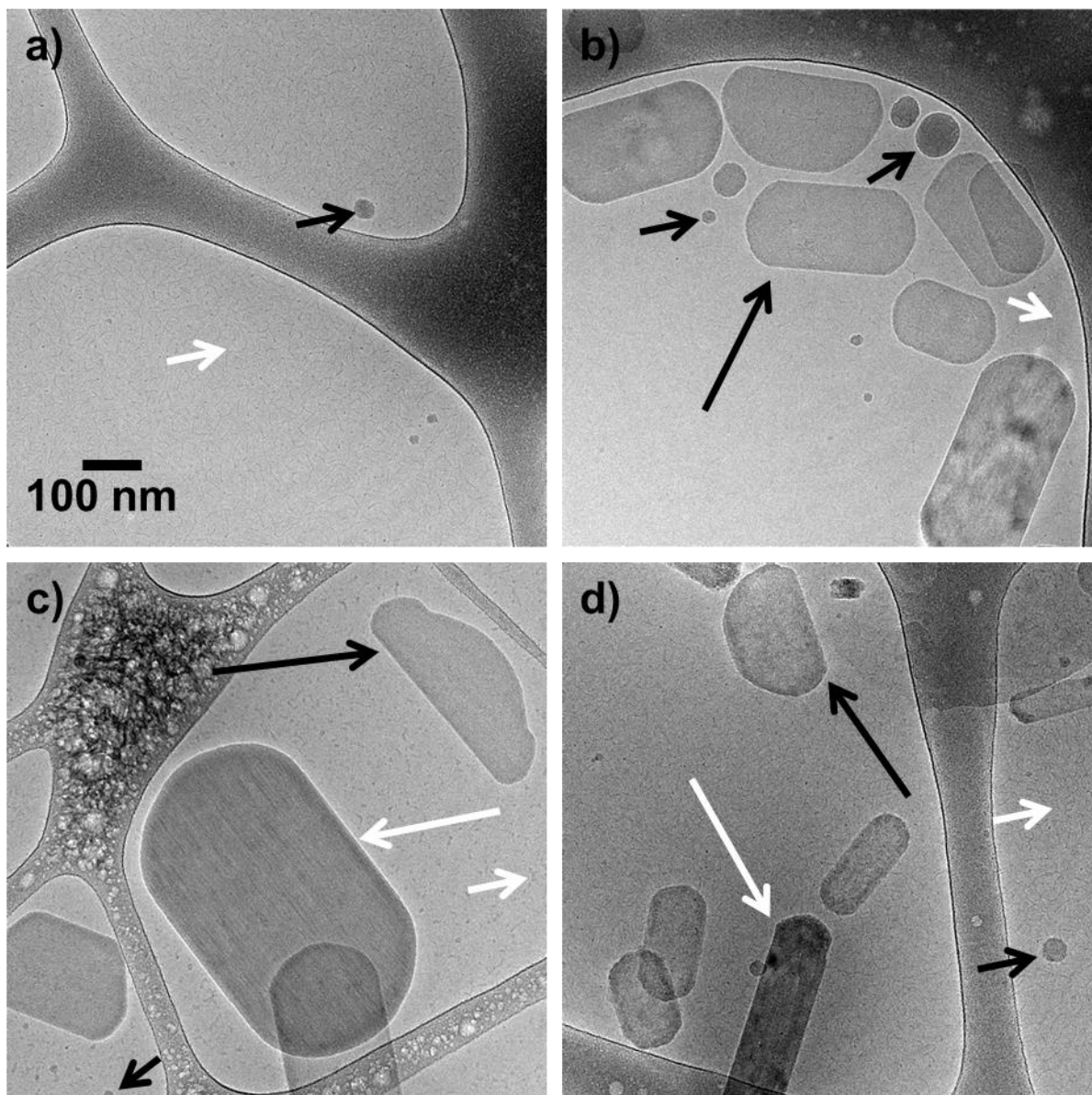
### 1) Size of the nanoplatelets

#### a. Influence of $\Phi_{\text{org}}$ on the nanoplatelets size

We showed in the previous chapter that the size of nanoplatelets did not depend much on the polymer concentration. The other parameter of the process that can be easily varied is the volumic fraction of organic phase in the emulsion,  $\Phi_{\text{org}}$  which allow to vary the total amount of C<sub>60</sub>. When  $\Phi_{\text{org}}$  is increased, the total amount of C<sub>60</sub> available for dispersion also increases. We showed that by increasing this amount, the final concentration of C<sub>60</sub> particles in water increases up to 8 g/L when  $C_{\text{pol}}=35$  g/L and  $\Phi_{\text{org}}=75\%$ .

Here, we show the influence of varying  $\Phi_{\text{org}}$  on the size of the particles. Figure 4.1 displays representative cryo-TEM pictures of samples prepared at various  $\Phi_{\text{org}}$ . First, in all cases we can observe worm-like micelles (WLM) resulting from the self-assembly of the polymer in excess (short white arrows). At low  $\Phi_{\text{org}}$  (10%, see Figure 4.1a), a low amount of small isotropic particles was obtained (short black arrows), and no nanoplatelets were observed. The latter were however observed (long black arrows) when  $\Phi_{\text{org}}$  was increased to 25% (Figure 4.1b). They clearly represent the majority of C<sub>60</sub> particles in terms of volume. Undefined isotropic particles are still present in lesser extent (short black arrows). When  $\Phi_{\text{org}}$  was increased up to 40% (Figure 4.1c), bigger nanoplatelets mostly in terms of width and thickness were observed (long white arrows), along with smaller nanoplatelets and very few isotropic particles. All nanoplatelets were surrounded by a white outline, called Fresnel fringe and caused by the high density of the particles. Fringes can be observed in the internal structure of the bigger nanoplatelets and some of them displayed white halos, which is typical of Bragg reflections.<sup>1</sup> Both observations indicate that these particles are crystalline. The Bragg reflections can also be observed for smaller nanoplatelets although they are thinner, and for the isotropic particles. To conclude, all types of C<sub>60</sub> particles are crystalline. Finally, when  $\Phi_{\text{org}}$  was increased up to 75% (Figure 4.1d), some platelets appear once again thicker than the others (white vs. black long arrows). Interestingly, they also appear to grow longer in one direction. Generally

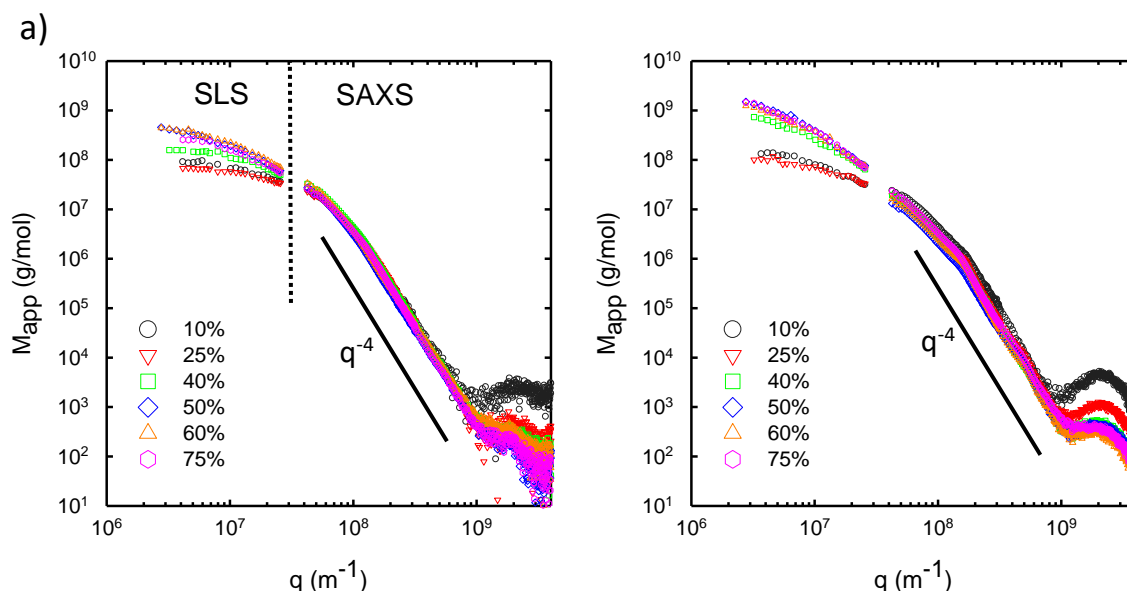
speaking, the nanoplatelets possess a very straight and sharp interface on the sides, but not in their extremities. This means that during the last steps of their formation at least, they grew only in the direction of extremities. Therefore, when bigger nanoplatelets are formed, they are actually longer but probably not larger nor thicker.



**Figure 4.1.** Representative cryo-TEM pictures of samples prepared at  $\Phi_{\text{org}}$ = a) 10% b) 25%, c) 40% and d) 75%. Short black arrows show undefined isotropic  $C_{60}$  particles. Long black arrows show  $C_{60}$  nanoplatelets. Short white arrows show WLM formed by 75C12. Long white arrows show bigger nanoplatelets.

The scattering intensity obtained by SLS and SAXS were converted in apparent molar mass by only taking into account the concentration and contrast factor of  $C_{60}$  (see section 2.4). It should be noted that the samples were diluted down to a few mg/L for SLS measurements in

order preventing them from absorbing the incident light. SLS gave access to  $q$  values comprised between  $3 \cdot 10^6$  and  $3 \cdot 10^7 \text{ m}^{-1}$ , and SAXS to  $q$  values between  $4 \cdot 10^7$  and  $4 \cdot 10^9 \text{ m}^{-1}$ . These data are combined for samples prepared at  $C_{\text{pol}}=10$  and  $35 \text{ g/L}$  (Figures 4.2a and 4.2b, respectively) at various  $\Phi_{\text{org}}$ . We can notice a good agreement between SLS and SAXS data, which validates the contrast factors computed for both techniques. It also means that dilution for SLS did not affect the structure of the particles. Whatever  $\Phi_{\text{org}}$ , the data obtained in SAXS between  $4 \cdot 10^7$  and  $1 \cdot 10^9 \text{ m}^{-1}$  superimpose which indicates that the structure of the particles is the same. SLS data indicate that the molar mass of the particles tends to increase when  $\Phi_{\text{org}}$  is increased, in good agreement with the previous observations with both DLS (see section 3.2.a, Figure 3.17) and cryo-TEM. SAXS data are not influenced by  $\Phi_{\text{org}}$ , which means that the local structure of the particles is the same. A Porod regime can be noticed, indicating a sharp interface between the particles and the solvent. Data obtained at large  $q$  scale ( $q > 1 \cdot 10^9 \text{ m}^{-1}$ ) will be discussed in section 4.2.a.

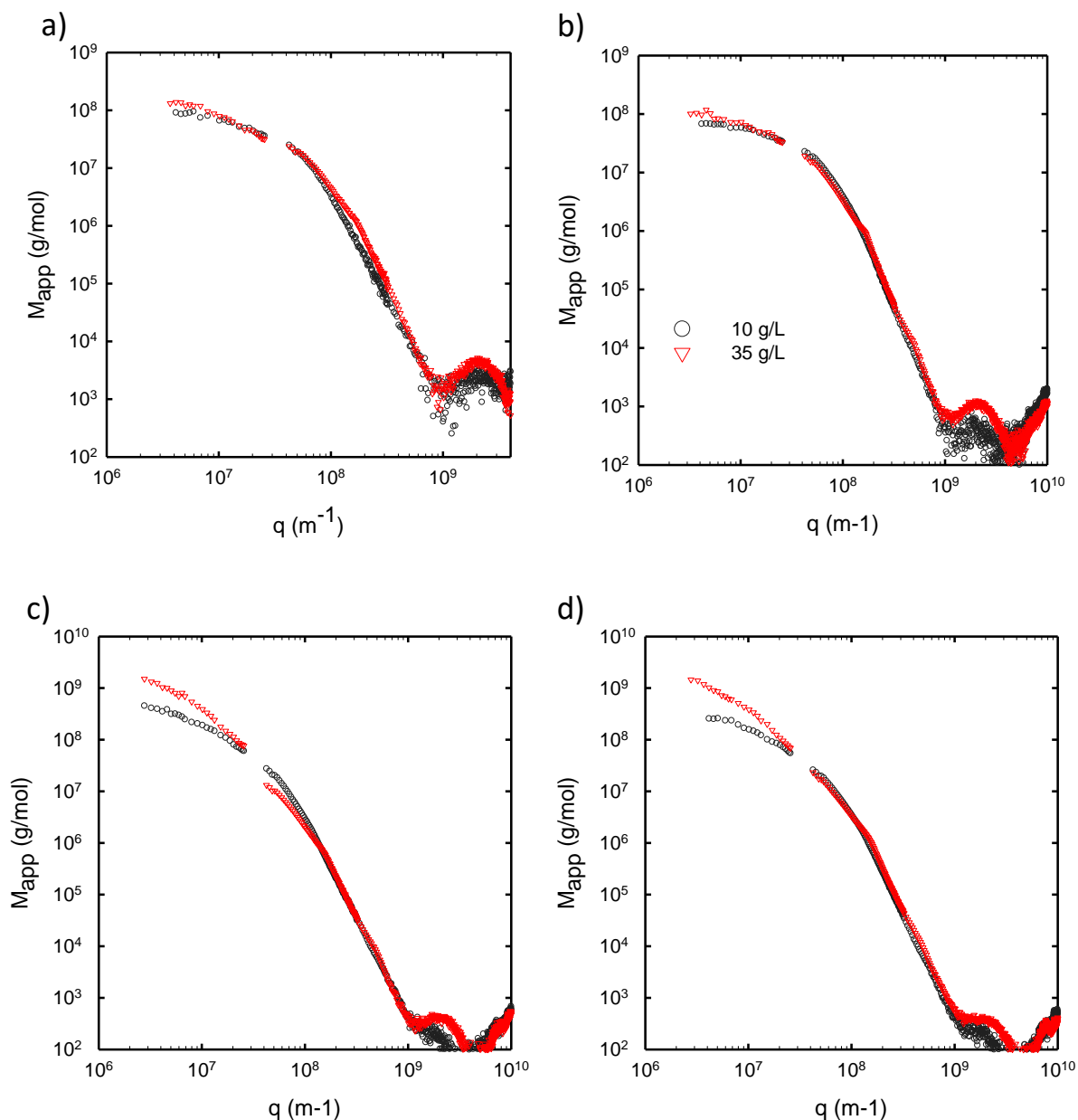


**Figure 4.2.** Variation of the apparent molar mass with the scattering wave vector  $q$  obtained thanks to a combination of SLS and SAXS measurements. Here,  $C_{\text{pol}}=$  a) 10 and b) 35 g/L and  $\Phi_{\text{org}}$  was varied as indicated in figure.

When data are compared at *iso*- $\Phi_{\text{org}}$  (Figure 4.3), one can see that they all superimpose between  $1 \cdot 10^8$  and  $1 \cdot 10^9 \text{ m}^{-1}$ , except for the presence of small oscillations in the scattered intensity when  $C_{\text{pol}}=35 \text{ g/L}$  (at  $1.7 \cdot 10^8$  and  $5 \cdot 10^8 \text{ m}^{-1}$ , see also Figure 4.2b), which will be discussed in section 4.2.a. This means that all particles have the same density.

At low  $\Phi_{\text{org}}$  values (10 and 25%, see Figures 4.3a and 4.3b) very few difference between  $C_{\text{pol}}=10$  and  $35 \text{ g/L}$  are seen over the whole  $q$  range. However, when  $\Phi_{\text{org}}$  is increased to 40-60% (Figure 4.3c), the particles formed with  $C_{\text{pol}}=35 \text{ g/L}$  have a higher molar mass than the

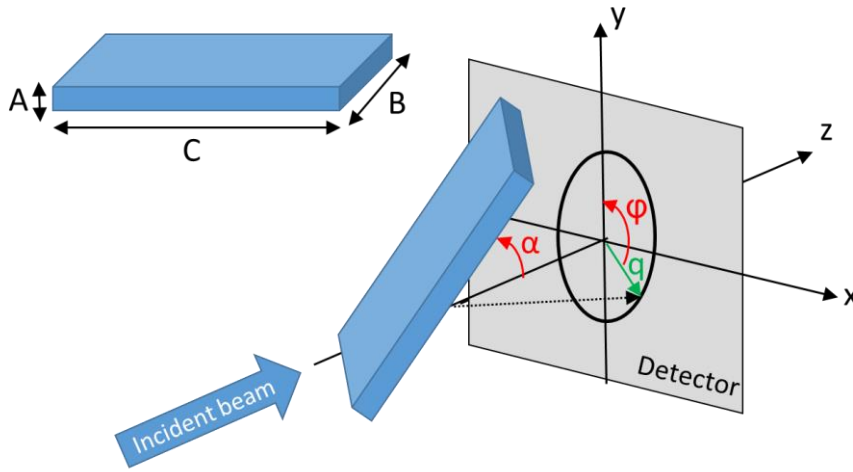
ones formed with  $C_{\text{pol}}=10$  g/L. Additionally, they scatter less in the  $4 \cdot 10^7$ - $1 \cdot 10^8$  m<sup>-1</sup> range, and reach the Porod regime at slightly higher  $q$  values. This can be attributed to an increase of the anisotropy of the objects when  $C_{\text{pol}}$  is increased. In the extreme case, when  $\Phi_{\text{org}}=75\%$ , the molar mass of the objects is nearly a decade higher when  $C_{\text{pol}}$  is increased from 10 to 35 g/L, but their intensity is the same in the whole  $q$  range covered by SAXS.



**Figure 4.3.** Variation of the apparent molar mass with the scattering wave vector  $q$  obtained thanks to a combination of SLS and SAXS measurements for  $C_{\text{pol}}=10$  (black) and 35 g/L (red). Here,  $\Phi_{\text{org}}=a)$  10%,  $b)$  25%,  $c)$  50% and  $d)$  75%.

### b. Size of the nanoplatelets

To go further in the analysis, we assumed that the particles were rectangular prisms as shown in Scheme 4.1. This model describes a massive parallelepiped with sides/sizes  $A \leq B \leq C$ . The lowest size  $A$  is set, and the dimensions  $B$  and  $C$  are set as ratios to  $A$ , i.e. instead of defining an absolute value for  $B$  and  $C$ , the ratios  $B/A$  and  $C/A$  are defined. This way, if polydispersity is applied on  $A$ , it is also applied on  $B$  and  $C$  and the parallelepiped shape is maintained. Since this object is anisotropic, its scattering also depends on its orientation with respect to  $q$ . Characteristic angles  $\alpha$  and  $\varphi$  are therefore defined.  $\alpha$  is the angle between the  $z$  axis (that is the direction of the incident beam) and  $C$ .  $\varphi$  is the angle between  $q$  and the  $y$  axis.



**Scheme 4.1.** Model representation of a rectangular prism, and of its characteristic dimensions in a scattering experiment.

The scattering amplitude  $A_p(q)$  is given by Eq. 4.1:<sup>2</sup>

$$A_p(q) = \frac{\sin(\frac{1}{2}q \cdot C \cdot \cos\alpha)}{\frac{1}{2}q \cdot \cos\alpha} \times \frac{\sin(\frac{1}{2}q \cdot B \cdot \sin\alpha \cdot \cos\varphi)}{\frac{1}{2}q \cdot \sin\alpha \cdot \cos\varphi} \times \frac{\sin(\frac{1}{2}q \cdot A \cdot \sin\alpha \cdot \sin\varphi)}{\frac{1}{2}q \cdot \sin\alpha \cdot \sin\varphi} \quad \text{Eq. 4.1}$$

The microscopy pictures displayed an isotropic orientation of the particles, although they are all laid flat because of the blotting. The form factor for randomly oriented rectangular prisms is obtained thanks to Eq. 4.2:<sup>2</sup>

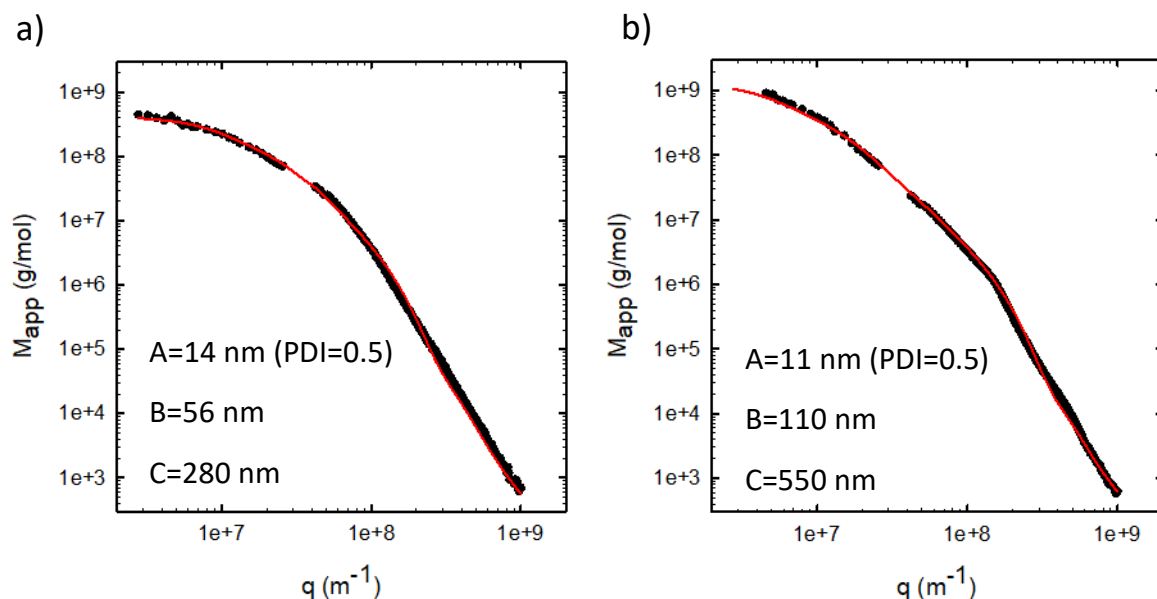
$$P(q) = \frac{1}{\pi} \int_0^{\pi} \int_0^{\pi/2} A_p^2 \cdot \sin\alpha \cdot d\alpha \cdot d\varphi \quad \text{Eq. 4.2}$$

This way, experimental combined SLS and SAXS data were fitted with the help of the SASView software, for two samples: Example 1 prepared with  $C_{\text{pol}}=10$  g/L and  $\Phi_{\text{org}}=40\%$  (Figure 4.4a), and Example 2 with  $C_{\text{pol}}=35$  g/L and  $\Phi_{\text{org}}=75\%$  (Figure 4.4b). First, it should be noted that it was necessary to apply polydispersity in order to take into consideration the smoothing of the



oscillations experimentally seen in the Porod regime. The polydispersity index was set at 0.5 for A, and no additional polydispersity on B and C was necessary.

The fits give an estimation of the thickness of the nanoplatelets, respectively 14 and 11 nm for the examples 1 and 2. These two values are of the same order of magnitude. Example 2 displayed bigger length and width, which can be related to higher  $R_h$  and  $M_w$  for samples prepared at higher  $\Phi_{org}$ . It could be concluded that increasing  $\Phi_{org}$  induced an increase of the size of the platelets, keeping their thickness almost constant.



**Figure 4.4.** Combined SLS and SAXS data plotted in terms of apparent molar mass over the  $q$  range, for samples obtained with a)  $C_{pol}=10$  g/L and  $\Phi_{org}=40\%$  and b)  $C_{pol}=35$  g/L and  $\Phi_{org}=75\%$ . Red lines are fits to the data considering a rectangular prism model with parameters indicated in the figure. PDI stands for PolyDispersity Index.

## 2) Internal structure

### a. Structure in SAXS

The SAXS data for samples prepared at  $C_{pol}=35$  g/L display small oscillations additionally to the form factor.

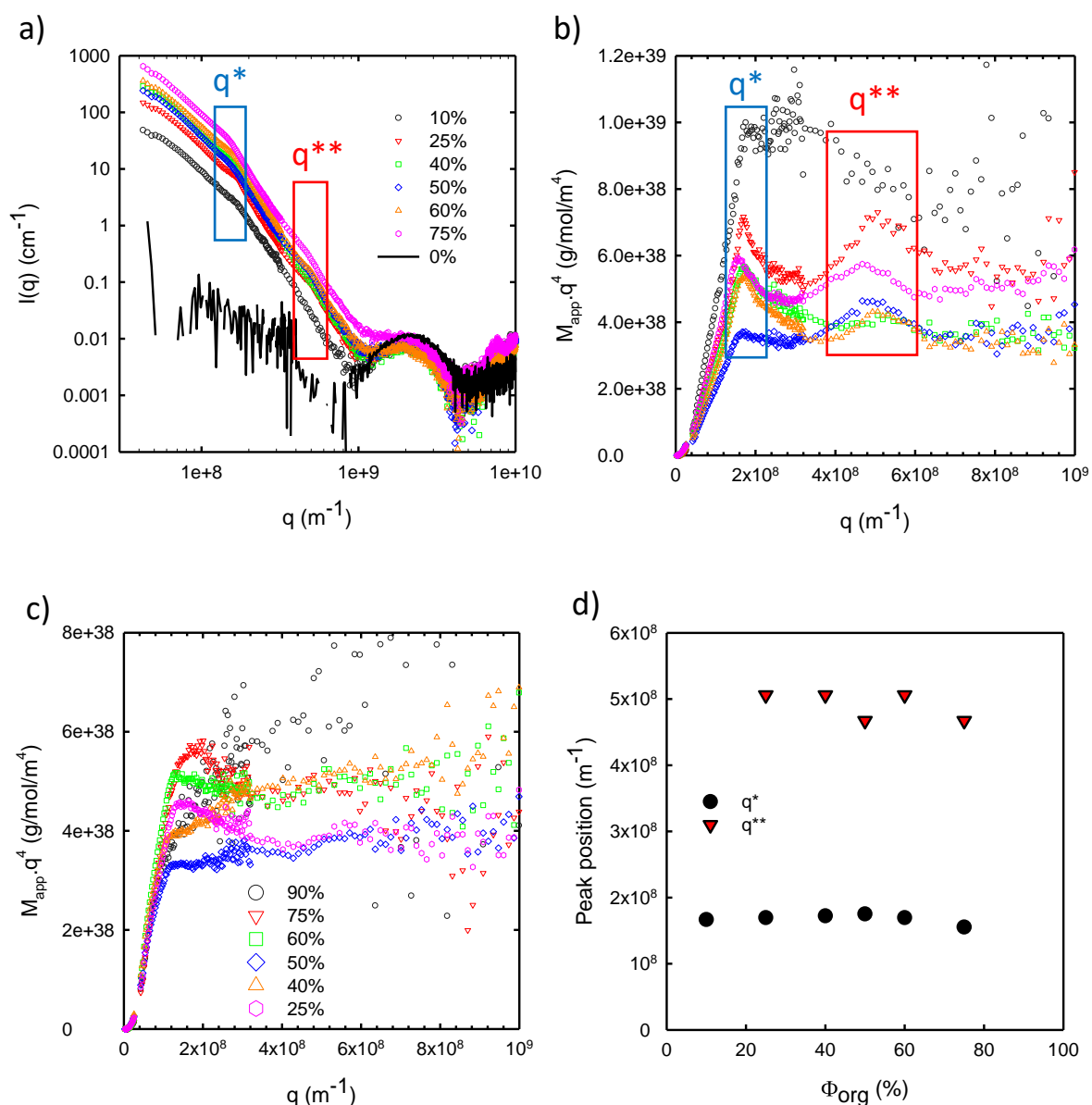
The most obvious one is seen at high  $q$  values (above  $10^{-9} \text{ m}^{-1}$ ), see Figure 4.2b. It is tempting to say that its intensity decreases with increasing  $\Phi_{org}$ , however when data are expressed in terms of scattered intensity (Figure 4.5a), the intensity is the same for all samples. Actually, a solution of polymer at the same concentration without C<sub>60</sub> particles displays the same feature. The oscillation at high  $q$  for the dispersion of nanoparticles is then related to the polymer which

displays the formation of worm-like micelles whose diameter corresponds to two times the size of the alkyl side chains.<sup>3</sup>

Also, two other less marked oscillations at  $q$  values noted  $q^*$  and  $q^{**}$  can be distinguished on Figure 4.5a. They can be better seen when plotting data in a Porod way, *i.e.* by multiplying the scattered intensity with  $q^4$ . see Figure 4.5b. Note that for samples prepared at  $C_{\text{pol}}=10$  g/L, the  $q^*$  peak was difficult to observe and the  $q^{**}$  was never observed, see Figure 4.5c. Moreover, the position of the peaks does not vary with  $\Phi_{\text{org}}$  (Figure 4.5d) which means that particles size or concentration do not have an influence on it. Therefore, interparticles interactions could be excluded. In addition, the first maximum is located around  $q^*=1.7 \cdot 10^8 \text{ m}^{-1}$ , and the second around  $q^{**}=5.0 \cdot 10^8 \text{ m}^{-1}=3q^*$ . Since we deal with nanoplatelets, one could think of a structure factor coming from lamellas ordered stacking. However, if it was the case we should also observe a second harmonic at  $2q^*$ , since we observe the  $3q^*$  harmonic. It might not be seen because of compensation of the maximum of structure factor by a minimum of form factor (Porod oscillation), however this is unlikely.

The peak at  $q^{**}$  is actually located at the same position as the structure factor maximum observed for a solution of polymer at 35 g/L in Small-Angle Neutron Scattering (SANS).  $q^{**}$  could then originate from the polymer but again its scattered intensity should be negligible on this  $q$  range, see Figure 4.5a. We could speculate that this is related to a large amount of polymer adsorbed at the interface of the particles. SANS measurements would allow to confirm this hypothesis, as the contrast of 75C12 is very high contrary to C<sub>60</sub> (The scattering length densities values for D<sub>2</sub>O, 75C12 and C<sub>60</sub> are respectively  $6.397 \cdot 10^{10}$ ,  $0.474 \cdot 10^{10}$  and  $5.501 \cdot 10^{10} \text{ cm}^{-2}$ ).





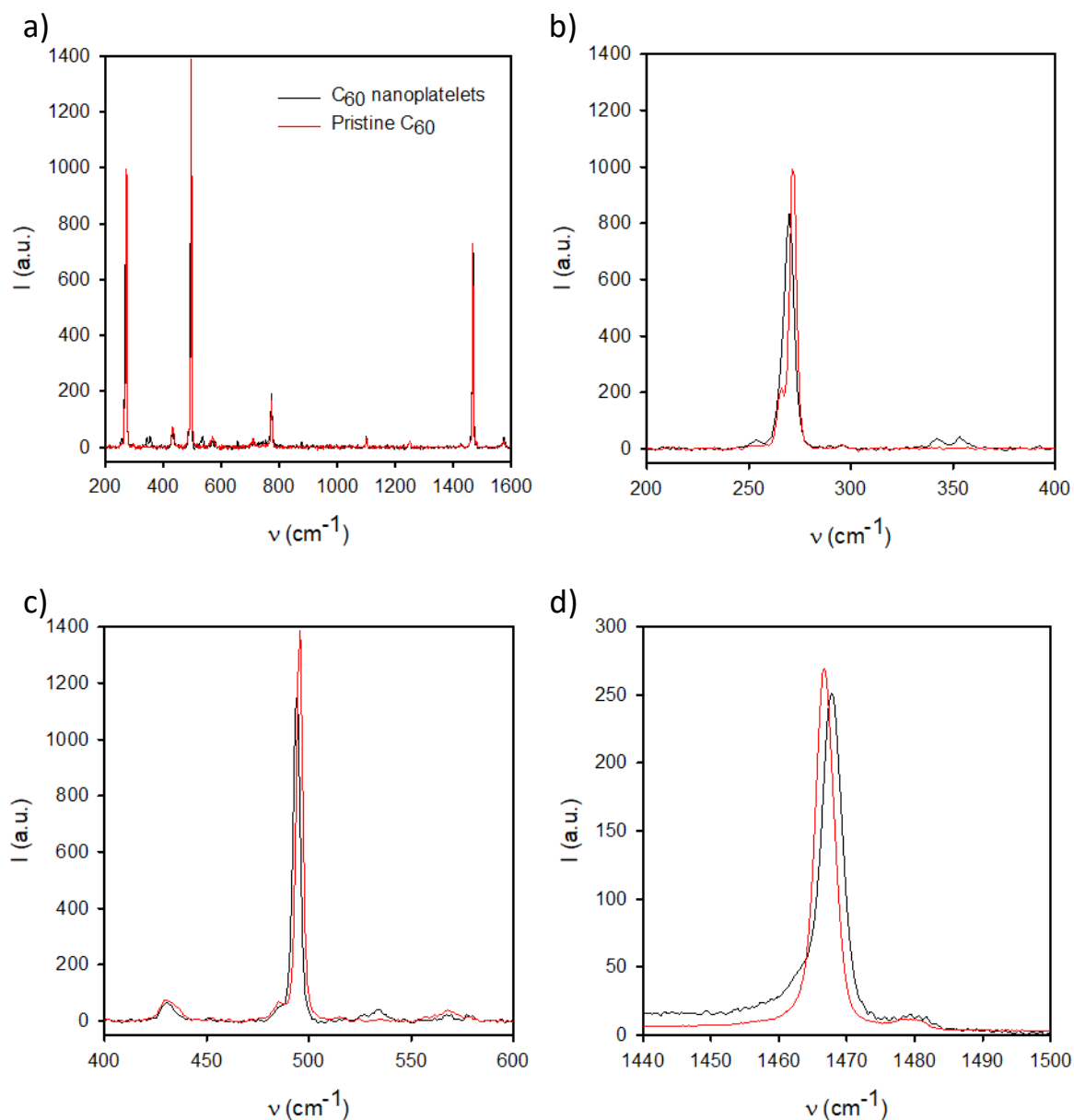
**Figure 4.5.** a) Scattered intensity as a function of  $q$  for SAXS experiments on samples with  $C_{pol}=35$  g/L and various  $\Phi_{org}$  indicated in figure. The black solid line is a control sample with the same  $C_{pol}$  but no fullerene. b) Porod representations of the same data. c) Porod representation of the data with  $C_{pol}=10$  g/L. d) Positions of the peaks as function of  $\Phi_{org}$  for  $C_{pol}=10$  g/L.

### b. Raman scattering

The Raman spectra of dried C<sub>60</sub> suspensions with and without 75C12 are displayed in Figure 4.6. Some of the characteristic bands of neat C<sub>60</sub> are slightly shifted to lower wavenumbers (from 272 to 270, from 495 to 494, from 1467 to 1468 and from 1573 to 1574 cm<sup>-1</sup>). All of these bands are slightly broader in presence of 75C12. On the molecular scale, it means that the vibrations of C<sub>60</sub> are affected by the polymer, which suggests that polymer is very close to it, inducing a mechanical strain on C<sub>60</sub>.

Additionally, new bands appeared in presence of polymer at 342, 353 and 534 cm<sup>-1</sup> (see Figures 4.6b and c). They do not correspond to 75C12 vibration bands nor to the substrate. These bands once again hint at the existence of strong interactions between C<sub>60</sub> and 75C12 at the molecular scale.

These measurements can be considered as preliminary, as they were made at the dried state. To better describe the system, Raman spectra measurements on single particles in solution trapped with an optical tweezer will be achieved in the future.



**Figure 4.6.** a) Raman spectrum of neat C<sub>60</sub> and C<sub>60</sub> nanoplatelets with 75C12 with a resolution of 1.09 cm<sup>-1</sup>. Magnifications are shown b) between 200 and 400 cm<sup>-1</sup> and c) between 400 and 600 cm<sup>-1</sup>. d) Spectrum between 1440 and 1500 cm<sup>-1</sup> with a resolution of 0.17 cm<sup>-1</sup>.

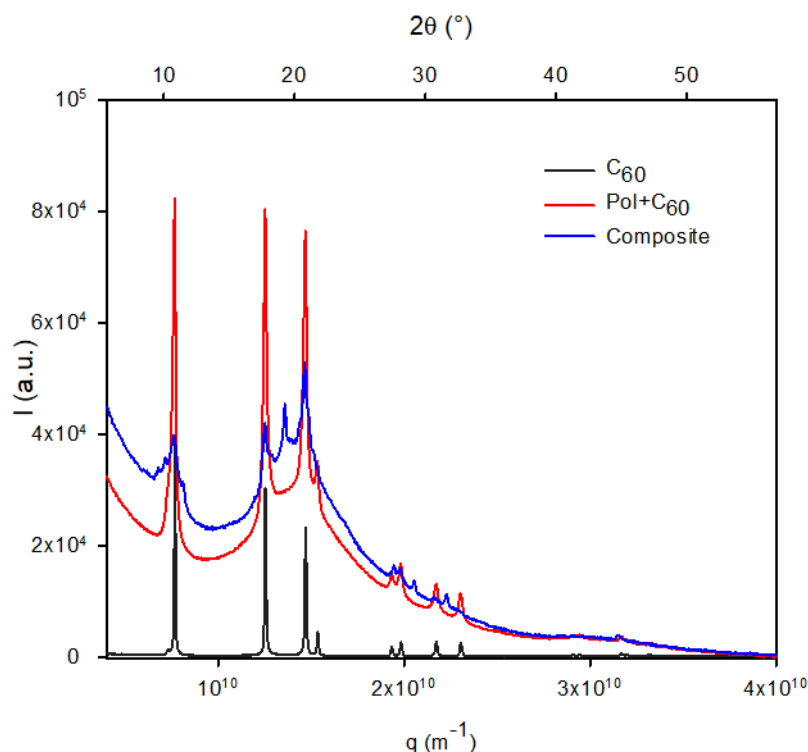
### c. Wide Angle X-Ray diffraction

As we briefly discussed in Chapter 3, the cryo-TEM pictures highlight the crystalline state of the particles. The unusual 2D morphology of the particles suggests that their crystallinity may be affected by the process or the presence of polymer. For this reason, we conducted Wide Angle X-Ray Diffraction (WAXD) experiments that give information at higher  $q$  than SAXS, in order to probe the intramolecular scale. Thus, these experiments allowed to cover  $q$  values comprised between  $4 \cdot 10^9$  and  $4 \cdot 10^{10} \text{ m}^{-1}$ . The diffraction patterns are shown in Figure 4.7. Neat C<sub>60</sub> exhibited a face-centered cubic structure (fcc), as expected for pure fullerene.<sup>4</sup> When it was milled together with the polymer, the fcc structure was still observed with broadened peaks. This can be explained by the decrease of the size of the crystals according to Scherrer equation (Eq.4.3):

$$R = \frac{K\lambda}{\beta \cos\theta} \quad \text{Eq. 4.3}$$

With  $R$  the mean size of the crystalline domains,  $K$  a dimensionless form factor  $\lambda$  the X-Ray wavelength,  $\beta$  the full width at half maximum of the peak, and  $\theta$  the diffraction angle.

In addition, an important background signal was noted and could be directly associated to the scattering by 75C12. When it comes to C<sub>60</sub> nanoplatelets, however, the crystalline order is different, see Figure 4.7. At  $2\theta \approx 10^\circ$ , several peaks appeared whereas a single peak was observed for pristine C<sub>60</sub>. A peak appeared at  $2\theta = 19.2^\circ$ , and the peak at  $21.8^\circ$  disappeared.



**Figure 4.7.** Diffraction patterns of pristine C<sub>60</sub> (black), co-ground C<sub>60</sub> and 75C12 (red) and C<sub>60</sub> nanoplatelets with 75C12 (blue).

The diffraction peaks of C<sub>60</sub> nanoplatelets are indexed in Table 4.1. They are compared with the diffraction peaks that should be observed in the case of fcc and hexagonal close-packed (hcp) structures which are the two lower-energy structures for C<sub>60</sub>.<sup>5</sup> The hcp structure displays peaks at very similar positions as fcc and additional peaks can be observed. This structure better describes the one of the nanoplatelets, as many of these additional peaks are also observed for the latter. Still, some inconsistencies remain. A peak should be observed around 15° in the case of a pure hcp structure, and the peaks at high angles (starting at 27°) seem to be shifted to lower angles for nanoplatelets compared to fcc and hcp. The peak at 30.89° is hardly seen and the peak at 32.7° is not detected.

**Table 4.1.** Position of peaks measured by WAXD, and comparison with fcc (from experimental data for pure C<sub>60</sub>) and hcp (from ref. 4 and 6) structures.

C <sub>60</sub> nanoplatelets		fcc		hcp	
Peak position (2 $\theta$ value in °)	Peak position (°)	Attribution (hkl)	Peak position (°)	Attribution (hkl)	
9.55	X	X	X	X	
10.10	X	X	10.14	1 0 0	
10.76	10.84	1 1 1	10.78	0 0 2	
11.39	X	X	X	X	
X	X	X	14.82	1 0 2	
17.66	17.70	2 2 0	17.64	1 1 0	
19.18	X	X	19.14	1 0 3	
20.71	20.76	3 1 1	20.70	1 1 2	
21.34	21.66	2 2 2	21.64	0 0 4	
27.61	27.43	3 3 1		2 1 0	
28.12	28.14	4 2 0	28.04	1 1 4	
29.17	X	X	X	X	
30.89	30.88	4 2 2	30.78	3 0 0	
31.71	X	X	X	X	
X	32.76	5 1 1	32.70	0 0 6	

From these observations, one can conclude that the crystalline structure of the C<sub>60</sub> nanoplatelets is far from trivial. These crystals might be a mixture of different crystalline phases including fcc and hcp phases,<sup>7</sup> but additional phases are still unidentified. The XRD data are not in agreement with the ones of C<sub>60</sub>-carbon disulfide co-crystals (the so-called crystal solvates 2C<sub>60</sub>.3CS<sub>2</sub>). Another possibility we considered is the polymerization of C<sub>60</sub> that is usually achieved under high pressures.<sup>8,9</sup> In this structure, C<sub>60</sub> molecules are covalently bound and display a mixture of rhombohedral and tetragonal crystalline structures.<sup>9</sup> In ref. 10, an orthogonal structure was claimed by the authors for a single crystal grown from a C<sub>60</sub> solution in CS<sub>2</sub>, however the crystallographic data are not available, so no comparison can be made.

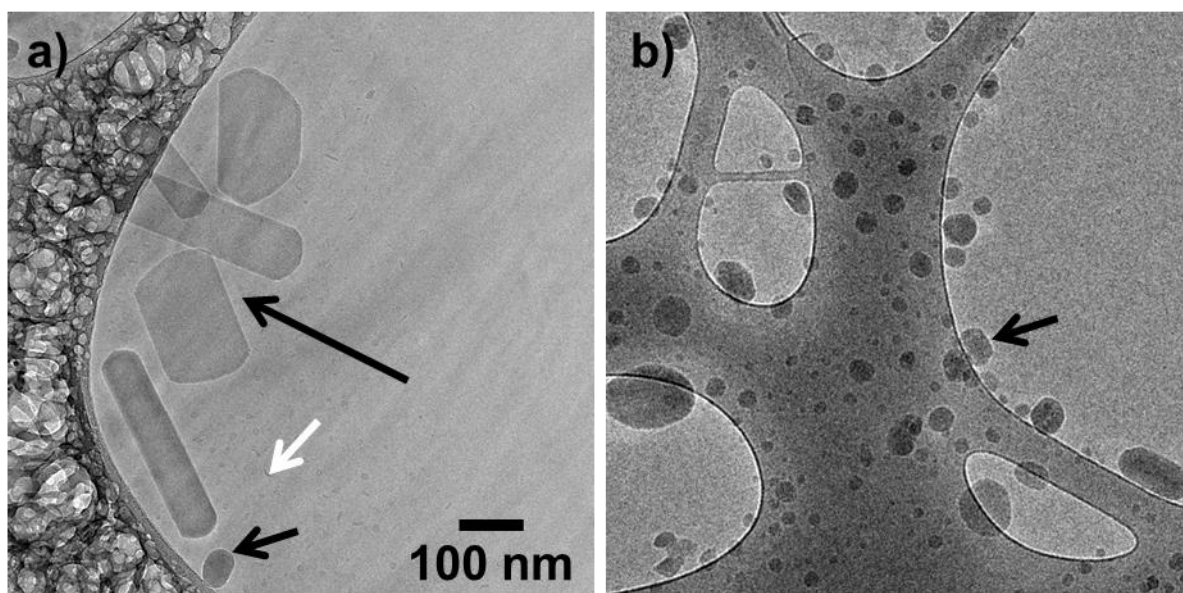
### 3) Formation of nanoplatelets with other stabilizers

The previous structural analysis of C<sub>60</sub> still does not explain why the growth, at least after some extent, only occurs in two dimensions. In Chapter 3, we discussed the role of the polymer in the crystallisation process and proposed the hypothesis that the growth into nanoplatelets occurred specifically at the interface, where the crystal can be sustained by C<sub>60</sub> molecules that are available in the organic phase while interacting with the polymer. The question is now whether this two-dimensional growth is possible to achieve with other stabilizers or if it is specific to 75C12. More precisely, the influence of the chemical structure of the stabilizer on the particle morphology will be assessed. We will now detail the use of other stabilizers, first polymers with a similar chemical structure as 75C12 and second commercial stabilizers that present common features with it.

#### a. Other XCn polymers

It is tempting to draw a link between the anisotropic morphology of the nanoplatelets and the anisotropic micelles formed by the amphiphilic polymer.<sup>11</sup> One could indeed think that polymeric self-assemblies could template the growth of C<sub>60</sub> nanocrystals. In order to confirm this hypothesis, we used other stabilizers with a similar chemical structure. On one hand, 45C12 is a copolymer equivalent to 75C12 but with only 45%mol of cationic moieties and which self-assembles into lamellae rather than worm-like micelles.<sup>3</sup> On the other hand, 75C4 is an equivalent of 75C12 but with much shorter alkyl side chains (4 vs. 12) and that consequently displays no self-assembly. We chose the formulation with C<sub>pol</sub>=10 g/L and Φ<sub>org</sub>=40%, as these conditions corresponded to the highest ratio of fullerene with respect to polymer, with high C<sub>60</sub> concentration (4 g/L) and yield (around 80%), as shown in Chapter 3.

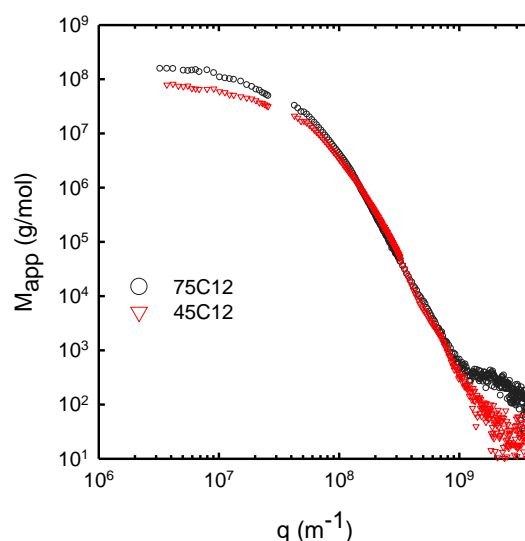
Fullerene dispersions were therefore obtained with C<sub>full</sub>=5.0 g/L with 45C12 and 1.7 g/L for 75C4. In the first case, it means that nearly 100% fullerene was dispersed. For 75C4, however, the dispersion yield is significantly lower (33%). The morphology of C<sub>60</sub> particles obtained with 45C12 and 75C4 was determined by cryo-TEM observations. Particles prepared with 45C12 (Figure 4.8a) were very similar to the ones prepared with 75C12 (Figure 4.1c). Nanoplatelets (long black arrow) are observed along with a minority of undefined, isotropic particles (short black arrow). The nanoplatelets appear slightly more elongated than with 75C12. Polymeric micelles in the shape of lamellas (short white arrow) can be observed in the background. 75C4 was not able to trigger the formation of nanoplatelets (Figure 4.8b). Only the second type of particles, which are undefined and much more isotropic, was formed. Once again, Bragg reflections are seen, meaning that they are probably crystalline.



**Figure 4.8.** Cryo-TEM pictures of  $C_{60}$  nanoparticles produced with a) 45C12 and b) 75C4 at  $C_{\text{pol}}=10$  g/L and  $\Phi_{\text{org}}=40\%$ .

Combined SLS and SAXS experiment corroborate these observations, as the internal structure of the particles prepared with 75C12 and 45C12 is the same, and their overall size is similar although slightly smaller with 45C12 which can be due to their slightly more elongated shape (Figure 4.9). One can conclude that anisotropic self-assembly of the polymer chains seems mandatory to produce anisotropic fullerene particles. Another hypothesis could be that an extent in terms of hydrophobicity is required to trigger the anisotropic growth of the crystals, but it is hard to draw a link with the growth mechanism.

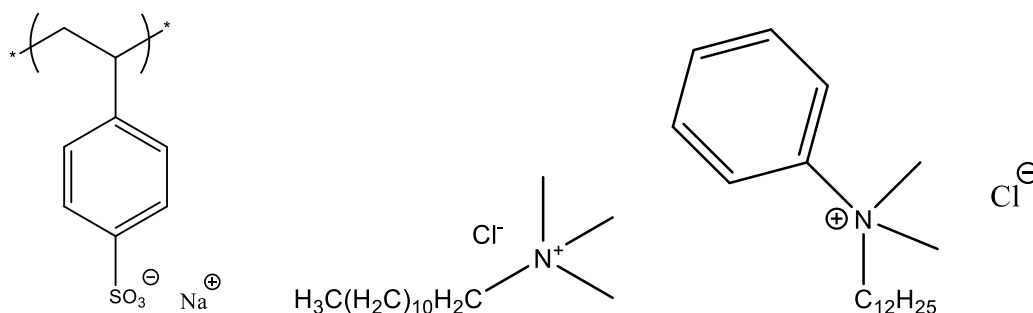




**Figure 4.9.** Combined SLS and SAXS measurements for particles prepared with 75C12 and 45C12 at  $C_{\text{pol}}=10$  g/L and  $\Phi_{\text{org}}=40\%$ .

#### b. De-formulation of cationic polymers

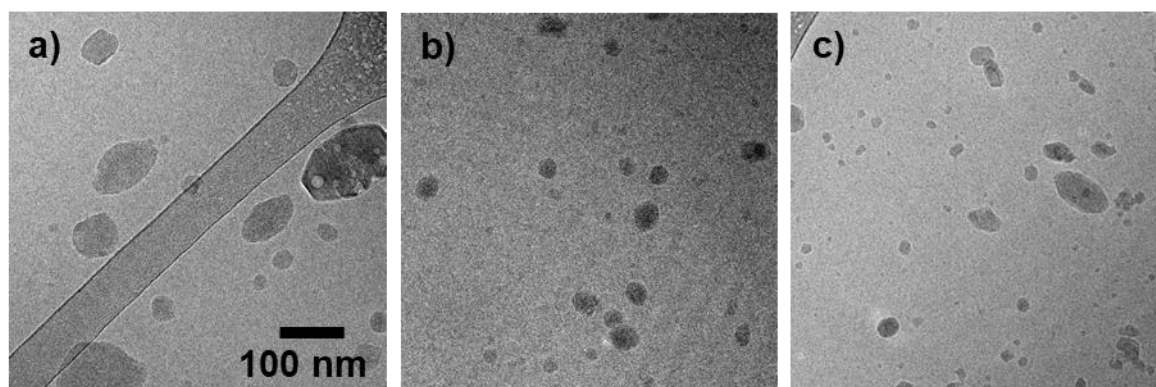
Using only polymers from the same family as 75C12 has its limitations for understanding the relationship between the chemical structure of the stabilizer and its ability to trigger the formation of C<sub>60</sub> nanoplatelets. Does the stabilizer need to be polymeric ? cationic ? containing aromatic units ? To address these questions, we produced C<sub>60</sub> particles in water in the presence of commercial stabilizers that have chemical structures partially identical to 75C12, as displayed in Figure 4.10. Poly(styrene sulfonate) (PSS) is also a polyelectrolyte based on a poly(styrene) backbone. Dodecyltrimethylammonium chloride (DTAC) is identical to the surfactant unit carried by the poly(styrene) backbone of 75C12. Benzyltrimethylammonium chloride (BDDAC) possesses one additional phenyl ring on one of the methyl groups carried by the nitrogen atom. It can therefore be seen as the functionalized repeating unit of 75C12 and 45C12 which were both able to drive the formation of C<sub>60</sub> nanoplatelets. The same conditions as in the previous part were used, except that  $C_{\text{pol}}$  was adjusted to reach *iso*-molarity with 75C12 repeating units. Therefore, the concentrations of PSS, DTAC and BDDAC were set respectively at 6.6, 6.6 and 9.4 g/L. These three stabilizers were able to efficiently disperse C<sub>60</sub> in these conditions with fullerene concentrations equal to 3.8, 3.6 and 3.1 g/L respectively.



**Figure 4.10.** Chemical structures of (from left to right): poly(styrene sulfonate) (PSS), dodecyltrimethylammonium chloride (DTAC) and benzyldodecyldimethylammonium chloride (BDDAC).

With PSS as a stabilizer, the morphology was intermediary between the thin nanoplatelets and isotropic particles, see Figure 4.11a. The shape of the particles was not well-defined, with many defaults on the surface, but the particles were elongated and displayed a pretty low contrast, indicative of a small thickness. They were not as faceted as with 75C12.

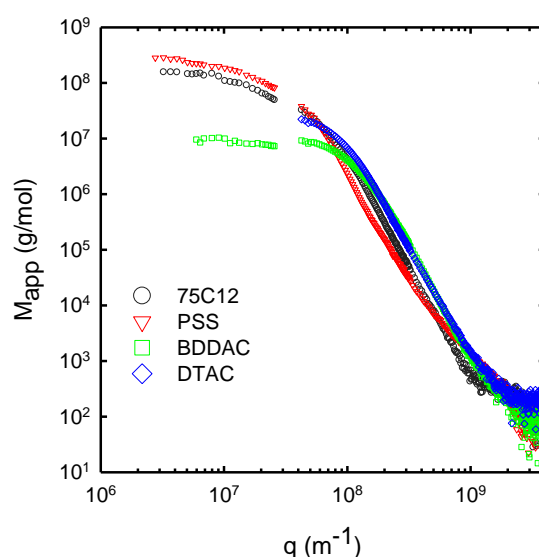
With the surfactants DTAC and BDDAC, the particles were isotropic (Figures 4.11b and c). Particles size was following the order PSS>>BDDAC>DTAC. Generally speaking, for the three stabilizers, only the biggest particles were elongated, suggesting that anisotropy appeared only in the last growth steps, as in the case of 75C12.



**Figure 4.11.** Cryo-TEM pictures of the C<sub>60</sub> particles prepared at  $\Phi_{\text{org}}=40\%$  with a) PSS (6.6 g/L), b) DTAC (6.6 g/L) and c) BDDAC (9.4 g/L).

Combined SLS and SAXS data for C<sub>60</sub> particles prepared with PSS are presented on Figure 4.12. The reaching of the Porod regime occurred at slightly lower  $q$  values for PSS, meaning that the particles are thicker than with 75C12 and 45C12. At high  $q$  values, the scattered intensity is deviating from the Porod regime because of PSS contribution, which becomes no more negligible. We were not able to collect SLS data for the DTAC sample because of the presence of aggregates. However, SAXS intensity tend toward a plateau with decreasing  $q$ .

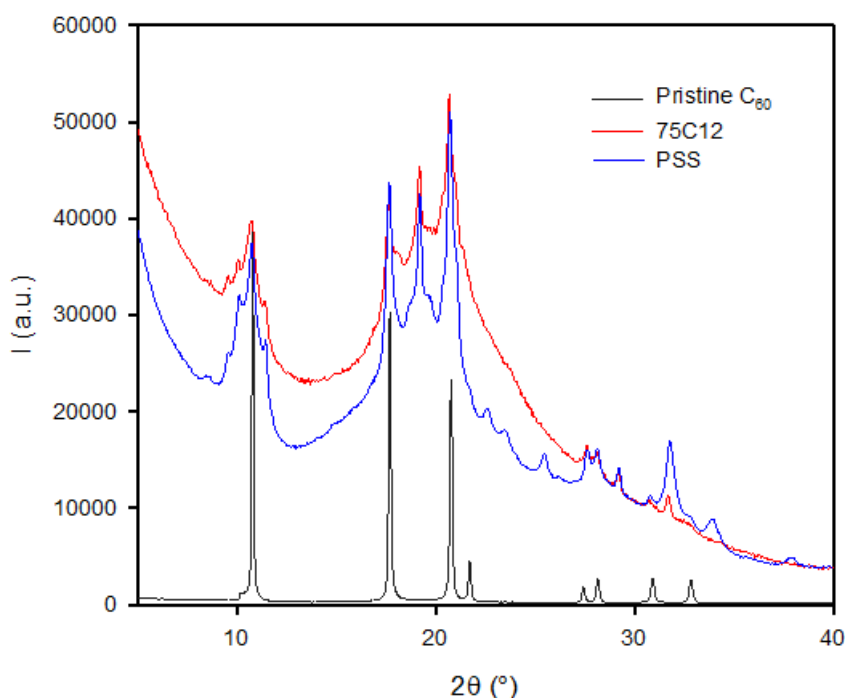
The corresponding molar mass, as well as for BDDAC, was much lower than with 75C12, in agreement with cryo-TEM observations. The transition between this plateau and the Porod regime is very sharp with DTAC and BDDAC, because the particles are isotropic, and occurs at higher  $q$  values than with 75C12, because they are smaller. In Porod regime, the scattered intensity was slightly higher for particles stabilized by DTAC and BDDAC. This can be assigned to a slightly higher density of the particles, maybe because of a more compact ordering of C<sub>60</sub> molecules.



**Figure 4.12.** Combined SLS and SAXS measurements for particles prepared with 75C12, PSS, DTAC and BDDAC.

The use of other stabilizers than 75C12 is an opportunity to learn more about the crystalline structure. Indeed, as we already discussed in the part 2.c of this chapter, it is still unclear if the peculiar crystalline order of C<sub>60</sub> nanoplatelets is due to the emulsification-evaporation process itself or to the presence of 75C12 during the growth of the particles. Therefore, WAXD measurements were made on particles obtained with PSS as a stabilizer. It was not possible to do the same with DTAC and BDDAC samples, because measurements had to be made on dried particles to minimize the noise due to water, and surfactant are very hygroscopic, making their complete freeze-drying impossible to achieve. The diffraction pattern of particles obtained with PSS is shown in Figure 4.13. One can observe that the diffraction peaks are very similar to the ones of the particles obtained with 75C12. However, additional diffraction peaks appeared at  $2\theta=22.60^\circ$ ,  $23.47^\circ$ ,  $25.51^\circ$ ,  $33.94^\circ$  and  $37.88^\circ$ . These peaks do not correspond to the fcc nor to the hcp lattices of C<sub>60</sub>. These peaks cannot be attributed to PSS itself since it does not display crystallinity. The additional peaks can therefore be attributed to the presence

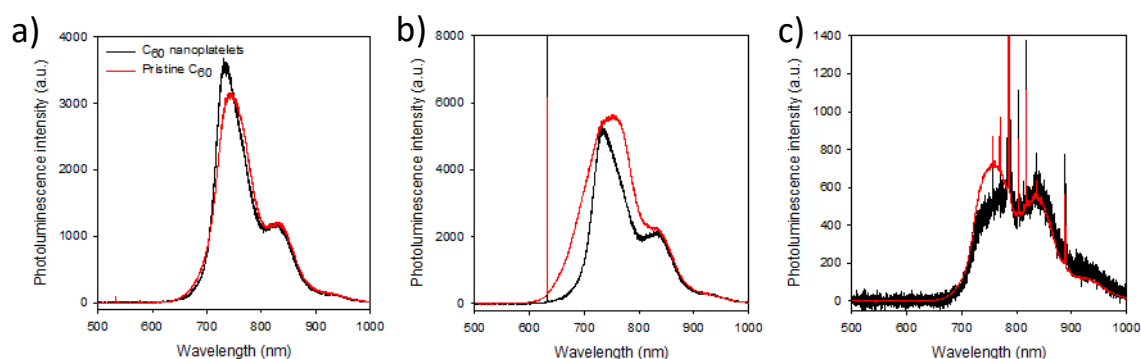
of an additional phase of  $C_{60}$ . Interestingly, the background noise associated to PSS was also very similar to the one of 75C12.



**Figure 4.13.** Diffraction pattern of pristine  $C_{60}$  and its particles obtained with the emulsification-evaporation process with 75C12 and PSS as stabilizers.

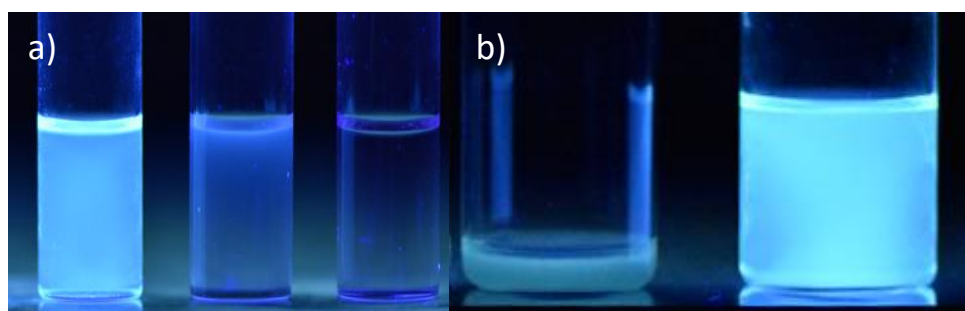
#### 4) Fluorescence of $C_{60}$ nanoplatelets

$C_{60}$  is known to weakly fluoresce in near infrared with no influence of the excitation wavelength.<sup>12, 13</sup> Fluorescence measurements were conducted with three excitation wavelengths: 532, 633 and 785 nm on pristine  $C_{60}$  and dried  $C_{60}$  nanoplatelets in presence of 75C12 (Figure 4.14). First, it should be noted that the emission spectra were similar for all excitation wavelengths, although the intensity was very low for the excitation at 785 nm, so the spectra are noisy. For pristine  $C_{60}$ , the principal emission band was broad and reached a maximum around 750 nm, and a second weaker band was located around 830 nm.  $C_{60}$  nanoplatelets displayed slightly narrowed emission spectra, especially for the excitation at 633 nm, and the first band was asymmetric. Because of the latter observation, the maximum emission was reached around 730 nm.



**Figure 4.14.** Fluorescence spectra of dried C<sub>60</sub> nanoplatelets (black) and pristine C<sub>60</sub> (red) for excitation wavelengths 532, 633 and 785 nm respectively from left to right.

On the other hand, in the UV region, C<sub>60</sub> is a good fluorescence quencher because of its ability to form charge transfer complexes when it is spatially close to the fluorescent specie.<sup>14</sup> The complex is called exciplex and is characterized by an isoemission point no matter the concentration of C<sub>60</sub>.<sup>15</sup> When it is formed, the fluorescence intensity decreases proportionally to the concentration of quencher. During this work, we noticed that 75C12 is fluorescent under UV irradiation, in both chloroform and water. Interestingly, when it is solubilized together with C<sub>60</sub> in chloroform, the fluorescence is dramatically lowered (Figure 4.15a). In water, after formation of C<sub>60</sub> nanoparticles with chloroform as a solvent, the fluorescence is also lowered compared to a control sample without C<sub>60</sub> (Figure 4.15b). These observations indicate that C<sub>60</sub> and 75C12 strongly interact in both solvents even though they do not display the same aggregation state in these two media. Quantitative measurements of fluorescence spectra will be made in the future to quantify the quenching ability of C<sub>60</sub> and to possibly display the formation of an exciplex.



**Figure 4.15.** Pictures of solutions under UV irradiation with a wavelength of 366 nm. a) Solutions in chloroform. From left to right, 75C12 (C=10 g/L), 75C12 (C=10 g/L) and C<sub>60</sub> (C=90 mg/L), C<sub>60</sub> (90 mg/L). b) Solutions in water with 75C12 (C=20 g/L) and C<sub>60</sub> (left: 30 mg/L and right: 0 mg/L).

## Conclusions

In this chapter, we focused on the structure of C<sub>60</sub> particles prepared with the emulsification-evaporation method in concentrated conditions. Two types of particles were obtained at the same time that were respectively undefined isotropic particles and faceted nanoplatelets. Both types of particles were crystalline, however WAXD measurements highlighted the existence of several crystal lattices in the mixture. The role of the stabilizer was clarified, as we showed that classical surfactants and polymers with a lower hydrophobicity do not induce the formation of nanoplatelets. Raman and fluorescence data highlighted the strong interaction between 75C12 and C<sub>60</sub>. The crystalline structure of C<sub>60</sub> particles still needs to be better understood, and their physical properties will be assessed in the future to identify potential applications.

## References

1. J. Dubochet, M. Adrian, J.-J. Chang, J.-C. Homo, J. Lepault, A. W. McDowell and P. Schultz, Cryo-electron microscopy of vitrified specimens. *Quarterly Reviews of Biophysics*, 1988, **21**, 129-228.
2. Nayuk, R.; Huber, K., Formfactors of Hollow and Massive Rectangular Parallelepipeds at Variable Degree of Anisometry. *Zeitschrift für Physikalische Chemie* **2012**, 226 (7-8), 837-854.
3. Limouzin-Morel, C.; Dutertre, F.; Moussa, W.; Gaillard, C.; Iliopoulos, I.; Bendejacq, D.; Nicolai, T.; Chassenieux, C., One and two dimensional self-assembly of comb-like amphiphilic copolyelectrolytes in aqueous solution. *Soft Matter* **2013**, 9 (37), 8931-8937.
4. Zhennan, G.; Jiuxin, Q.; Xihuang, Z.; Yongqing, W.; Xing, Z.; Sunqi, F.; Zizhao, G., Buckminsterfullerene C60: Synthesis, spectroscopic characterization and structure analysis. *The Journal of Physical Chemistry* **1991**, 95 (24), 9615-9618.
5. Quo, Y.; Karasawa, N.; Goddard, W. A., Prediction of fullerene packing in C60 and C70 crystals. *Nature* **1991**, 351 (6326), 464-467.
6. Ginzburg, B. M.; Tuichiev, S.; Tabarov, S. K.; Shepelevskii, A. A.; Shibaev, L. A., X-ray diffraction analysis of C60 fullerene powder and fullerene soot. *Technical Physics* **2005**, 50 (11), 1458-1461.
7. Li, Z. G.; Fagan, P. J., Coexistence of fcc and hcp phases of C60. Microstructural characterization of C60 and metal complexes of C60. *Chemical Physics Letters* **1992**, 194 (4), 461-466.
8. Pei, C.; Feng, M.; Yang, Z.; Yao, M.; Yuan, Y.; Li, X.; Hu, B.; Shen, M.; Chen, B.; Sundqvist, B.; Wang, L., Quasi 3D polymerization in C60 bilayers in a fullerene solvate. *Carbon* **2017**, 124, 499-505.
9. Núñez-Regueiro, M.; Marques, L.; Hodeau, J. L.; Béthoux, O.; Perroux, M., Polymerized Fullerite Structures. *Physical Review Letters* **1995**, 74 (2), 278-281.
10. Kikuchi, K.; Suzuki, S.; Saito, K.; Shiromaru, H.; Ikemoto, I.; Achiba, Y.; Zakhidov, A. A.; Ugawa, A.; Imaeda, K.; Inokuchi, H.; Yakushi, K., Structure and superconductivity of single crystalline C60. *Physica C: Superconductivity* **1991**, 185-189, 415-416.
11. Dutertre, F.; Gaillard, C. d.; Chassenieux, C.; Nicolai, T., Branched Wormlike Micelles Formed by Self-Assembled Comblike Amphiphilic Copolyelectrolytes. *Macromolecules* **2015**, 48 (20), 7604-7612.
12. Catalan, J.; Elguero, J., Fluorescence of fullerenes (C60 and C70). *Journal of the American Chemical Society* **1993**, 115 (20), 9249-9252.
13. Sun, Y. P.; Wang, P.; Hamilton, N. B., Fluorescence spectra and quantum yields of buckminsterfullerene (C60) in room-temperature solutions. No excitation wavelength dependence. *Journal of the American Chemical Society* **1993**, 115 (14), 6378-6381.
14. Wang, J.; Wang, D.; Moses, D.; Heeger, A. J., Dynamic quenching of 5-(2'-ethyl-hexyloxy)-p-phenylene vinylene (MEH-PPV) by charge transfer to a C60 derivative in solution. *Journal of Applied Polymer Science* **2001**, 82 (10), 2553-2557.
15. Lin, H.; Weng, Y.; Huang, H.; He, Q.; Zheng, M.; Bai, F., Photoinduced partial charge transfer between conjugated polymer and fullerene in solutions. *Applied Physics Letters* **2004**, 84 (16), 2980-2982.





## Chapter 5. Nanocomposite hydrogels functionalized by C<sub>60</sub> nanoplatelets: effect on the mechanical properties

1) Elaboration and characterization of the nanocomposite hydrogels.....	169
a. Composition of the fullerene/polymer composite powders.....	169
b. Preparation of the nanocomposite hydrogels .....	170
c. Structure of the nanocomposite hydrogels .....	171
2) Rheological properties of the nanocomposite hydrogels .....	173
a. Stiffness and dynamics of the networks .....	173
b. Non-linear mechanical properties .....	177
Conclusions .....	179
References .....	180



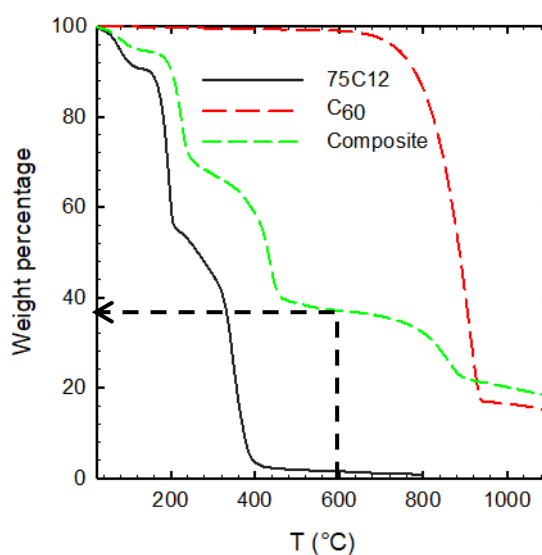
## Chapter 5. Nanocomposite hydrogels functionalized by C<sub>60</sub> nanoplatelets: effect on the mechanical properties

In this chapter, we describe the incorporation of the C<sub>60</sub> nanoparticles in a hydrogel matrix formed by 75C12, their stabilizer. First, the elaboration of hydrogels will be described and the aggregation state of C<sub>60</sub> particles will be discussed. Then, we will present the rheological properties of these nanocomposite hydrogels.

### 1) Elaboration and characterization of the nanocomposite hydrogels

#### a. Composition of the fullerene/polymer composite powders

As it was described in section 2.2.c, composite powders consisting in the amphiphilic polymer 75C12 and C<sub>60</sub> fullerene were prepared by freeze-drying a large quantity of aqueous colloidal suspensions with C<sub>pol</sub>=10 g/L and C<sub>full</sub>=4 g/L. The composites, as well as pure polymer and fullerene, were analyzed by TGA between 20 and 1100°C to quantify the content of polymer and fullerene, see Figure 5.1. The neat polymer displayed three weight losses. First, water evaporated around 100°C and represented 8% of the total weight, which is sound given the polyelectrolyte nature of the polymer. It's worthy to note that to simplify further calculations, we considered this small amount as part of polymer concentration, as it is equally present before and after freeze-drying. The polymer degraded in two steps, respectively at 200 and 350°C. C<sub>60</sub> degraded only above 800°C which is in good agreement with the literature.<sup>1</sup> 15% residuals remained when 1100°C were reached. The signal for the composite is a combination of the two degradation patterns. However, it should be noted that there were more residuals in the composites than in pristine C<sub>60</sub> (e.g. 19% for the composite vs. 16% for pure C<sub>60</sub>, in Figure 5.1). From the TGA of the composites, the polymer content was therefore considered as the weight loss at 600°C. From one batch to another, the polymer content varied from 62 to 67%. This observation is consistent with the concentrations of polymer and fullerene that was estimated in the colloidal suspensions prior to freeze drying.



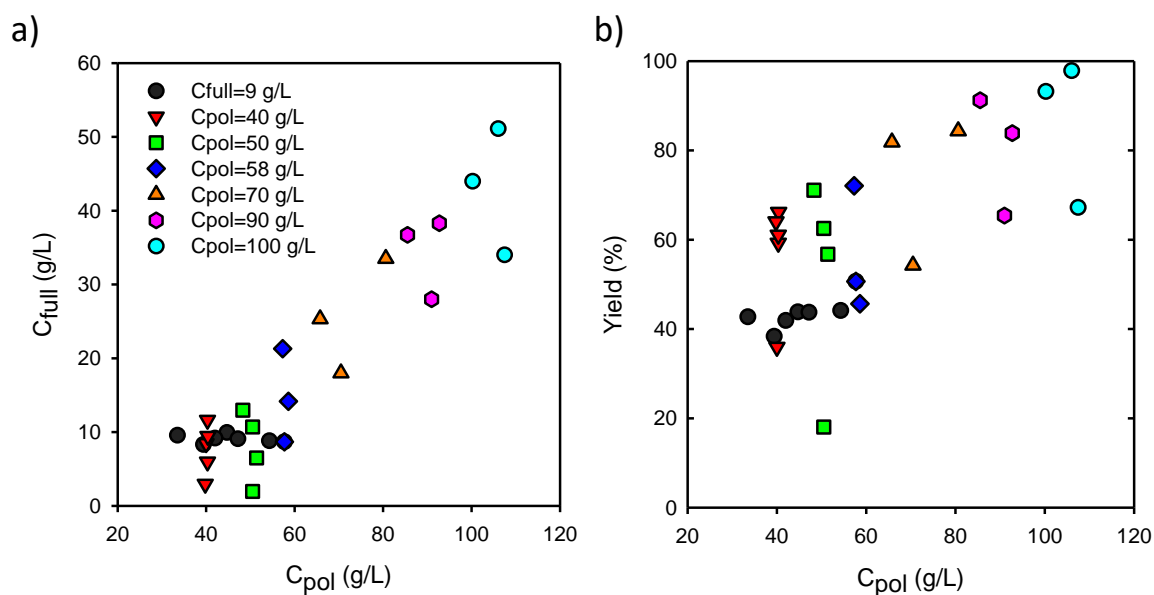
**Figure 5.1.** TGA thermogram for 75C12,  $C_{60}$  and their composite with 63% polymer and 37% fullerene after freeze-drying. The dashed arrow indicates the point at which the fullerene composition is measured for the composite sample.

#### b. Preparation of the nanocomposite hydrogels

The nanocomposite hydrogels were obtained through re-dispersion of the composite powders in water at 80°C, during 24 hours. The samples were not stirred during re-dispersion, because the stirring favored the formation of inhomogeneities in the form of a deposit on the glass walls. In some cases, composite powders were mixed with neat polymer (also powdered) in order to vary  $C_{full}$  and  $C_{pol}$ . In this way, several series of hydrogels were prepared with either constant  $C_{full}$  or  $C_{pol}$ . The polymer concentration was deduced from the polymer content in the composite powder, knowing the weight of composite powder and the total volume of the sample. Since fullerene might not totally re-disperse, we cannot deduce directly the fullerene concentration ( $C_{full}$ ) from the weight of composite. Therefore, we performed UV absorption measurements using  $\epsilon=105$  L/g/cm (for the absorption maximum around 340 nm) as shown in section 3.1.b.  $C_{full}$  values found from absorption in water were consistent with the ones obtained after extraction in toluene, confirming that the value of  $\epsilon$  is also reliable for the nanocomposite hydrogels. Hydrogels with  $C_{pol}$  ranging from 33 to 58 g/L keeping constant  $C_{full}$  to 10 g/L were obtained, as well as samples with constant  $C_{pol}=40-50-65-85-100$  g/L and various values of  $C_{full}$  as shown in Figure 5.2a.

When plotted in terms of re-dispersion yield, defined as the ratio between successfully re-dispersed  $C_{60}$  particles and their total amount introduced in the system (Figure 5.2b), it can be seen that the amount of re-dispersed particles increased with polymer concentration. When re-dispersed, it is possible that part of the particles already destabilized by sedimentation within

the 24 hours of the thermal treatment used to prepare the samples. Indeed, at 80°C the viscosity of neat 75C12 is much lower than at room temperature but is still pretty high for high  $C_{pol}$  values (above 50 g/L).<sup>2</sup> Therefore, for low  $C_{pol}$  the particles might sediment, but much less at higher  $C_{pol}$  because of the increased viscosity of the continuous medium. However, such a fast destabilization is in contradiction with the stability of the suspensions prepared by emulsification-evaporation (see section 3.1.d). If particles sediment this fast, they must be much bigger. Therefore, we investigated their aggregation state as described in the following.

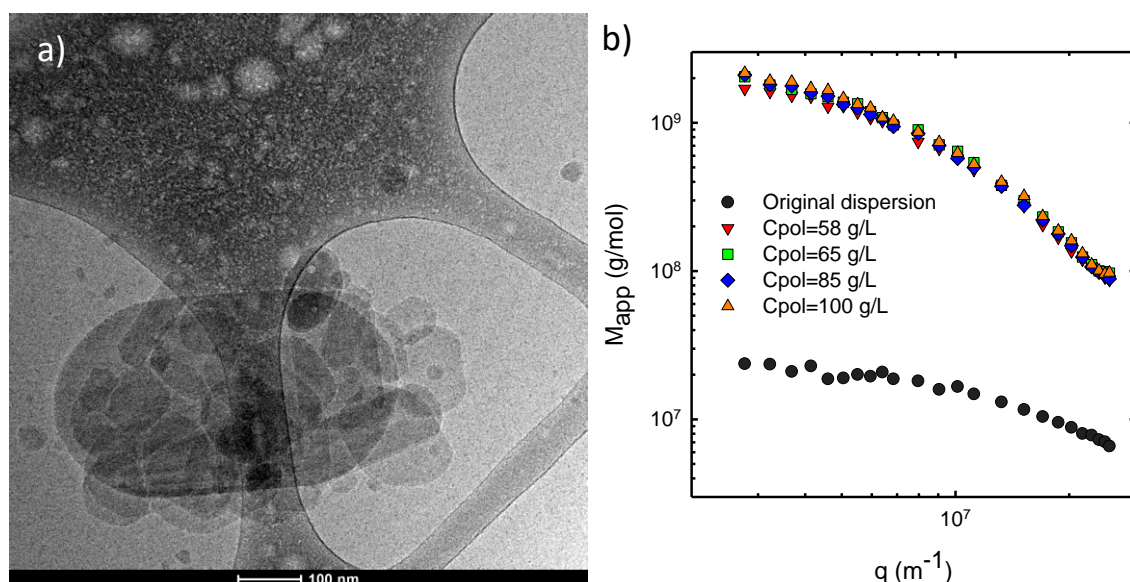


**Figure 5.2.** a)  $C_{60}$  and 75C12 concentrations (noted  $C_{full}$  and  $C_{pol}$ , respectively) for various series of samples as indicated in the figure. b) Same data represented in terms of re-dispersion yield for  $C_{60}$  particles.

### c. Structure of the nanocomposite hydrogels

The dispersion state of particles was assessed by cryo-TEM and light scattering as shown in Figure 5.3a and 5.3b, respectively. In both cases, it can be seen that particles are aggregated when compared to the original suspension. Cryo-TEM picture shows that several nanoplatelets are stacked onto each other (Figure 5.3a). However, the nanoplatelets can still be seen which means that the process does not induce a change in their structure. Static light scattering data indicate a general increase of the scattering intensity after the drying/re-dispersion treatment with composite powder only (Figure 5.3b). At low  $q$  values, the plateau value which is equal to the weight average molar is increased by two orders of magnitude by comparison with the original dispersion. The angular dependency of the scattered intensity is also stronger after freeze-drying, indicating an increase of the size. One can observe that all the samples displayed reproducible scattering profiles, which means that no matter the concentration at which they are prepared, the aggregation state of  $C_{60}$  particles is the same. From this we can

conclude that particles aggregate during freeze-drying and the re-dispersion at 80°C fails at breaking these aggregates. Magnetic stirring during the re-dispersion step did not help at exfoliating the nanoplatelets. Also, it should be mentioned that the uses of ultrasound to break the aggregates is precluded due to the high viscosity of the dispersions. Please note that these two analyses required to dilute the samples. For cryo-TEM, the sample was diluted in order to decrease the viscosity for the preparation of the grids (down to  $C_{pol}=10$  g/L and  $C_{full}=4$  g/L). For light scattering the samples were diluted approximately thousand-fold to decrease the absorption of light by C<sub>60</sub>. The structure was therefore not observed as it is in the hydrogel system. In general, the presence of macromolecules at high concentration helps exfoliating such 2D nanoparticles by intercalating between the particles. It is thus possible that particles exfoliate in concentrated conditions such as hydrogels. However, to verify it, one should use cryofracture, which was not accessible in the frame of this study, followed by electron microscopy.



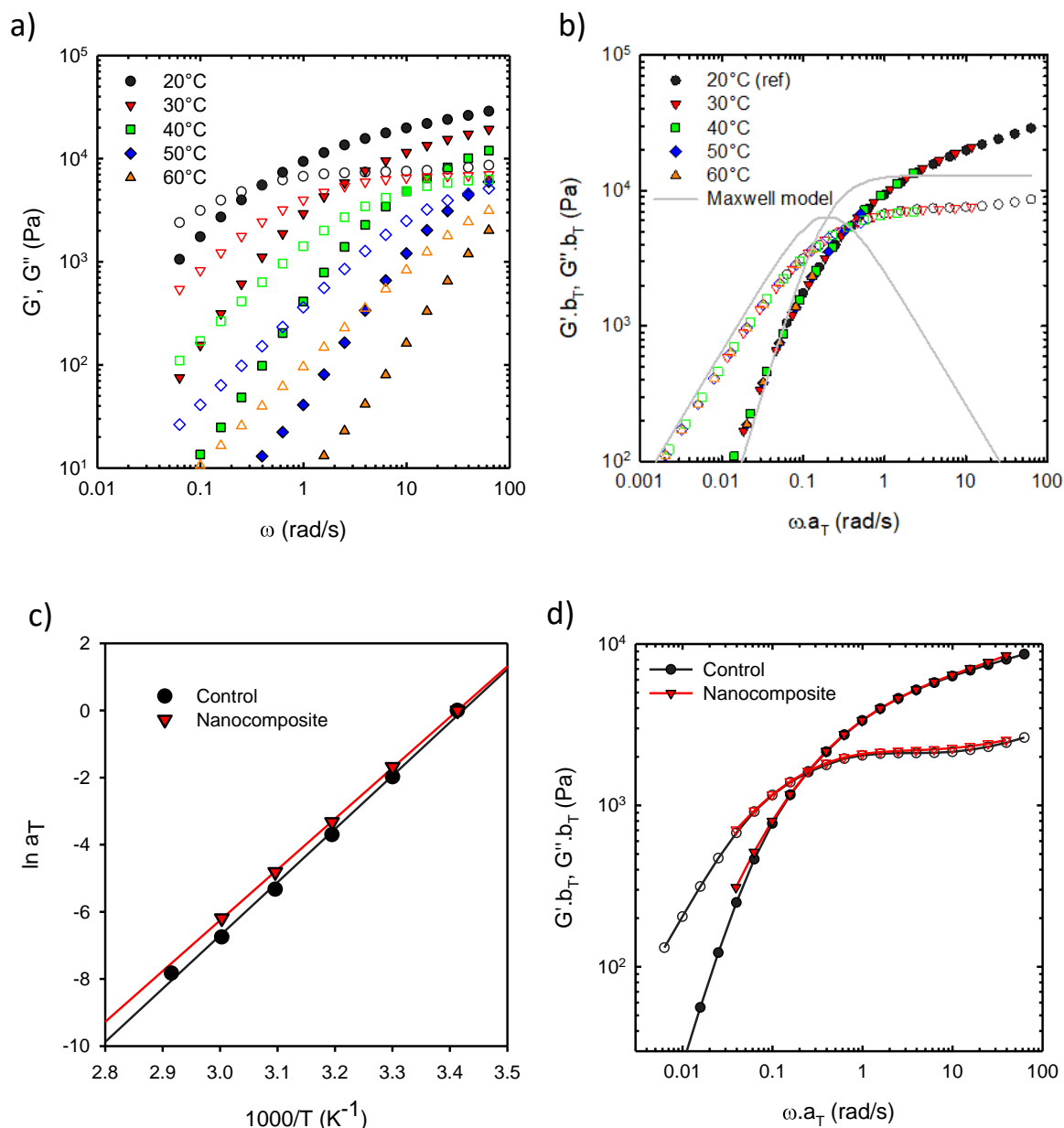
**Figure 5.3.** a) Cryo-TEM picture of an aggregate of C<sub>60</sub> nanoplatelets after re-dispersion of the freeze-dried powder in water, with  $C_{pol}=10$  g/L and  $C_{full}=4$  g/L. b) Apparent molar mass of the particles before and after freeze-drying/re-dispersion for hydrogels prepared at various polymer concentrations (indicated in legend).



## 2) Rheological properties of the nanocomposite hydrogels

### a. Stiffness and dynamics of the networks

The mechanical properties of the nanocomposite hydrogels were assessed by dynamic rheology. All the hydrogels behaved as viscoelastic liquids (Figure 5.4a) since at low frequency,  $G' < G''$  and slopes of 2 and 1 were observed respectively for  $G'$  and  $G''$  as function of frequency.  $G'$  and  $G''$  cross at a frequency  $\omega_c$  and at high frequency,  $G' > G''$ . However, no plateau value for  $G'$  is observed at high frequency. That is why the elastic modulus of the gel  $G$ , has been considered as being the value for  $G'$  at  $100\omega_c$  and  $T=20^\circ\text{C}$ . When achieving the measurements at various temperature ranging from 20 up to  $60^\circ\text{C}$ , it was possible to build a master curve (Figure 5.4b). The master curve did not follow the behavior of a Maxwell liquid as it could be expected from a viscoelastic liquid with a single relaxation time. In addition, the behavior of a solid, *i.e.* a slope of 0 and -1, respectively for  $G'$  and  $G''$ , that should be observed for  $\omega > \omega_c$  was not. Indeed, another relaxation occurred in this frequency range. This relaxation, named Rouse relaxation, originates from frictions between polymer chains and the solvent. All these conclusions indicate that the hydrogels display a very broad distribution of their relaxation times.

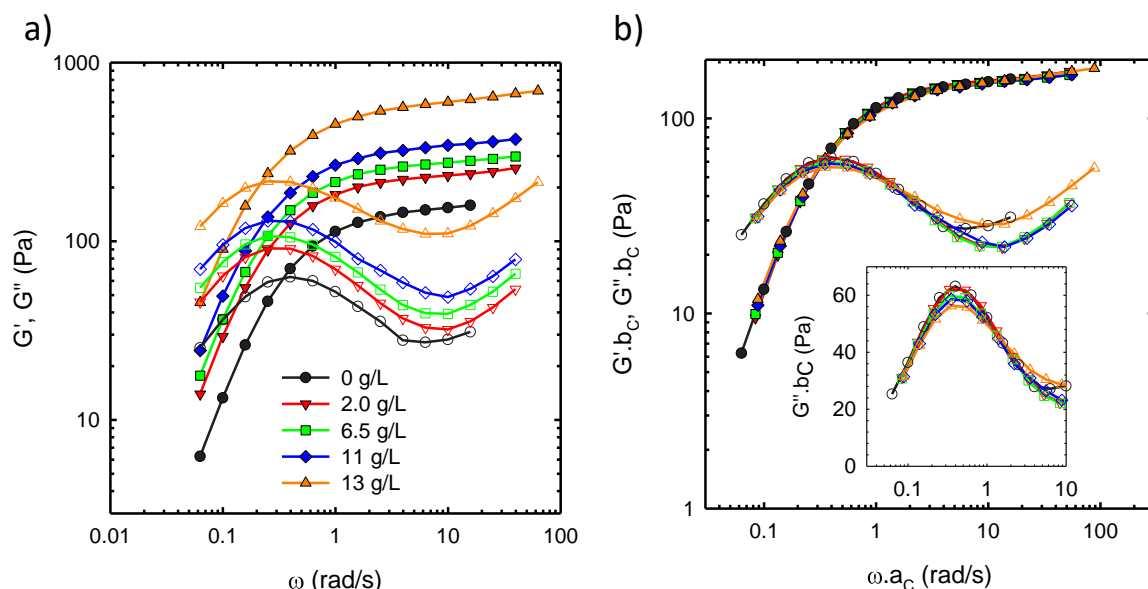


**Figure 5.4.** a) Storage ( $G'$ , close symbols) and loss ( $G''$ , open symbols) moduli as a function of frequency ( $\omega$ ) for a hydrogel with  $C_{\text{poi}}=100$  g/L and  $C_{\text{full}}=51$  g/L measured at various temperatures as indicated in the figure and  $\gamma=10\%$ . b) Master curve of rheological data using  $T_{\text{ref}}=20^\circ\text{C}$ . The gray solid line is a Maxwell model with  $G=10$  kPa and  $\tau=3$  s. c) Arrhenius plot of shift factors for the same hydrogel and a control sample with  $C_{\text{poi}}=100$  g/L. d) Superimposition of the frequency dependence of the viscoelastic moduli for the nanocomposite gel on the data of a control gel with  $C_{\text{poi}}=100$  g/L.

The temperature dependence of the frequency shift coefficients is described by an Arrhenius law (Figure 5.4c), with an activation energy equal to 140 kJ/mol a value which is similar to the one obtained for the neat hydrogels.<sup>2</sup> Also, when data of the nanocomposite were shifted (by a factor 1.6 for  $\omega$  and 3.4 for  $G'$  and  $G''$ ), they superimposed with the control gel, see Figure

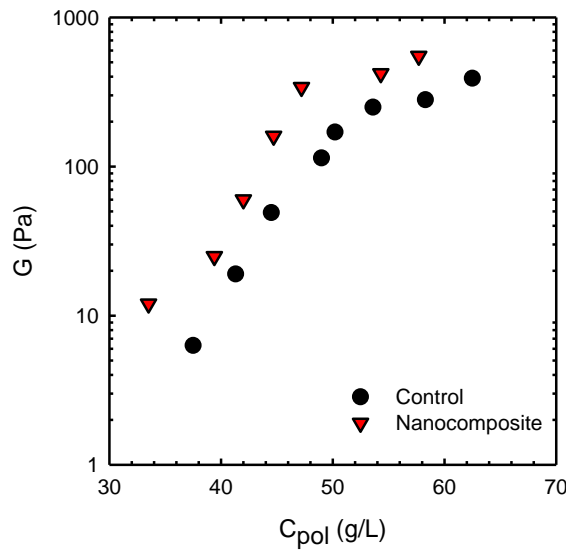
5.4d. To conclude, the shape of the dynamics of the hydrogel were unchanged in the presence of particles but absolute value for  $G$  and  $\tau$  were affected.

When fullerene particles are added to the hydrogel matrix, an increase of both  $G'$  and  $G''$  is observed (Figure 5.5a). Adding 2 g/L particles resulted in an increase of  $G$  by a factor 1.5. The increase goes further as long as particles are added. The highest fullerene concentration, 13 g/L, resulted in an increase of  $G$  by a factor 4. Interestingly, the crossing of  $G'$  and  $G''$  is shifted to lower frequencies when particle concentration increases, which means that the average relaxation time is increased (here from 3s for the control to 4.5s for the hydrogel containing 13 g/L particles). We built a master curve for the frequency dependence of  $G'$  and  $G''$  data by applying shift coefficients (namely  $a_c$  and  $b_c$ ) using the control hydrogel as a reference, see Figure 5.5b. All  $G'$  data perfectly superimposed, but some differences can be noted for  $G''$ . The semi-log representation of  $G''$  shows that the spectrum broadens when particles concentration increases. This is typical of a broadening of the relaxation times distribution. This can be due to the participation of both free and adsorbed polymer chains to the network, that might exhibit different relaxation processes. The high frequency behavior of the control sample is slightly different from the nanocomposite hydrogels. The Rouse relaxations are thus different in the presence of particles, although the effect is not systematic as one can see for the 13 g/L sample.



**Figure 5.5.** a) Evolution of storage (closed symbols) and loss (open symbols) moduli over angular frequency for various fullerene concentrations (indicated in legend) with  $\gamma=10\%$  at  $C_{pol}=50$  g/L. b) Master curve obtained by shifting data in (a) with factors noted  $a_c$  (X axis) and  $b_c$  (Y axis). The reference was the sample with  $C_{full}=0$  g/L. The insert is a semi-log representation of the loss modulus.

Figure 5.6 displays the evolution of elastic modulus upon C<sub>pol</sub> for neat and composite hydrogels with a constant concentration of fullerene particles of 10 g/L. The concentration dependence of G displays the same shape for both but the increase of G occurs at lower C<sub>pol</sub> for the composite hydrogels which means that the percolation concentration was shifted to lower C<sub>pol</sub> in presence of fullerene nanoparticles. Elastic moduli were systematically higher in presence of fullerene at a constant C<sub>pol</sub>. One could ascribe the increase of modulus to the decrease of accessible volume to the polymer because of the particles. However, here they represent only 1 wt%, which is 0.6 vol% (with a density of pure C<sub>60</sub> equal to 1.65).



**Figure 5.6.** Evolution of the elastic modulus upon polymer concentration for hydrogels with 0 (black circles) and 10 g/L (red triangles) particles.

Figure 5.7a displays the elastic modulus variation upon C<sub>full</sub> for constant C<sub>pol</sub> values. Nanocomposite hydrogels were systematically stiffer than control samples, and increasing the particles concentration resulted in an increase of elastic modulus. The contribution of particles to the stiffness of an hydrogel in the case of particles that don't interact with the matrix and simply act as fillers can be described with the Guth and Gold model:<sup>3, 4</sup>

$$G = G_0(1 + 2.5\Phi_p + 14.1\Phi_p^2) \quad \text{Eq. 5.1}$$

with  $\Phi_p$  the volume fraction occupied by the particles:

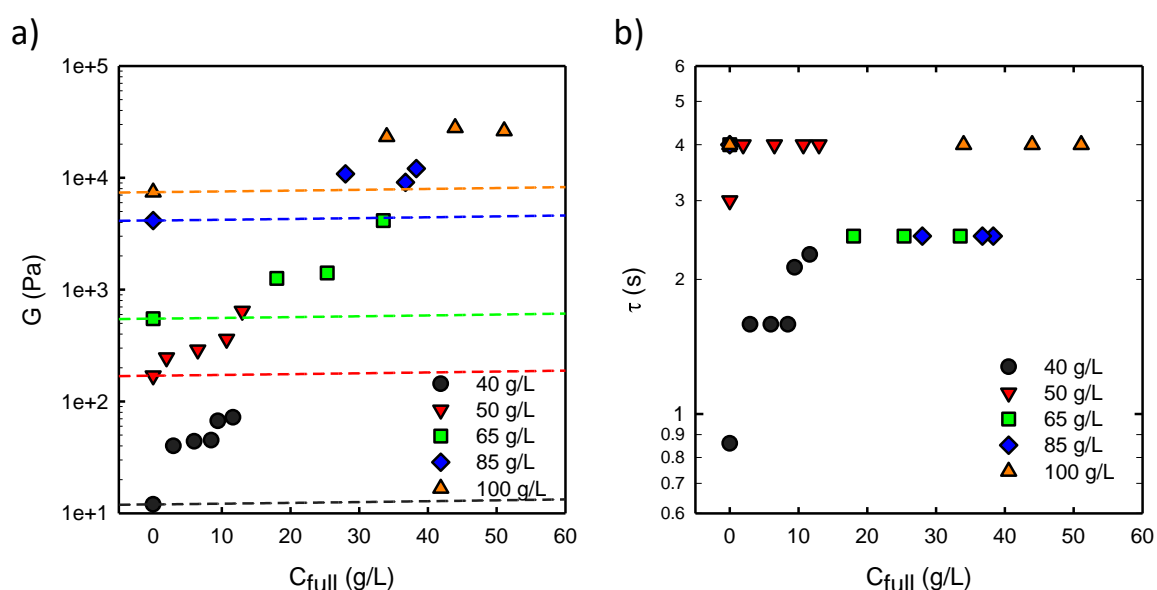
$$\Phi_p = C_{full} \times d \quad \text{Eq. 5.2}$$

with d the particles density. Considering that the particles have the same density than pristine C<sub>60</sub>, we used d=1.65 g/cm<sup>3</sup>.

This model predicts the elastic modulus as a function of particles concentration. One can see that in the case of filler, the particles concentration is too low to have an impact on the stiffness

of the hydrogels. Therefore, the fact that C<sub>60</sub> nanoparticles reinforce the hydrogels means that they strongly interact with the matrix (see also chapter 4). The increase of the relaxation time in the presence of particles also indicates that the relaxation mechanisms are modified when C<sub>60</sub> is introduced within the network.

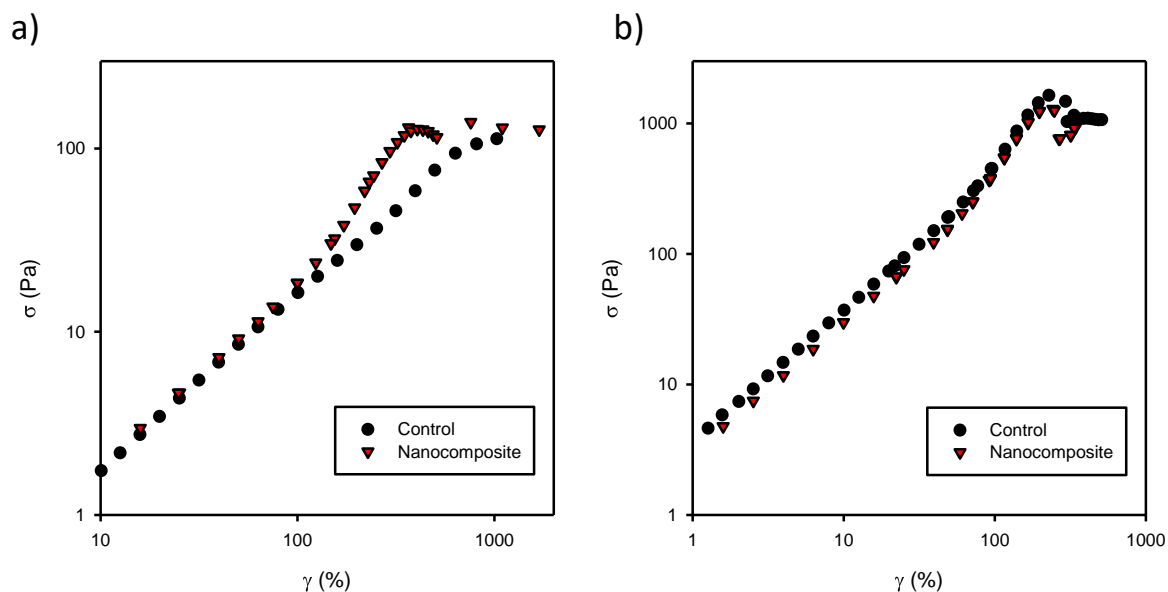
Figure 5.7b displays the average relaxation times for the same samples. At low polymer concentration (40 g/L), adding particles increases the relaxation time, in other words, dynamics is slowed down. Please note that this polymer concentration is very close to the percolation point, and the addition of particles seems to help building the network. At high polymer concentrations ( $\geq 65$  g/L), the average relaxation time is not affected much by the presence of particles.



**Figure 5.7.** Evolution of a) the elastic modulus and b) the mean relaxation time upon fullerene concentration for hydrogels with various polymer concentrations indicated in legend. In (a), the dashed lines correspond to the Guth and Gold model computed from the control modulus.

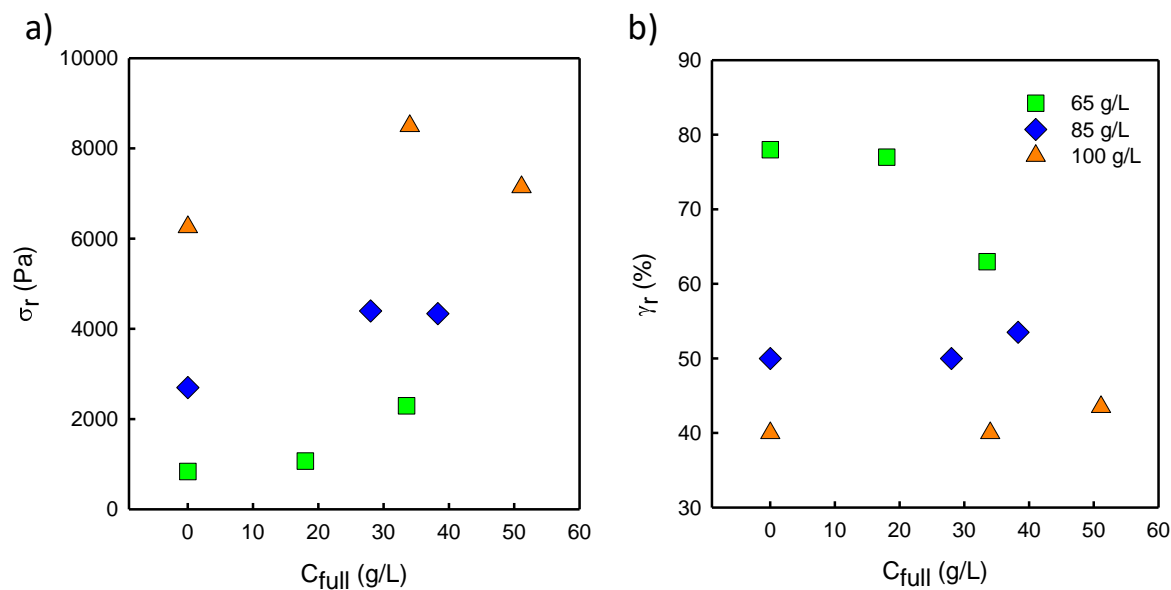
### b. Non-linear mechanical properties

The behavior of the hydrogels under strain was studied by dynamic rheology. Control and nanocomposite hydrogels were compared at *iso-G*. In all cases, at low strains, a linear dependency of stress over strain is characteristic of the linear regime. In this regime,  $\sigma = G \cdot \gamma$ , with  $\sigma$  the stress,  $G$  the elastic modulus and  $\gamma$  the strain, for a given frequency and temperature. For low elastic modulus values (e.g. 15 Pa, see Figure 5.8a), the nanocomposites displayed shear-thickening before rupture contrary to the control samples. The rupture was taken as the point where stress reached its maximum value. For higher elastic modulus values (e.g. 300 Pa, see Figure 5.8b), control and nanocomposite hydrogels displayed shear-thickening of the same order of magnitude.



**Figure 5.8.** Stress evolution over strain for hydrogels with  $G$ =a) 15 Pa and b) 300 Pa, at  $\omega$ =10 rad/s,  $T$ =20°C.

The stress values at rupture (defined by the maximum stress point, see section 2.6.c) are displayed in Figure 5.9a. Increasing particles concentration induces an increase of stress at rupture, which means that gels can resist bigger loads before breaking. At some extent, it does not seem that useful to add more particles: for  $C_{pol}$ =85 and 100 g/L, the stress at rupture is the same for the nanocomposite hydrogels. This value is still higher than for the control. Also, when strain at rupture is considered (Figure 5.9b), adding more particles has no effect on the strain at rupture.



**Figure 5.9.** Stress (a) and strain (b) values at rupture for hydrogels with different  $C_{pol}$  as function of particles concentration, at  $\omega=10$  rad/s and  $T=20^\circ\text{C}$ .

## Conclusions

Hydrogels containing  $C_{60}$  nanoparticles were prepared by drying of aqueous suspensions followed by re-dispersion, with particles concentration up to 50 g/L. The presence of particles induced a shift of percolation concentration to lower values with respect to neat hydrogels and an increase of the elastic modulus. The mechanical reinforcement demonstrates that strong interactions between particles and the polymer matrix occur. The nanocomposite hydrogels could for example be used as inks for optical devices since particles are kinetically stabilized in the gel matrix, that can be melted by gentle heating.



## References

1. Milliken, J.; Keller, T. M.; Baronavski, A.; McElvany, S. W.; Callahan, J. H.; Nelson, H., Thermal and oxidative analyses of buckminsterfullerene, C<sub>60</sub>. *Chemistry of Materials* **1991**, 3 (3), 386-387.
2. Dutertre, F.; Benyahia, L.; Chassenieux, C.; Nicolai, T., Dynamic Mechanical Properties of Networks of Wormlike Micelles Formed by Self-Assembled Comblike Amphiphilic Copolyelectrolytes. *Macromolecules* **2016**, 49 (18), 7045-7053.
3. Carlsson, L.; Rose, S.; Hourdet, D.; Marcellan, A., Nano-hybrid self-crosslinked PDMA/silica hydrogels. *Soft Matter* **2010**, 6 (15), 3619-3631.
4. Guth, E., Theory of Filler Reinforcement. *Rubber Chemistry and Technology* **1945**, 18 (3), 596-604.

## Chapter 6. C<sub>60</sub> aqueous colloidal suspensions by Ouzo effect

1) Solutions of C <sub>60</sub> in n-butylamine .....	183
a. Choice of the co-solvent .....	183
b. Interactions between C <sub>60</sub> and n-butylamine .....	184
2) Elaboration of Ouzo C <sub>60</sub> particles .....	188
a. Ouzo region mapping .....	188
b. Stability upon ageing .....	189
c. Characterization of the particles .....	192
i. Morphology .....	192
ii. Influence of the volume fraction of C <sub>60</sub> solution .....	193
iii. Influence of fullerene concentration .....	197
3) Stabilization by 75C12 .....	198
a. Effect on the state diagram and stability .....	198
b. Effect on the size of the particles .....	200
Conclusions .....	203
References .....	205



## Chapter 6. C<sub>60</sub> aqueous colloidal suspensions by Ouzo effect

In this chapter, we propose the preparation of C<sub>60</sub> nanoparticles in water using Ouzo effect. The selection of an appropriate co-solvent, n-butylamine, will first be discussed, with an insight on its reactivity with C<sub>60</sub>. Then, the determination of binodal and spinodal lines will be shown, and particles characterization by transmission electron microscopy, light scattering and analytical centrifugation will be detailed. We varied two parameters: the concentration of C<sub>60</sub> in n-butylamine prior mixing with water and the volume fraction of the C<sub>60</sub> solution in the final mixture. Last, we will discuss the influence of the addition of the amphiphilic polymer used throughout this study, 75C12, on the state diagrams, size and stability of the particles.

### 1) Solutions of C<sub>60</sub> in n-butylamine

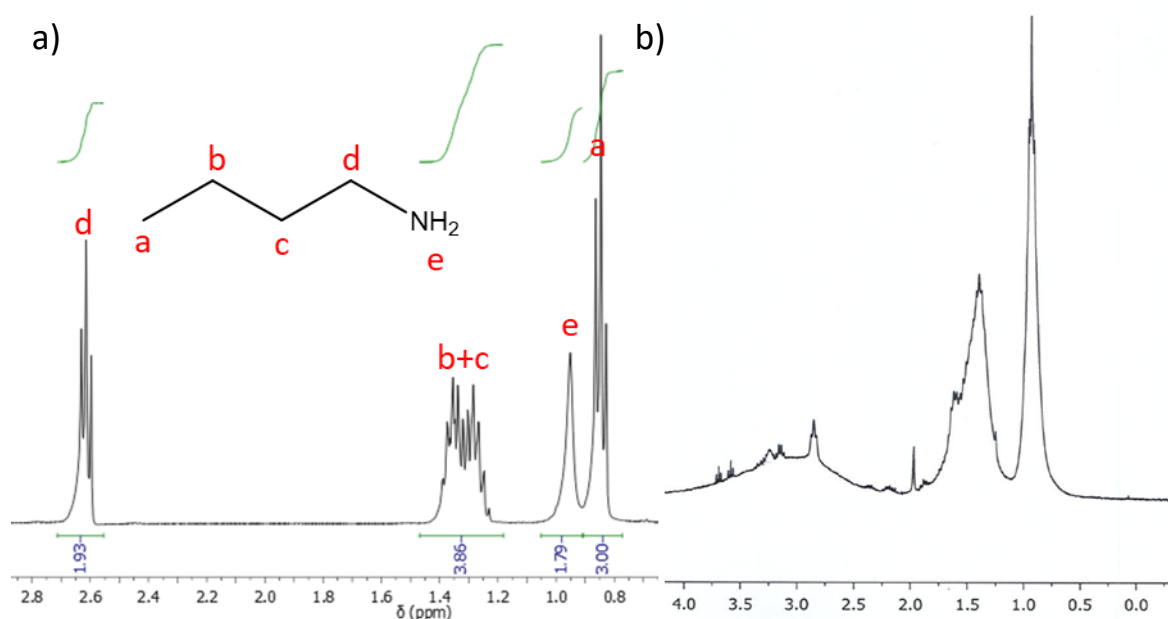
#### a. Choice of the co-solvent

As we discussed in section 1.2.b.i, Ouzo effect provides the possibility to disperse a hydrophobic compound in water as colloidal particles or droplets. The prerequisite is to find an appropriate water-miscible solvent that can dissolve this hydrophobic compound. Ouzo seems therefore promising for the straightforward elaboration of C<sub>60</sub> aqueous colloidal suspensions. It has actually already been used in the literature, although it was not named this way.<sup>1, 2</sup> THF was used for this purpose, as it is one of the best polar solvents for C<sub>60</sub> (solubility value is ca. 10 mg/L in THF).<sup>1, 3</sup> Additionally, THF can be easily removed by evaporation thanks to its low boiling point and is very accessible. However, the solubility value is low compared to apolar solvents such as carbon disulfide, toluene or even chloroform, which can solubilize C<sub>60</sub> up to 7.6, 2.8 and 0.09 g/L, respectively,<sup>4</sup> so the final concentration in water can be expected to be very low. In addition, THF is toxic and was proven to stick to the surface of C<sub>60</sub> nanoparticles, making them highly toxic as well.<sup>5</sup> Other polar solvents that could be considered are electron donors that can interact with C<sub>60</sub> through donor-acceptor interactions, such as N-methylpyrrolidone (NMP) or pyridine, that both display good solubility for C<sub>60</sub> (0.89 g/L).<sup>4</sup>

Here, we propose to use n-butylamine (noted nBA) as a good solvent. In literature, the solubility value was reported as 3.6 g/L,<sup>6</sup> which is higher than for all the polar solvents cited above. Also, it is less toxic than them. In section 1.1.b.iii, we discussed the ability of aliphatic primary and secondary amines to react with C<sub>60</sub> through nucleophilic addition. The reactivity of n-butylamine with C<sub>60</sub> will now be discussed.

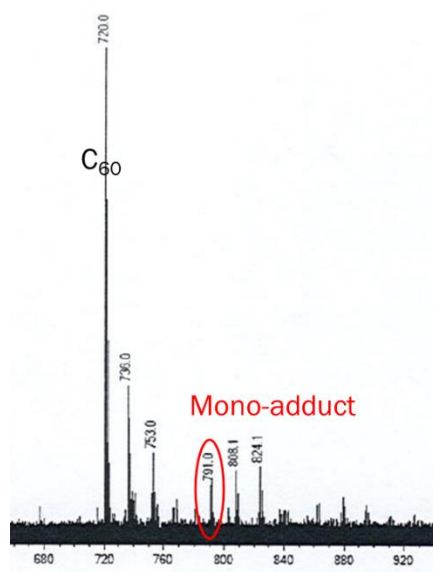
b. Interactions between C<sub>60</sub> and n-butylamine

Before using n-butylamine as solvent, the chemical structure of C<sub>60</sub> in solution in nBA needs to be addressed, especially regarding the very low kinetics of reaction. When the <sup>1</sup>H NMR spectrum of pure nBA (Figure 6.1a) is compared to the one of C<sub>60</sub> recovered from a solution in nBA (Figure 6.1b), the signals of nBA are observed in the second case. However, the signals are larger which means the presence of several adducts of fullerene corresponding to the addition of 1 to several amine groups on C<sub>60</sub>. From NMR, it is however not possible to estimate the number of adducts.



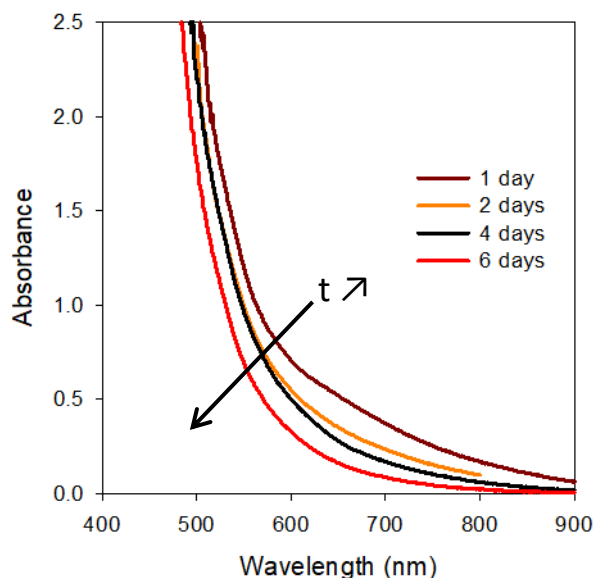
**Figure 6.1.** <sup>1</sup>H NMR spectrum of n-butylamine (a) and C<sub>60</sub> recovered from a solution in n-butylamine (1 g/L) (b).

Therefore, mass spectroscopy (MALDI-TOF) was carried out on the aminated C<sub>60</sub>, see Figure 6.2. The characteristic peak corresponding to C<sub>60</sub> is observed at 720 m/z. The mono-adduct of nBA is also seen at 791 m/z. Several peaks can also be noted every 16 m/z, which can be assigned to the addition of oxygen atoms, *i.e.* oxidation of C<sub>60</sub> in the meantime. In addition, 1 g/L and 10 g/L (excess) C<sub>60</sub> solutions in nBA were prepared in two different conditions: either under air with no protection from light, and under argon atmosphere with protection from light. In all cases, Thin-Layer Chromatography in toluene showed that the polarity of the generated specie is much higher than pure C<sub>60</sub> (retention factors were equal to 1 and 0.12 for pure and modified C<sub>60</sub>, respectively). The retention factor was not affected by the concentration of the reactive medium nor by the atmosphere where the reaction proceeds. Therefore, it seems difficult to inhibit this reaction.



**Figure 6.2.** Mass spectrum of C<sub>60</sub> recovered from a solution in n-butylamine (1 g/L).

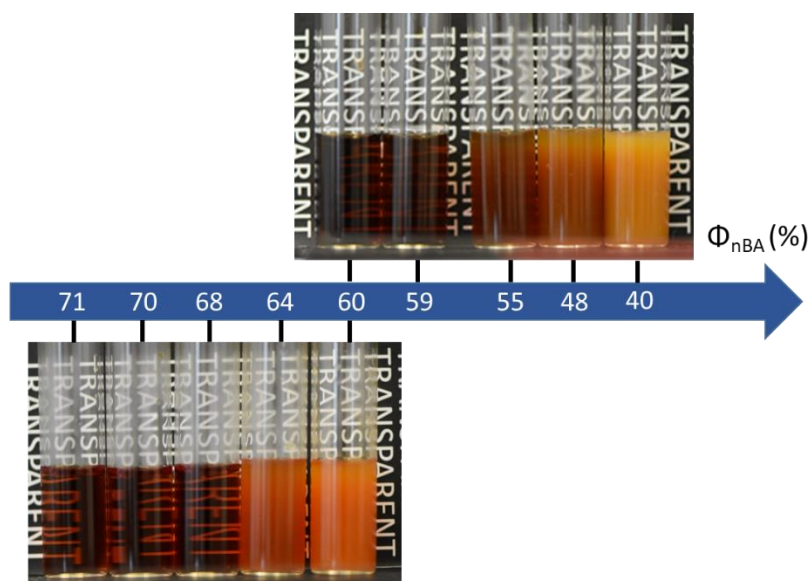
Qiao et al. showed that the reaction kinetics between aliphatic amines and C<sub>60</sub> are very slow, and they can be studied spectroscopically.<sup>7</sup> The visible light absorption spectra of a C<sub>60</sub> solution in n-butylamine after various ageing times are shown in Figure 6.3. Contrary to solutions in toluene or water, C<sub>60</sub> solutions in nBA do not display absorption maxima. The absorption is relatively low at high wavelengths and diverges at lower ones. The global absorption decreases with increasing stirring times. The absorption results from electronic transitions originating from the high conjugation of C<sub>60</sub>. Consecutive reactions with nBA lower the overall conjugation of the molecule, thus reducing its absorption of light. Therefore, it can be concluded that nBA still grafted on the surface of C<sub>60</sub> even after 6 days of stirring.



**Figure 6.3.** Visible light absorption spectra of a 4 g/L C<sub>60</sub> solution in n-butylamine (ageing time indicated in the figure).

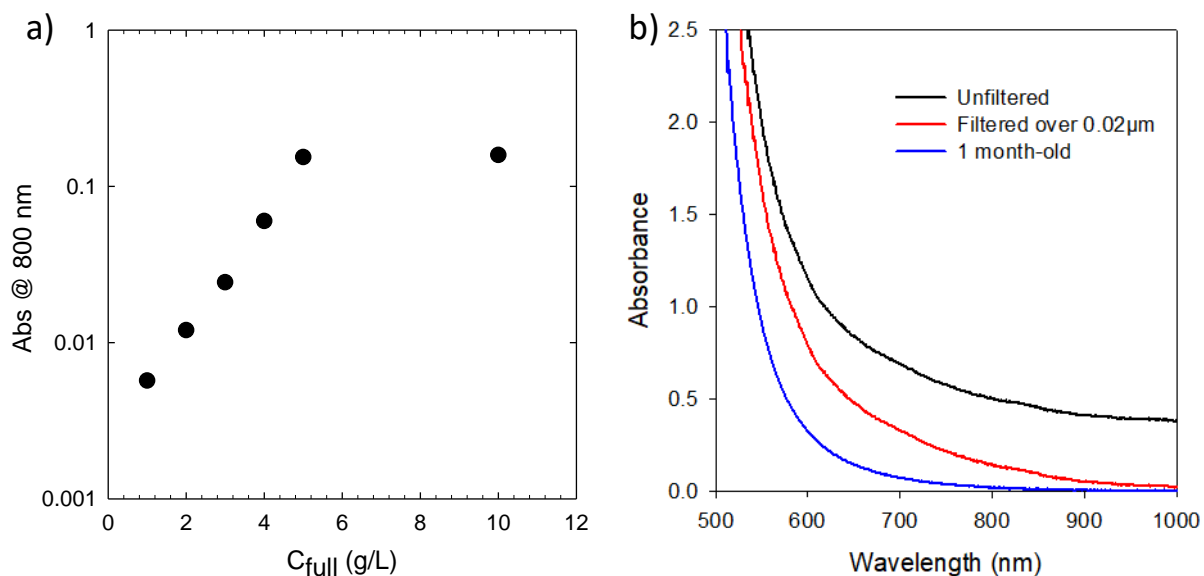
Our concern is then whether the number of nBA adducts is of importance regarding the Ouzo dispersion. For this reason, we prepared C<sub>60</sub>/nBA/water mixtures by adding various amounts of water on top of 2.4 g/L C<sub>60</sub> solutions in nBA, with ages respectively equal to 1 day and 9 months. Pictures of mixtures with various volume fractions of nBA solutions ( $\Phi_{\text{nBA}}$ ) are shown in Figure 6.4. According to visible light absorption spectroscopy, the mixtures prepared with the fresh C<sub>60</sub> solution in nBA were darker than the ones prepared with the old solution. The appearance of turbidity is shifted to higher  $\Phi_{\text{nBA}}$  values when the solution is older. Also, we noted that particles prepared from an old solution of C<sub>60</sub> in nBA were totally destabilized after 1 day, whereas particles prepared from a fresh solution were stable. This can be surprising because one could expect a fullerene that possesses more amine adducts to be more polar, thus more hydrophilic. From this observation, we decided to only use 1-day old solutions of C<sub>60</sub> in nBA for the remaining of this study.



**Fresh**

**Figure 6.4.** Pictures of C<sub>60</sub>/n-butylamine/water mixtures prepared with C<sub>60</sub> solutions in nBA (2.4 g/L) that were aged 1 day (top) or 9 months (bottom). Various volume fractions of C<sub>60</sub> solution were used as indicated in figure.

Based on a 24 hours stirring time, we evaluated solubility of C<sub>60</sub> in nBA by visible light spectroscopy, see Figure 6.5a. One can see that the absorbance follows the Beer-Lambert law (see section 2.2.a) up to 5 g/L of fullerene. A solution prepared at 10 g/L displayed the same absorbance as a 5 g/L solution, we then concluded that saturation occurred at 5 g/L after 1 day of stirring. It should be mentioned that in all cases solutions were filtered over 0.02  $\mu\text{m}$ . An unfiltered 10 g/L solution indeed displayed a baseline (Figure 6.5b) due to the presence of insoluble C<sub>60</sub>. However, after 1 month of ageing, no more baseline was observed, which shows that the ageing time has dramatic consequences on the solubility values and could explain why we found a higher solubility than in the literature.<sup>6</sup> When C<sub>60</sub> is solubilized in nBA, both solubilization and reaction occur at the same time. The solubility must depend on the number of amine grafts on fullerene. Therefore, the solubility value of C<sub>60</sub> in nBA depends on the age of the solution. A solution prepared with C=24 g/L displayed an excess even after 4 months of ageing, which means that there is a limit solubility comprised between 10 and 24 g/L on long time scales. Since we will only use fresh solutions in the following, we will use fullerene concentrations in nBA up to 5 g/L.



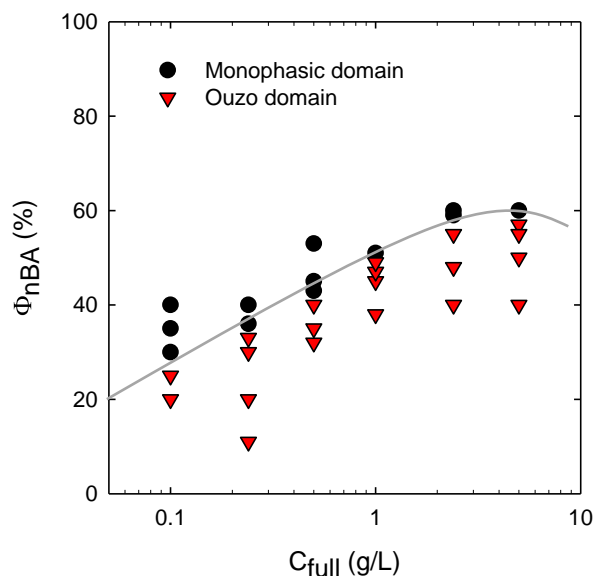
**Figure 6.5.** a) Absorbance at 800 nm as function of C<sub>60</sub> concentration in nBA. b) Absorption spectra of 10 g/L C<sub>60</sub> solutions in nBA. When not precised, the age of the solutions was 1 day.

## 2) Elaboration of Ouzo C<sub>60</sub> particles

### a. Ouzo region mapping

When elaborating particles by Ouzo effect, one wants to map the compositions for which particles are generated. Based on macroscopic observations of the turbidity, we established the state diagram of the C<sub>60</sub>/nBA/water ternary mixture at  $t=0$  as shown in Figure 6.6, for C<sub>60</sub> concentrations in nBA (C<sub>full</sub>) comprised between 0.1 and 5 g/L, the saturation value. The diagram is displayed as volume fraction of mother solution of C<sub>60</sub> in nBA ( $\Phi_{nBA}$ ) as function of the concentration of C<sub>60</sub> in this mother solution (C<sub>full</sub>), see Figure 6.6. Such a representation allows to draw a two-dimensional diagram instead of a three-dimensional one.<sup>8</sup> One can see that the binodal, *i.e.* the limit between Ouzo and monophasic systems, occurs at increasing  $\Phi_{nBA}$  when C<sub>full</sub> increases, in good agreement with the literature.<sup>8-10</sup> Since we are interested in making as concentrated as possible suspensions, we did not investigate low volume fractions of nBA solution. Therefore, we did not find any conditions for which a fast destabilization occurred (within one hour). For this reason, no spinodal has been displayed and will be discussed here. The highest concentration for an Ouzo sample was obtained with C<sub>full</sub>=5 g/L and  $\Phi_{nBA}$ =56%, which lead to concentration of 2.8 g/L fullerene in the final mixture. Although this is lower than what we obtained with the emulsification-evaporation method, it should be reminded that no stabilizer is used here, and still the concentration is higher than what is seen in the literature for neat C<sub>60</sub>. Please note that a powder of C<sub>60</sub> recovered from a solution in nBA

could not be dispersed in water by magnetic stirring. Therefore, the chemical modification alone cannot explain such high concentrations and Ouzo process is the key for achieving a stable dispersion of C<sub>60</sub> in water in the absence of any stabilizer.



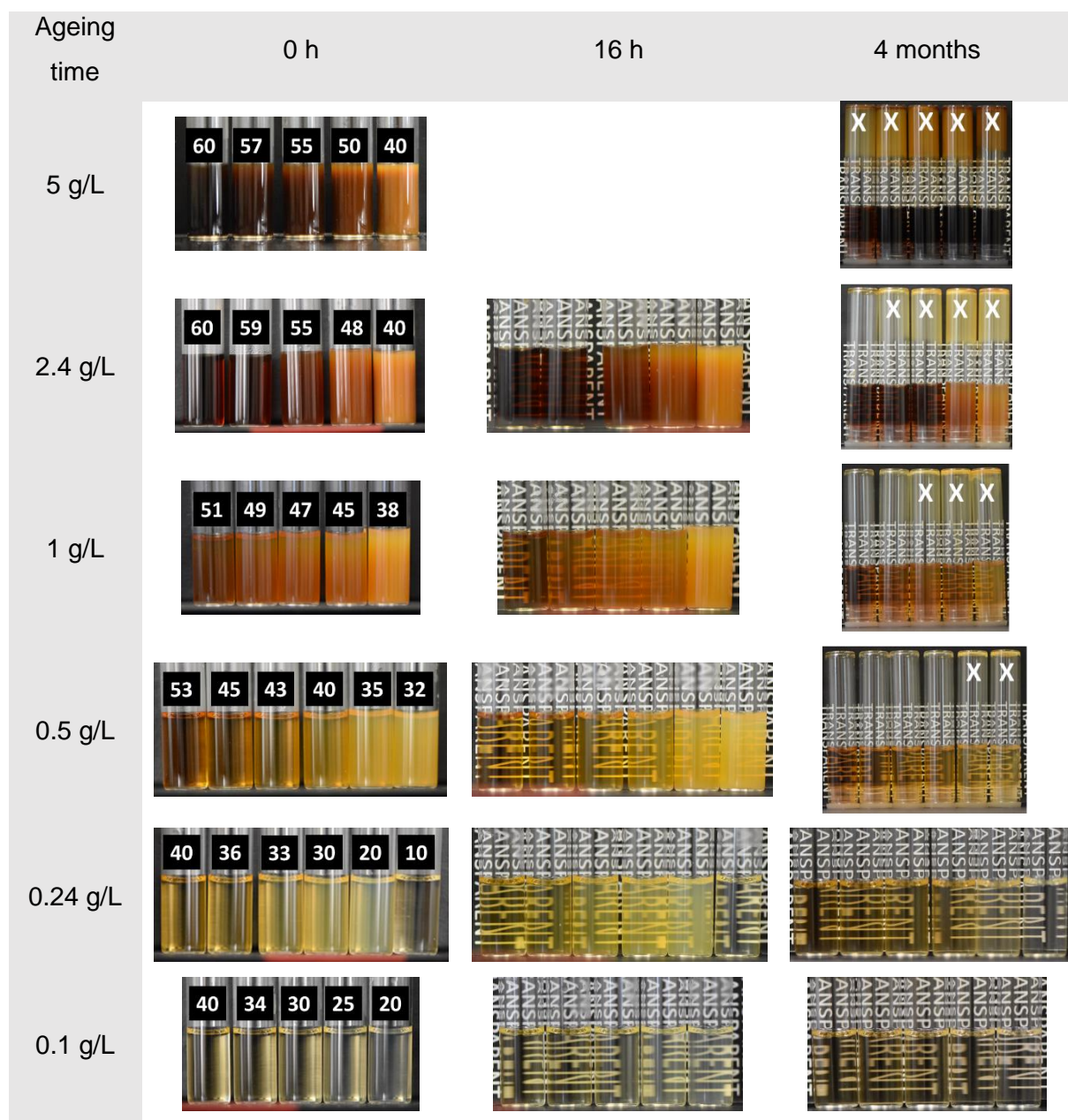
**Figure 6.6.** Ouzo state diagram for the C<sub>60</sub>/n-butylamine/water ternary mixture, at 20°C and t=0. The gray line represents the binodal.

### b. Stability upon ageing

The stability of the suspensions prepared by Ouzo effect upon ageing was followed by macroscopic observations as displayed in Figure 6.7. After 16 hours, all samples were still stable, and no significant difference was seen with t=0. After 48 hours (not shown), the samples were still stable, except for the sample prepared at C<sub>full</sub>=1 g/L and Φ<sub>nBA</sub>=38% for which a small deposit was observed at the bottom of the tube, however it was still turbid. After 4 months of ageing, all the samples in the Ouzo region for C<sub>full</sub>≥2.4 g/L were destabilized. A light-brown excess of fullerene particles deposited on the glass walls and at the bottom of the tube. Please note that even though some deposit was observed, the continuous phase was still turbid for samples far from the binodal (e.g. C<sub>full</sub>=2.4 g/L, Φ<sub>nBA</sub>=40 and 48%). For C<sub>full</sub>=1 and 0.5 g/L, similarly, a deposit was observed for Φ<sub>nBA</sub>≤47 and 35%, respectively, but the samples close to the binodal (Φ<sub>nBA</sub>=49 and 40%, respectively) were still stable. The sample with C<sub>full</sub>=0.5 g/L, Φ<sub>nBA</sub>=43%, which was monophasic at t=0, even became slightly turbid. It is well-known that the transparent mixtures are not ideally homogeneous ones. Simply, the droplets are too small to induce turbidity. The domain where these small droplets exist is called Surfactant-Free MicroEmulsion (SFME).<sup>10</sup> The boundary between Ouzo and SFME is only based on turbidity, which makes its precise localization difficult. For C<sub>full</sub>=0.24 g/L, the global turbidity and coloration decreased with time. No excess fullerene was observed. A slight turbidity is seen

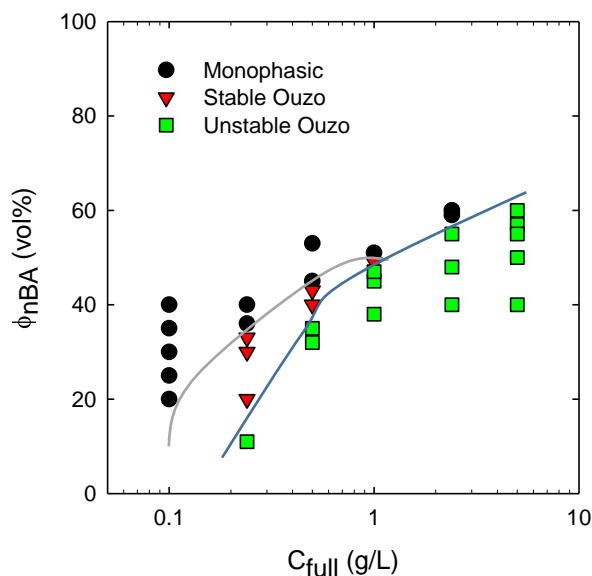
from  $\Phi_{\text{nBA}}=33$  to 20%. The sample with  $\Phi_{\text{nBA}}=10\%$  was not turbid. For  $C_{\text{full}}=0.1$  g/L, we observed no deposit, but also no more turbidity.

It is important to note that the continuous phases after destabilization were still very colored. This means that the unstable, big particles represent only part of the C<sub>60</sub> in the system, the other part being either in the form of individual molecules or small aggregates. From the LaMer model, we can conclude that the saturation value for C<sub>60</sub> in the corresponding nBA/water mixtures is relatively high (see section 1.2.b). It was not possible to re-suspend the particles by hand- or vortex-shaking after destabilization, which indicates that the latter occurred after gradual aggregation of the particles upon ageing.



**Figure 6.7.** Pictures of  $C_{60}$ /nBA/water Ouzo mixtures taken at various ageing times, with  $C_{full}$  indicated on the left. Volume fractions of nBA solution are indicated on the tube at  $t=0$ . Deposit is symbolized by an X symbol. Please note that the samples with  $t=4$  months were put upside down to display the deposit on the glass walls, except for  $C_{full}=0.24$  and  $0.1$  g/L.

In Figure 6.8, we represented a state diagram for  $t=4$  months. We considered as unstable all the samples that displayed an excess of particles. The limit between stable and unstable Ouzo is called the “Ouzo limit”. One can see that the particles were stable in only a small region. The most concentrated stable suspension was prepared with  $C_{full}=1$  g/L and  $\Phi_{nBA}=49\%$ , which lead to concentration of  $0.5$  g/L fullerene in the final mixture.



**Figure 6.8.** Ouzo state diagram for the C<sub>60</sub>/n-butylamine/water ternary mixture, at 20°C and t=4 months. The gray line represents the binodal and the blue line, the spinodal.

### c. Characterization of the particles

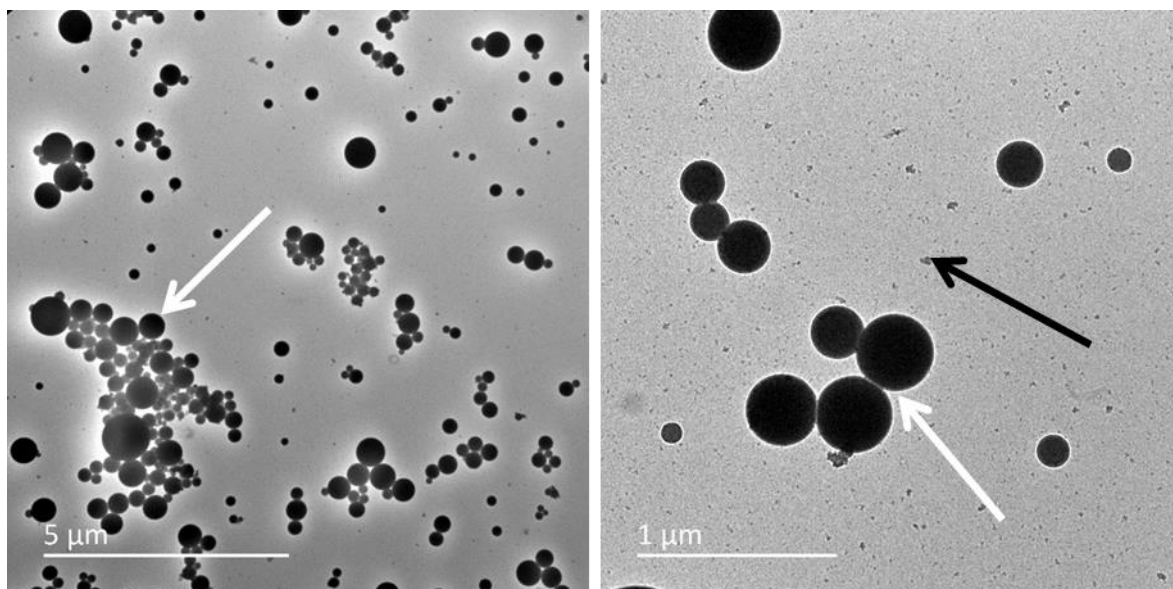
Because of the SFME domain, the particles cannot be directly characterized by static and dynamic light scattering (SLS&DLS) since another relaxation process arises from domains of nBA in water (or the inverse) which overcomes the scattering signal from the C<sub>60</sub> particles. Additionally, nBA is aggressive toward organic materials like the poly(carbonate) tubes for analytical centrifugation or the carbon membrane of copper grids for TEM. Also, for potential applications, it is mandatory to remove nBA which was achieved by dialysis as explained in section 2.2.b. Only then, we characterized particles size and morphology. It is worth noting that the concentration of C<sub>60</sub> in water could not be determined by UV-vis spectroscopy, because no absorption maxima were observed as in n-butylamine (see Figure 6.5b), even after removal of the latter.

#### i. Morphology

Particles prepared at  $C_{full}=2.4$  g/L and  $\Phi_{nBA}=10\%$  were observed with TEM, see Figure 6.9. Spherical and polydisperse particles can be seen (white arrows). It should be noted that the suspension was dried prior analysis. Therefore, the high aggregation state of the particles is probably caused by aggregation during drying. However, due to the high size of the particles, it was not possible to use cryo-TEM here, because the blotting step to form the water film on the grid would remove all the big particles. Their diameter typically varies between 0.1 and 1  $\mu\text{m}$ . Their high contrast, even for the smallest ones, indicates that they are dense. Around the sphere, a white halo can be seen, coming presumably from Bragg reflections. It can thus be expected that the particles are crystalline, although complementary WAXD measurements are



required to conclude it. Smaller particles can also be seen in the background (black arrow). They seem less spherical than the big ones. They probably result from the remaining C<sub>60</sub> in the continuous phase after destabilization of the big particles (see section 6.2.b). Again, we cannot say whether they were already present as very small particles or as individual molecules, because the sample is dried here.



**Figure 6.9.** Dried TEM pictures of a sample prepared with  $C_{\text{full}}=2.4$  g/L and  $\Phi_{\text{nBA}}=10\%$ , after dialysis against water. White arrows show big spherical C<sub>60</sub> particles. Black arrow shows a small particle in the background.

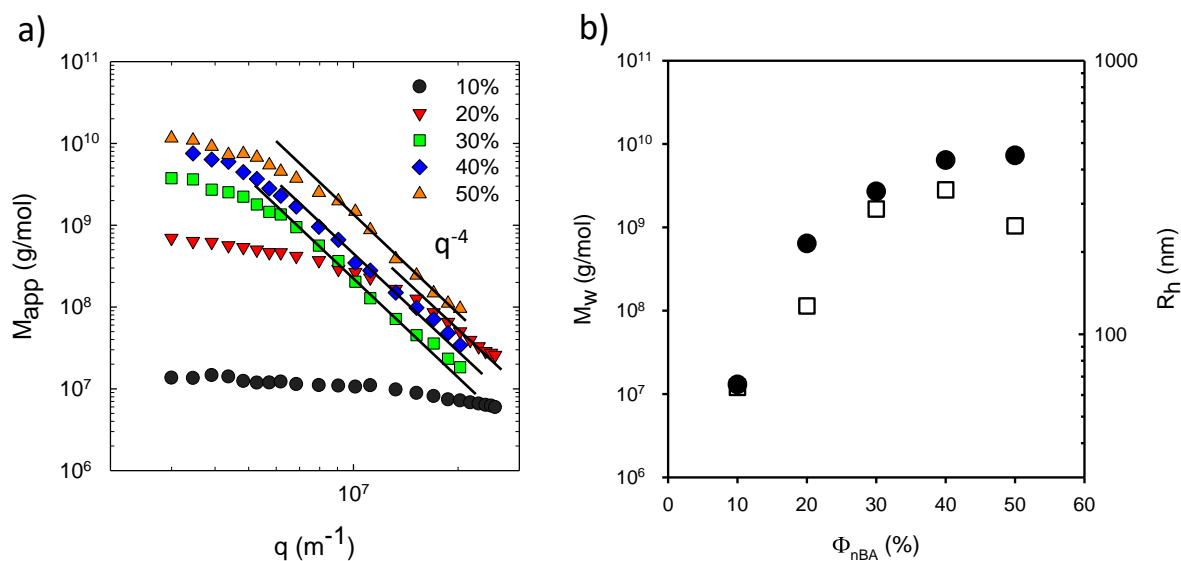
## ii. Influence of the volume fraction of C<sub>60</sub> solution

Despite their big sizes, particles were characterized by light scattering to obtain information about their internal structure and density. In Figure 6.10a, the apparent molar mass ( $M_{\text{app}}$ ) was plotted against the scattering wave vector,  $q$ . Please note that the absolute values must be taken carefully, because i) the concentration was deduced from the C<sub>60</sub>/nBA/water mixture, assuming that dialysis did not affect that much the total volume, thus the concentration of particles, ii) we used a  $dn/dC=1$  mL/g that we previously determined for C<sub>60</sub> (see section 3.2.a), but C<sub>60</sub> is actually chemically modified by amine grafting, which may affect its contrast. We have therefore probably underestimated the value of  $M_{\text{app}}$  here. However, since all the samples which appear on the plot were prepared with the same solution, and dialyzed in the same way, a comparison can at least be fairly achieved. The dependence of  $M_{\text{app}}$  on  $q$  is very strong. At high  $q$  values, one can observe a  $q^{-4}$  dependence for  $\Phi_{\text{nBA}} \geq 20\%$ , corresponding to a Porod regime and almost no intermediate scattering regime between the plateau at low  $q$  and the Porod at high  $q$ . Therefore, we can conclude that the particles are rather dense and spherical, in agreement with TEM observations. At low  $q$  values, the apparent molar mass tends toward



a plateau corresponding to the molar mass of the particles,  $M_w$ . Even though the particles are too big to accurately estimate their  $R_g$ , one can consider that the particle size follows the order of  $\Phi_{nBA}$ : 40>50=30>>20>>10%.

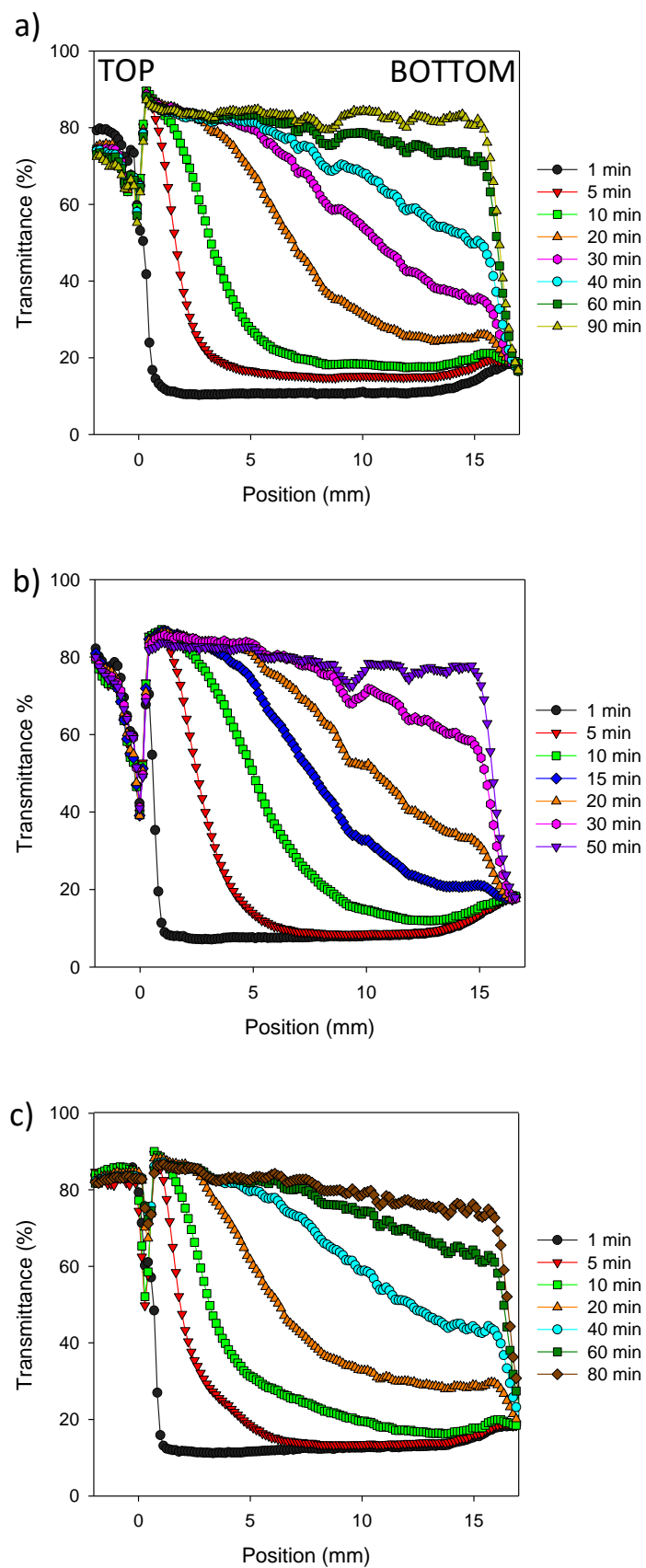
$M_w$  was plotted against  $\Phi_{nBA}$  in Figure 6.10b for  $C_{full}=2.4$  g/L. The molar mass increased with increasing  $\Phi_{nBA}$ , following roughly the same tendency as for their size in SLS. The influence of  $\Phi_{nBA}$  is much more important when it tends to 0, that is when producing smaller particles. In terms of  $R_h$ , the tendency is very similar to the size in SLS, see Figure 6.10b, and  $R_h$  can be increased by a factor 5 upon increasing  $\Phi_{nBA}$  from 10 to 40%. This is in contradiction with the literature, where the size of the particles should decrease with increasing  $\Phi_{nBA}$ , because the quality of solvent increases.<sup>8,9</sup> However, in literature the size measurements are carried out in the mixture, without removing the co-solvent, contrary to the present work. Furthermore, we believe that, additionally to Ouzo particles, other particles were generated during the dialysis treatment (see section 1.2.b.iii). The latter particles are much bigger because the process for their formation is very slow (one day). It is then difficult to establish what is the origin of some of the particles (Ouzo vs. dialysis) because again light scattering measurements on Ouzo particles obtained as they are is precluded.



**Figure 6.10.** a) Apparent molar mass plotted as a function of the scattering vector for various volume fractions of nBA (given in the figure) solution with  $C_{full}=2.4$  g/L. Solid lines have a slope equal to -4. b)  $M_w$  (close circles) values taken as the value of apparent molar mass at  $q=0$ , and  $R_h$  (open squares) as function of volume fraction of nBA solution.

Therefore, we used analytical centrifugation to further characterize the particles (see section 2.3.c). Transmittance profiles upon centrifugation are shown in Figure 6.11 for samples prepared at  $C_{full}=2.4$  g/L. The samples with  $\Phi_{nBA}=30$  and 50% are very similar. At the beginning

of the centrifugation, the transmittance is low all over the tube. After 20 minutes, a plateau of transmittance at the bottom of the sample indicates that a population of particles has already destabilized, while another is still suspended and slowly sedimenting. The profile is bent, meaning that the particles which do sediment are polydisperse. After 90 minutes of centrifugation, the samples are fully destabilized. The sample with  $\Phi_{nBA}=40\%$  displays a similar tendency, however the time scales are shorter. The sample, more turbid at  $t=0$  (8% transmittance vs. 12% for the two others), was destabilized within 50 minutes, which is nearly 2 times less than the others. It can thus be concluded that particles formed with  $\Phi_{nBA}=40\%$  are bigger than with  $\Phi_{nBA}=30$  or  $50\%$ . Therefore, analytical centrifugation measurements are in fair agreement with  $R_h$  value measured in DLS.

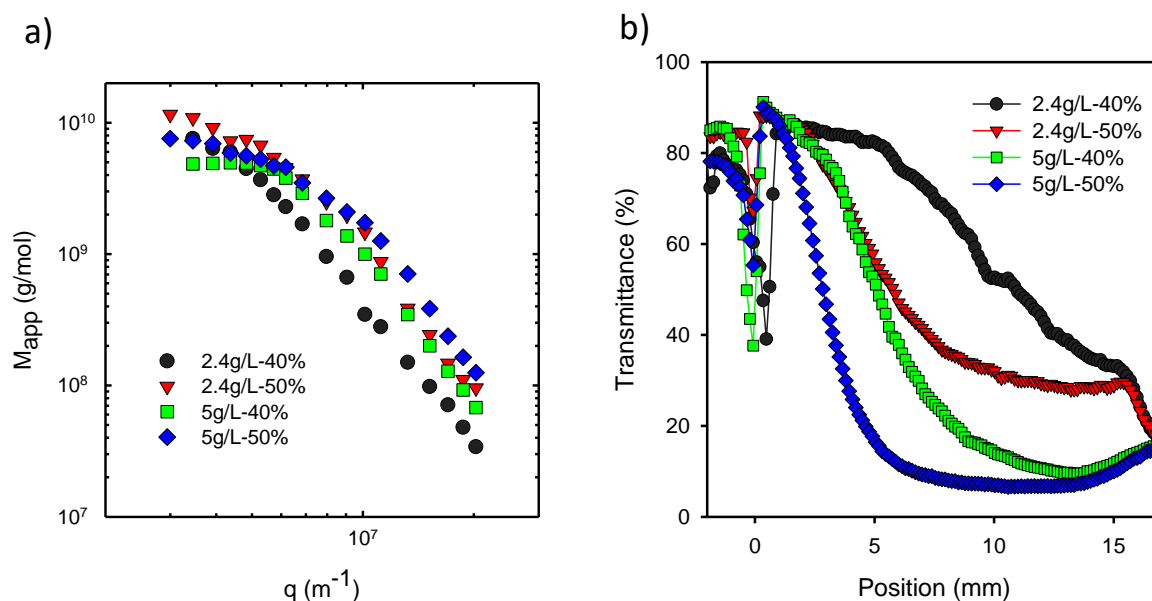


**Figure 6.11.** Transmission profiles upon centrifugation at 100g for samples prepared with  $C_{full}=2.4$  g/L and  $\Phi_{nBA}=30\%$  (a), 40% (b) and 50% (c).

## iii. Influence of fullerene concentration

The effect of  $C_{\text{full}}$  was investigated with both light scattering and analytical centrifugation. Samples were prepared with two mother concentrations: 2.4 and 5 g/L, with two volume fractions:  $\Phi_{\text{nBA}}=30$  and 40%. From SLS measurements (Figure 6.12a), the particles seem bigger for  $C_{\text{full}}=2.4$  g/L, because curves are shifted to lower  $q$  values for both  $\Phi_{\text{nBA}}$ .

Transmission profiles after 20 minutes of centrifugation at 100g, which corresponds to 33 hours at 1g, are given in Figure 6.12b. Clearly, the particles prepared with  $C_{\text{full}}=2.4$  g/L are much bigger than with 5 g/L, because they sedimented more. In addition, for  $C_{\text{full}}=5$  g/L, the profiles are less bent and do not display a plateau transmittance at the bottom of the tube, which can be explained by a lower dispersity in comparison to 2.4 g/L. This is once again in contradiction with literature.<sup>8-10</sup> We suggest that C<sub>60</sub> prepared at 5 g/L might not have reacted with nBA in the same extent as in the 2.4 g/L solution. If so, the fullerene is less functionalized by amines, and we already know that it is more stable when it is less functionalized (see section 6.1.b). Another possibility is that, since there is more C<sub>60</sub> in the 5 g/L solution, much more particles are formed upon addition of water, meaning that the additional particles hypothetically formed during dialysis, that are bigger, represent a lower proportion of the sample.



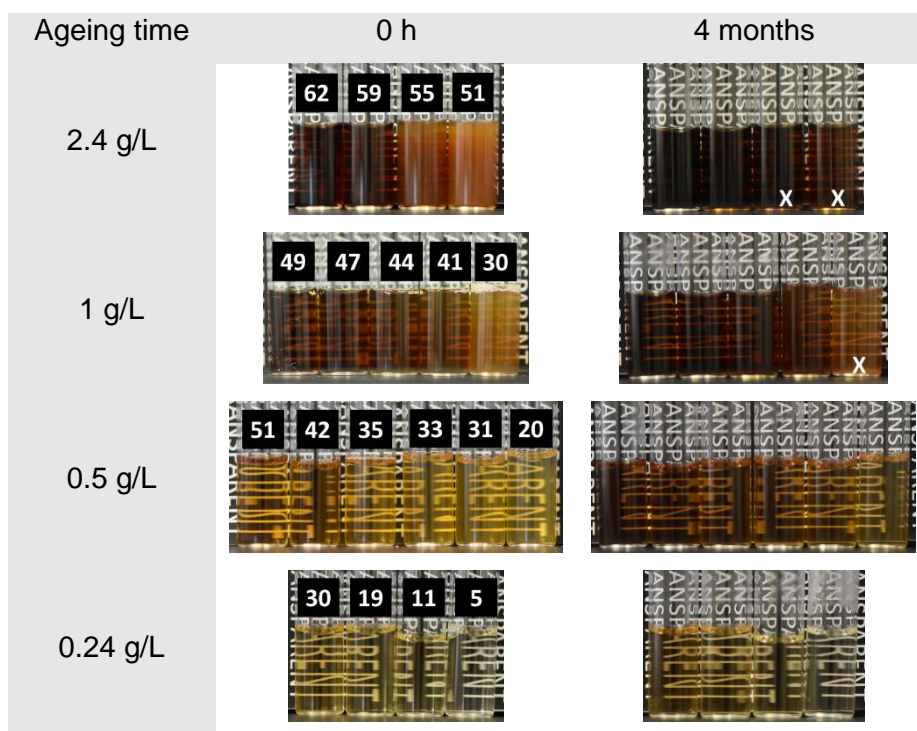
**Figure 6.12.** a) Apparent molar mass as a function of the scattering vector. b) Transmission profiles after 20 minutes of centrifugation at 100g.  $C_{\text{full}}$  and  $\Phi_{\text{nBA}}$  are given in the figure.

### 3) Stabilization by 75C12

It is well-known that the addition of surfactants or amphiphilic polymers reduces the size of the particles and enhances their stability.<sup>11</sup> Therefore, we added 75C12 in the formulation to study its effect on the size and stability of C<sub>60</sub> Ouzo particles.

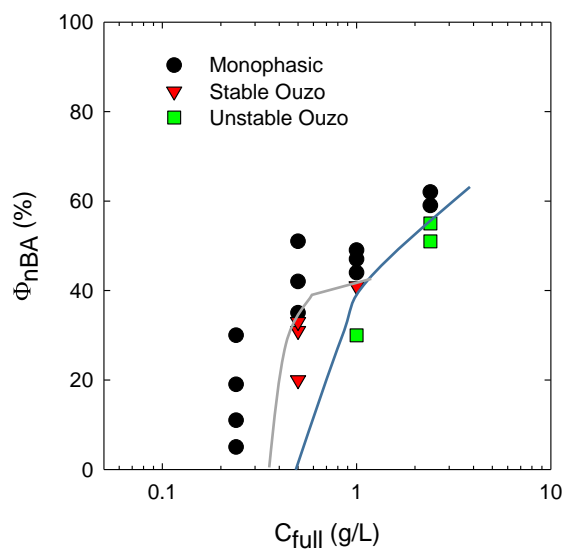
#### a. Effect on the state diagram and stability

The influence of 75C12 on the state diagram at  $t=0$  was assessed by adding a polymer solution with  $C_{\text{pol}}=10$  g/L instead of pure water to the C<sub>60</sub> solutions in nBA. Please note that 75C12 did not precipitate with the addition of nBA in any extent, although it is not soluble in nBA, so the latter cannot be considered as a good solvent for 75C12. Pictures of the samples are shown in Figure 6.13. The samples appear less turbid than without polymer. Also, the samples prepared with  $C_{\text{full}}=0.24$  g/L were not turbid at all with 75C12. After ageing for 4 months, the samples with  $C_{\text{full}}=2.4$  g/L still destabilized, however with  $C_{\text{full}}=1$  g/L only the sample prepared at  $\Phi_{\text{nBA}}=30\%$  displayed a deposit, and the samples with  $C_{\text{full}}=0.5$  g/L were all stable, in contrast with the samples prepared without 75C12 (see section 6.2.b). It should be noted that in the presence of 75C12, the excess fullerene was dark, and did not stick to the glass walls, contrary to the samples prepared without polymer. The addition of 75C12 might therefore prevent any further amination of C<sub>60</sub> once they are dispersed. Please note that as without polymer, it was not possible to re-suspend deposited particles by hand- or vortex-shaking. Contrary to samples prepared without polymer, there was no case where a sample came from turbid to transparent or the reverse way, after ageing.



**Figure 6.13.** Pictures of  $C_{60}/75C12/nBA$ /water Ouzo mixtures taken at various ageing times, with  $C_{full}$  indicated on the left. Volume fractions of nBA solution are indicated on the tube at  $t=0$ . Deposit is symbolized by an X symbol.

The state diagram after 4 months of ageing is displayed in Figure 6.14. From comparison with Figure 6.8 (section 6.2.b), one can see that the binodal is shifted towards lower  $\Phi_{nBA}$  values for  $C_{full}=2.4$ , 1 and 0.5 g/L. This can be interpreted as an increase of the quality of solvent, *i.e.* water in the presence of 75C12. Although the Ouzo samples at  $C_{full}=2.4$  g/L are not stable over long times, the monophasic ones remained stable contrary to the case where no polymer was added. The samples prepared with  $C_{full}=0.5$  g/L were all stabilized by 75C12. The Ouzo region is narrowed in the presence of 75C12, in favor of the SFME domain, which might be interesting to explore.

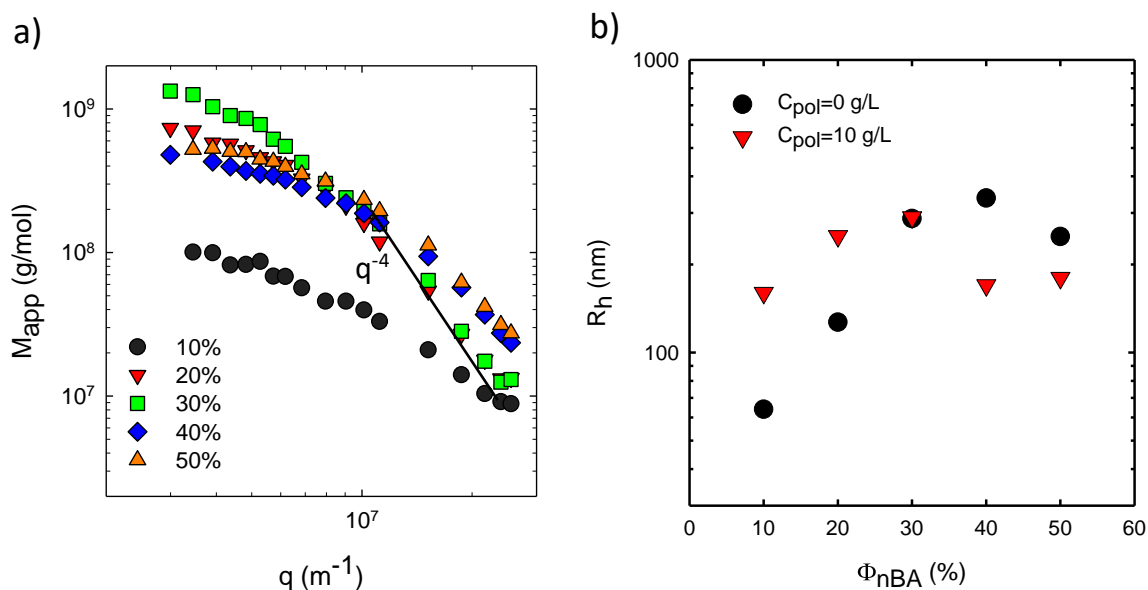


**Figure 6.14.** Ouzo state diagram for the C<sub>60</sub>/n-butylamine/75C12 10 g/L in water mixture, at 20°C and t=4 months. The gray line represents the binodal and the blue line, the spinodal.

#### b. Effect on the size of the particles

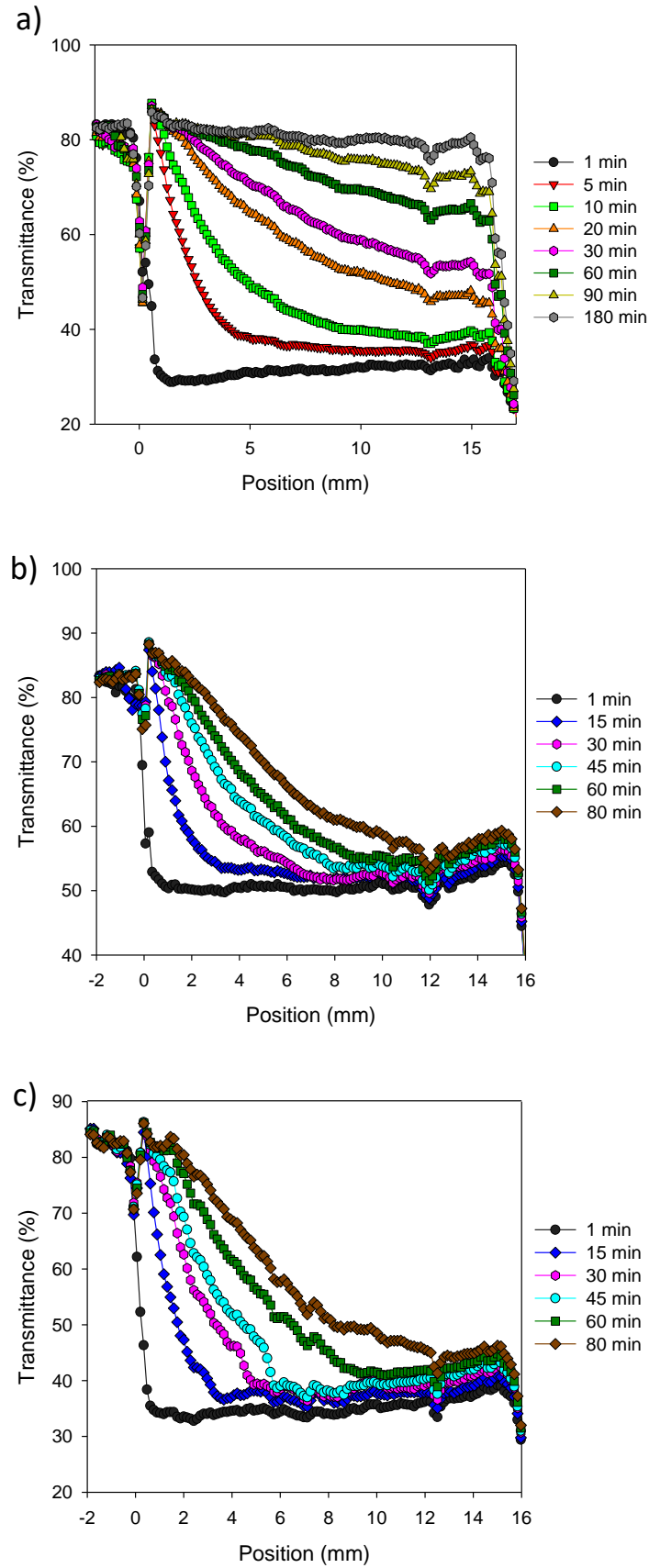
After dialysis, the particles were once again analyzed by light scattering. In terms of  $q$ -dependence (Figure 6.15a), the particles produced with  $\Phi_{nBA}=20$  and 30% were bigger than particles with other  $\Phi_{nBA}=10, 40$  and 50%. In terms of  $R_h$ , the tendency is the same (Figure 6.15b). Thus, particles formed at low  $\Phi_{nBA}$  (10 and 20%) were bigger than without polymer, but at high  $\Phi_{nBA}$  (40 and 50%), they were smaller. The absolute value of molar mass (after extrapolating to  $q=0$ ) is once again not fully correlated with the size. Generally speaking, the  $q$ -dependence of the samples prepared with 75C12 (Figure 6.14a) is lower than without it (Figure 6.10a), since Porod regime (with a  $q^{-4}$  dependence) is only observed for two of these samples, and only at higher  $q$  values.





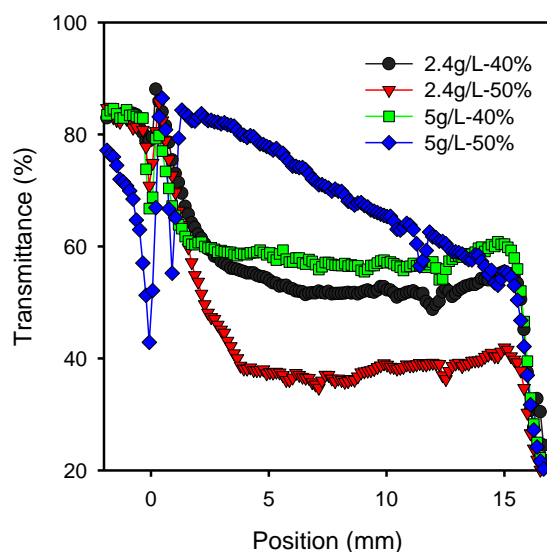
**Figure 6.15.** a) Apparent molar mass plotted as function of the scattering vector for various volume fractions of nBA solution given in the figure, with  $C_{full}=2.4$  g/L and  $C_{pol}=10$  g/L. Solid line has a slope equal to -4. b)  $M_w$  (close circles) values taken as the value of apparent molar mass at  $q=0$ , and  $R_h$  (open squares) as function of volume fraction of nBA solution.

In addition to light scattering, the samples were once again studied by analytical centrifugation, see Figure 6.16. First, the turbidity of the samples is much lower at  $t=0$  than without polymer (e.g. for  $\Phi_{nBA}=50\%$ , transmittance is equal to 35% with 75C12 vs. 12% without it). In all cases, sedimentation is much slower than without polymer (see Figure 6.11 for comparison). It is worth noting that the polymer concentration was low enough to have no consequence on the viscosity of the continuous phase,<sup>12</sup> therefore the samples can be directly compared to the ones without polymer. For example, for  $\Phi_{nBA}=30\%$  full destabilization took 180 min at 100g, which is two times longer than without polymer. We concluded that particles obtained with  $\Phi_{nBA}=30\%$  were much bigger than the ones obtained with  $\Phi_{nBA}=40$  and 50%, which are very similar at all centrifugation times, except for the turbidity that was lower for  $\Phi_{nBA}=40\%$ , probably because the particles concentration was lower. The samples are still polydisperse in size, however it is difficult to distinguish two distinct populations, and no particles sediment after short centrifugation times. Therefore, it seems that 75C12 inhibits the growth of big particles during dialysis.



**Figure 6.16.** Transmission profiles upon centrifugation at 100g for samples prepared with  $C_{full}=2.4$  g/L and  $\Phi_{nBA}=30\%$  (a),  $40\%$  (b) and  $50\%$  (c).

Samples with  $C_{\text{full}}=2.4$  and 5 g/L in the presence of 75C12 were analyzed by analytical centrifugation, see Figure 6.17. After 20 minutes of centrifugation at 100g, both samples with  $C_{\text{full}}=2.4$  g/L were still stable, and so was the sample with  $C_{\text{full}}=5$  g/L and  $\Phi_{\text{nBA}}=40\%$ . The sample with  $C_{\text{full}}=5$  g/L and  $\Phi_{\text{nBA}}=50\%$  was much less stable. In addition, it was much more turbid at  $t=0$  than the others (12% transmittance), which indicates a bigger particle size. This could be a result from depletion-induced aggregation by the polymer, and that could happen when particles concentration is high. In the majority of the cases, the samples are however much more stable with 75C12 than without it.



**Figure 6.17.** Transmission profiles after 20 minutes of centrifugation at 100g.  $C_{\text{full}}$  and  $\Phi_{\text{nBA}}$  are given in figure.

## Conclusions

C<sub>60</sub> fullerene nano- and microparticles were dispersed in water by Ouzo effect using a peculiar solvent, n-butylamine, in order to reach high concentrations. The n-butylamine reacts with C<sub>60</sub>, which requires a careful control of the age of the solutions before processing them. Transmission electron microscopy pictures evidenced the spherical and dense morphology of the particles, and their high dispersity. A suspension with a concentration of fullerene equal to 0.5 g/L was stable during 4 months without any stabilizer. The dialysis performed to remove n-butylamine generates particles that are bigger than the Ouzo particles. The presence of 75C12 as a stabilizer efficiently reduced this effect, but also reduced the size of the Ouzo region on the state diagram. The addition of the polymer helped at generating smaller particles that remained more stable due to their smaller sizes.

More systematic study regarding the size of the particles and their stability upon ageing, with and without polymer, still has to be made. For example, the question whether destabilization occurs only by sedimentation or by gradual aggregation of the particles is still unanswered and could be answered by comparing stability at 1g and 100g. Indeed, centrifugation increases sedimentation speed but does not influence the gradual aggregation. In addition, the influence of the dialysis step on the dispersion state of C<sub>60</sub> still has to be understood, and a quantification of the concentration of particles generated by Ouzo and dialysis could help understanding the phenomena taking place during this step.

This new Ouzo effect use could be helpful for the design of well-defined spherical particles of C<sub>60</sub> in water for a biomedical application for example, or for the design of materials for specific applications in optoelectronics. Most importantly, the ability to generate aqueous suspensions with concentrations on a g/L scale without any stabilizer that are stable for several days at least, with a very simple process that does not require any equipment, is very promising.

## References

1. Deguchi, S.; Alargova, R. G.; Tsujii, K., Stable Dispersions of Fullerenes, C<sub>60</sub> and C<sub>70</sub>, in Water. Preparation and Characterization. *Langmuir* **2001**, *17* (19), 6013-6017.
2. Douglas, L.; Markus, N.; Mutsuo, M.; Junzo, S., Complexation of C<sub>60</sub> Fullerene with Cholesteryl Group-Bearing Pullulan in Aqueous Medium. *Chemistry Letters* **2000**, *29* (1), 64-65.
3. Semenov, K. N.; Charykov, N. A.; Keskinov, V. A.; Piartman, A. K.; Blokhin, A. A.; Kopyrin, A. A., Solubility of Light Fullerenes in Organic Solvents. *Journal of Chemical & Engineering Data* **2010**, *55* (1), 13-36.
4. Ruoff, R. S.; Tse, D. S.; Malhotra, R.; Lorents, D. C., Solubility of fullerene (C<sub>60</sub>) in a variety of solvents. *The Journal of Physical Chemistry* **1993**, *97* (13), 3379-3383.
5. Markovic, Z.; Todorovic-Markovic, B.; Kleut, D.; Nikolic, N.; Vranjes-Djuric, S.; Misirkic, M.; Vucicevic, L.; Janjetovic, K.; Isakovic, A.; Harhaji, L.; Babic-Stojic, B.; Dramicanin, M.; Trajkovic, V., The mechanism of cell-damaging reactive oxygen generation by colloidal fullerenes. *Biomaterials* **2007**, *28* (36), 5437-5448.
6. Boucher, D.; Howell, J., Solubility Characteristics of PCBM and C<sub>60</sub>. *The Journal of Physical Chemistry B* **2016**, *120* (44), 11556-11566.
7. Qiao, J. L.; Gong, Q. J.; Du, L. M.; Jin, W. J., Spectroscopic study on the photoinduced reaction of fullerene C<sub>60</sub> with aliphatic amines and its dynamics — strong short wavelength fluorescence from the adducts. *Spectrochimica Acta Part A: Molecular and Biomolecular Spectroscopy* **2001**, *57* (1), 17-25.
8. Vitale, S. A.; Katz, J. L., Liquid Droplet Dispersions Formed by Homogeneous Liquid-Liquid Nucleation : The Ouzo Effect. *Langmuir* **2003**, *19* (10), 4105-4110.
9. Ganachaud, F.; Katz, J. L., Nanoparticles and Nanocapsules Created Using the Ouzo Effect: Spontaneous Emulsification as an Alternative to Ultrasonic and High-Shear Devices. *ChemPhysChem* **2005**, *6* (2), 209-216.
10. Goubault, C.; Iglicki, D.; Swain, R. A.; McVey, B. F. P.; Lefeuvre, B.; Rault, L.; Nayral, C.; Delpech, F.; Kahn, M.; Chevance, S.; Gauffre, F., Effect of nanoparticles on spontaneous «Ouzo» emulsification. *Journal of Colloid and Interface Science* **2021**.
11. Lepeltier, E.; Bourgaux, C.; Couvreur, P., Nanoprecipitation and the Ouzo effect : Application to drug delivery devices. *Advanced Drug Delivery Reviews* **2013**, *71*, 86-97.
12. Dutertre, F.; Benyahia, L.; Chassenieux, C.; Nicolai, T., Dynamic Mechanical Properties of Networks of Wormlike Micelles Formed by Self-Assembled Comblike Amphiphilic Copolyelectrolytes. *Macromolecules* **2016**, *49* (18), 7045-7053.









## General conclusion

The goal of this PhD project was to design nanocomposite hydrogels based on the assembly of an amphiphilic polymer, 75C12, and  $C_{60}$  fullerene. 75C12 self-assembled into worm-like micelles in water that can form physical gels when the concentration is high enough, by branching of the micelles. The gels are able to self-heal after breakage, but remain brittle. The idea was to form  $C_{60}$  particles in water stabilized by 75C12 and to integrate them in the hydrogel matrix to obtain a mechanical reinforcement and to provide the functionality of fullerene to these materials. The choice of 75C12 was also dictated by its chemical structure that could help at establishing weak interactions (hydrophobic,  $\pi$ -stacking) with fullerene.

The elaboration of the  $C_{60}$  particles in water at concentration high enough for applicative properties is a big challenge due to the intrinsic hydrophobicity of fullerene. An emulsification-evaporation process was developed using ultrasounds, for which processing conditions were varied. In a first approach, chloroform was used to co-solubilize 75C12 and  $C_{60}$ . The concentration of the resulting suspensions was low due to the low solubility of  $C_{60}$  in this solvent. The dispersion yield increased with polymer concentration, and full dispersion was achieved with only 0.1 g/L polymer. Interestingly, the particles that were generated in this way were tunable in size from 50 nm down to quasi-molecular state, by only varying polymer concentration. Solubilizing 75C12 in water instead of chloroform prior the emulsification step did not affect that much the results. However, since less polymer migrated to the oil/water interface than in the previous case, more polymer was needed to reach a full dispersion and to decrease the size of the particles.

When chloroform is replaced by carbon disulfide, much more  $C_{60}$  can be solubilized prior to emulsification. Moreover, despite the fact that  $CS_2$  is unable to solubilize 75C12, the latter was still able to go to the interface and to stabilize the particles. The change of solvent did not change much the results for low concentrations of fullerene. However, when the latter was increased up to saturation in carbon disulfide, the concentration of the final aqueous colloidal suspensions was also increased, and a concentration of up to 8 g/L of fullerene in water at best was reached, which is ca. 6 times higher than the highest value reported in literature for neat  $C_{60}$ . The suspensions were fairly stable and their absorption spectrum was shown to depend on the size of the particles which required the quantification of  $C_{60}$  concentration in water to be achieved by using a specific band in UV.

The most surprising outcome was the morphology of the particles generated in these conditions. Cryo-TEM pictures evidenced that the nanoparticles were mostly nanoplatelets, with a small thickness around 10 nm according to small-angle X-ray scattering experiments,

and polydisperse lengths and widths of few hundreds of nanometers. The size of the nanoplatelets was not tunable via the polymer concentration, but it was controllable through the volume fraction of the organic solvent used in the emulsification step. These platelets were only obtained with 75C12 and a polymer with a similar chemical structure, 45C12, that self-assembled into lamella-shaped micelles rather than worm-like ones. Another polymer of this family that does not self-assemble, 75C4, poly(styrene sulfonate) and surfactants with chemical structures close to the one of 75C12 and 45C12, dodecyltrimethylammonium chloride and benzyldodecyldimethyl-ammonium chloride, did not drive the formation of such nanoplatelets. Therefore, the self-assembly into anisotropic micelles seems to be a prerequisite for the formation of nanoplatelets. However, the mechanism for formation of nanoplatelets and the requirements regarding the best chemical structure that the stabilizer should present are still not fully understood. In addition, one could wonder if the dimensions of the nanoplatelets could be controlled. The growth of the particles may occur within the hydrophobic microdomains of the polymeric micelles which could help at relating the thickness of the nanoplatelets to the size of the micelles, however no demonstration of this has been made yet.

The nanoplatelets are crystalline as demonstrated by cryo-TEM pictures and X-ray diffraction. The crystalline order of pure  $C_{60}$ , which is either face-centered cubic or hexagonal close packed structure, is observed. However, additional diffraction rays were observed, that could originate from a new ordering of  $C_{60}$ . This structure is yet unidentified however it should be related to the original growth of the nanoplatelets. From cryo-TEM pictures, it was observed that only the extremities of the nanoplatelets in the direction of their length are round-shaped, the other edges being linear. The growth therefore should happen only in one direction. The co-existence of several  $C_{60}$  phases is probably related to the co-existence of two morphologies: the nanoplatelets that are majority and the less-defined isotropic particles. In the future, this possibility will be tested by acquiring cryo-TEM pictures on individual particles in order to achieve Fourier transforms on each type of them and determine individually their crystalline structure.

Nanocomposite hydrogels were then elaborated by freeze-drying the aqueous colloidal suspensions followed by re-dispersion in water; this way of processing leads to the stacking of the platelets. The incorporation of  $C_{60}$  particles in the network induced an increase of its stiffness, without influencing its dynamics and temperature/time dependence. Despite the presence of stacked platelets as fillers, the nanocomposite hydrogels were able to display self-healing properties after breakage. This demonstrates strong interactions between  $C_{60}$  and 75C12. The nanocomposite hydrogels are new materials containing a high concentration of  $C_{60}$  (up to 50 g/L), which could open new doors for fullerene-based materials. For instance, we

can envision to use them as inks for the design of optoelectronic devices. At rest the nanoparticles are stable due to the gel nature of the suspensions and upon flow, shear-thinning properties allow the ink to be deposited easily onto surfaces.

As an alternative to the emulsification-evaporation method, the Ouzo effect was used to elaborate C<sub>60</sub> particles in water with a very simple and easy to scale-up process. A peculiar co-solvent, n-butylamine, was used to reach high C<sub>60</sub> concentrations, up to 2.8 g/L. The Ouzo particles were spherical and very polydisperse in size, with a size varying between 0.1 and 1 μm. Their stability was good even in the absence of any stabilizer. The addition of 75C12 helped at increasing the stability of the particles by reducing the average size. We did not try to integrate them into 75C12 gels yet, but it can be expected that their shape may induce other mechanical properties for the nanocomposite hydrogels than nanoplatelets. The amine reacted with C<sub>60</sub>, so the particles cannot be considered as pristine C<sub>60</sub>. Still, many things have to be explored further. For example, since C<sub>60</sub> contains amine functions on its surface, varying the pH to tune the ionization degree of these fullerene derivatives could induce interesting co-assemblies with the cationic polymer.

To conclude, we used two widely-used processes, emulsification-evaporation and Ouzo effect, to produce C<sub>60</sub> particles. Thanks to the variety of processing conditions, we were able to elaborate isotropic particles with sizes below 50 nm for the first process, and above 100 nm for the second one. We also reported the formation of fullerene nanoplatelets with sizes of several hundreds of nm. The physical and biological properties of the nanoplatelets still have to be assessed and some characterizations are ongoing. The nanoplatelets have already proved to be able to mechanically reinforce hydrogels, paving new ways for fullerene-based materials.

For the nanoplatelets, one of the most interesting challenges ahead is the control of their dimensions. To achieve it, the mechanism of their formation must be better understood. This can be made by studying their crystalline structure, individually with cryo-TEM pictures as we proposed above, to model their growth mechanism. In addition, the role of the stabilizer in the formation of nanoplatelets could be better caught by using other polymers or surfactants that would also self-assemble into anisotropic micelles. If the thickness of the nanoplatelets can effectively be controlled by the size of the micelles, an interesting choice could be other polymers from the same family as 75C12 with longer alkyl chains, that form thicker micelles as it was already demonstrated in the past.<sup>1</sup>

In the frame of this work, the emulsification-evaporation process has exclusively been used for neat C<sub>60</sub> particles generation. It could be extended to other fullerene derivatives, such as [6,6]-phenyl-C<sub>61</sub>-butyric acid methyl ester (PCBM), which is a very widely used compound in the

elaboration of optoelectronic devices such as organic photovoltaic cells. PCBM is very soluble in chloroform (28.8 g/L)<sup>2</sup>, so the latter solvent would give the opportunity to co-solubilize it with 75C12. In this way, particles of PCBM with various sizes and morphologies could be obtained, which has a high potential for the design of aqueous inks for photovoltaic applications.<sup>3</sup> Other fullerene derivatives could be used, such as anionic species or fullerenes functionalized with alkyl chains, in order to increase the interactions with 75C12 (electrostatic in the first case, hydrophobic in the second). These enhanced interactions could have a positive influence on the mechanical properties of nanocomposite hydrogels derived from them.

For Ouzo particles, tuning the solvent quality could lead to interesting self-assemblies of fullerene. The solvent quality could be varied thanks to parameters such as ionic strength (via addition of salt in water), pH (to tune the ionization degree of aminated fullerene), and/or addition of various stabilizers. If the particles can indeed be positively charged at low pH, adding negatively charged stabilizers could induce strong attractive interactions and form original co-assemblies. We believe this work opened many new doors for the processing of fullerene in water, and Ouzo in particular have a high potential for biomedical applications.

## References

1. Limouzin-Morel, C.; Dutertre, F.; Moussa, W.; Gaillard, C.; Iliopoulos, I.; Bendejacq, D.; Nicolai, T.; Chassenieux, C., One and two dimensional self-assembly of comb-like amphiphilic copolyelectrolytes in aqueous solution. *Soft Matter* **2013**, *9* (37), 8931-8937.
2. Boucher, D.; Howell, J., Solubility Characteristics of PCBM and C60. *The Journal of Physical Chemistry B* **2016**, *120* (44), 11556-11566.
3. Holmes, N. P.; Marks, M.; Kumar, P.; Kroon, R.; Barr, M. G.; Nicolaidis, N.; Feron, K.; Pivrikas, A.; Fahy, A.; Mendaza, A. D. d. Z.; Kilcoyne, A. L. D.; Müller, C.; Zhou, X.; Andersson, M. R.; Dastoor, P. C.; Belcher, W. J., Nano-pathways: Bridging the divide between water-processable nanoparticulate and bulk heterojunction organic photovoltaics. *Nano Energy* **2016**, *19*, 495-510.



**Titre :** Hydrogels nanocomposites obtenus par auto-assemblage de polymères amphiphiles et de fullerène

**Mots clés :** Fullerène  $C_{60}$ , polymère amphiphile, suspensions colloïdales, hydrogels nanocomposites, émulsification-évaporation, effet Ouzo

**Résumé :** Cette thèse traite de l'élaboration de particules colloïdales de fullerène  $C_{60}$  en milieu aqueux en combinant un polymère amphiphile comme stabilisant, et deux procédés de dispersion. Un premier procédé d'émulsification-évaporation impliquant des ultrasons a permis d'obtenir une grande variété de particules en termes de morphologies et tailles. On peut former des particules isotropes de 2 à 50 nm et des nanofeuillets de fullerène de 10 nm d'épaisseur et de longueur et largeur de quelques centaines de nm. Le mécanisme de nucléation-croissance des particules est discuté, ainsi que la caractérisation structurale surtout des nanofeuillets, par des techniques de diffusion de la lumière et des rayons X et par cryomicroscopie électronique à transmission permettant de les sonder à différentes échelles de longueur.

Les particules s'avèrent être cristallines. L'incorporation de telles particules dans des hydrogels a permis d'en augmenter la rigidité, sans affecter leur capacité à se régénérer après rupture. Le second procédé : l'effet Ouzo, a été utilisé pour élaborer des particules de fullerène sphériques et plus grosses qu'avec l'autre méthode (tailles variant entre 100 et 1000 nm). Le diagramme de phase a été établi, ainsi que l'influence de divers paramètres procédé sur la taille des particules. De nouveau, l'ajout de polymère amphiphile a permis d'obtenir des particules plus stables comme établi par des études de centrifugation analytique.

**Title :** Nanocomposite hydrogels from the self-assembly of an amphiphilic polymer and fullerene

**Keywords :**  $C_{60}$  fullerene, amphiphilic polymer, colloidal suspensions, nanocomposite hydrogels, emulsification-evaporation, Ouzo effect

**Abstract :** This thesis reports on the design of colloidal particles of fullerene  $C_{60}$  dispersed in water mediated by the use of an amphiphilic polymer which acts as a stabilizer, and through two dispersion processes. The first one is emulsification-evaporation assisted by ultrasounds. A wide variety of morphologies and sizes of nanoparticles was then produced, ranging from isotropic particles (with size between 2 and 50 nm) to nanoplatelets whose thickness was approximately 10 nm, and the length and width a few hundreds of nm. A nucleation-growth mechanism for the nanoparticles is discussed, as well as their structural investigation using scattering techniques (light and X-ray) combined with cryo-transmission electron microscopy for covering a wide length scale.

The particles appeared to be crystalline. The incorporation of such nanoparticles within hydrogels resulted in an increase of their stiffness, without affecting their ability to self-heal after rupture. The second dispersion process, namely the Ouzo effect, was used to produce fullerene spherical particles which were spherical and larger than with the other method (sizes varying between 100 and 1000 nm). The phase diagram has been established and various processing parameters have been tuned for modifying the size of the particle. Here again, the use of the amphiphilic polymer has allowed to make the particles much more stable as characterized by analytical centrifuge measurements.